Geocell-Reinforced Unpaved and Paved Roads with Recycled Asphalt Pavement (RAP) Bases: Experimental Study and Damage Model Development

By

Jitendra Kumar Thakur
B.E., Tribhuvan University, Nepal, 2007
M.Sc., University of Kansas, 2011

Submitted to the graduate degree program in Civil, Environmental, and Architectural Engineering and the Graduate Faculty of the University of Kansas in partial fulfillment of the requirements for degree of Doctor of Philosophy

_____

Dr. Jie Han, Chairperson

_____

Dr. Yaozhong Hu

Committee members

_____

Dr. Anil Misra

_____

Dr. Robert L. Parsons

_____

Dr. Steven D. Schrock

Date defended:

_____

The dissertation Committee for Jitendra Kumar Thakur certifies

that this is the approved version of the following dissertation:

Geocell-Reinforced Unpaved and Paved Roads with Recycled

Asphalt Pavement (RAP) Bases: Experimental Study and

Damage Model Development

Dr. Jie Han

_____

Chairperson

Date approved:

_____

ABSTRACT

Recycled Asphalt Pavement (RAP) is a removed and reprocessed pavement material from deteriorated asphalt pavements containing asphalt binder and aggregates. The use of RAP can reduce the cost of construction materials, reduce the amount of waste to be land-filled, and conserve natural resources by requiring less virgin aggregate and asphalt in road construction projects. Literature showed that RAP bases had more permanent deformation under static and dynamic loading compared to conventional aggregate base. Geocell is one type of geosynthetic products manufactured in a form of three-dimensional interconnected honeycomb shape polymeric cells. Geocell was used in this study to reinforce RAP bases in unpaved and paved roads. The objective of this study is to understand the behavior of unpaved and paved roads with unreinforced and geocell-reinforced RAP bases.

Fifteen large-scale laboratory cyclic plate loading tests were conducted on unpaved and paved road sections with unreinforced or geocell-reinforced RAP bases. The unpaved road sections consisted of unreinforced or geocell-reinforced RAP bases over weak or moderate (target CBR = 2% or 5%) subgrade, whereas paved road sections consisted of hot mix asphalt (HMA) surface over unreinforced or geocell-reinforced RAP bases over moderate (target CBR = 5%) subgrade to investigate their performance and shake down responses under cyclic loading. The test results showed that geocell improved the performance of RAP bases as compared with the unreinforced bases by increasing the percentage of resilient deformation and reducing the permanent deformations and the vertical stresses transferred to the subgrade. A

thin (about 50 mm) HMA surface significantly improved the performance of RAP bases. The thicker geocell-reinforced RAP base behaved as a slab with bending resistance and the thinner base behaved as a slab initially at a smaller deformation and then as a tensioned membrane at a larger deformation. The geocell-reinforced RAP bases showed a stable shakedown response whereas the unreinforced RAP base showed an unstable shakedown response.

Based on cyclic plate loading test results, damage models for the empirical correlation between the permanent strain and/or the resilient strain with the number of loading cycles were developed for unpaved and paved roads including unreinforced and geocell-reinforced RAP bases. The mechanistic empirical model can be incorporated in the AASHTO Mechanistic Empirical Pavement Design Guide (MEPDG), which will promote the sustainable use of RAP with geocell for roadway construction.

DEDICATION

The author dedicates this work to his parents,

Mr. Ram Swarth Thakur and Mrs. Kamalesh Devi

ACKNOWLEDGEMENT

The gratitude is extended to my elder brother (Ajay Thakur), elder sisters (Anju, Indu, Rinku), brother in laws (Ashok, Mukesh and Arun), and sister in law (Sadhna Thakur). Last but not least, my very special thanks go to my parents, Mr. Ram Swarth Thakur and Mrs. Kamalesh Devi, whom I owe everything as I am today. They always support me and encourage me with their best wishes.

TABLE OF CONTENTS

LIST OF FIGURES

xviii

LIST OF TABLES

CHAPTER 1

INTRODUCTION

1.1   *Problem Statements*

According to the National Asphalt Pavement Association (NAPA), the United States has more than 3.2 million km of paved roads, out of which 94% are flexible pavements (Copeland et al., 2010).   Flexible pavements those have reached the end of their service lives are frequently rehabilitated by removing the existing hot mix asphalt (HMA) surfaces and replacing the removed portion with new HMA. A large amount of recycled asphalt pavement (RAP) materials are created every year during the rehabilitation and reconstruction of existing flexible pavements. RAP is obtained either by milling or a full depth recovery method. Milling involves the mechanical removal of up to 50 mm thick pavement surface in a single pass whereas a full-depth recovery method uses a pneumatic pavement breaker or rhino horn on a bulldozer (Viyanant et al., 2007) to remove the whole pavement surface. According to NAPA, the United States produced about 500 million tons of asphalt pavement materials each year. The use of RAP has been in practice since 1930s and is necessary to reduce the cost of construction materials; to reduce waste of petroleum-based products; and to conserve natural resources by requiring less virgin aggregate and asphalt in road construction projects. A survey conducted by the North Carolina Department of Transportation (NCDOT) on behalf of the Federal Highway Administration (FHWA) and the American Association of State Highway and Transportation Officials (AASHTO) in 2007 and 2009 showed that

1

use of RAP was increasing across the nation (Copeland et al., 2010). About 100 million tons of RAP were used by different transportation agencies of the United States each year, compared to 72 million tons used annually in the early 1990s (Copeland et al., 2010).

Literature review shows that RAP has been mostly used with new asphalt binder to form hot-mix asphalt (HMA) concrete as a pavement layer. The amount of RAP used in the HMA concrete typically ranges from 15 to 50%. The FHWA supports the use of RAP as an alternative to virgin aggregate and asphalt in pavement construction. Papp et al. (1998) reported that use of RAP as a granular base material in pavement construction can be a sustainable option for pavement construction. According to the Recycled Material Resource Center (RMRC, 2008), typical RAP contains 3 to 7% asphalt binder and 93 to 97% aggregate. Literature revealed that 100% RAP could not produce base course of high quality. Several studies have been conducted in the past to improve the performance of RAP bases by blending RAP with virgin aggregates, stabilizing RAP using chemical additives and have found that increasing virgin aggregate content in the blends decreased resilient modulus (M_R) and permanent deformation and increased CBR of blended RAP samples, whereas increasing fly ash content increased M_R and CBR and decreased permanent deformation of fly ash-stabilized RAP. However, limited research has been conducted to investigate the performance of RAP stabilized with geosynthetics, especially geocell.

Most studies on geocell reinforcement to date have been based on sand or aggregate as infill materials. Currently, great emphasis is placed on sustainable construction and infrastructure with green technology because the demand for

2

sustainable and environmental friendly roads is increasing day by day. One way to construct environmentally sound roads is through the use of recycled asphalt pavement (RAP) materials. Peter Stephanos, the director of the FHWA Office of Pavement Technology stated that "recently, most state DOTs are seriously considering the economic and environmental benefits of using RAP in greater proportions and facing challenges to maintain high-quality pavement infrastructures" (Copeland et al., 2010). Very limited studies (for example, Han et al. 2011; Bortz et al. 2012) have been conducted to improve the performance of RAP bases using geosynthetics, especially geocell. No widely accepted design and analysis methods for geocell-reinforced roads are available, which have limited the usage of geocell. No study has been done to develop a damage model for permanent deformations of geocell-reinforced RAP pavements.

1.2   *Objective and scope*

The objectives of this study are to understand the load transfer mechanism and deformation behavior of unpaved and paved roads with geocell-reinforced RAP bases under cyclic loading and develop damage models for empirical correlation between the permanent strain and/or the resilient strain with the number of loading cycles for unreinforced and geocell-reinforced RAP unpaved and paved roads. These models can be incorporated in the AASHTO Mechanistic Empirical Pavement Design Guide (MEPDG), which will promote the sustainable use of RAP with geocell for roadway construction. Development of the damage models will assist pavement engineers to evaluate the deformation behavior and life of RAP pavements under repeated loading.

In this study, a series of laboratory cyclic plate loading tests were conducted on unpaved and paved roads with unreinforced and geocell-reinforced RAP bases over weak (CBR = 2%) and moderate (CBR = 5%) subgrades in a large test box to investigate the benefits of geocell confinement, HMA layer, base thickness, and base and subgrade strengths in improving the performance of RAP bases. The typical sections of unpaved and paved roads with unreinforced and geocell-reinforced RAP bases are shown in **Figs. 1.1 (a**, **b)** and **1.2 (a**, **b)**, respectively. The improvements in the performance are presented in terms of reduction in the surface permanent deformation and increase in the resilient deformation. The reduction in surface permanent deformation was presented in terms of traffic improvement factor (TIF). In addition, the test results were used to develop damage models for permanent deformations of unreinforced and geocell-reinforced RAP bases.

(a) Unreinforced base   **(b)** Geocell-reinforced base

Fig. 1.1   Unpaved road

(a) Unreinforced base   **(b)** Geocell-reinforced base
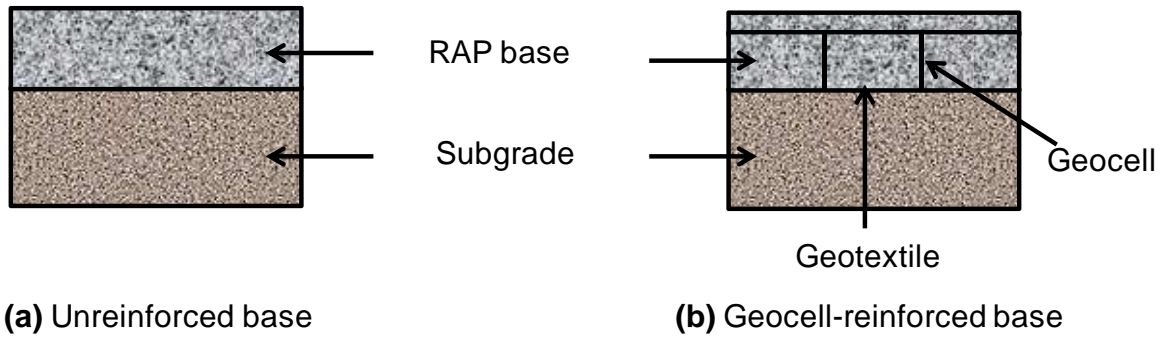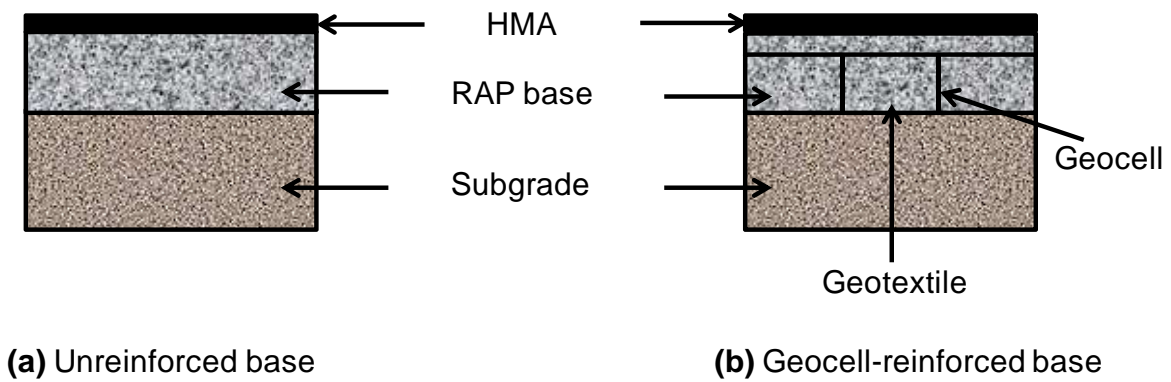
Fig. 1.2   Paved road

1.3   Organization of this dissertation

This dissertation consists of the following seven chapters:

Chapter 1 - Introduction: This chapter describes problem statements, objectives, and scope of this study.

Chapter 2- Literature review: This chapter includes review of past studies relevant to this research. These studies were focused on the recycled asphalt pavement (RAP), blended RAP aggregate bases, chemical stabilized RAP bases, geocell-reinforced

bases, design and analysis of geocell-reinforced bases, and damage models for permanent deformations of granular bases.

Chapter 3 - **Materials and their properties**: This chapter covers the properties of all the materials (geocell, geotextile, HMA, Tack coat, RAP, and subgrade) used in this study.

Chapter 4- **Large-scale cyclic plate loading tests on unpaved roads**: This chapter describes the test equipment and procedures, instrumentations, and analyzes the test results obtained from large-scale laboratory cyclic plate loading tests conducted on unpaved road sections with unreinforced and geocell-reinforced RAP bases under cyclic loading.

Chapter 5- **Large-scale cyclic plate loading tests on paved roads**: This chapter describes the test equipment and procedures, instrumentations, and analyzes the test results obtained from large-scale laboratory cyclic plate loading tests conducted on paved road sections with unreinforced and geocell-reinforced RAP bases under cyclic loading.

Chapter 6- **Development of damage model**: Based on the test results obtained from cyclic plate loading tests discussed in chapters 4 and 5, damage models were developed for unpaved and paved roads with unreinforced and geocell-reinforced RAP bases and are presented in this chapter.

Chapter 7- Conclusions and recommendations: This chapter presents the conclusions from this study and the recommendations for future study.

CHAPTER 2

LITERATURE REVIEW

2.1   Introduction

This chapter provides a literature review on the related topics of this study which include overview of recycled asphalt pavement (RAP) and geocell; geosynthetics and their reinforcement mechanism, previous experimental studies on blended RAP aggregate base, chemical stabilized RAP base, geosynthetic-reinforced RAP base; design/analysis method for geocell-reinforced base; damage model for permanent deformation of granular bases.   In addition, this chapter also discusses about the findings and limitations of the studies discussed in the literature review.

2.2   Recycled asphalt pavement (RAP)

According to the National Asphalt Pavement Association (NAPA), more than 90% of U.S. roads and highways are paved with hot-mix asphalt (HMA) (Copeland et al., 2010). The federal, state, and local transportation agencies are facing an increasing demand of raw materials needed for new and rehabilitation road projects.   RAP is the surplus material generated from the reprocessing of removed flexible pavements.   It contains asphalt binder and aggregates.   HMA producers and different transportation agencies are suggesting RAP as an alternative to virgin aggregate and asphalt to fulfill the shrinking supply of raw materials and deal with the rising costs of aggregates and binders (Copeland et al., 2010).

2.2.1 Current production and use of RAP

The use of RAP was practiced as early as 1915 and gained popularity in the mid-1970s when asphalt binder prices increased significantly as a result of the Arab oil embargo. The FHWA estimated that 100.1 million tons of asphalt pavements were milled off each year during resurfacing and widening projects and about 80.3 million tons were reused in the construction of roads, roadbeds, shoulders, and embankments (Missouri Asphalt Pavement Association, 2010). RAP has been increasingly used with virgin aggregate and asphalt binder to make HMA or warm-mix asphalt.

According to the User Guidelines for Byproducts and Secondary Use Materials in Pavement Construction (FHWA-RD-97-148, 2008), RAP can be used as a granular base material in paved and unpaved roadways, parking areas, bicycle paths, gravel road rehabilitation, shoulders, residential driveways, trench backfill, engineered fill, and culvert backfill. According to FHWA, RAP can be used as granular base or subase aggregate, embankment or fill material, or used with hot-mix asphalt, cold-mix asphalt, and cold in-place asphalt (Thakur, 2011).

Copeland (2011) reported the results of survey conducted by North Carolina Department of Transportation (NCDOT) on behalf of AASHTO and RAP ETG (expert task group) to determine the amount of RAP used across all 50 States of the United States as well as Ontario, Canada. The survey results showed that approximately 50% states in 2009 used more RAP in surface and intermediate layers of pavements than in 2007. **Fig. 2.2.1** presents the percentages of RAP used and permitted by the number of State Department of Transportation (DOT) in the intermediate and surface layers of pavement. **Fig. 2.2.1** shows that the maximum permitted amount of RAP is not being

9

used throughout the nation. Fewer states allow the use of RAP in surface layer than in intermediate layers.
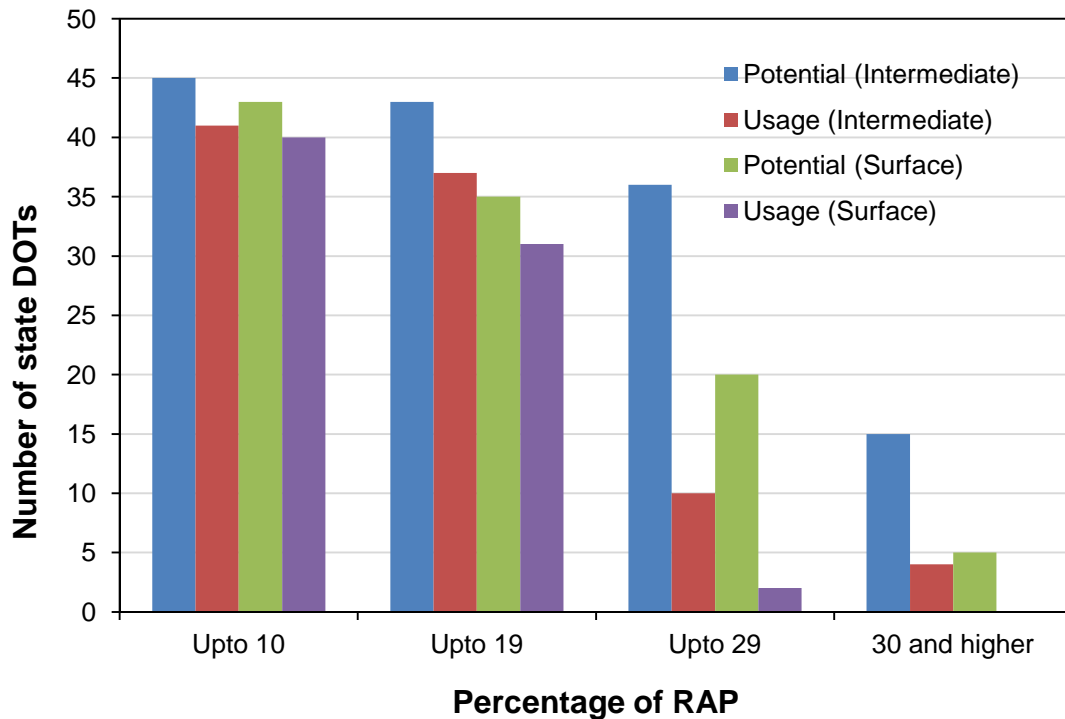
Fig. 2.2.1   Potential and usage of RAP in intermediate and surface layers (modified from Copeland, 2011)

West (2011) reported that the amount of RAP used in HMA mixes across the United States was around 12 to 15% and NAPA had aimed to raise it to 25% by the end of 2013. McGarrah (2007) conducted extensive literature review to investigate the practices of different DOTs regarding the use of RAP in grnular base course materials and the results are presented in **Table 2.2.1**. New Jersey and Colorado DOTs used 100% RAP as base course materials in 2007. However, these two material departments modified these values, which are presented in **Table 2.2.1**. For Minnesota

and Utah DOTs, the maximum percentages given in the table are the maximum asphalt contents allowed in the RAP blend.

Table 2.2.2 presents the test results of survey conducted by AASHO regarding the usage of RAP in asphalt bound base and HMA surface for the construction of pavements by the state DOTs in the United States.

Table 2.2.1 Practices of DOTs regarding use of RAP as granular base material (modified from McGarrah, 2007)

State	RAP (%)
Florida	0
Illinois	0
Montana	50-60
New Jersey	50
Minnesota	3
Colorado	50
Utah	2
Texas	20
California	50
New Mexico	Unknown
Rhode Island	Unknown
South Dakota	0

Table 2.2.2   Percentages of RAP used by state DOTs in pavement construction
(modified from Han et al., 2012)

State	% limit of RAP	
	Asphalt bound base	HMA surface
Alaska	20	0
Arizona	25	20
California	NA	15
Colorado	15	20
Delaware	NA	35
DC	25	15
Florida	40-45	20
Illinois	NA	30
Iowa	20	NA
Kansas	30-40	15
Louisiana	30	15
Maine	30-35	15-25
Michigan	18-27	17
Mississippi	30	15
Montana	25-50	10
New Mexico	NA	35
North Dakota	NA	20
Ohio	30-40	25-Oct
Oklahoma	30	15
Oregon	30	15
Tennessee	35	20
Texas	15-40	10-20
Utah	NA	30
Wisconsin	35	25
Wyoming	NA	30

2.2.2 Advantages of using RAP

The following are the advantages of using RAP (Thakur, 2011):

(i)   It preserves the natural environment.

(ii)   It reduces the amount waste disposal.

(iii) It reduces demand for aggregate and bituminous binder.

(iv)   It reduces energy and transportation costs in getting construction materials (aggregate and asphalt binder).

(v)   It provides cost effective material for highway construction.

(vi)   It demonstrates reasonable life cycle cost and good engineering performance.

2.2.3 Barriers against use of RAP

Copeland et al. (2011) reported the following common barriers among state DOTs and contractors in the publication "FHWA-HR t-11-021" as shown in **Table 2.2.3**.

Table 2.2.3 Common barriers against use of RAP (modified from Copeland et al., 2011)

Common Barriers	State DOTs	Quality concerns
		Consistency of RAP
		Binder grade and bending
		Mix design procedures
		Volumetric requirements
		Durability and cracking performance
		Use with polymers
	Contractors	State DOT specifications
		Control of RAP
		Dust and moisture content
		Increased quality control

2.2.4 Requirements for greater use of RAP

Copeland et al. (2010) reported the top 10 requirements for greater use of RAP in the publication FHWA-HRT-10-001.

(i) Performance tests for evaluating RAP mixtures

(ii) Best practices of mix design and constructions

(iii) Ability to characterize RAP without harmful solvents

(iv) Determination of necessary changes in binder performance grade

(v) Determination of amount of RAP mixed with virgin HMA

(vi) Field performance data on high-RAP mixtures

(vii) Ability to replicate plant heating in labs for virgin and RAP binder blending

(viii)   Assistance to states RAP specifications and current practices

(ix)   Improved understanding of variability of RAP

(x)   Implementation of best practices for processing RAP, including evaluating the need for fractionation

2.3   *Geosynthetics and their reinforcement mechanism*

Geosynthetics manufactured from polymeric materials have been widely used as construction materials to solve many civil engineering problems since 1970s. Geosynthetics are used to improve the performance of unpaved and paved roads for over 40 years (Giroud and Han, 2004). Geotextile, geogrid, and geocell are used with RAP in limited research to improve its performance. Geotextile and geogrid are planar geosynthetics whereas geocell is a three-dimensional honeycomb type of geosynthetic. Geogrid and geocell improve the performance of RAP layers by providing confinement whereas geotextile improves the performance by providing a tensioned membrane effect.

The most efficient location of geosynthetic in roadway construction is at the interface of subgrade and granular base course (Das et al., 1998). Geosynthetic installed at this location provides full or partial separation, lateral confinement of granular base materials, tensioned membrane or beam effect when deformed extensively. The tensioned membrane or beam effect is referred to as the tension developed in the curved geosynthetic-reinforced base to resist the vertical load (Rajagopal et al., 1999). Nonwoven geotextile provides separation, filtration, and drainage where as woven geotextiles provides separation and reinforcement. Geogrid

and geocell provides reinforcement by providing lateral confinement. Geogrids can provide confinement and reinforcement to base and subgrade due to their tensile strength and stiffness.

Pokharel et al. (2010) reported that the geocell provided the vertical confinement in two ways: (1) the friction between the infill material and the geocell wall and (2) the geocell-reinforced base acts as a mattress to restrain the soil from moving upward outside the loading area. Han et al. (2008a, b) reported that geocells increased the bearing capacity and elastic modulus of the reinforced sand by providing confinement to the infill material. Mhaiskar and Mandal (1992) identified the hoop stress induced in the geocell wall as the key factor towards resisting loads.

2.4   Experimental studies on RAP

Literature indicates that 100% RAP could not produce base course of high quality. Several researchers have suggested that high quality base course could be obtained by blending RAP with virgin aggregates, stabilizing RAP with chemical additives such as cement, lime, fly ash, etc., and confining RAP with geocell. Fly ash is a fine, glass-like powder material recovered from gases created by coal-fired electric power generation. Millions of tons of fly ash were produced by U.S. power plants annually. Stabilizing RAP with fly ash is attractive and sustainable solution because fly ash traditionally has been disposed in landfills. Cementitious fly ashes can improve the strength and stiffness of soil through cementation and provides sustainable solution (Edil et al., 2002). Geocells are used to reinforce base courses of roads to improve the performance of base course materials by providing lateral confinement to the infill materials (Han et al., 2011;

Thakur, 2011; Thakur et al. (2011); Thakur et al., 2012b; Pokharel, 2010). This section provides the literature review of previous experimental works on treated RAP bases (blended RAP aggregate base, chemically stabilized RAP base, and geocell-reinforced RAP base). However, limited research has been done to improve the quality of RAP base using geocell.

2.4.1 Blended RAP aggregate base

Resilient modulus (M_R)

The M_R tests were conducted by Clary et al. (1997), Bennert et al. (2000), Cosentino et al. (2003), and Abdelrahman et al. (2010) on blends of RAP and aggregates commonly used for base course applications. The M_R of RAP was higher than the virgin aggregate base materials in these investigations, and the M_R of RAP-aggregate blends increased with an increase in bulk stress and RAP content in the blends. The bulk stress (θ) model $M_R = K_1 * \theta^{K_2}$ was proposed by them for different blends to predict M_R. The model parameters (K_1 and K_2) were determined by them based on M_R test results. The values of model parameters (K_1 and K_2) proposed by different authors are shown in **Table 2.4.1**. The K_1 and K_2 values were modified for Clary et al. (1997), Cosentino et al. (2003), and Abdelrahman et al. (2010) to keep consistency with the units. The K_1 ranged from 4.39 to 43.1 where as K_2 ranged from 0.36 to o.66. The M_R and θ used in this model should be in MPa and kPa units, respectively. The M_R increased approximately in linear pattern with an increase in RAP content as shown in **Fig. 2.4.1**.

17

Table 2.4.1 Bulk stress (θ) model parameters for prediction of M_R of RAP-aggregate blends ($M_R = K_1 * \theta^{K_2}$)

Reference	M_R test method	RAP content (%) in blends of RAP-aggregate	Model Parameters		R^2
			K_1	K_2	
Modified from Clary et al. (1997)	AASHTO T 294 - 94	0	4.64	0.66	0.88
		10	4.39	0.65	0.97
		30	5.67	0.65	0.97
		50	7.84	0.6	0.97
		100	16.07	0.51	0.93
Bennert et al. (2000)	AASHTO TP 46 - 94	0	9.55	0.5	NA
		25	17.35	0.45	
		50	13.49	0.52	
		75	19.49	0.46	
		100	43.1	0.36	
Modified from Cosentino et al. (2003)	LTTP Protocol P46	60	7.67	0.59	0.85
		80	10.78	0.6	0.95
		100	9.6	0.64	0.98
Modified from Abdelrahman et al. (2010)	LTTP Protocol P46	0	4.79	0.63	0.96
		30	4.59	0.66	0.99
		50	9.2	0.57	0.97
		70	19.09	0.46	0.94
		100	27.39	0.43	0.85
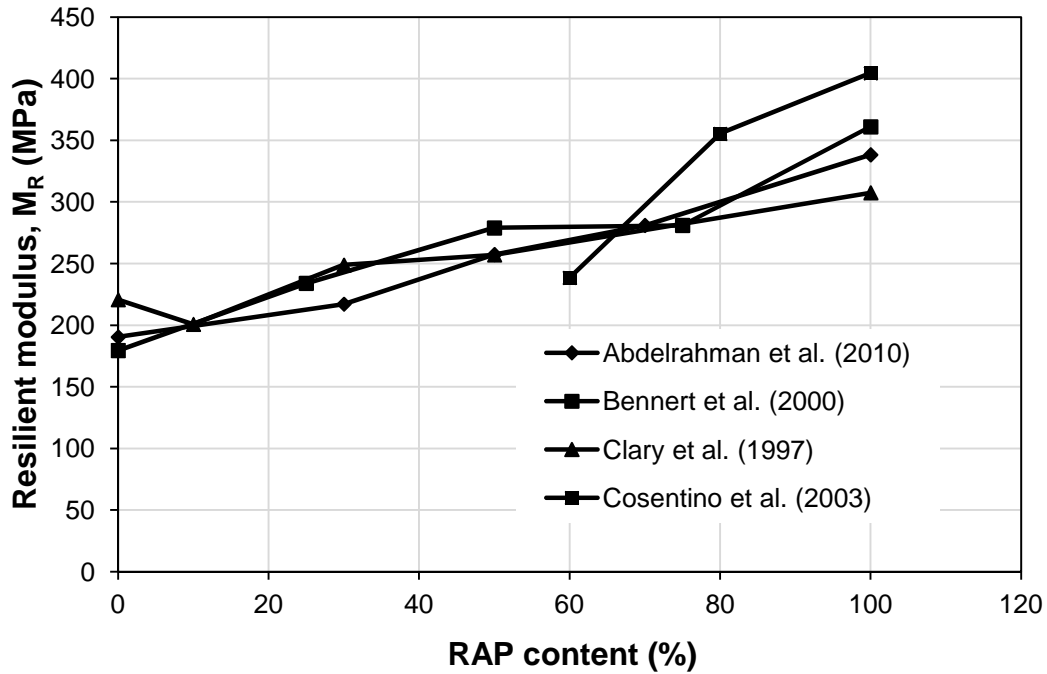
Fig. 2.4.1 RAP content versus resilient modulus (M_R) of RAP-aggregate blends at

bulk stress of 345 kPa

California Bearing Ratio (CBR)

Taha et al. (1999), Bennert and Maher (2005), Guthrie et al. (2007), and Cosentino et al.

(2012) conducted CBR tests on blended RAP aggregate specimens. It was found by all

authors that CBR of blends decreased with an increase in RAP content as shown in

Fig. 2.4.2. However, this result contrasts to the M_R test result which may be because of

the difference in the nature of these two tests. These investigations showed that the

CBR values of 100% RAP ranged from 11 to 33%.
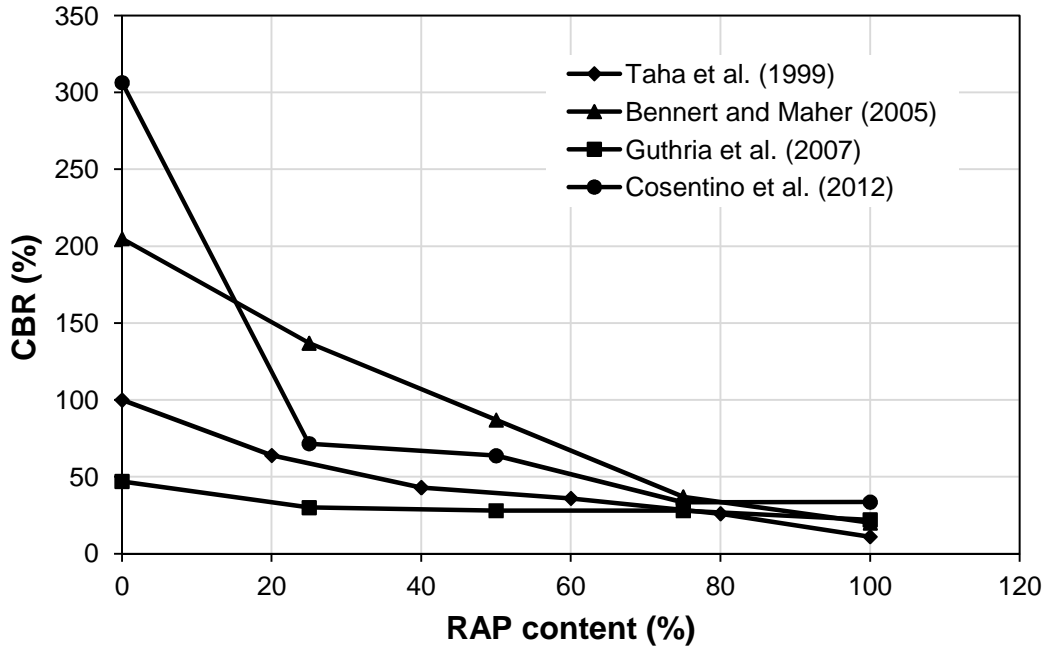
Fig. 2.4.2   CBR versus RAP content for RAP-aggregate blends

Shear strength

Garg and Thompson (1996), Cosentino et al. (2003), Bennert and Maher (2005), Kim and Labuz (2007) , and Attia (2010) evaluated shear strength parameters (friction angle and cohesion) of RAP blended aggregate specimens and the test results are as shown in **Figs. 2.4.3a** and **b**. It was found under these investigations that friction angle and cohesion of 100% RAP specimen varied from 44° to 45° and 17 to 131 kPa, respectively. The cohesion obtained for RAP may be because of the presence of asphalt binder that would help particles to stick each other when forced together. The blends showing higher friction angle showed lower cohesion and vice versa.

20
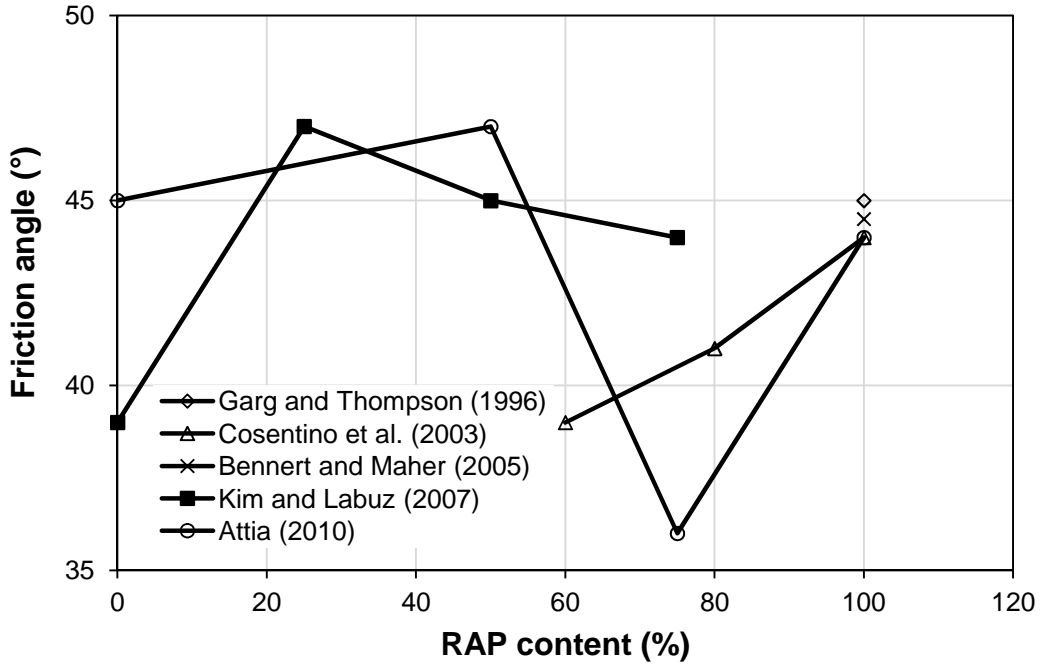
(a) Friction angle versus RAP content
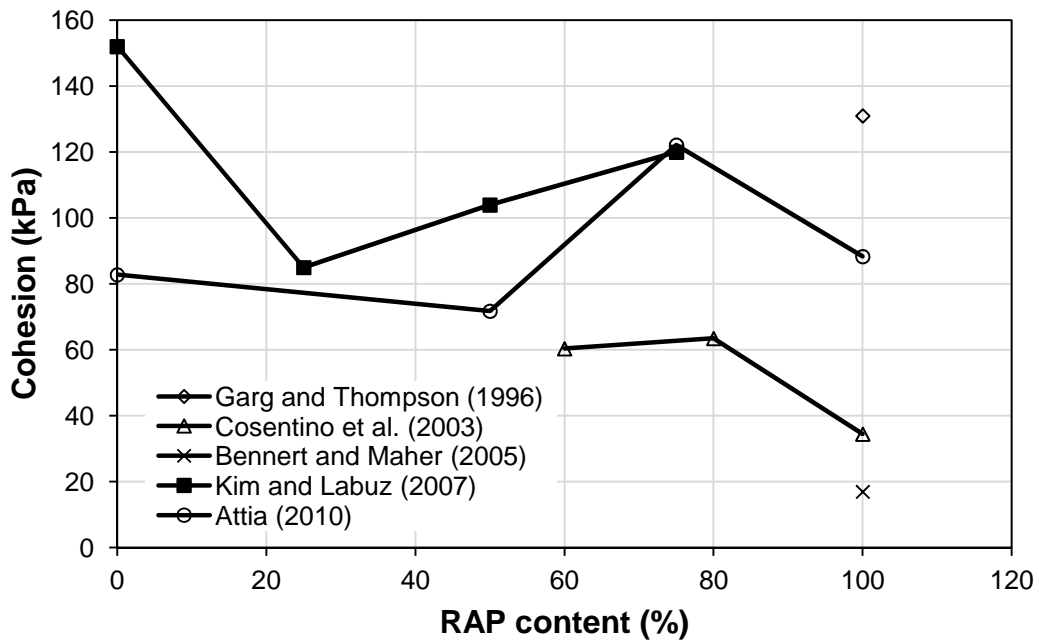
(b) Cohesion versus RAP content

Fig. 2.4.3 Effect of RAP content on shear strength parameters of RAP-aggregate

blends

21

Permanent deformation

Garg and Thompson (1996), Attia (2010), Bennert et al. (2000), Kim and Labuz (2007), and Wen and Wu (2011) evaluated permanent deformation of blended RAP aggregate specimens and found that permanent deformation of the blends increased with an increase in RAP contents as shown in **Fig. 2.4.4**. It can be seen that the permanent strain (ε_p) increased with the number of loading cycles. The rate of the increase in the permanent strain decreased with an increase of the loading cycles. The relation ε_p (%) = $A* N^B$ was proposed to predict the permanent strain of RAP-aggregate blends based on test results obtained by different researchers. The values of parameters A and B proposed in this study are presented in **Table 2.4.2**. The values of A ranged from 0.01 to 0.39 where as those of B ranged from 0.22 to 0.44. Wen et al. (2010) evaluated permanent deformation of fly ash (FA) stabilized RAP specimens and found that permanent strain of blends decreased with an increase in fly ash content in the blends.
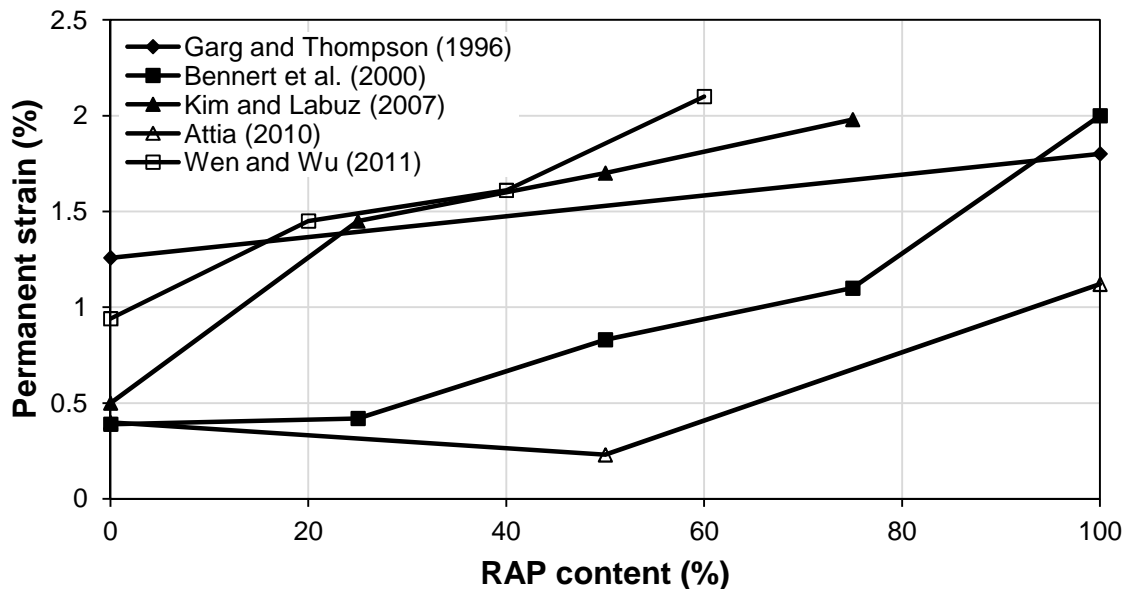
Fig. 2.4.4   Effect of RAP content on permanent deformation of blends of RAP aggregate

Table 2.4.2 Permanent strain model parameters [ε_p (%) = A* N^B]

Reference	RAP content (%)	Model parameters		R^2
		A	B	
Garg and Thompson (1996)	100	0.39	0.22	1
Attia (2010)	50	0.02	0.32	0.98
	100	0.01	0.44	0.93
Bennert et al. (2000)	50	0.05	0.34	0.9
	100	0.1	0.41	0.96
Kim and Labuz (2007)	50	0.23	0.28	0.99

Creep deformation

Cosentino et al. (2003) conducted creep tests on blended RAP-soil specimen under a fully confined condition at two vertical static stresses using the Brainard Kilman Terraload Consolidation Load Frame and confirmed that RAP crept under static loading. The creep deformation behavior is shown in **Fig. 2.4.5**. In this figure, RAP0_231kPa stands for the 0% RAP or 100% soil sample tested under 231 kPa applied vertical pressure, RAP80_231kPa stands for RAP-soil (80%-20%) blended sample tested under 231 kPa applied vertical pressure, and RAP100_231 kPa stands for 100% RAP sample tested under 231 kPa vertical stress. The soil used for blending with RAP was weak organic soil. The 100% soil sample crept most followed by blends containing 80% RAP and 60% RAP. They found that Creep deformation of samples increased with an increase in the applied vertical stress and RAP contents. The rate of the increase in the creep deformation decreased with time.
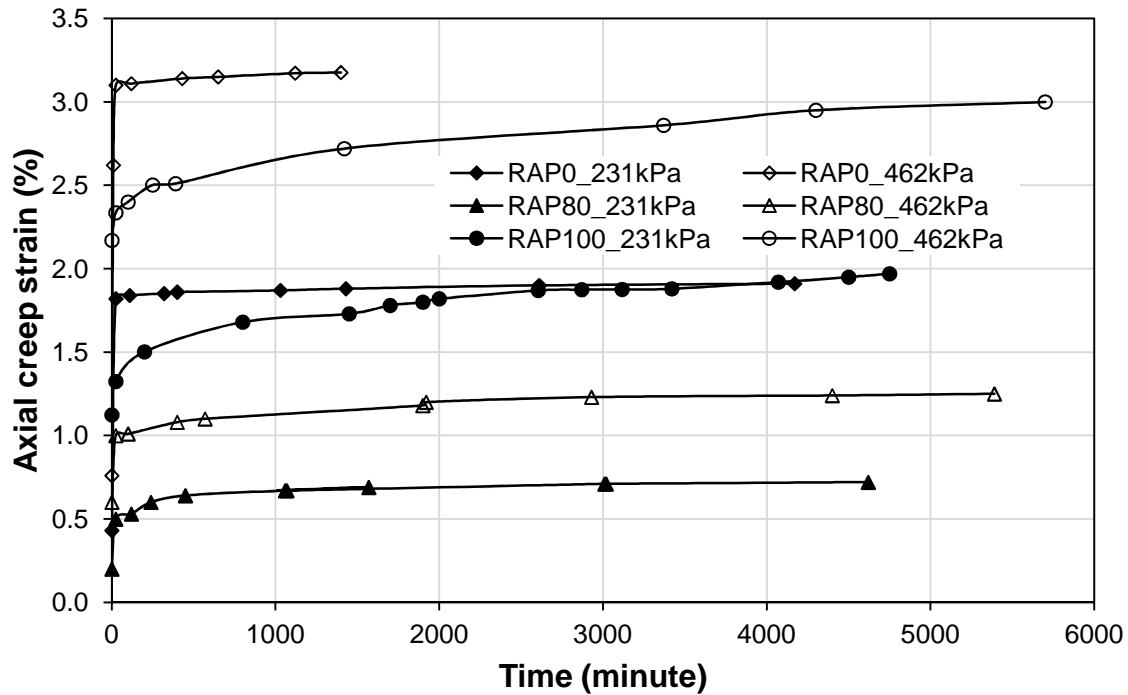
Fig. 2.4.5 Effect of RAP content and vertical stress on creep behavior of blends of RAP-aggregate (redrawn and modified from Cosentino et al., 2003)

2.4.2 Chemically stabilized RAP base

<u>Resilient modulus (M_R)</u>

Potturi (2006) conducted M_R tests on 7-days cured cement stabilized and cement-fiber stabilized RAP specimens. The cement contents were controlled at 0, 2, and 4% for cement stabilized specimens and 2, 4, and 6% for cement fiber stabilized specimens. The percentage of fibrillated polypropylene fiber content was kept at 0.15%. It was found that the M_R increased with an increase in bulk stress and cement content, and cement-fiber stabilized RAP specimens had higher M_R than cement stabilized RAP specimens as shown in **Fig. 2.4.6**. Li et al. (2007) conducted M_R tests at a deviatoric stress of 21 kPa on 14 days cured fly ash stabilized RAP specimens and Wen et al.

(2010) conducted M_R tests at a bulk stress of 83 kPa on 7 and 14 days cured fly ash stabilized RAP specimens. They found that the M_R increased with an increase in fly ash content and curing period.
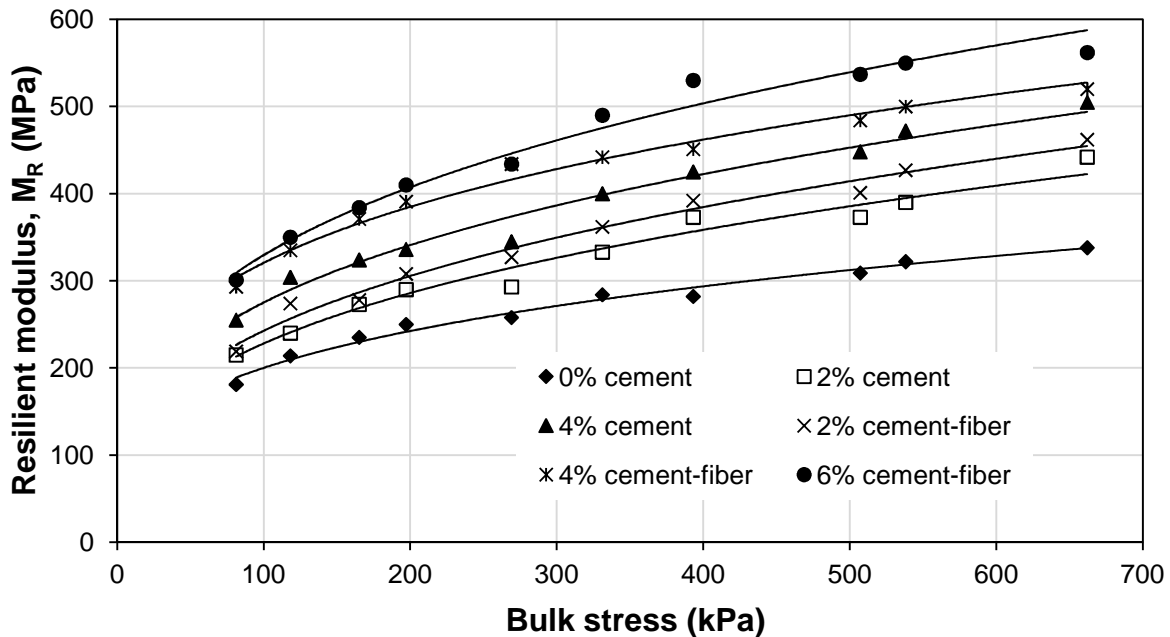
Fig. 2.4.6 Cement and cement-fiber stabilized RAP specimens (redrawn and modified from Potturi, 2007)

California bearing ratio (CBR)

Li et al. (2007) conducted CBR tests on RAP and fly-ash stabilized RAP (SRAP) mixed in the field and laboratory to investigate the effects of fly ash on strength improvement. Ten percent of Class C fly ash was used to stabilize RAP bases. They found that SRAP had significantly higher CBR than RAP. CBR of RAP ranged from 3 to 17 (mean = 9), CBR of laboratory mixed SRAP ranged from 70 to 95 (mean = 84), and the CBR of field-

mix SRAP ranged from 13 to 53 (mean = 29). Wen et al. (2008) conducted CBR tests on 7 days cured fly ash stabilized RAP and found that CBR of RAP increased linearly with an increase in fly ash content as shown in **Fig. 2.4.7**. Cosentino et al. (2012) conducted CBR tests on 7 days cured cement stabilized RAP-aggregate blends and found that CBR of RAP increased linearly with an increase in cement content.
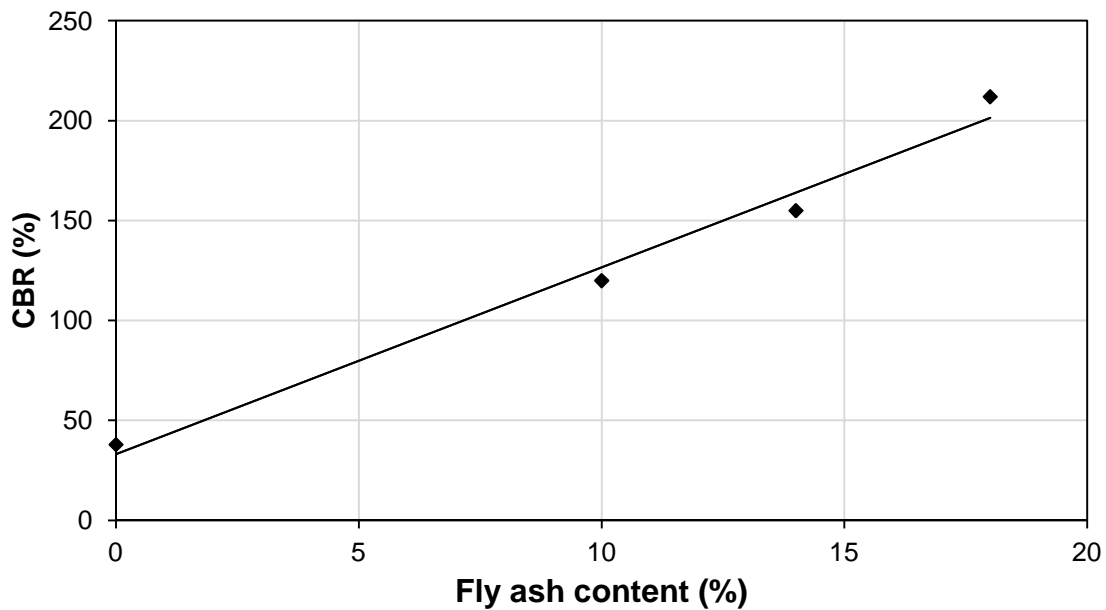
Fig. 2.4.7   CBR versus fly ash content (redrawn and modified from Wen et al., 2008)

Permanent deformation

Gnanendran and Woodburn (2003) measured permanent deformation of cement stabilized and lime stabilized RAP materials during resilient modulus tests. They concluded that the accumulation of permanent strain could be reduced by 80% by treating it with either 5% lime or 2% cement.

Wen et al. (2008) measured the total permanent deformations during resilient modulus tests for untreated RAP, fly ash treated RAP, and virgin aggregate. The

untreated RAP bases had largest permanent deformation followed by virgin aggregate and fly ash treated RAP. They found that permanent deformation decreased with an increase in fly ash content.

Wu (1999) constructed and tested 11 test sections (Three sections were stabilized with a cationic, medium setting polymerized asphalt emulsion; five were stabilized with a cationic medium setting asphalt emulsion; and three were stabilized with 13% Class C fly ash) from 1992 to 1996 on Kansas Route 27. All the test sections had 100 mm stabilized RAP base with a 38 mm hot mix asphalt overlay. They found that fly ash stabilized RAP bases had lower rutting deformation than others.

2.4.3 Geosynthetic-reinforced RAP base

Geotextile, geogrid, and geocell are used for stabilizing RAP bases. The permanent deformation, creep deformation, stress distribution, and strength and stiffness improvement factor for gesynthetic-reinforced RAP bases are discussed in this section:

Permanent deformation

Bortz et al. (2012) conducted moving wheel tests on eight asphalt pavements with two unreinforced well graded crushed limestone aggregate (AB-3) bases and six geocell-reinforced bases with AB-3, quarry waste (QW), and RAP as infill materials over subgrade. The subgrade used was AASHTO A-7-6 clay and was prepared to obtain target CBR of 6% and 12%. The following bases were prepared: (i) 300 mm thick unreinforced AB-3 (ii) 75 mm thick geocell-reinforced QW with 25 mm thick cover (iii) 75 mm thick geocell-reinforced RAP with 25 mm thick cover (iv) 75 mm thick geocell-

reinforced AB-3 with 25 mm thick cover (v) 200 mm thick unreinforced AB-3 (vi) 150 mm thick geocell-reinforced QW with 50 mm thick cover (vii) 150 mm thick geocell-reinforced RAP with 50 mm thick cover (viii) 150 mm thick geocell-reinforced AB-3 with 50 mm thick. The bases (i) to (iv) were prepared over subgrade with CBR of 6% and were paved with 50 mm thick HMA layer, whereas bases (v) to (viii) were prepared over CBR of 12% and were paved with 100 mm thick HMA layer. All eight test sections were tested to evaluate the effect of base, cover and HMA thicknesses, geocell reinforcement in terms of rut depth and stress distribution at the interface of subgrade and base at a number of passes of the wheel load. They concluded that a minimum cover of 50 mm over geocell and a minimum HMA layer of 100 mm over base were necessary for better performance of pavements. Geocell-reinforced waste materials (RAP and QW) performed as good as geocell-reinforced AB-3. The pavement sections constructed over firm subgrade (CBR = 12%) performed better than those over moderate subgrade (CBR = 6%) as shown in **Fig. 2.4.8**. In this figure, RAP (moderate) and RAP (firm) stand for asphalt pavement with geocell-reinforced RAP bases over moderate and firm subgrades, respectively. The same representation holds for AB-3 and QW. **Fig. 2.4.8** does not show the rut behavior at 100,000 and 500,000 number of passes for pavement sections constructed over moderate subgrade since these sections failed before 100,000 passes.
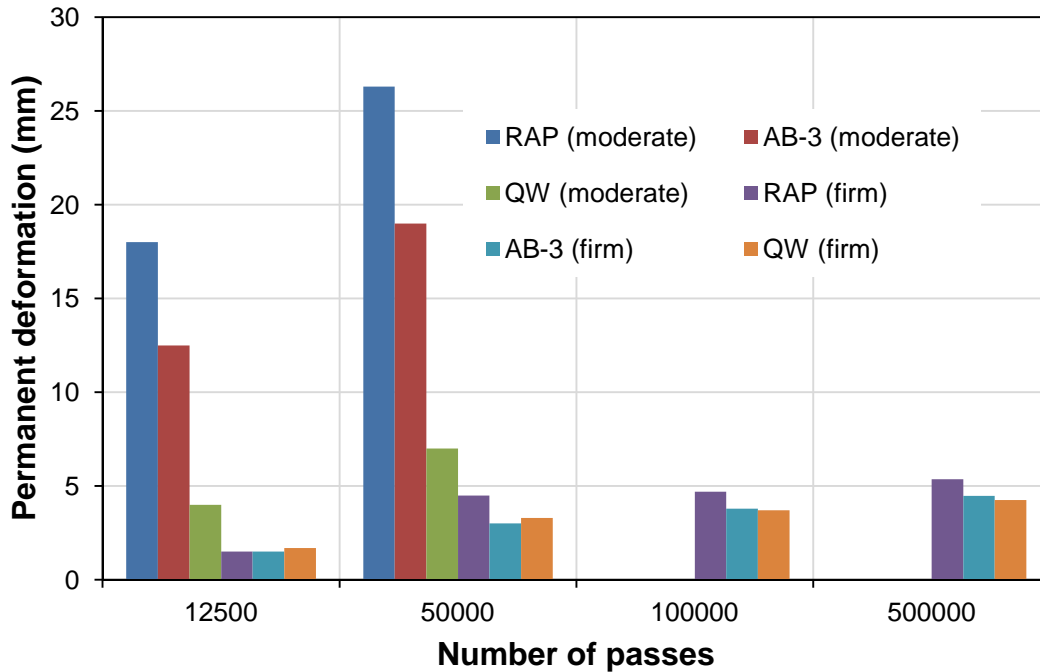
Fig. 2.4.8   Permanent deformation at wheel path versus number of passes (redrawn and modified from Bortz et al., 2012)

Donovan (2011) conducted dynaflect tests on five pavement test sections, each of length 150 m constructed at city of Edmonton, Canada to investigate the possibility of the use of recycled aggregate in roadway construction. The pavement structures of each section consisted of cement stabilized subgrade (CSS) overlaid by granular aggregate base (GAB), asphalt concrete base (ACB), and Asphalt concrete overlay (ACO). The city had added second lift of ACO after two years of original construction (in year 2004). The total thickness of asphalt layer for each section is the same (50 mm thick ACB + 60 mm thick first ACO + 50 mm thick second ACO = 160 mm) with variation in type and thickness of granular aggregate base course. Sections 1 and 2 used natural

aggregate and crushed natural aggregate, respectively, where as sections 3 to 5 used recycled crushed aggregate as granular base course. Recycled crushed aggregate consisted of 60% recycled concrete aggregate (RCA), 25% RAP and 15% other materials such as cement treated granular base aggregate, brick and other recyclable materials. The thicknesses of GAB for sections 1 to 4 were 325 mm while that for section 5 was 150 mm. Each section had 150 mm thick CSS except section 3 which had 325 mm thick CSS. Geotextile and geogrid were installed on top of subgrade in sections 3 and 5, respectively. All other remaining sections were unreinforced. The deflection test results are shown in **Fig. 2.4.9**. The recycled crushed aggregate sections performed better than natural aggregate and crushed natural aggregate sections. The deformation of each section increased with time. The deformation values measured on year 2005 were less than those on year 2004. This may be because of placement of second lift of ACO in year 2004. The section 4 performed best followed by the sections 5, 3, 1, and 2 in long term as shown in **Fig. 2.4.9**. They concluded the following: geotextile can have positive effect when subgrade soil is very weak; geogrid improved the life of pavement section and can reduce the thickness of granular base by 50% as compared with similar unreinforced base to provide same performance; recycled crushed aggregate can successfully be used as granular base course.
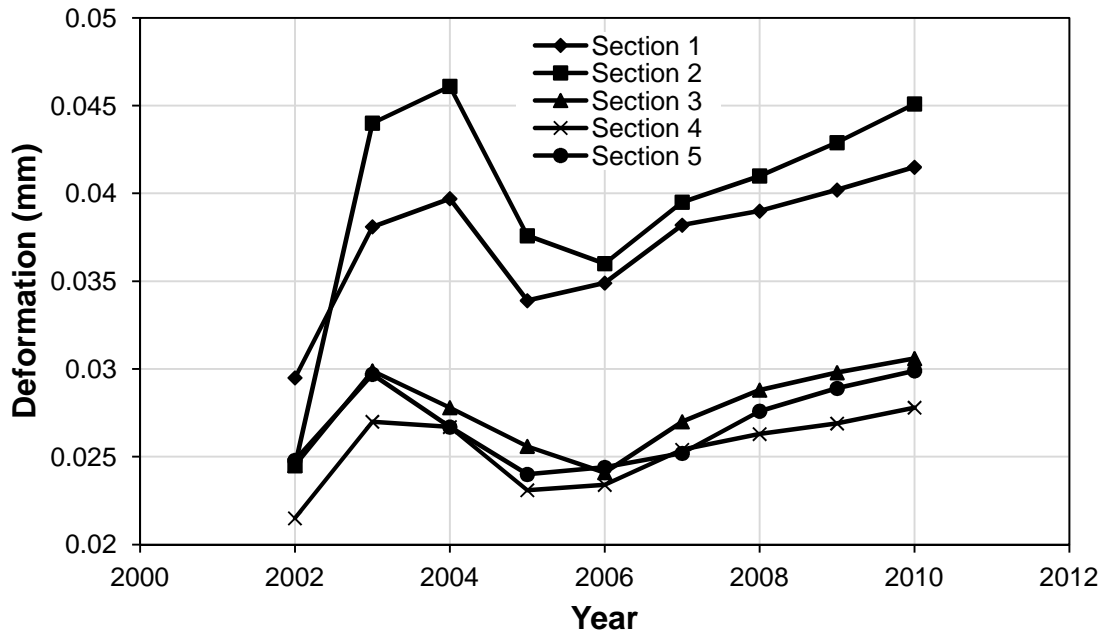
Fig. 2.4.9   Deformation behavior of pavement sections

Foye (2011) presented the work of a design-build contractor who used geosynthetic stabilization technique for reconstruction of 19,500 m^2 asphalt parking lot on a site with very weak subgrade. The remedial design parking lot section consisted of very weak subgrade soil overlaid by 200 mm thick geocomposite (nonwoven geotextile-geogrid) stabilized blended RAP aggregate base, 64 mm thick dense graded asphalt course, and 25 mm thick asphalt wearing course. The geocomposte was placed at the interface of subgrade and granular base course. It was found that the geocomposite stabilized parking lot section performed well and the use of geocomposite reduced the cost of construction from about $890,000 (estimated for original cut and replace specification) to about $200,000. In addition, geocomposite stabilization technique saved time, resources, and energy compared with traditional cut and replacement techniques.

31

<u>Creep deformation</u>

Thakur et al. (2011, 2012) conducted static plate loading tests in a test box and a compaction mold to investigate the effects of confinement, stress, and cover on creep deformations of unreinforced and geocell-reinforced RAP bases. They evaluated the creep deformation behavior of the following RAP specimens under two applied vertical stresses (276 and 552 kPa): unreinforced base (a RAP base prepared in a test box without geocell), single geocell-confined sample (a RAP sample prepared by placing RAP into the single geocell pocket), single geocell-confined base (a RAP base prepared by placing RAP into the single geocell pocket and the test box), multi geocell-confined base (a RAP base prepared by placing RAP into the multi geocell pockets and the test box), fully confined sample (a RAP sample prepared by placing RAP into the modified Proctor compaction mold). The axial creep strain versus time curves for the RAP at five confining conditions at the applied vertical stresses of 276 and 552 kPa are shown in **Fig. 2.4.10**. The geocell reduced the immediate creep deformations of the geocell-reinforced RAP samples or bases by 18 to 73% as compared with the unreinforced RAP base. The fully confined sample had 81 to 86% lower creep deformation than unreinforced base. RAP samples or bases at 552 kPa crept more compared with those at 276 kPa under the same confining conditions. It can be concluded that RAP crept more at the higher vertical stress and lower degree of confinement and vice versa.
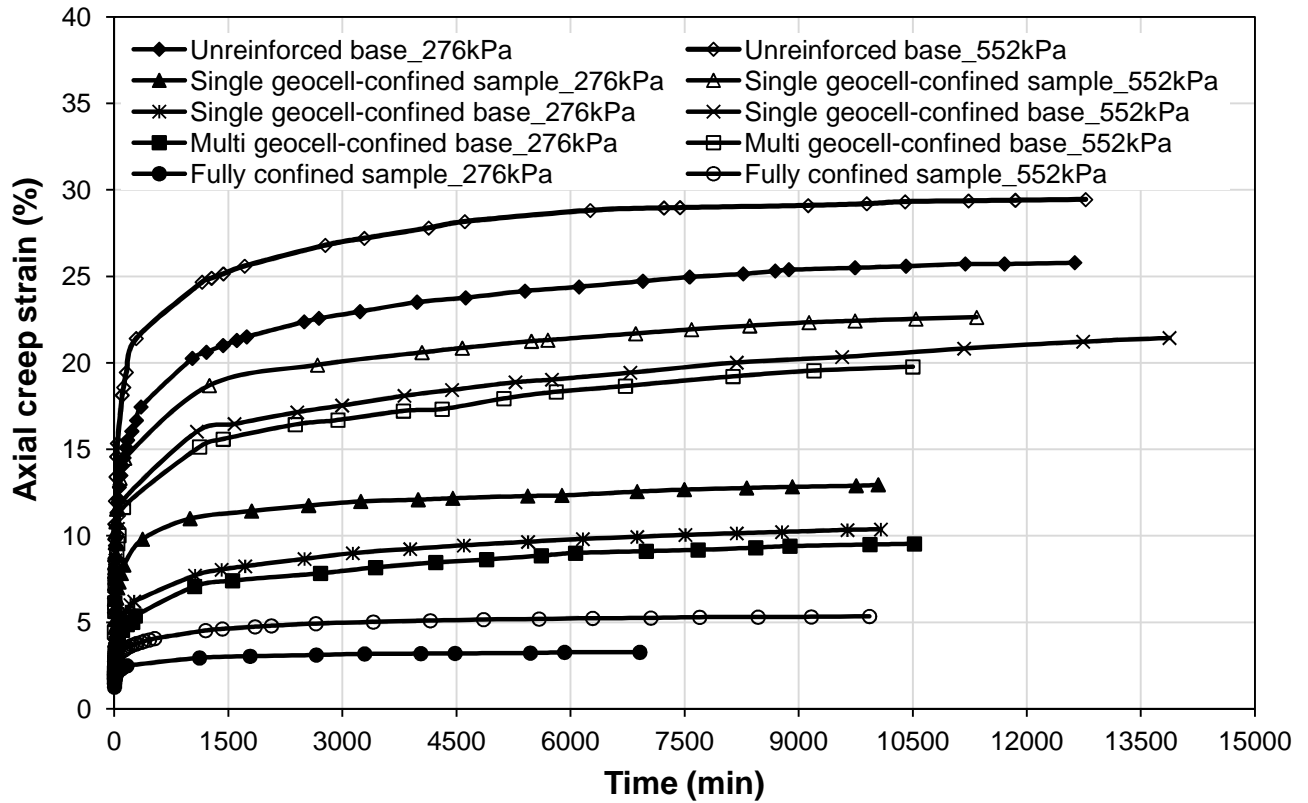
Fig. 2.4.10 Effect of confinement and vertical stress on creep behavior of RAP bases (redrawn and modified from Thakur et al., 2012c)

Vertical stress distribution

Han et al. (2011) conducted moving wheel tests on five geocell-reinforced and two unreinforced RAP bases over weak subgrade of target CBR 3% to evaluate the effect of geocell reinforcement in terms of rut depth and stress distribution angle at a number of passes of the wheel load. Two types of recycled asphalt materials, named RAP and FRAP (fractioned RAP or RAP with finer gradation) were used in this study. The following base sections were prepared and tested: 300 mm thick unreinforced RAP, 150 mm thick geocell-reinforoced RAP with a 20 mm thick RAP cover, 100 mm thick geocell-reinforced RAP with a 70 mm thick RAP cover, double layered geocell-reinforced RAP

with a 30 mm thick RAP cover above a 100 mm thick bottom geocell layer and a 70 mm thick RAP cover above a 100 mm thick top geocell layer, 250 mm thick unreinforced FRAP, 100 mm thick geocell-reinforced FRAP over a 100 mm thick unreinforced FRAP base course with a 50 mm thick FRAP cover, and 75 mm thick geocell-reinforced FRAP over a 100 mm thick unreinforced FRAP base course with a 75 mm thick FRAP cover. They found that the novel polymeric alloy (NPA) geocell improved the life of unpaved sections by a factor of 1.3 for the reinforced section with one layer of 75 mm high geocell and 1.8 for the reinforced section with one layer of 100 mm high geocell at a rut depth of 75 mm as compared with the unreinforced section at the same rut depth. They concluded that the geocell reduced the rut depth and vertical stresses transferred to the subgrade by distributing the load over a wider area. For demonstration purpose, the vertical stresses at the interface of subgrade and FRAP base versus the number of passes are shown in **Fig. 2.4.11**. The measured vertical stresses at the interface of base and subgrade were much lower than the tire pressure of 552 kPa applied on the road surface for each section. The vertical stress increased or remained constant with number of passes for unreinforced section and decreased with number of passes for reinforced sections. They reported this phenomenon as the slab effect of geocell-reinforced bases.

34
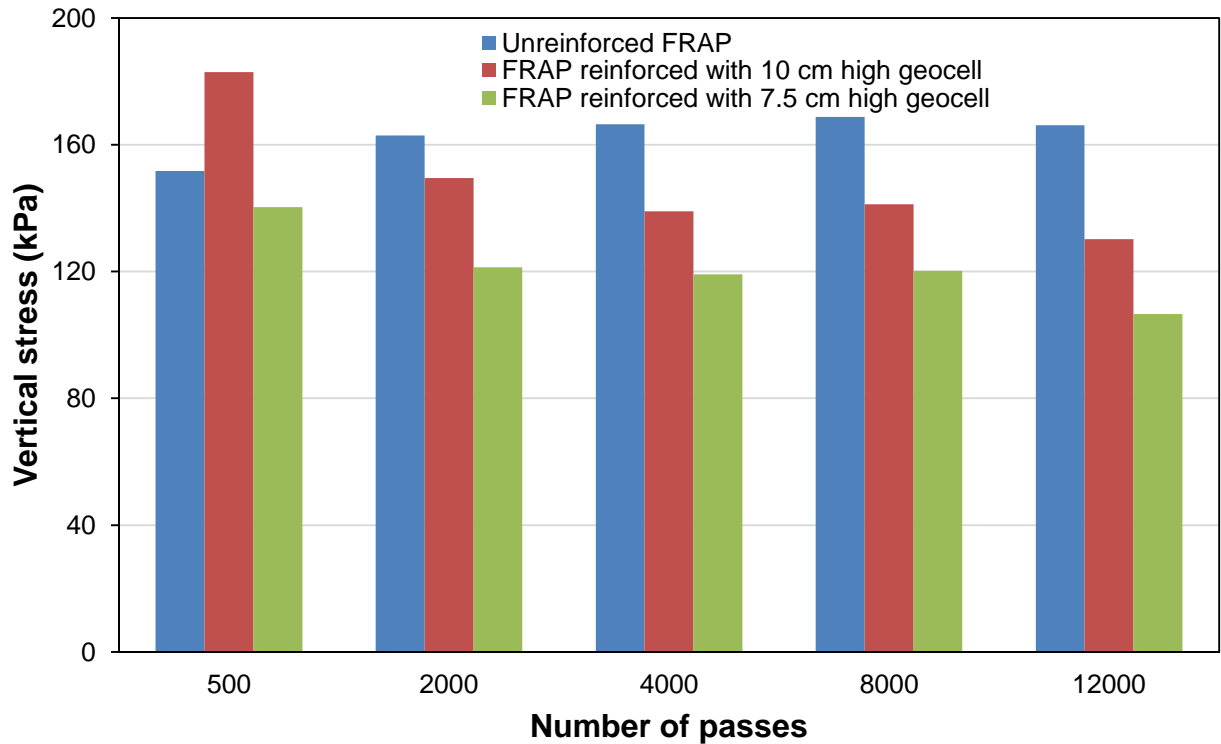
Fig. 2.4.11 Vertical stress at the interface of base and subgrade versus the number of passes (redrawn and modified from Han et al., 2011)

Strength and stiffness

Thakur et al. (2012b) also investigated the vertical stress-displacement responses of the following RAP specimens: unreinforced sample (unreinforced RAP sample extruded from a Proctor compaction mold), unreinforced base (a RAP base prepared in a test box without geocell), single geocell-confined base (a RAP base prepared by placing RAP into the single geocell pocket and the test box), multi geocell-confined base (a RAP base prepared by placing RAP into the multiple geocell pockets and the test box). The applied vertical stress versus displacement curves are shown in **Fig. 2.4.12**. They found that the unreinforced RAP sample failed at 172 kPa while other sections did not

fail up to a vertical stress of 586 kPa and showed a linear vertical stress-displacement response. The stress-displacement responses were analyzed in terms of a modulus improvement factor. The test results showed that the moduli of the single geocell-confined and the multi geocell-confined bases were increased by 1.2 and 1.6 times compared to the unreinforced base, respectively.
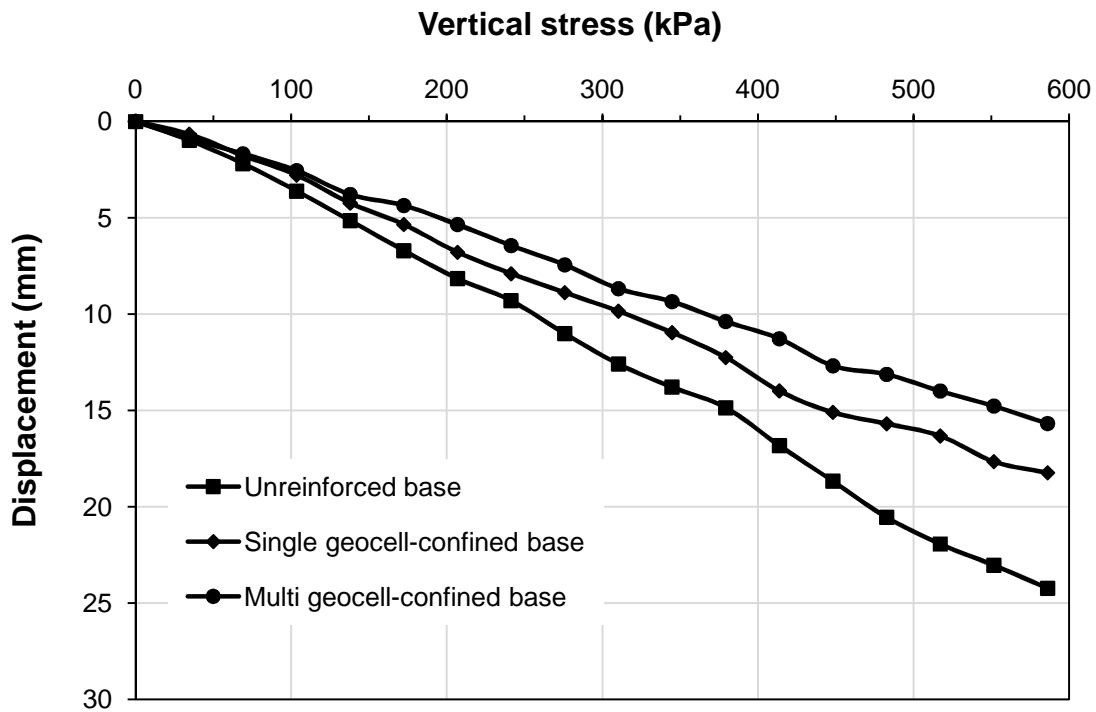
Fig. 2.4.12   Vertical stress-displacement curves for unreinforced and geocell-reinforced RAP bases (modified from Thakur et al., 2012b)

2.5   Design/Analysis method for geocell-reinforced base

There are limited design/analysis procedures for geocell confinement in pavement systems including those presented in Mengelt et al. (2000), Presto Geosystems (2007),

Pokharel (2010), and Yang (2010). The design/analysis procedures are validated to a limited extent and further validation and/or improvement of these procedures is needed. So far, Presto Geosystems (2007) has been used in practice to design/analyze geocell confinement in pavement systems. Mengelt et al. (2000) used the pavement damage analysis approach; Pokharel (2010) and Presto Geosystems (2007) used the stress distribution approach; and Yang (2010) used the mechanistic-empirical approach to design/analyze geocell-reinforced bases.

2.5.1 Pavement damage analysis approach

Mengelt et al. (2000) performed cyclic triaxial tests on the single geocell-reinforced soil to determine the resilient modulus and the rutting potential of the geocell-reinforced soil. Based on the test data, they proposed a simple method to design geocell-reinforced bases/subbases in flexible pavements. Mengelt et al. (2000) developed a design chart which correlates the pavement life (in ESALs) of unreinforced bases/subbases to that of reinforced ones. The unreinforced pavement design can be achieved using the design software KENLAYER; then the life of the corresponding pavement with geocell-reinforced subbases can be estimated with the design chart. A series of hypothetical unreinforced and single geocell-reinforced pavement layers were analyzed using resilient moduli measured in this study. The pavement damage analysis routine in KENLAYER software (Huang 1993) was used to estimate the fatigue and rutting life of typical unreinforced and geocell-reinforced asphalt pavements to determine the degree of improvement that can be expected. The thickness, resilient modulus, and damage function for each layer of the pavement are required to determine the number of

repetitions to induce fatigue cracking and rutting failure using KENLAYER. The life of the pavement is taken as the lowest number of load repetitions required to induce failure by one of the two mechanisms: (i) fatigue cracking and (ii) rutting. In this design method, the design number of ESALs required for a geocell-reinforced pavement is determined based on the projected traffic demand for the pavement. The necessary asphalt concrete layer thickness is interpolated for the reinforced section from the graph such that the pavement will fail by fatigue cracking. The ESALs for the unreinforced pavement are determined from the graph developed by Mengelt et al. (2000) which correlates ESALs of unreinforced and reinforced pavements. The damage functions are selected from the tables generated using Henkel and Gilbert's theory, which are presented in the report or from another appropriate source. A pavement cross section corresponding to the ESALs for the unreinforced pavement is found iteratively using KENLAYER and the final selection of the pavement design is done based on economic considerations.

2.5.2 Stress distribution approach

Pokharel (2010) developed a simplified design method for Novel Polymeric Alloy (NPA) geocell-reinforced unpaved roads by modifying the method developed by Giroud and Han (2004). He introduced a modulus improvement factor (I_f) which was proposed by Han et al. (2007) to account for modulus increase of the base course by geocell confinement and set the maximum limit of the modulus ratio to 7.6 for geocell-reinforced unpaved roads. The stress distribution angle reduction rate factor (k') depending on the geocell reinforcement was introduced and calibrated based on

large-scale laboratory cyclic plate loading tests and full-scale moving wheel tests on geocell-reinforced granular bases over weak subgrade. The California Bearing Ratios (CBR) of the subgrade and base course, the number of loading cycles or wheel passes required for 50 to 75 mm rut, the height of geocell, and the thickness of base course were the variables used to calibrate this design formula. The design formula was verified by the test data. This method can also be used for other geocell-reinforced unpaved roads by calibrating the k' value for other geocell products using cyclic plate loading tests and/or moving wheel tests.

Presto Geosystem (2007) developed the design method for determining aggregate thickness requirements for unreinforced and geocell-reinforced unpaved. The heaviest single or dual wheel load is considered as the design load that the unpaved road is required to support. Effective contact radius of the design wheel load is determined based on tire pressure and design wheel load. The bearing capacity coefficients for unpaved haul roads developed by the US Forest Service are taken as 2.8 and 3.3 for high traffic with little rutting and low traffic with significant rutting, respectively. Maximum allowable stress on the subgrade is determined based on bearing capacity coefficient and subgrade shear strength. The required thickness of unpaved road without the geocell confinement system is a function of radius of loaded area and tire pressure, and the maximum allowable stress on the subgrade is determined using the Boussinesq equation. The total required thickness of unpaved road with geocell confinement is a function of the geocell depth, the depth of placement below the applied load, the wheel load, the tire pressure and the infill material properties. The vertical stress at the top and bottom of the geocell section is calculated

using the Boussinesq equation. The horizontal stress on the geocell wall is calculated based on vertical stress and active earth pressure coefficient. The reduction in stress directly beneath the center of the loaded area due to stress transfer to the geocell walls is calculated using the Boussinesq equation based on geocell depth, diameter, average horizontal stress on the geocell walls, and the angle of shearing resistance between granular infill material and geocell walls. The total vertical resisting stress provided by the geocell structure is calculated and added to the maximum allowable stress on the subgrade to determine the total required thickness of unpaved road with the geocell confinement system. A subbase layer in addition to the geocell-reinforced base section is required if the total required thickness is greater than the surface thickness. The thickness of subbase layer is equal to the total required thickness minus the surface thickness and the geocell section depth. A 25 mm to 50 mm thick aggregate wearing surface is typically recommended to protect the top of geocell walls.

2.5.3 Mechanistic empirical design approach

Yang (2010) developed three dimensional numerical models to simulate the behavior of geocell-reinforced soil under static and repeated loadings. A non-linear elastoplastic model was used to simulate infill soil where a linearly elastic plate was used to represent a geocell in reinforced soil under static loading. In addition, a mechanistic empirical model was developed for geocell-reinforced soil under repeated loading with some modifications in the stress-dependent response model of the current Mechanistic Empirical Pavement Design Guide (MEPDG). These modifications include the three-dimensional constitutive equation of tangent resilient modulus, the compaction-induced

initial horizontal stress in the soil, and the residual stress increase due to the accumulated permanent deformation of geocell with the number of load passes. A parametric study was also performed based on the calibrated numerical models to investigate the effects of the following factors: (i) thickness of the geocell-reinforced layer, (ii) geocell modulus, (iii) subgrade stiffness and strength, (iv) interface shear modulus between geocell and soil, and (v) infill material modulus. Yang (2010) concluded that the developed numerical model well simulated the experimental results for the geocell-reinforced soils.

2.6 Damage model for Permanent deformation

Lekarp et al. (2000) conducted literature reviews and reported several empirical permanent deformation models for granular materials developed by different researchers [Barksdale (1972), Veverka (1979), Khedr (1985), Paute (1988), Sweere (1990), Paute (1996)]. Tseng and Lytton (1989) developed mechanistic-empirical permanent deformation models for different layers of flexible pavements. They conducted cyclic triaxial tests on granular soils and developed empirical as well as mechanistic empirical permanent deformation models by fitting the curve of permanent strain (ε_p) or the ratio of permanent strain to resilient strain ($\varepsilon_p/\varepsilon_r$) against the number of loading cycles. The permanent deformation models developed by different researchers for granular materials are presented in **Table 2.6.1**. However, no study has been done to develop a damage model for permanent deformation of geocell-reinforced RAP pavements.

41

Table 2.6.1 Permanent deformation models for granular materials

Damage Models	Reference	Remarks
$\varepsilon_p = A + B \cdot \log N$	Barksdale (1972)	Parameters A and B were calibrated using test results
$\dfrac{\varepsilon_p}{\varepsilon_r} = A \cdot N^B$	Veverka (1979)	Parameters A and B were calibrated using test results
$\dfrac{\varepsilon_p}{N} = A \cdot N^{-B}$	Khedr (1985)	Parameters A and B were calibrated using test results
$\varepsilon_p = A \cdot N^B + C$	Paute (1988)	Parameters A,B and C were calibrated using test results
$\dfrac{\varepsilon_p}{\varepsilon_r} = \left(\dfrac{\varepsilon_0}{\varepsilon_r}\right) \cdot e^{-\left(\frac{\rho}{N}\right)^{\beta}}$	Tseng and Lytton (1989)	Parameters ε_0, ρ and β were calibrated using test results
$\varepsilon_p = A \cdot N^B$	Sweere (1990)	Parameters A and B were calibrated using test results
$\varepsilon_p = A \cdot \left[1 - \left(\dfrac{N}{100}\right)^B\right]$	Paute (1996)	Parameters A and B were calibrated using test results

2.6.1 Empirical versus mechanistic empirical design method

Empirical method is developed based on the test results or observation alone and does not consider the mechanics of materials or system behavior or pavement theory. The empirical method is the empirical relationship between performance, load, and pavement for a particular load, a geographic location, and a climatic condition and

hence is site specific and applicable only to those areas with the same characteristics such as soil type, pavement material type, and climate. Therefore, the use of an empirical method is limited as the material properties of pavement layers, climatic conditions, and loading types vary from site to site.

The mechanistic empirical (ME) method is a logical engineering approach, which is based on the mechanics of materials that relates traffic load or environmental conditions to pavement response, such as stress and strain. The main advantage of an ME method is that the analysis is based on the performance of individual layers of a pavement, rather than only on the pavement's surface performance. Samad (2011) reported that M-E software like KENLAYER facilitated the transition of a design method from empirical to mechanistic. Arsad (2007) reported the following advantages of ME design over the empirical methods:

(i)   It allows an evaluation of changes in traffic loading, climatic condition, pavement layer properties on pavement performance

(ii)   The impact of variability in construction can be assessed

(iii)   Actual engineering properties are assigned to the materials used in the pavement

(iv)   Pavement responses related to actual modes of pavement failure are evaluated

(v)   Databases of materials used as input in pavement design can be developed and updated as information becomes available

The mechanistic empirical (ME) design process is illustrated as shown in **Fig.**

43

2.6.1. The M-E design process consists of three main components (input parameters, structural models, and damage models).   Pavement configuration (i.e., number of layers, thickness of each layer, and type of material for each layer), material properties for each layer (i.e., resilient modulus and Poisson's ratio, etc.), and expected traffic (i.e., axle loads, number of load repetitions, tire pressure, contact area, and traffic speed, etc.) are the main input parameters.   The effect of climate conditions, such as temperature and moisture from rainfall, are taken into account by modifying the material properties.   A pavement structure can be modeled as a multi-layered elastic system (**Fig. 2.6.2**) or as a finite element mesh representation.   The modulus of elasticity and Poisson's ratio of ith layer as shown in **Fig. 2.6.2** are E_i and V_i, respectively.   A layered elastic analysis is used in most current mechanistic design methods for evaluating pavement responses (i.e., stress, strain, and deflection).   The computer software, such as KENLAYER (Huang, 1993), can be used to evaluate pavement responses under the given loading conditions.   It is important to know the location and amount of maximum stress and strain in the pavement system under the given loading condition to avoid pavement failure under the actual loading condition.   The pavement responses (i.e. stresses and strains) obtained using KENLAYER are then used in the damage model to relate them to the predicted pavement performance.   A damage model is an equation which is used to predict the life of pavements in terms of number of load repetitions to failure for pavement distresses, such as fatigue cracking, rutting, etc.   The predicted performance is checked for design reliability and the final design section for the pavement is selected by iterative procedures.

44
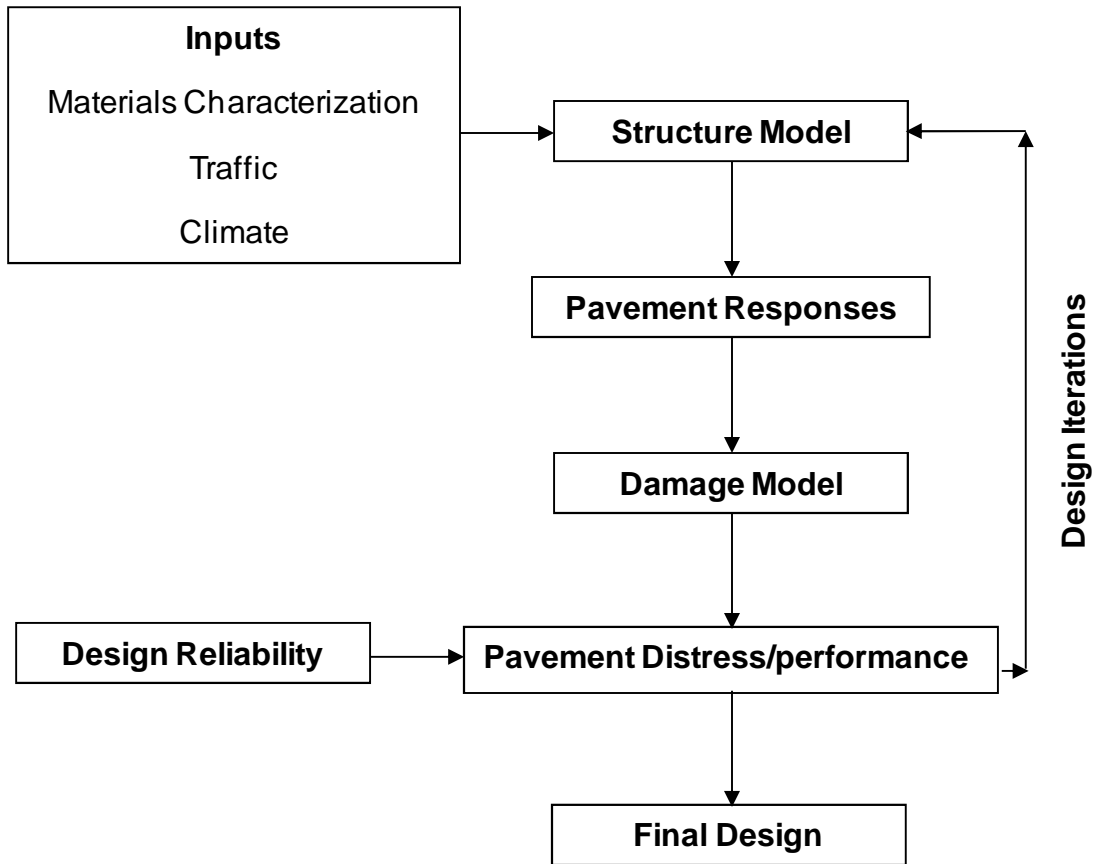
Fig. 2.6.1   Component of Mechanistic-Empirical Design Process (Thompson, 1992)
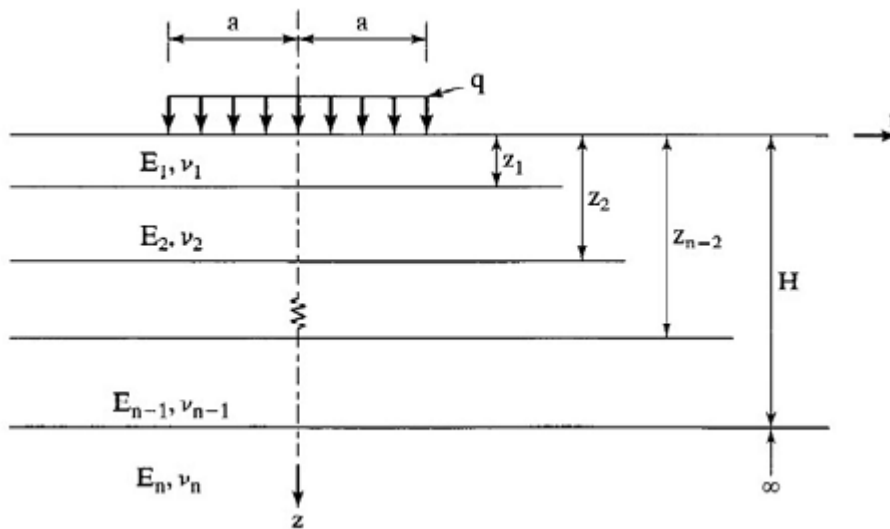
Fig. 2.6.2   Multi-layered elastic system in cylindrical coordinates (Huang, 1993)

2.6.2 KENLAYER Computer Program

Huang (1993) developed the KENLAYER computer program, which can be used to evaluate the responses (stresses, strains, and displacements) at different locations of flexible pavements under traffic loading. KENLAYER is the solution for an elastic multi-layer system under a circular loaded area. The solutions are superimposed for multiple wheels, applied iteratively for nonlinear layers, and collocating at various times for viscoelastic layers. The KENLAYER can thus be applied to layered systems with each layer behaving differently (i.e., linear elastic or nonlinear elastic or viscoelastic) under single, dual, dual-tandem, or dual-tridem wheels. The KENLAYER evaluates the fatigue and rutting life of flexible pavements. Traffic loading and material properties are the two main input parameters which are keyed in KENLAYER using menu "LAYERINP". The structural analysis of a flexible pavement by KENLAYER is based on the Burmister layered theory. KENLAYER is also used to determine the fatigue and rutting life of flexible pavements by performing damage analysis for fatigue cracking and permanent deformation, respectively.

2.6.3 Mechanistic Empirical Pavement Design Guide (MEPDG)

The current Mechanistic Empirical Pavement Design Guide (MEPDG) used the modified form of the permanent deformation model developed by Tseng and Lyton (1989) to predict the permanent deformation of granular base materials. The model has been calibrated in the NCHRP Project-1-37a using a large amount of permanent deformation data collected from the Long Term Pavement Performance (LTPP) Program. The calibrated permanent deformation model for granular base materials is shown as

follows:

$$PD = K_{S1} \cdot \beta_{S1} \cdot h_{Soil} \cdot \varepsilon_v \cdot \left(\frac{\varepsilon_0}{\varepsilon_r}\right) \cdot e^{-\left(\frac{\rho}{N}\right)^{\beta}}$$

$$\text{Log}\beta = -0.61119 - 0.017638 \, W_c$$

$$\rho = 10^9 \left(\frac{-4.89285}{1-(10^9)^{\beta}}\right)^{\frac{1}{\beta}}$$

$$\left(\frac{\varepsilon_0}{\varepsilon_r}\right) = \frac{0.15 \cdot e^{(\rho)^{\beta}} + 20 \cdot e^{\left(\frac{\rho}{10^9}\right)^{\beta}}}{2}$$

where

PD = accumulated permanent deformation in a layer

β_{s1} = local calibration constant for the rutting in the unbound layers (by default β_{s1} =

   1)

k_{s1} = global calibration coefficients (k_{s1} = 1.673 for granular materials and k_{s1} = 1.35

   for fine-grained materials)

ε_v = average vertical strain in a layer which can be determined using layered elastic

theory of pavement

h_{soil} = layer thickness

W_C = water content.

2.7 Summary

The following conclusions can be made from the past studies:

   (i)   Recycled Asphalt Pavement (RAP) material has a structural value and can be

47

used as subbase and base course layers.

(ii) Use of RAP is considered a sustainable technology which preserves natural environment, reduces the amount of waste disposal, and provides cost effective material for roadway construction.

(iii) Geocell provides confinement and tension membrane effects which result in an increase in stiffness and bearing capacity of base courses.

(iv) Resilient modulus of blended RAP aggregate base increased with an increase in RAP content and bulk stress and that of chemical stabilized RAP increased with an increase in stabilizing agent content, curing time of sample, and bulk stress.

(v) CBR of blended RAP aggregate base decreased with an increase in RAP content and that of chemical stabilized RAP base increased with an increase in stabilizing agent content.

(vi) Permanent deformations of blended RAP aggregate and geocell-reinforced RAP bases increased with increasing number of loading cycles. Permanent deformation of blended RAP aggregate increased with an increase in RAP content. Permanent deformation of chemical stabilized RAP decreased with an increase in stabilizing agent content. The rate of permanent deformation decreased with the increasing number of loading cycles. The blending, chemical stabilization, and geosynthetic reinforcement improved the performance of RAP bases.

(vii) RAP crept more at the higher vertical stress and lower degree of confinement. Blending and geocell confinement improved creep performance of RAP bases.

(viii) Geocell improved the performance of RAP bases by reducing the permanent and creep deformations, vertical stress transferred to the subgrade, increasing the percentage of resilient deformation, and increasing the modulus of the RAP bases.

CHAPTER 3

MATERIALS AND THEIR PROPERTIES

This chapter discusses the properties of different materials used in the experimental study obtained from different laboratory tests.

3.1 Geocell

The geocell, made of novel polymeric alloy (NPA), was manufactured and provided by *PRS* Mediterranean, Ltd. in Israel. It has three-dimensional honeycomb-interconnected cells used to confine RAP as shown in **Figs. 3.1.1a** and **b**. The geocell used in this study had 1.1-mm wall thickness, 100 and 150 mm cell heights, 19.1-MPa tensile strength, and 355-MPa elastic modulus at 2% strain. The tensile strength and elastic modulus were determined by Pokharel (2010) based on the tensile tests of geocell sheets at a strain rate of 10%/min at 23°C. The tensile stress-strain curve of geocell is shown in **Fig. 3.1.2**. In addition, the geocell used in unpaved and paved road test sections had two and five perforations of 100 mm^2 area each on each pallet, respectively. The creep resistance and other material properties of geocell are shown in **Tables 3.1.1** and **3.1.2**, respectively**.**

(a) Bundled geocell during transportation
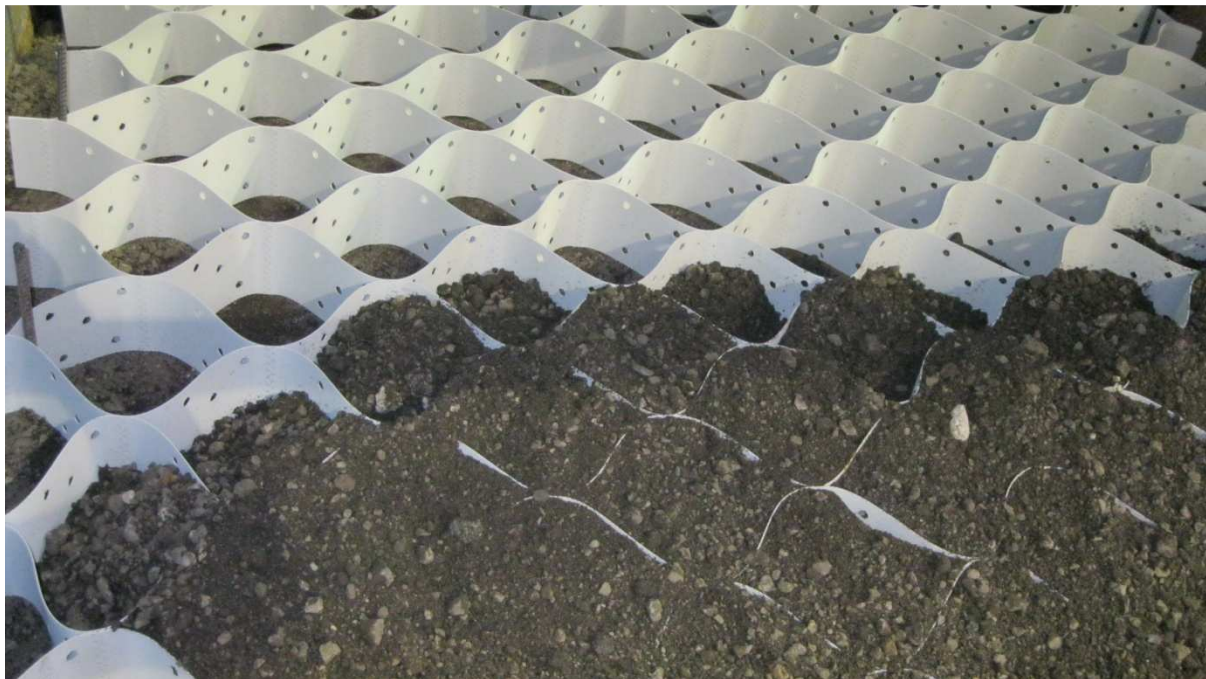
(b) Expanded geocell infilled with RAP

Fig. 3.1.1   Geocell

51
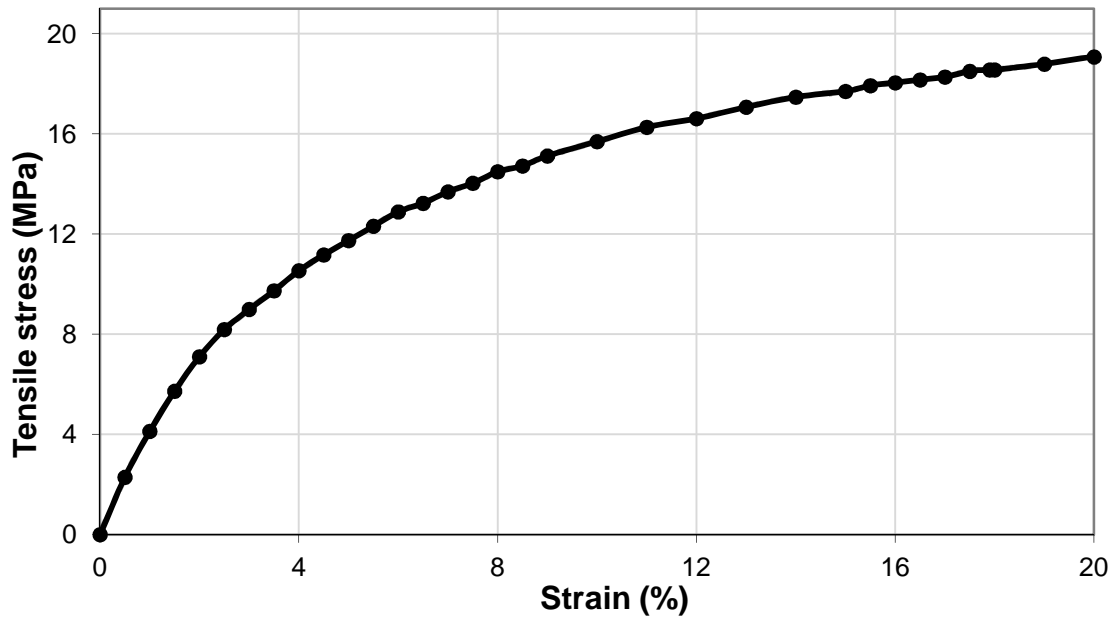
Fig. 3.1.2   Tensile stress-strain curve of geocell specimen (Pokharel, 2010)

Table 3.1.1   Creep resistance properties of the geocell
(provided by the manufacturer)

Time (years)	Stress to create 10% strain at 23℃ (N/mm)
25	5.82
50	5.65
75	5.56

Table 3.1.2 Material properties of the geocell (provided by the manufacturer)

Properties		Description	Unit	Test Method
Tensile strength		□20	N/mm	PRS method
Tensile modulus at 1% strain		462	N/mm	
Allowed strength for design of 50 years		□5.7	N/mm	ASTM D 6992
Creep reduction factor		□3.5		ASTM D 6992
Coefficient of thermal expansion (CTE)		≤80	ppm/℃	ISO 11359-2 ASTM E 831
Flexural storage modulus at	30℃	□750	MPa	ISO 6721-1 ASTM E 2254
	45℃	□650		
	60℃	□550		
	80℃	□300		
Oxidative induction time (OIT)		≥100	min	ISO 11375-6 ASTM D 3895 (OIT @ 200℃, 25 kPa)
Durability of UV degradation		≥400	min	ASTM D 5885 (HPOIT @ 150℃, 3500 kPa)

3.1.1 Creep test of geocell

The creep test of the geocell under tension was performed in a loading frame designed and fabricated for the geotechnical laboratory at the Department of Civil, Environmental, and Architectural Engineering at the University of Kansas. The test frame had two metal clamps holding the test specimen for loading and two plexiglass

clamps at 150 mm apart for displacement measurement. The test frame had a hanging rod with a metal base plate to support weight. The details of the test frame are shown in **Fig. 3.1.3**. The creep test of the 100 mm high geocell specimen was conducted at a room temperature of approximately 25°**C** to investigate the creep behavior of the geocell material. The tensile load of 4.3 kN/m (i.e., 430 N in total) was maintained during the creep test for 1 month. The load was chosen based on the allowable tensile strength of the geocell and a creep reduction factor of 2.5. The deformation with time was monitored during the test. The measured deformations were used to calculate the tensile creep strains. The tensile creep strain versus time curve was plotted and is shown in **Fig. 3.1.4**. The maximum creep strain observed at the end of 1 month was about 1.5%.
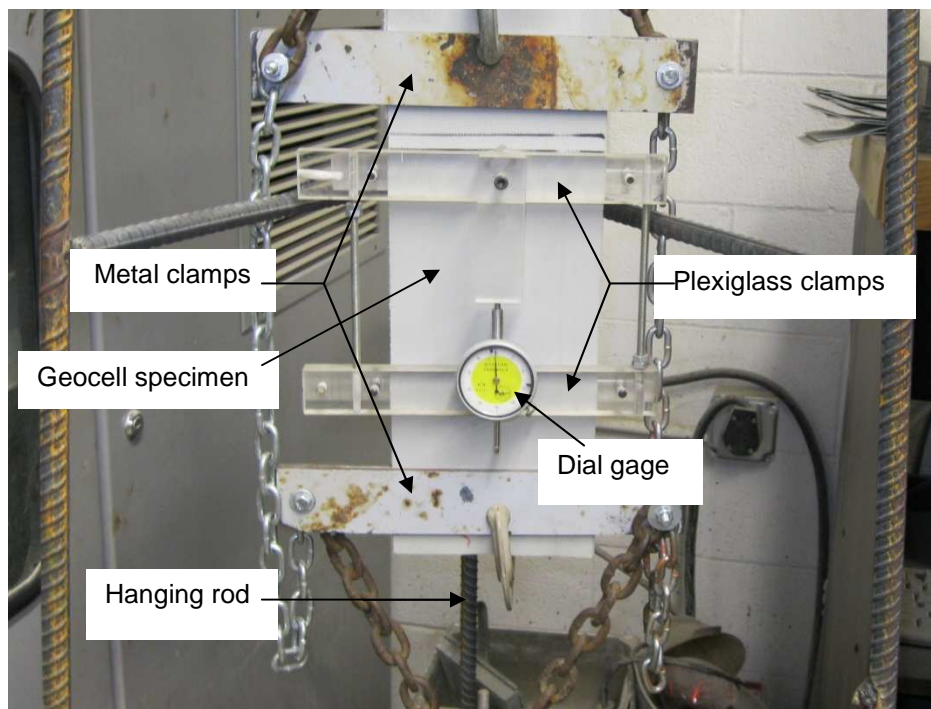
Fig. 3.1.3   Setup for tensile creep test of geocell (Thakur et al., 2012)
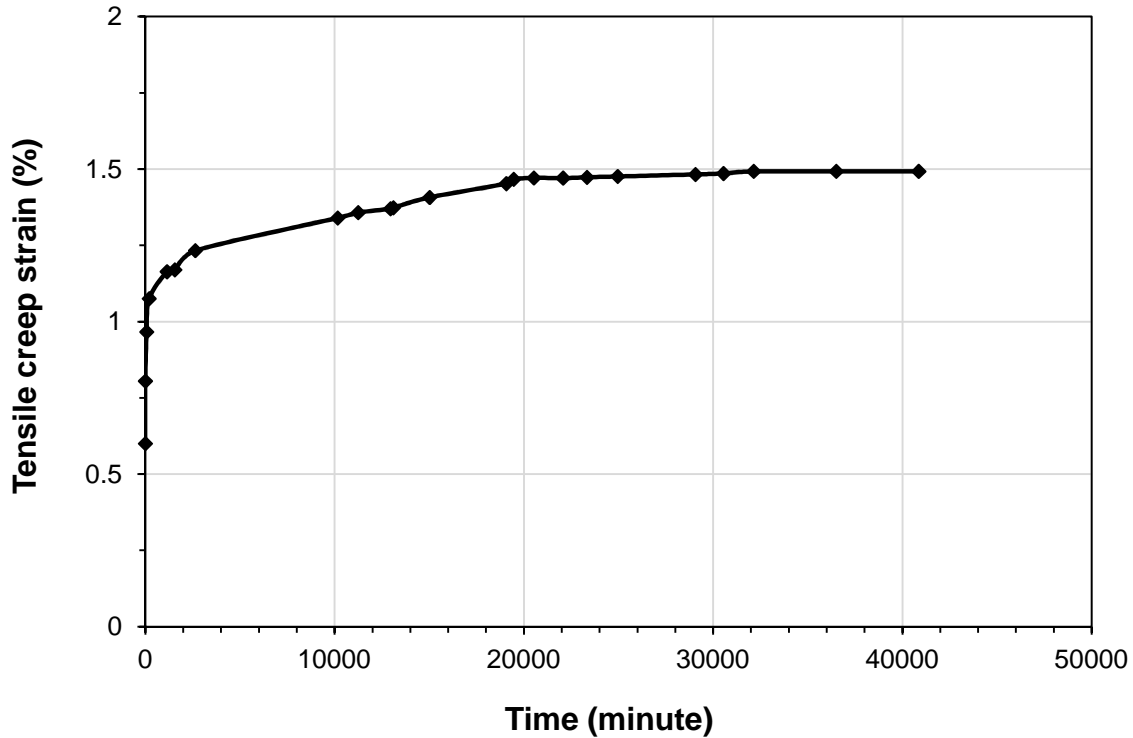
Fig. 3.1.4 Creep behavior of the geocell subjected to 430 N tensile load

(Thakur et al., 2012)

3.2 *Geotextile*

A 3.5 oz (99.65 g) non-woven geotextile was placed at the interface of subgrade and base course as a separator in all the reinforced test sections in the large geotechnical test box. The material properties of geotextile are shown in **Table 3.2.1**, and are same as those reported in Thakur et al. (2012).

Table 3.2.1   Material properties of the geotextile (provided by the manufacturer)

Properties	Description	Unit	Test Method
Grab tensile strength	0.401	kN	ASTM D 4632
Grab elongation	50	%	ASTM D 4632
Trapezoid tear strength	0.178	kN	ASTM D 4533
Puncture resistance	0.267	kN	ASTM D 4833
Mullen burst strength	1378	kPa	ASTM D 3786
Permittivity	2.2	1/s	ASTM D 4491
Water flow	6095	$1/min/m^2$	ASTM D 4491
Apparent opening size (AOS)	0.212	mm	ASTM D 4751

3.3   Subgrade

A mixture of 25% Kaolin and 75% Kansas River (KR) sand was used as a subgrade layer for all test sections. The poorly-graded sub-rounded KR sand had a mean particle size (d_{50}) = 0.54 mm, coefficient of curvature (Cc) = 0.95, coefficient of uniformity (C_u) = 3.1, and specific gravity = 2.62 (Pokharel, 2010). **Fig. 3.3.1** shows the gradation curve of the KR sand. The liquid and plastic limits of the subgrade soil were found to be 30% and 22%, respectively. The standard Proctor compaction and unsoaked CBR curves of the subgrade are shown in **Fig. 3.3.2**. The subgrade had a maximum dry density of about 2.01 g/cm^3 at an optimum moisture content of 10.8%, and a CBR value of 2% at 11.4% moisture content and a CBR value of 5% at 10.4% moisture content.
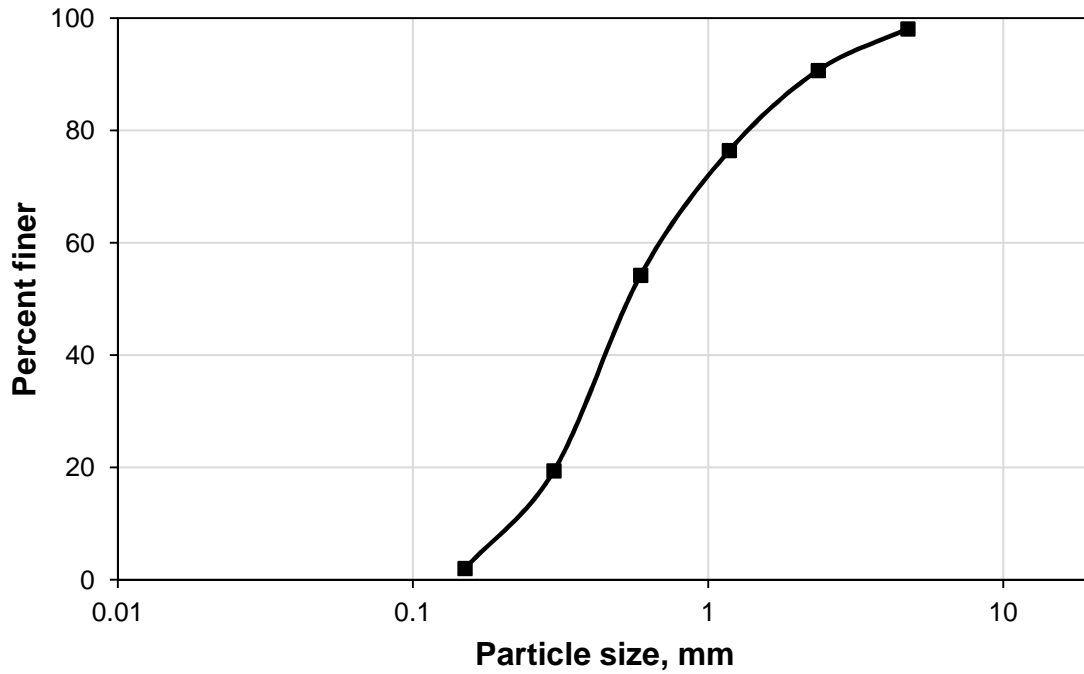
Fig. 3.3.1　　Gradation curve of KR sand (Pokharel, 2010)
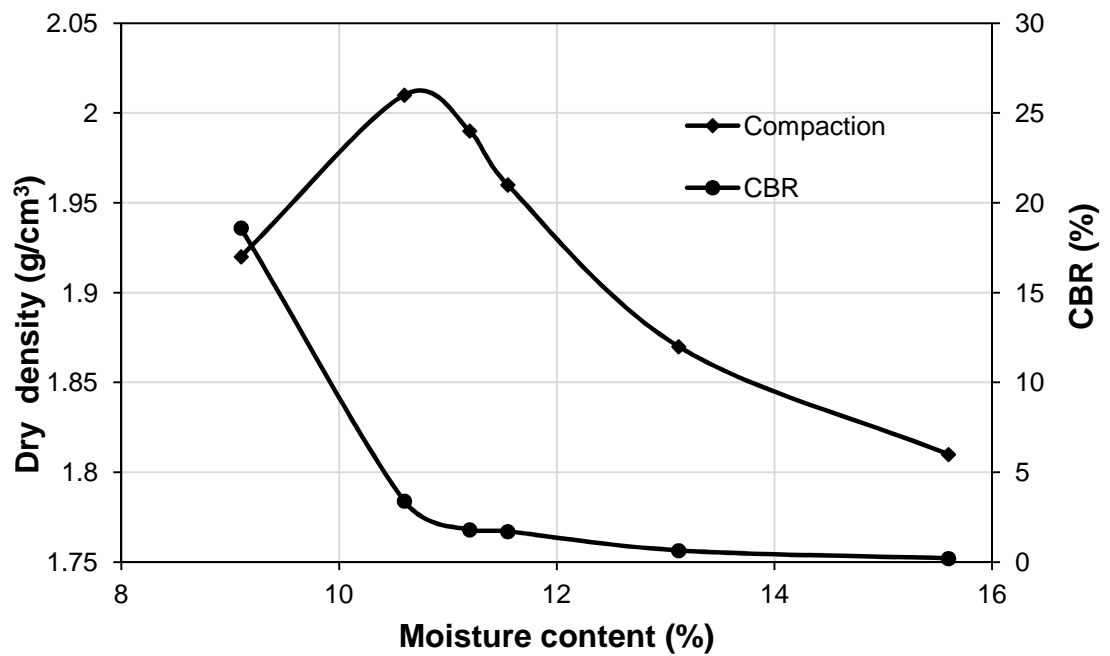
Fig. 3.3.2　　Standard Proctor compaction and CBR curves of subgrade

(Pokharel, 2010)

3.4 Recycled Asphalt Pavement (RAP)

Recycled asphalt pavement (RAP) milled from a city street in Lawrence, Kansas was used as the base material in this study. It was a fractionated RAP material (sometimes named as FRAP) and provided by a local plant, R.D. Johnson Excavating, Co., Lawrence, Kansas. **Fig. 3.4.1** shows the picture of RAP used in this study. The properties of the RAP material were determined by laboratory tests following different ASTM standards and are presented in **Table 3.4.1**. The fine and coarse aggregates were extracted from RAP by an ignition method whereas asphalt was extracted by a centrifuge method for determining its properties. **Fig. 3.4.2** shows the gradation curves of the RAP aggregates extracted by the ignition method before and after compaction. There were minor changes in the gradation curves after compaction. Average minimum and maximum index densities of RAP were found to be 1.415 g/cm^3 and 1.740 g/cm^3, respectively. Five modified Proctor compaction tests were performed on RAP specimens at different moisture contents following ASTM D 1557 to obtain the compaction curve as shown in **Fig. 3.4.3**. The maximum dry density was about 1.96 g/cm^3, which corresponds to the optimum moisture content (OMC) of 6.6%. Also, five unsoaked California Bearing Ratio (CBR) tests were performed on laboratory-compacted RAP specimens at different moisture contents following ASTM D 1188 to obtain the CBR versus moisture content curve as shown in **Fig. 3.4.3**. The test procedure and equipment used to determine different properties of RAP were discussed in Thakur (2011).
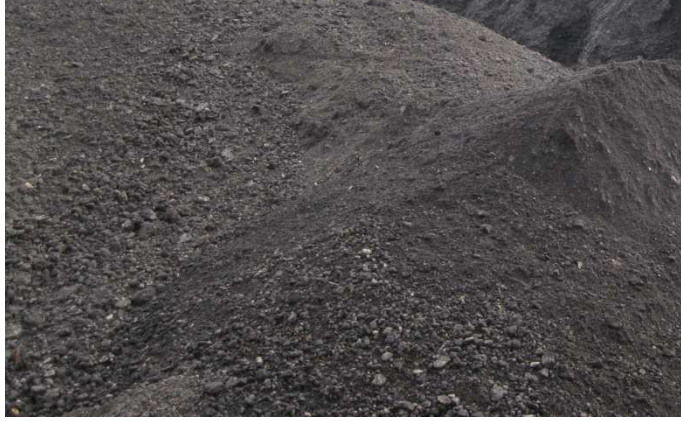
Fig. 3.4.1   Picture of RAP material

Table 3.4.1   Properties of the RAP and subgrade materials

	Aggregate			Test Method
	Bulk specific gravity	Fine aggregate	2.48	ASTM C 128
		Coarse aggregate	2.39	ASTM C 127
	SSD bulk specific gravity	Fine aggregate	2.56	ASTM C 128
		Coarse aggregate	2.49	ASTM C 127
RAP Material	Uncompacted void content	Fine aggregate	39.15%	ASTM C 1252 (Method B)
	Mean particle size (d_{50}) (mm)		2.0	
	Coefficient of curvature (C_c)		0.85	
	Coefficient of uniformity (C_u)		8.33	
	Asphalt Binder			
	Binder content	Centrifuge method	6.71%	ASTM D 2172
		Ignition method	6.87%	ASTM D 6307
	Viscosity of asphalt binder at 135°C (Pa-s)		1.408	ASTM D 1856
Kansas River (KR) sand used in subgrade mix	Specific gravity		2.62	ASTM C 128
	Mean particle size (d50) (mm)		0.54	
	Coefficient of curvature (Cc)		0.95	
	Coefficient of uniformity (Cu)		3.1	
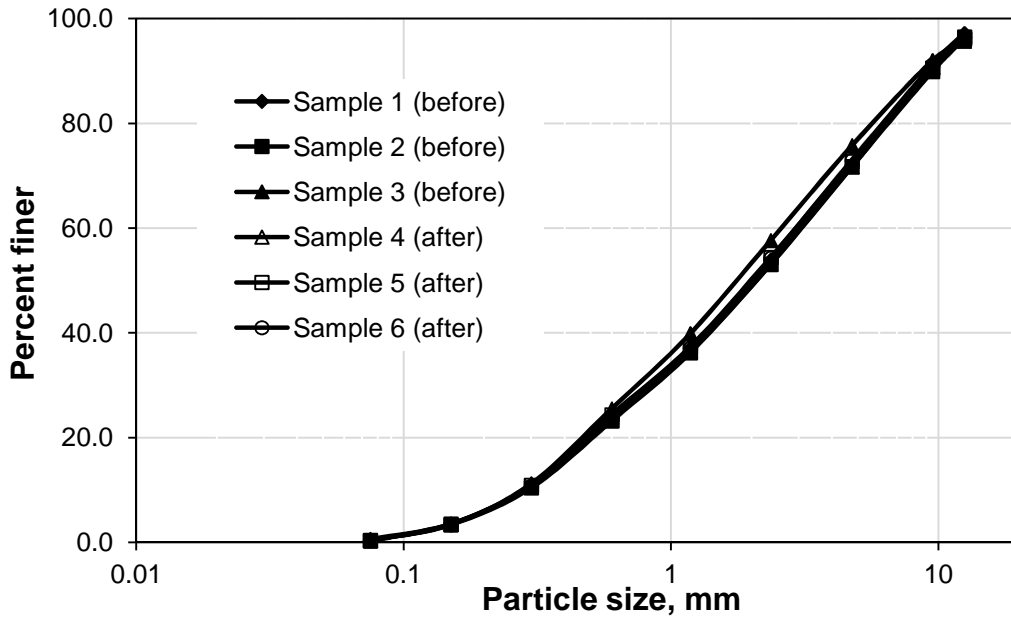
Fig. 3.4.2   Gradation curve of RAP aggregate (Thakur et al., 2012)
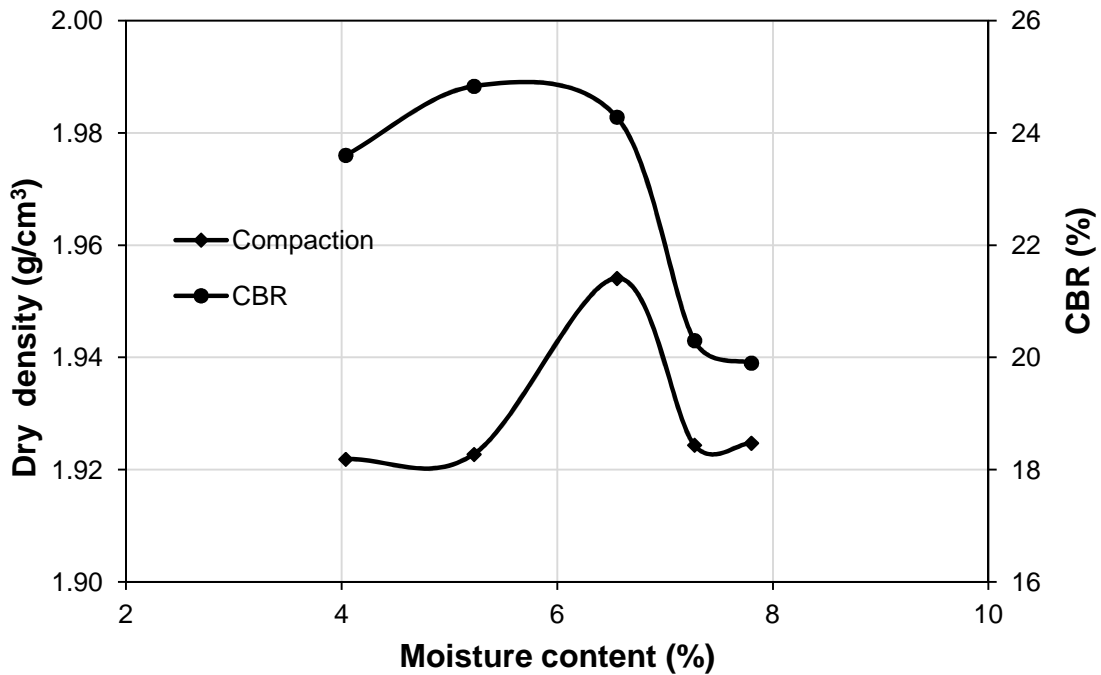
Fig. 3.4.3   Modified Proctor compaction and CBR curves of RAP (Thakur et al., 2012)

3.4.1 Shear strength

Shear strength test results for RAP and interface shear test results for geocell-RAP interface presented in Thakur (2011) are found incorrect because of the defects in the test equipment which was found after publishing those results. Hence the large direct shear box tests and interface shear tests were repeated on RAP and geocell-RAP interface, respectively using the equipment in proper conditions and the test results are presented in this section.

Geocell-RAP interface shear test

Interface shear test is used to determine the shear resistance of a geosynthetic sheet against soil or one geosynthetic sheet against another geosynthetic sheet under a constant rate of shear deformation. Peak shear strength of soil is its maximum resistance to shear stresses just before failure. Geocell infilled with soil has been used for various purposes including road applications. Hence it is necessary to evaluate the interface shear strength between geocell and infill RAP.

Five interface shear tests were performed in accordance with ASTM D 5321-02 at five different normal stresses (i.e. 34, 52, 69, 86, and 103 kPa) using a large direct shear box to determine the interface shear strength of geocell against RAP at the moisture content corresponding to 98% compaction. The lower shear box was originally bigger in the plan area than the upper shear box having dimensions of 300 mm x 300 mm x 100 mm high. The plan area of the lower box was made same as the upper box after placing wooden plank. The tests were performed at a shear strain rate of 2.54 mm per minute. **Fig. 3.4.4** presents different steps of an interface shear test performed.
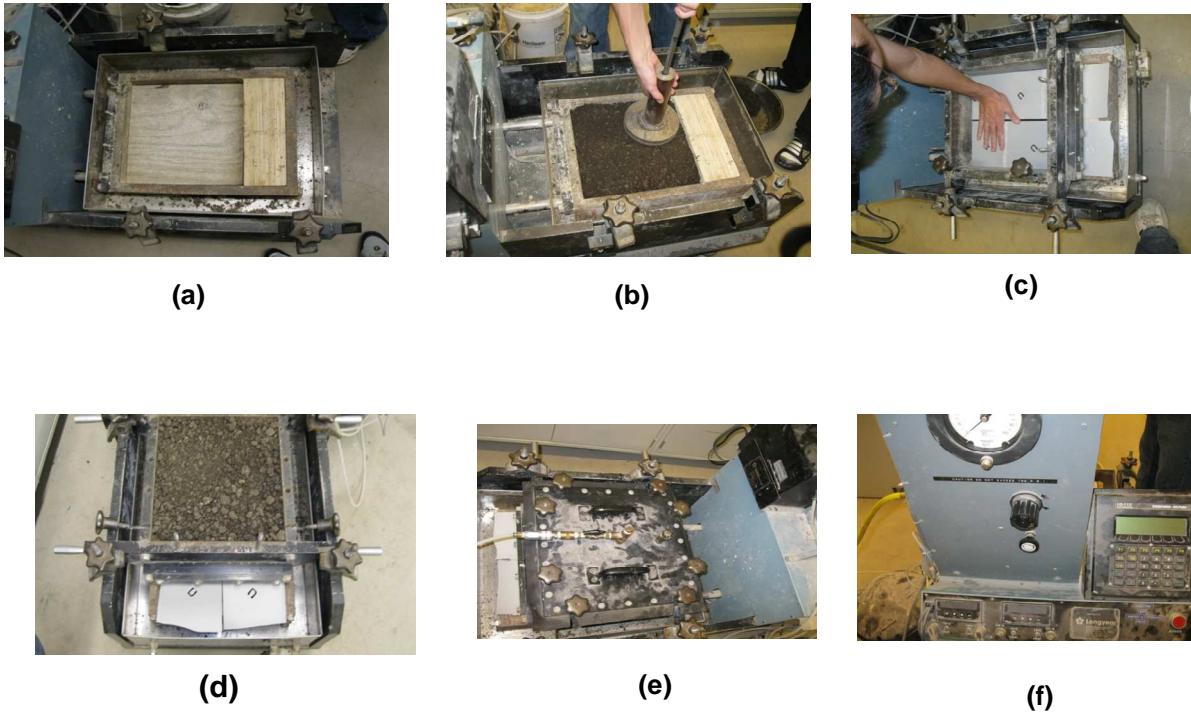
Fig. 3.4.4   Steps for interface shear test: (a) lower box before RAP is placed, (b) placing RAP inside the lower box and compacting, (c) placing geocell on the compacted RAP and then placing the upper box, (d) placing RAP inside the upper Box and then compacting, (e) placing and tightening the top plate and connecting the air pressure hose, and (f) applying air pressure and starting the test

Fig. 3.4.5 presents the shear stress-displacement curves obtained from the geocell-RAP interface shear tests. For all the tests, shear stresses increased rapidly with increasing horizontal displacements for up to about 10 mm displacement, and then they increased marginally throughout the tests. Hence the only peak shear strength at each normal stress was observed and the residual strength was approximately equal to the peak shear strength.   The observed peak shear strengths at different normal

stresses are reported in **Table 3.4.2** and the shear strength envelopes for interface shear tests are shown in **Fig. 3.4.6**. The interface cohesion and friction angle were found to be 2.4 kPa and 37.8°, respectively.
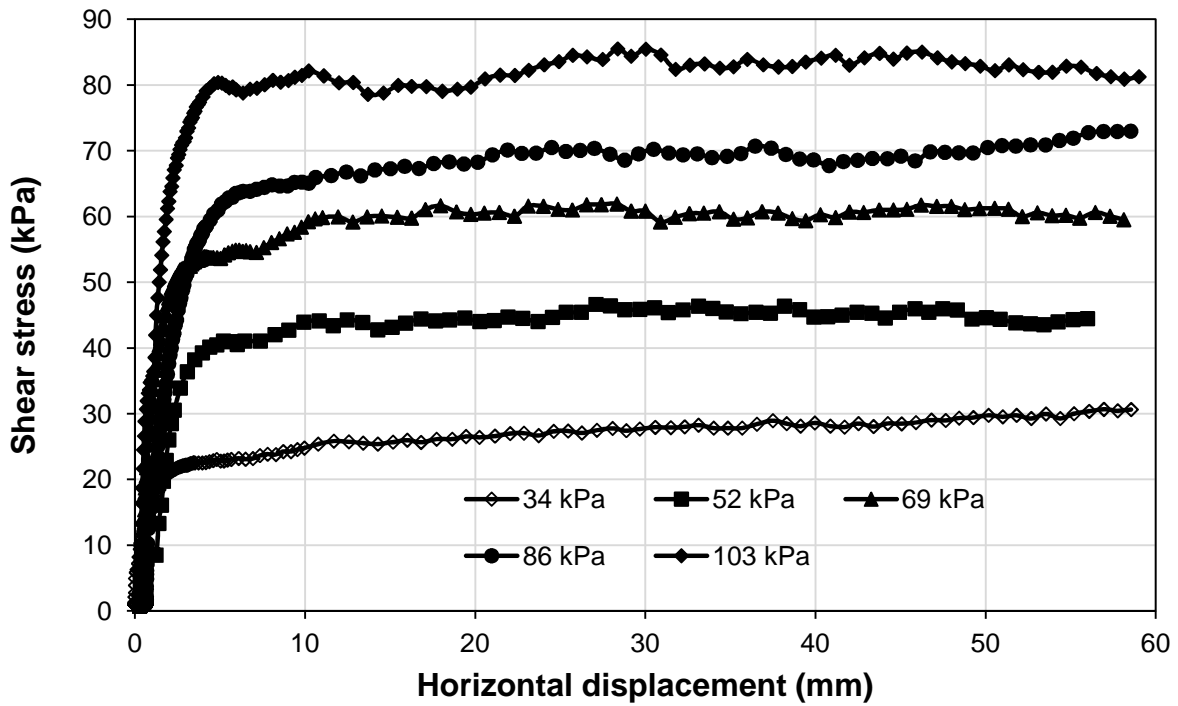
Fig. 3.4.5   Shear stress-displacement behavior of geocell-RAP interface at different normal stresses

Table 3.4.2　　　　　Peak shear strengths at different normal stresses for interface shear tests

Normal stress (kPa)	Peak shear strength (kPa)
34	25.8
52	44.1
69	59.8
86	65.9
103	81

$y = 0.7695x + 2.3755$
$R^2 = 0.9795$
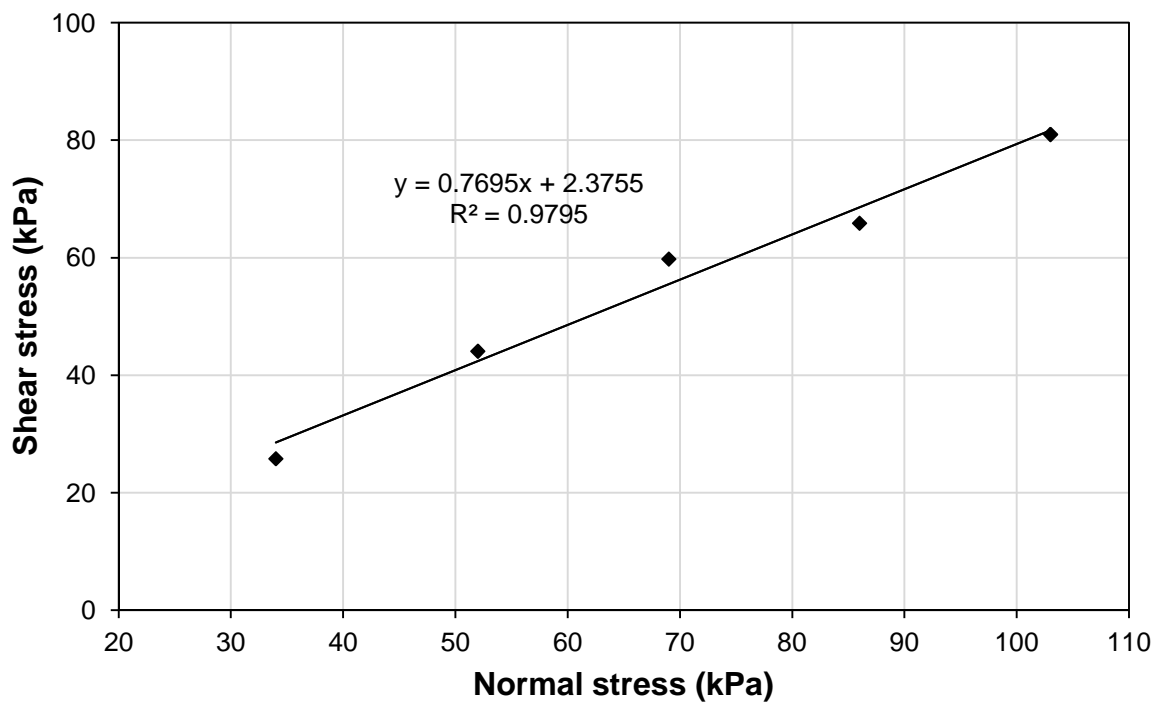
Fig. 3.4.6　　　Shear strength envelope for interface shear test

<u>Large direct shear box test on RAP</u>

Five direct shear tests were performed in accordance with ASTM D 5321-02 at five different normal stresses (i.e. at 34, 52, 69, 86, and 103 kPa) using the large direct shear box to determine the shear strengths of RAP at the moisture content of 5.6% corresponding to 98% compaction. The lower shear box was bigger in the plan area than the upper box having dimensions of 300 mm x 300 mm x 100 mm high; however, the heights of both boxes were equal. The tests were performed at a shear displacement rate of 2.54 mm per minute. The steps of the direct shear tests were same as the interface shear test which is shown above in **Fig. 3.4.4**.

Fig. 3.4.7 presents the shear stress-displacement curves for RAP. For all the tests, the shear stresses increased rapidly with increasing horizontal displacements for up to about 10 mm displacement, and then they increased marginally throughout the tests for some samples and for other samples they remained almost constant. Hence the only peak shear strength at each normal stress was observed and the residual strength was approximately equal to the peak shear strength. The observed peak shear strengths at different normal stresses are reported in **Table 3.4.3** and the shear strength envelopes for large direct shear tests are shown in **Fig. 3.4.8**. The cohesion and friction angle of RAP were found to be 20 kPa and 42°, respe ctively.
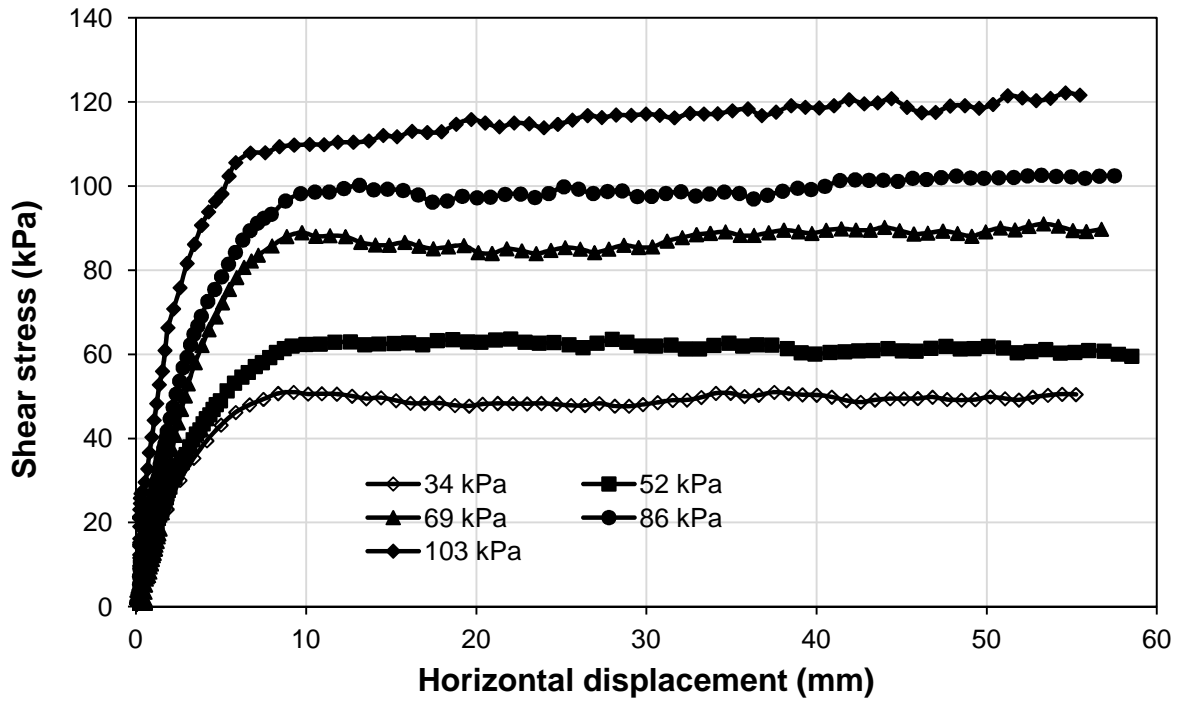
Fig. 3.4.7   Shear stress-displacement behavior of RAP at different normal stresses

Table 3.4.3   Peak shear strengths at different normal stresses for direct shear tests

Normal stress (kPa)	Peak shear strength (kPa)
34	51
52	62
69	88
86	98
103	110
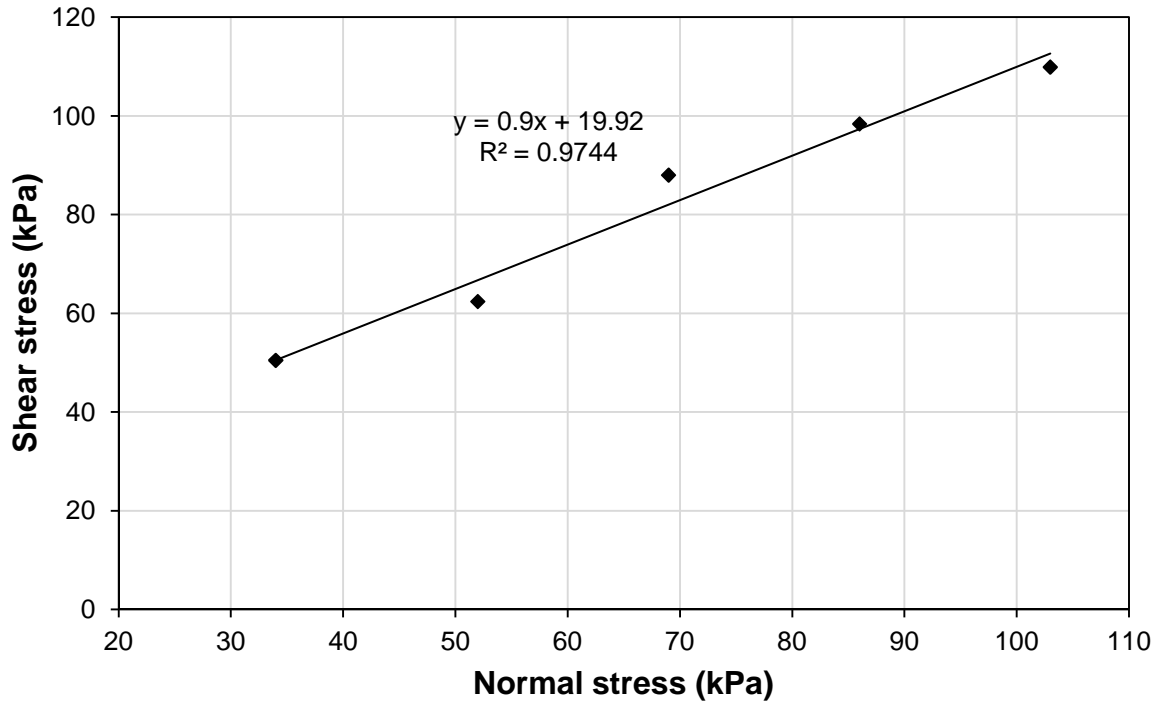
Fig. 3.4.8   Shear strength envelopes for direct shear tests

Interaction coefficient (C_i) between geocell and RAP and interface efficiencies of cohesion and friction angle were determined based on the results of interface and direct shear tests discussed above.   Interaction coefficient and interface efficiencies of cohesion and friction angle were calculated using the equations given below:

$$Interaction\ coefficient\ (C_i) = \frac{Interface\ shear\ strength}{RAP\ shear\ strength}$$

$$Interface\ efficiency\ on\ cohesion\ (E_c) = \frac{Interface\ cohesion\ of\ RAP\ to\ geocell}{Cohesion\ of\ RAP}$$

$$Interface\ efficiency\ on\ friction\ angle\ (E_\varphi) = \frac{\tan\ (Interface\ friction\ angle)}{\tan\ (frinction\ angle\ of\ RAP)}$$

The interaction coefficients were calculated and are reported in **Table 3.4.4**.

Table 3.4.4 Interaction coefficient

Normal stress (kPa)	Interface shear strength (kPa)	Shear strength of RAP (kPa)	Interaction coefficient (C_i)	Average interaction coefficient (C_i)
34	25.8	51	0.51	
52	44.1	62	0.71	
69	59.8	88	0.68	0.66
86	65.9	98	0.67	
103	81	110	0.74	

The average interaction coefficient and interface efficiencies on cohesion and friction angle between geocell and RAP were found to be 0.67, 0.12, and 0.86, respectively.

3.5   Tack coat

Slow setting asphalt emulsion, commonly known as tack coat, was applied between HMA surface and RAP base.   The tack coat material was provided by SunFlower Paving, Inc., Lawrence, Kansas.

3.6   Hot mix asphalt (HMA)

Hot mix asphalt (HMA) concrete brought from the local plant, R.D. Johnson Excavating, Co., Lawrence, Kansas, was used as the surface course layer for all paved road test sections.   The HMA is a Superpave mix- SM9.5 with asphalt binder content of about 5.6%.   The asphalt binder was Superpave PG 64-22.   Based on the data provided by

the plant, the HMA consisted of 94.3% aggregate and 5.7% asphalt binder. The aggregate used in HMA mixes was a blend of 20.3% crushed limestone aggregate (Type A: maximum size of aggregate = 19 mm), 17.3% crushed limestone aggregate (Type B: maximum size of aggregate = 6.25 mm), 24.4% crushed limestone aggregate (Type C: maximum size of aggregate = 4.75 mm), 9.2% natural sand aggregate, and 28.8% RAP. **Table 3.6.1** presents the specific gravity and water absorption of all aggregates used in the HMA mix. The composite specific gravity of the mixed aggregate was found to be 2.58 based on the percentages of different types of aggregates in the mix and their individual specific gravity data. The properties of asphalt binder were provided by the plant and are reported in **Table 3.6.2.**

Table 3.6.1   Specific gravity and water absorption of aggregates used in HMA mix

(provided by plant)

Type of aggregate	Bulk specific gravity	Water absorption (%)
Crushed aggregate (Type A)	2.53	2.5
Crushed aggregate (Type B)	2.52	3
Crushed aggregate (Type C)	2.51	4.2
Natural sand aggregate	2.6	0.5
RAP	2.71	NA

Note: NA stands for not available

Table 3.6.2 Properties of asphalt binder used in HMA mix (provided by plant)

Properties	Test method	Units	Results	Specifications	
Pen@ 25℃	ASTM D-5	mm	68	Min	Max
SP. Gravity @60℉ (API gravity)	ASTM D-70		5.509		
SP. Gravity @15.6℃ (Sp. Gravity)	ASTM D-70		1.033		
Flash point	ASTM D-92	℃	316	230	
Absolute viscosity (Vacuum capillary viscometer)@ 140℉	ASTM D-2171	poise	1976		
Rotational viscosity (Rotational viscometer)@ 135℃	ASTM D-4402	Pa-s	0.383		3
Dynamic Shear @ 64℃	AASHTO T-315 (Orig DSR)	kPa	1.14	1	
Phase angle @ 64℃		Deg	86.8		
Mass loss	ASTM D RTFO	wt %	-0.091	-1	1
Dynamic Shear @ 64℃	AASHTO T-315 (RTFO DSR)	kPa	3.55		
Phase angle @ 64℃		Deg	82.4		
Dynamic Shear @ 25℃	AASHTO T-315 (PAV DSR)	kPa	3778		
Phase angle @ 25℃		Degrees	43.7		
Average stiffness @12℃	AASHTO T-313-BBR	M-Pa	147		
Average M-value @12℃			0.32	0.3	

CHAPTER 4

LARGE-SCALE CYCLIC PLATE LOADING TESTS ON UNPAVED

ROADS

Nine large-scale laboratory cyclic plate loading tests were conducted on unpaved road test sections in a large geotechnical test box available at the University of Kansas. The unpaved road test sections consisted of unreinforced RAP bases (150 and 300 mm thick) or geocell-reinforced RAP bases (150, 200, and 300 mm thick) over weak or moderate (target CBR = 2% or 5%) subgrade.

4.1 Test materials

4.1.1 Geosynthetics

The geocells (100 and 150 mm high) were used to reinforce RAP bases and a non-woven geotextile was placed at the interface of subgrade and RAP base course as a separator in all the test sections. The properties of geocells and geotextile were presented in Chapter 3.

4.1.2 Subgrade

A mixture of 25% Kaolin and 75% Kansas River (KR) sand was used as a subgrade layer for all test sections. The properties of subgrade materials were presented in Chapter 3. The subgrade was compacted at 11.4 and 10.4% moisture content to

achieve CBR values of 2 and 5%, respectively.

4.1.3 Base material

The same RAP, the properties of which were presented in Chapter 3, was used as the base material. The RAP base was compacted at 5.5% moisture content to achieve 95% of the maximum dry density.

4.2   Test box and loading system

Large-scale cyclic plate loading tests were conducted in a steel box at the geotechnical laboratory at the University of Kansas. The overall dimensions of the box were 2.2 m long, 2.0 m wide, and 2.0 m high. Unpaved road test sections were constructed inside the box. The bottom and three sides of the box were fixed and constructed of steel plate reinforced with square steel tubing while the front of the box was constructed of detachable steel channel sections of height 150 mm fixed with nuts and bolts to permit the construction of test sections. A servo hydraulic MTS loading system was used to apply a cyclic load on test sections in the box. The loading system consisted of a loading frame, a hydraulic actuator, and a servo-control unit. A hydraulic actuator with a load rating of 245 kN was used to apply cyclic loads on the steel loading plate that was seated on the surface of the test section. This cyclic load wave as shown in **Fig. 4.2.1** has a 2.0 second initial period where the load of 0.5 kN is held constant, followed by a linear load increase from 0.5 to 40 kN over a 0.3 second rise time, followed by a 0.2 second period where the load is held constant, followed by a linear load decrease from 40 to 0.5 kN over a 0.3 second, and finally followed by a 0.5 second period of 0.5kN

load before the load cycle is repeated, resulted in a load wave frequency of 0.77 Hz. The peak load was selected to simulate a single wheel load of 40 kN (equivalent to an axle load of 80 kN and a tire contact pressure of 550 kPa). The loading plate connected to the actuator was 300 mm in diameter and 30 mm thick. A 10 mm thick rubber pad was attached to the bottom of the loading plate to ensure full contact and minimize stress concentrations at the edge of the plate. A servo-control unit was connected both to a data acquisition system and a hydraulic control valve. The test box with the loading system is shown in **Fig. 4.2.2**.
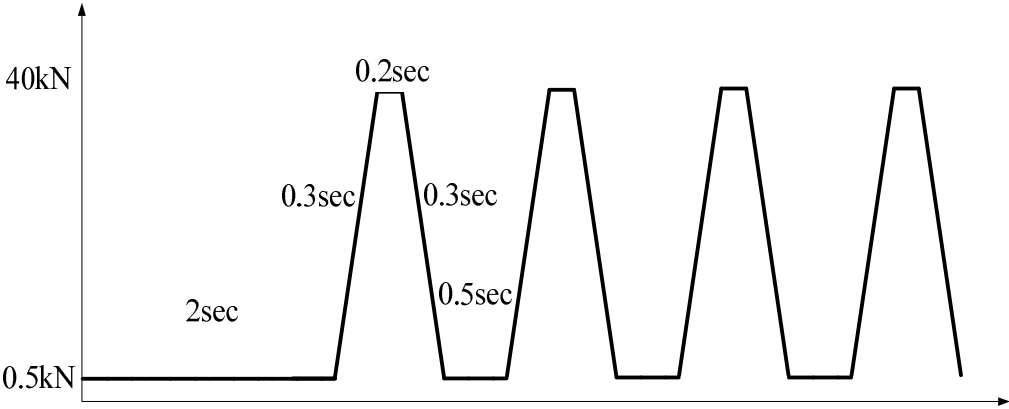
Fig. 4.2.1   Cyclic loading wave (Thakur et al., 2012)

Fig. 4.2.2   Large geotechnical testing box with the loading actuator

4.3   Test section preparation and instrumentation

Nine unpaved road test sections were prepared in the large test box.   Four (one unreinforced and three geocell-reinforced) and five (two unreinforced and three geocell-reinforced) bases were prepared over weak (target CBR = 2%) and moderate (target CBR = 5%) subgrades, respectively.   **Fig. 4.3.1** shows the schematic diagram for the set-up of the cyclic plate loading test.   The detailed cross-sections of the test sections on weak and moderate subgrades are shown in **Fig. 4.3.2**.
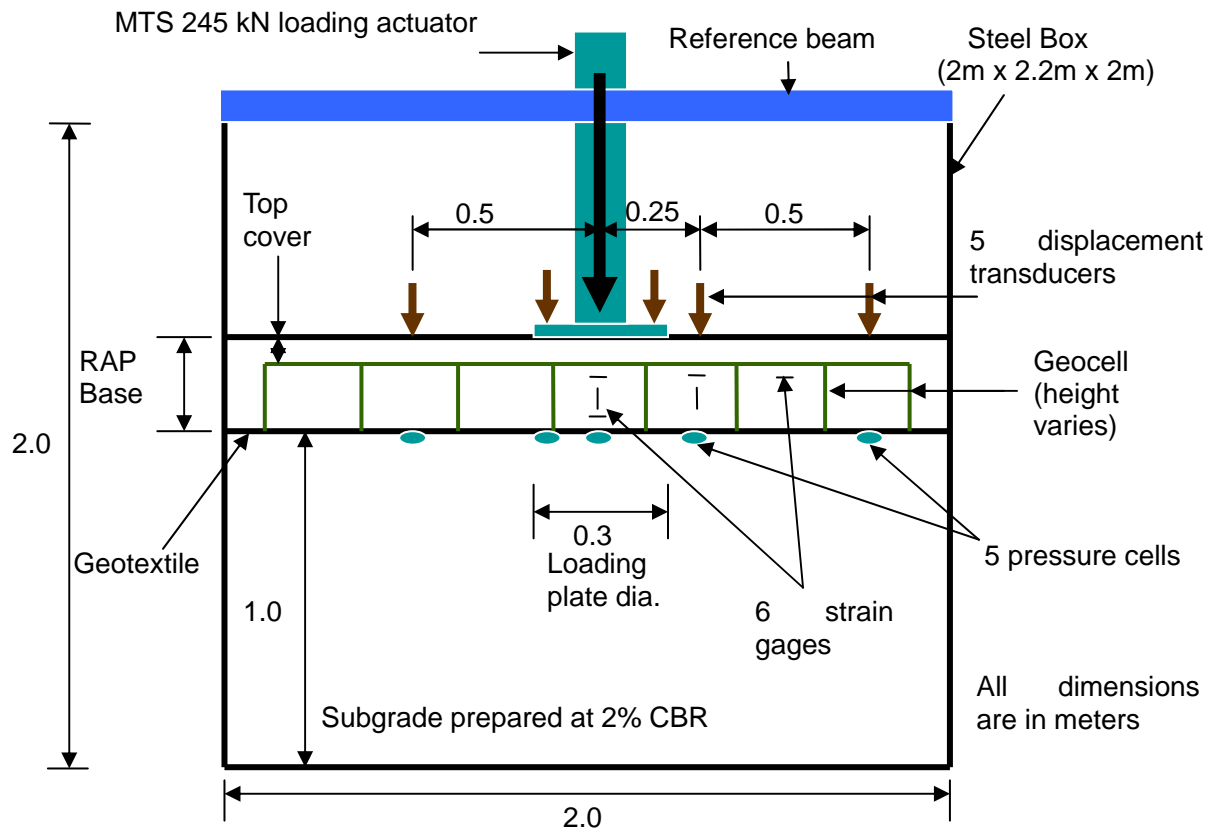
Fig. 4.3.1 Schematic diagram for the set-up of the cyclic plate loading test (Thakur et

al., 2012)
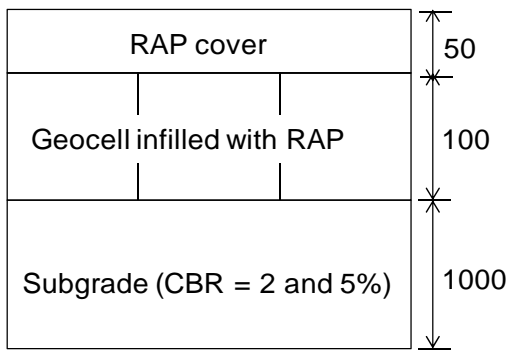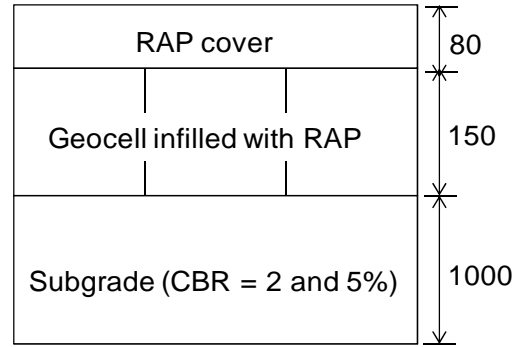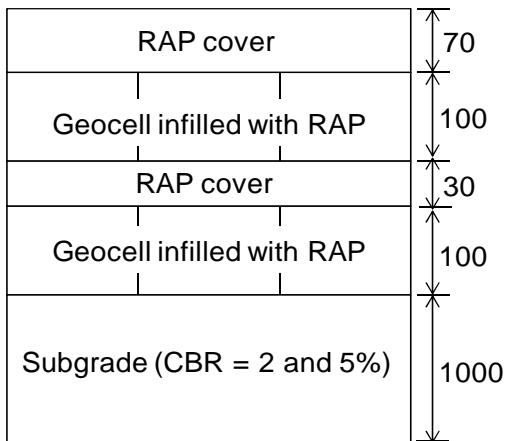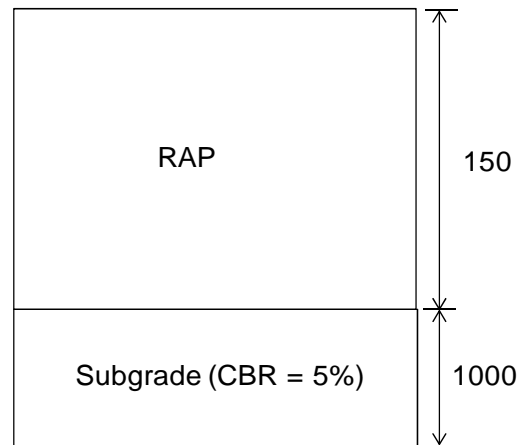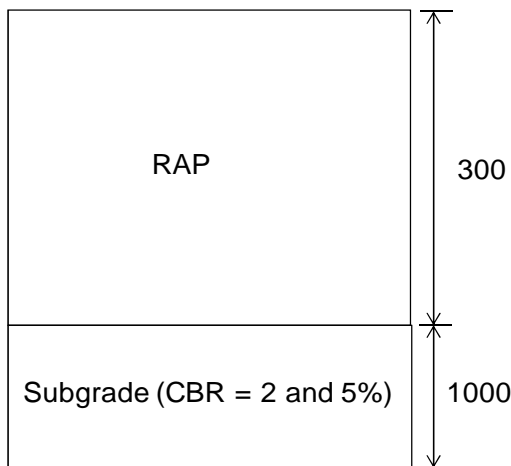
Fig. 4.3.2 Unpaved test sections: (a) 150 mm thick geocell-reinforced RAP base, (b) 230 mm thick geocell-reinforced RAP base, (c) 300 mm thick geocell-reinforced RAP base, (d) 150 mm thick unreinforced RAP base, and (e) 300 mm thick unreinforced RAP base

77

Each test section included 1,000 mm thick subgrade soil layer prepared and compacted at 11.4% and 10.4% moisture contents to obtain target CBR values of 2% and 5%, respectively. The subgrade soil was prepared by mixing 75% KR sand and 25 % Kaolin with required amount of water using shovel. The prepared mix was first placed, raked level, and then compacted in lifts inside a box using a vibratory plate compactor as shown in **Fig. 4.3.3**. The thicknesses of each lift for the bottom 600 mm thick and the remaining 400 mm thick subgrade soil were 150 mm and 100 mm, respectively.

Fig. 4.3.3   Compacting subgrade using the vibratory plate compactor

The subgrade strength was checked by vane shear tests during the subgrade preparation as shown in **Fig. 4.3.4**.

Fig. 4.3.4   Vane shear test

After preparing the subgrade at a desired CBR, four strain gauge type earth pressure cells having a thickness of 11.3 mm, an outer diameter of 50 mm, a sensing area diameter of 46 mm, and a weight of 160 g were installed on the top of the subgrade. The earth pressure cells having the maximum capacities of 500, 500, 250, and 250 kPa were installed at the center, 12.5 mm, 25 mm, and 50 mm away from the center of the loading plate, respectively. To install the pressure cells, circular holes of a slightly larger diameter than the pressure cell were dag out with a hand trowel. The bottom of each hole was leveled by hand tamping. The pressure cells were then horizontally placed as shown in **Fig. 4.3.5** and then covered with the subgrade backfill and gently compacted over the pressure cells by hand tamping to ensure that the density of backfill subgrade was nearly same as the surrounding soil.

Fig. 4.3.5   Installing pressure cell on top of subgrade

The reinforced bases constructed over weak and moderate subgrades were 150, 230, and 300 mm thick. The unreinforced bases constructed over moderate subgrade were 150 and 300 mm thick while that constructed over weak subgrade was 300 mm thick. After installation of pressure cells, a layer of geotextile was placed on top of the subgrade and the geocells installed with strain gages were placed on top of geotextile for reinforced sections. Half-square grid general purpose strain gages were installed on the geocell walls to measure induced strains due to the deformation of the geocell under the application of the load. The surface of the geocell wall was smoothened by a sand paper and cleaned by isopropyl alcohol before installing the strain gages. The strain gages were then installed to the smoothened wall surface using Cyanoacrylate adhesive and then covered with N-1 (VH10L) general purpose coating material. Three strain gages were installed on the central cell just under the loading plate (one each at top, middle and bottom of the wall), two gages were installed at the top and middle of

the geocell wall on the adjacent cell, and one gage was installed at the top of the geocell wall on the next neighbouring cell as shown in **Fig. 4.3.6**, in which the symbol, location, and orientation of each strain gage are provided. The strain gages had grid resistance of 120 ± 0.6% ohms, gage facor of 2.1± 0.5%, grid length of 6.35 mm, and grid width of 3.18 mm and are the same as those reported in Thakur et al. (2012). The total number of strain gages installed in 150, 230, and 300 mm reinforced sections were 6, 6, and 12 respectively.
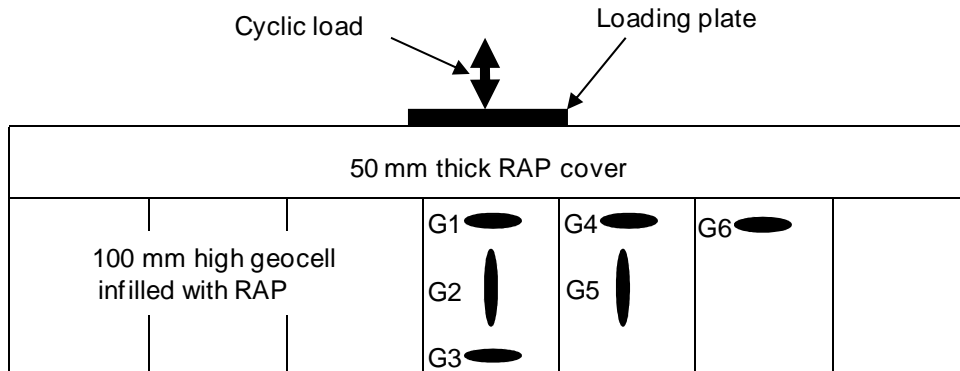
(a) 150 mm thick geocell-reinforced section
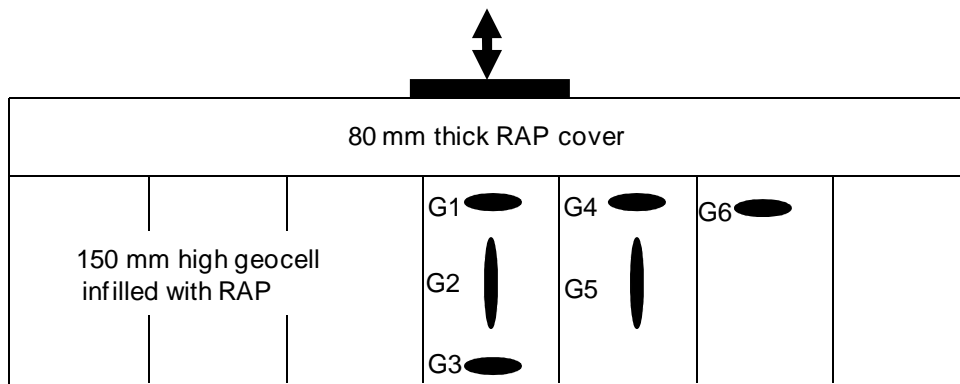
(b) 230 mm thick geocell-reinforced section

Fig. 4.3.6   Symbols, locations, and orientations of strain gages
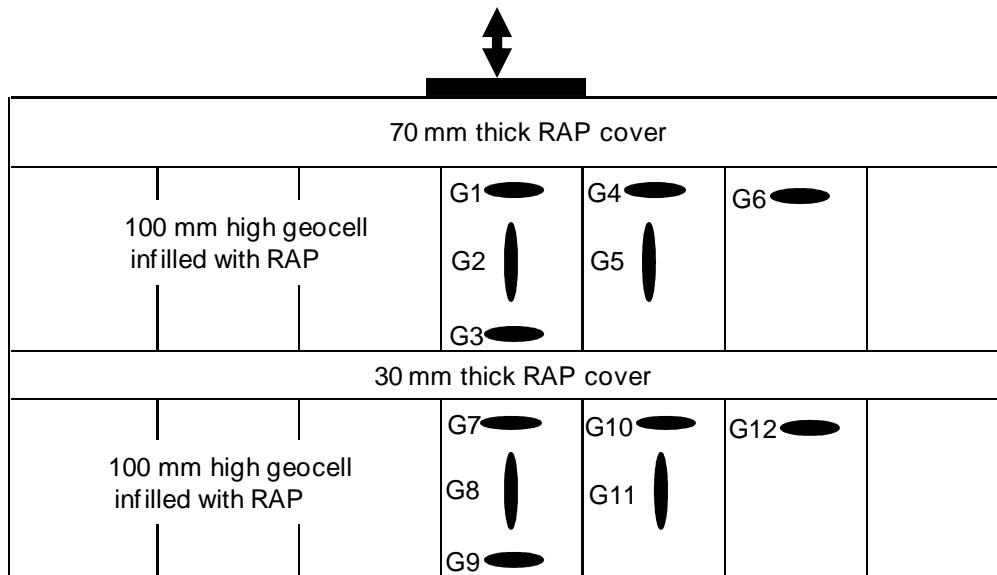
(c) 300 mm thick geocell-reinforced section

Fig. 4.3.6 Symbols, locations, and orientations of strain gages (continued)

The layout for the installation of geocell inside the test box on top of geotextile is shown in **Fig. 4.3.7**. The geocells placed on top of geotextile were stretched out in a near circular pattern as recommended by Pokharel (2010) as shown in **Fig. 4.3.8**. Short rebar stakes were used as pegs to install the geocells.
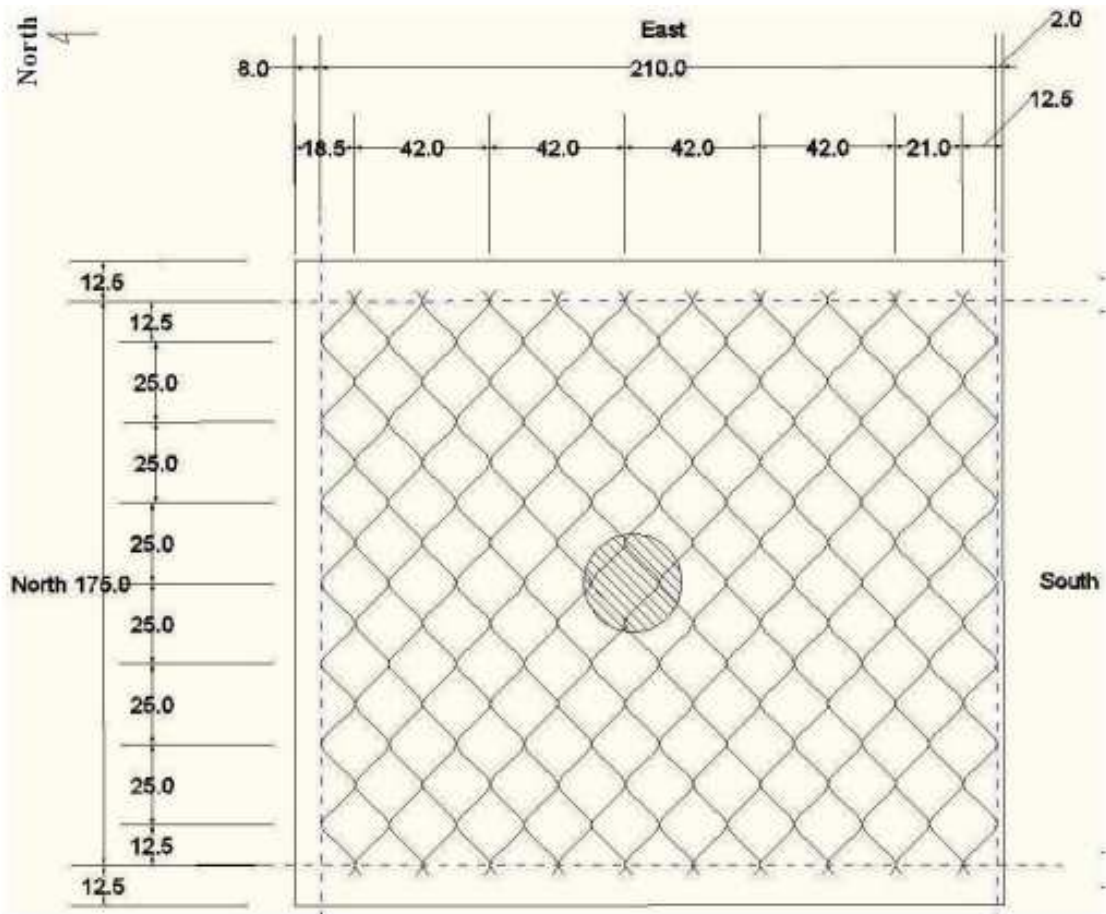
Fig. 4.3.7   Layout for the installation of geocell inside the test box (Pokharel, 2010)

Fig. 4.3.8   Installing geotextile and geocell on top of subgrade

For the 150 and 230 mm thick reinforced bases, 100 and 150 mm high geocells were installed on the top of geotextile, respectively. The geocells were filled with RAP and was compacted manually by tamping each cell individually as shown in **Fig. 4.3.9**. A RAP cover with a required thickness was added on the filled geocell and was compacted using the vibratory plate compactor to obtain the target base course thicknesses of 150 and 230 mm. Similarly, the 300 mm thick reinforced base was prepared in four lifts (i.e., 100 mm high geocell plus 30 mm thick cover plus 100 mm high geocell plus 70 mm thick cover). For the 150 and 300 mm thick unreinforced bases, RAP was placed on top of subgrade and was compacted using the vibratory plate compactor in one and three (100 mm each) lifts, respectively. For each section, the RAP material of each lift was compacted at 5.5% moisture content to obtain the target maximum dry density of 95%. The quantities (weights) of subgrade and RAP materials for each lift were calculated by multiplying the moist density of the material by the volume of the box (corresponding to each lift) to fill.

Fig. 4.3.9   Compacting RAP inside geocell pocket using hand tamping

The strengths of subgrade and base course were determined by conducting the DCP tests one day after the preparation of the base courses. The DCP test was conducted as shown in **Fig. 4.3.10** till the depth of penetration in subgrade was reached at least 300 mm.

Fig. 4.3.10   DCP test

Five strain gage type displacement transducers manufactured by Tokyo Sokki Kenkyujo, Co., Ltd., Japan were used to measure surface deformations of the RAP bases. Two transducers with 100 mm range were installed at the center on the loading plate, one with 100 mm range was installed at 250 mm away from the center, and one each of 50 mm range was installed at 500 and 750 mm away from the center of the

loading plate. The transducers installed away from the center sat on small metal plates placed on the top of the base course. All the transducers were mounted on a steel reference beam set at the top of test box as shown in **Fig. 4.3.11**. The vertical stresses at the interface of subgrade and base course, the surface deformations, and the strains in the geocell walls were measured by pressure cells, displacement transducers, and strain gages, respectively. All the displacement transducers, earth pressure cells, and strain gauges were connected to the data recorders before starting the cyclic plate load test. Four smart dynamic strain data recorders DC-204R as shown in **Fig. 4.3.11** were used to record the data measured by all sensors. One recorder was used as the master and other three served as slaves and were synchronized with the master recorder. A total of 16 connection ports (4 on each recorder) were available for recording data. Only a limited number of strain gages were connected to the recorder due to limited number of ports available during testing of the 300 mm thick reinforced section and only final measurements for remaining strain gages were recorded by connecting them to the recorder at the end of test. The accuracies of earth pressure cells, displacement transducers, and strain gages were 0.001 kPa, 0.01 mm, and 10^{-6}, respectively.

Displacement transducer
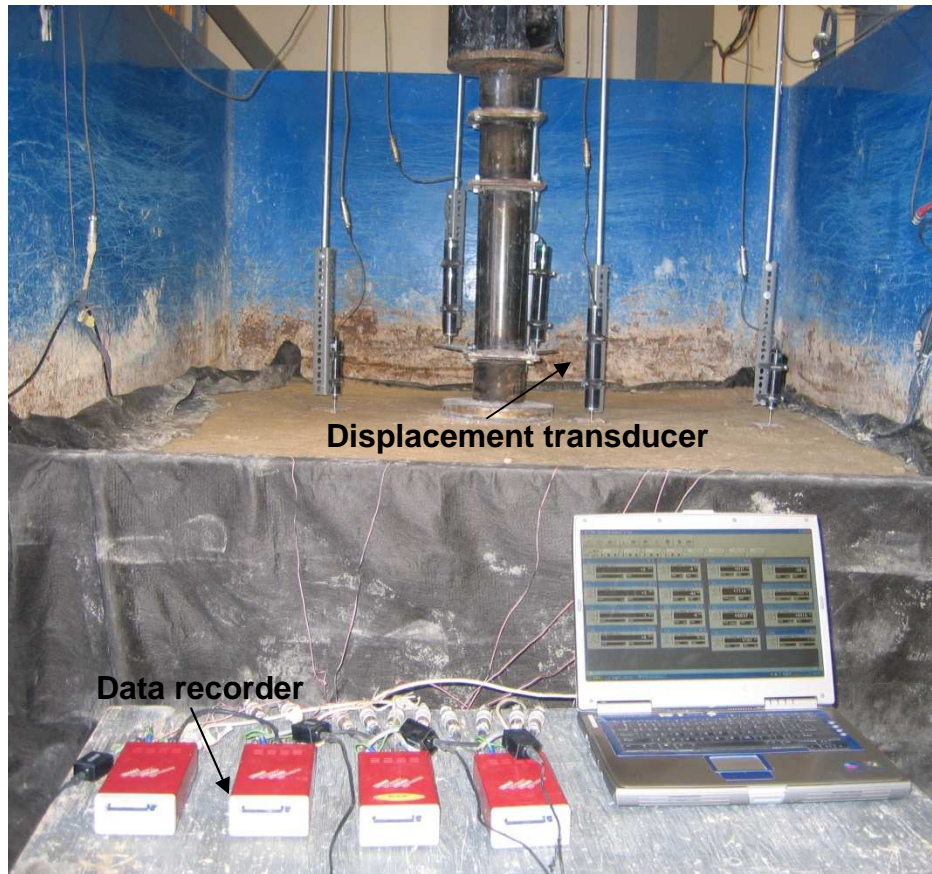
Data recorder

Fig. 4.3.11   Installing displacement transducers and connecting sensors to data

recorders and data recorders to the laptop before running a test

Each cyclic test was planned to stop when the maximum displacement reached 85 mm. However, some tests were terminated before reaching the target maximum displacement when the problem appeared in the test equipment. The displacement of each test section was measured by a ruler after the completion of the cyclic plate loading test shown in **Fig. 4.3.12**.

Figure 4.3.12   Displacement measurement after the cyclic plate loading test

Sand cone tests were conducted after the plate loading tests to verify the density of base courses as shown in **Fig. 4.3.13**. In addition, RAP bases were exhumed and profile measurements were taken in order to obtain the deformed shapes of the test sections after cyclic plate loading tests. The manually measured displacement profiles were presented in Thakur (2011) and are not presented in this dissertation.

Fig. 4.3.13   Sand cone test

4.4   Test results and discussions

The test sections are represented by the short names as shown in Table 4.4.1 to make discussion and presentation of test results easier.

Table 4.4.1   Representations of the unpaved road test sections

Test sections	Representation
150 mm thick reinforced base over weak subgrade	150 mm R_W
230 mm thick reinforced base over weak subgrade	230 mm R_W
300 mm thick reinforced base over weak subgrade	300 mm R_W
300 mm thick unreinforced base over weak subgrade	300 mm UR_W
150 mm thick reinforced base over moderate subgrade	150 mm R_M
230 mm thick reinforced base over moderate subgrade	230 mm R_M
300 mm thick reinforced base over moderate subgrade	300 mm R_M
150 mm thick unreinforced base over moderate subgrade	150 mm UR_M
300 mm thick unreinforced base over moderate subgrade	300 mm UR_M

4.4.1 Quality control test results

The required strengths of the subgrade layer were checked by conducting five vane shear tests at five different locations at depths of 100, 175, and 250 mm just after the preparation of subgrade and four DCP tests at four different locations one day after the preparation of a base course. After each cyclic plate loading test, two sand cone tests were conducted to evaluate the density of the compacted RAP base. The CBR values of subgrade and base layers were calculated from vane shear and DCP test data using the correlations provided in **Eqs. 4.4.1** and **4.4.2**, respectively.

$$CBR = \frac{C_u}{20.5} \qquad\qquad (\textbf{4.4.1}) \qquad [\text{Pokharel, 2010}]$$

where C_u = undrained shear strength of subgrade in kPa obtained from vane shear test.

$$CBR = \frac{292}{PI^{1.12}} \qquad\qquad (\textbf{4.4.2}) \qquad [\text{Webster et al., 1992}]$$

where PI = penetration index (mm/blow) obtained from DCP test.

The CBR profiles obtained from DCP tests for all test sections are shown in **Fig. 4.4.1**. The average, standard deviation (σ), and coefficient of variance (COV) for the CBRs of base and subgrade, and the relative compaction of base course were determined from the vane shear, DCP, and sand cone tests and are presented in **Table 4.4.2**. The average CBR values of the subgrades obtained from the DCP tests were slightly higher than those from vane shear tests. This difference may be because the DCP tests were conducted one day after the preparation of test sections. Average CBR values of each base course ranged from 10.2 to 11.4% except 230 mm thick reinforced

90

base over weak subgrade. The 230 mm thick reinforced base over weak subgrade had

lower CBR because of inadequate compaction. The less compacted 230 mm thick

reinforced base course over weak subgrade had poor performance which will be

discussed later. The standard deviations for the CBR and the relative compaction

ranged from 0.23 to 1.4% and 0.2 to 2.9%, respectively.
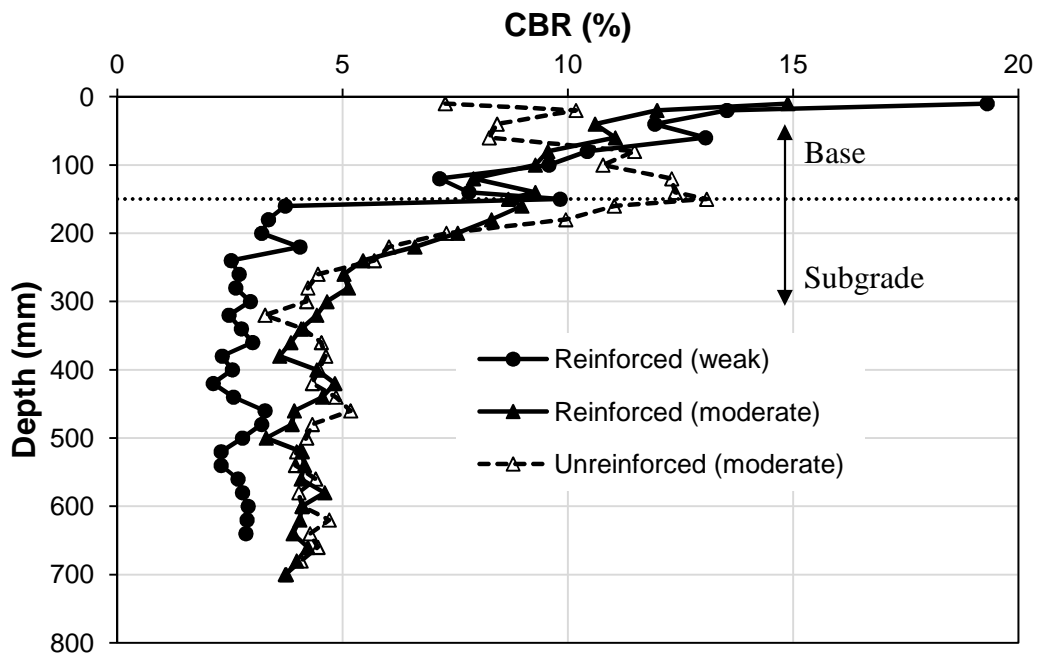
(a) 150 mm thick base

Fig. 4.4.1   CBR profiles obtained from DCP tests
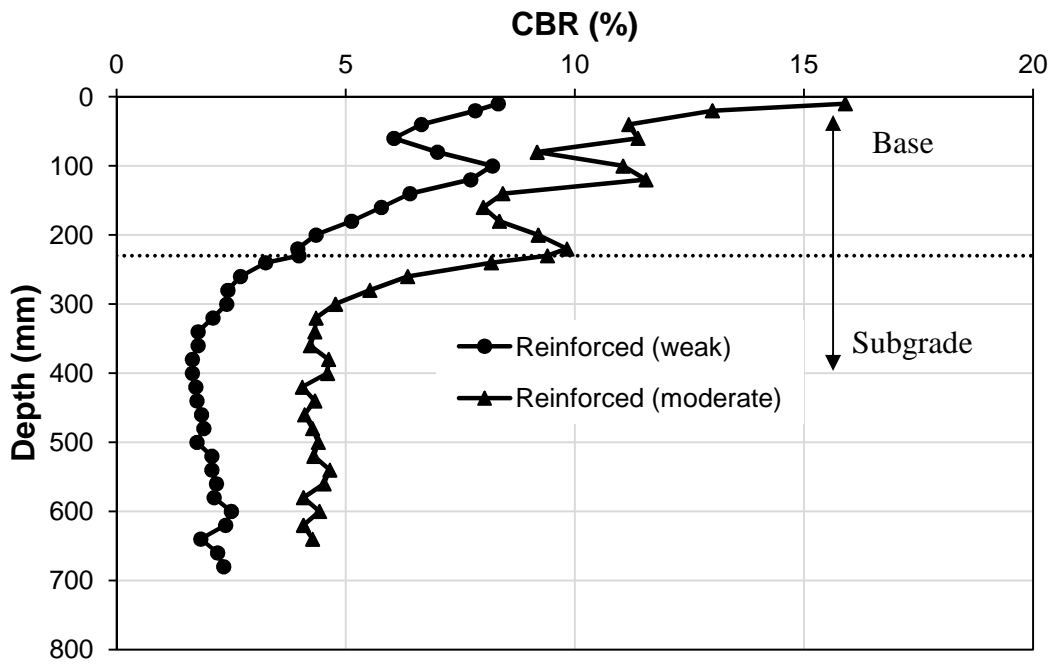
(b) 230 mm thick base
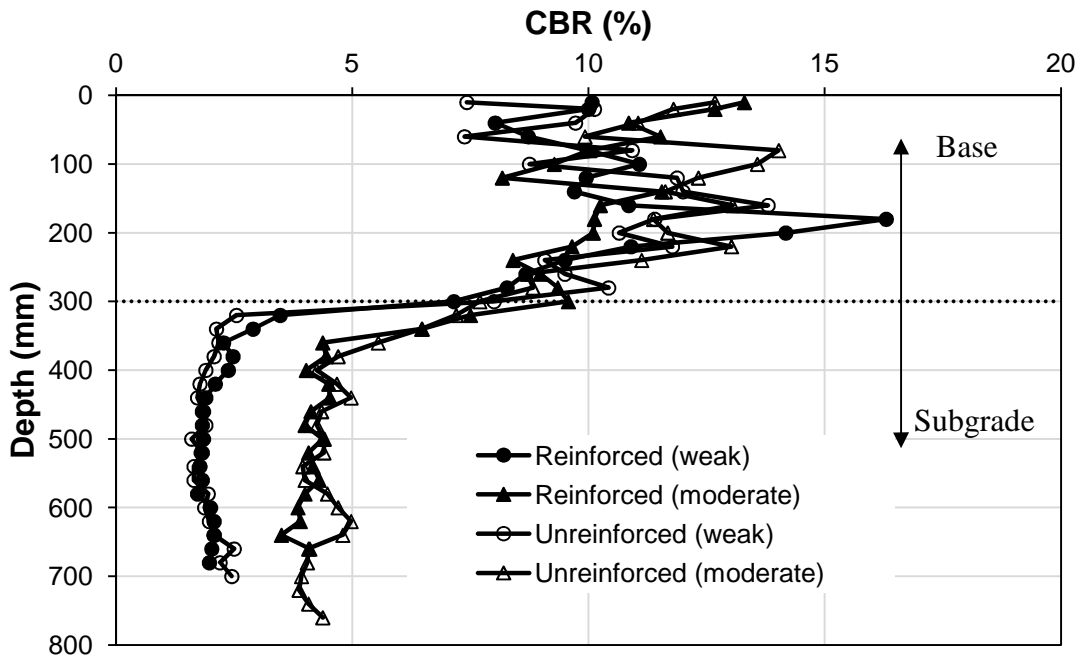
(c) 300 mm thick base

Fig. 4.4.1   CBR profiles obtained from DCP tests (continued)

Table 4.4.2 CBR and relative compaction of test sections

Test sections	Subgrade CBR (%) (Vane shear/DCP)			Base CBR (%)			Relative compaction (%)		
	Average	σ	COV	Average	σ	COV	Average	σ	COV
150 mm R_W	2.1 / 2.8	0.40/0.44	19.0/15.7	11.4	2.60	22.8	93	2.9	3.1
230 mm R_W	1.9 / 2.1	0.24/0.39	12.6/18.6	6.3	1.56	24.8	84	2.1	2.5
300 mm R_W	2.0 / 2.1	0.25/0.44	12.5/21.0	10.2	2.28	22.4	91	1.6	1.8
300 mm UR_W	1.9 / 2.0	0.23/0.28	12.1/14.0	10.2	1.79	17.5	91	1.4	1.5
150 mm R_M	4.8 / 4.8	0.52/1.4	10.8/29.2	10.4	2.10	20.2	87	0.7	0.8
230 mm R_M	4.6 / 4.7	0.64/0.95	13.9/20.2	10.5	2.20	21.0	91	2.3	2.5
300 mm R_M	4.5 / 4.6	0.46/0.97	10.2/21.1	10.2	1.43	14.0	89	0.2	0.2
150 mm UR_M	4.8 / 5.0	0.48/1.1	10.0/22.0	10.5	2.07	19.7	96	2.0	2.08
300 mm UR_M	4.5 / 4.6	0.37/0.80	8.2/17.4	11.4	1.82	16.0	88	1.8	2.05

4.4.2 Recorded surface deformation

Fig. 4.4.2 presents the recorded displacements of the loading plate (averaged from two displacement transducers installed on the loading plate) developing with the number of loading cycles during all the tests, which included the accumulated permanent (plastic) deformation and the resilient deformation (elastic rebound).   The total surface deformations at each loading cycle were measured by the displacement transducers installed on top of the prepared sections. The permanent deformations and resilient deformations were separated from the total deformation and are discussed later in this chapter.
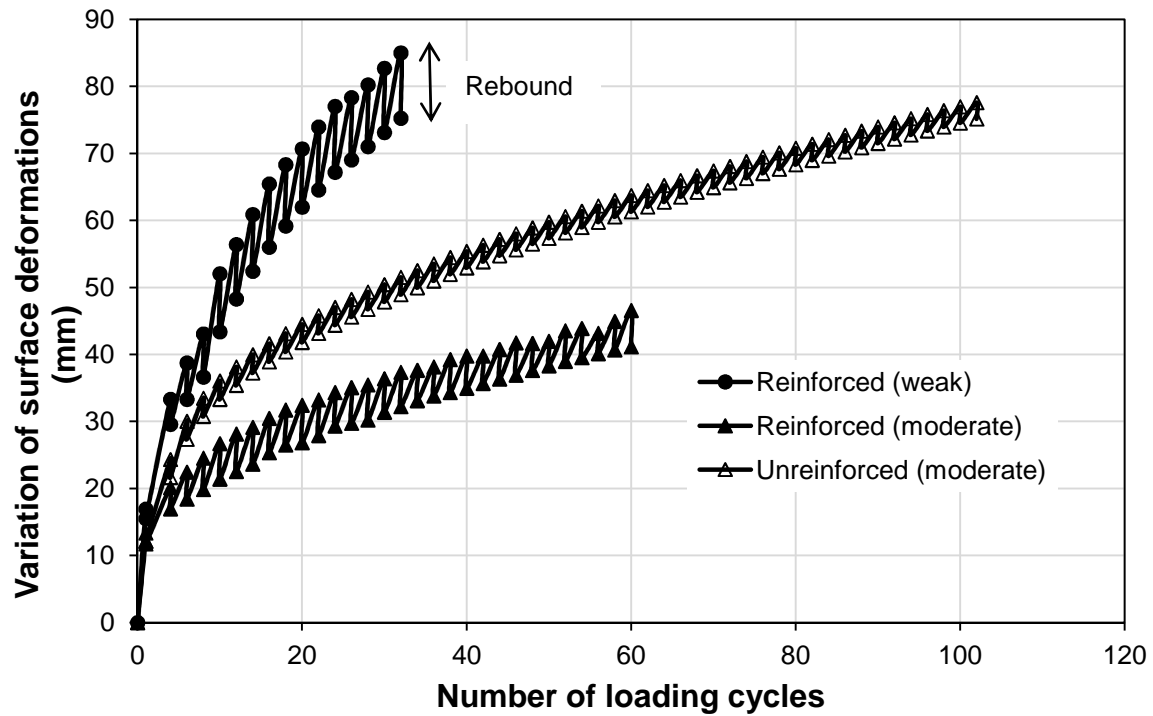
(a) 150 mm thick base
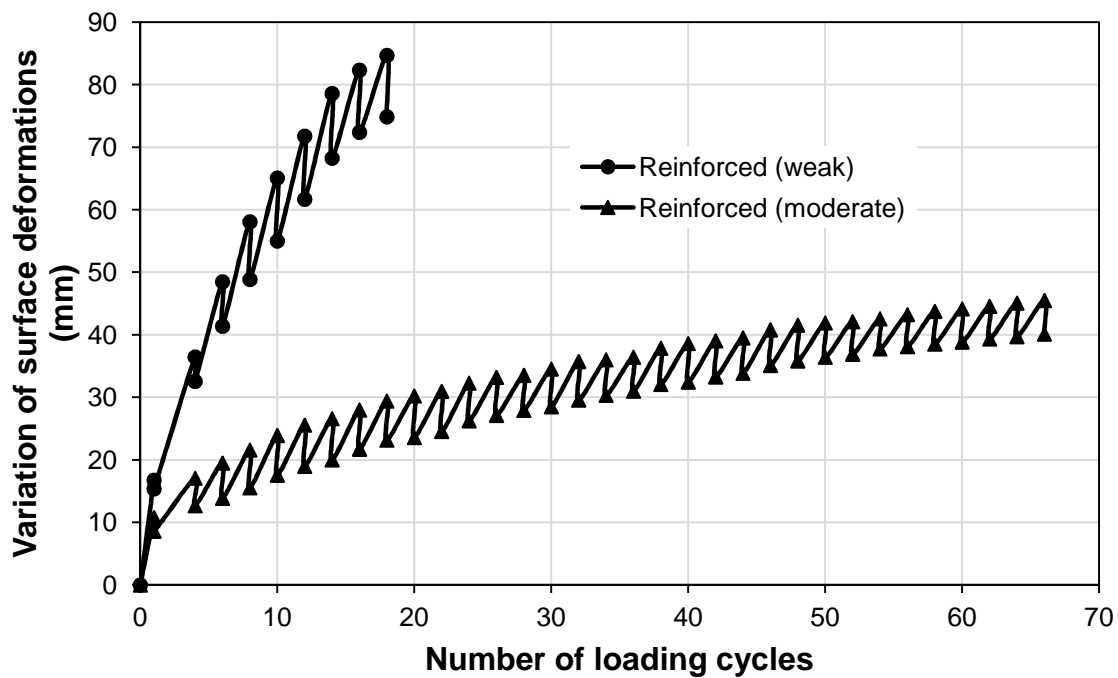
(b) 230 mm thick base

Fig. 4.4.2   Variation of surface deformations versus the number of loading cycles
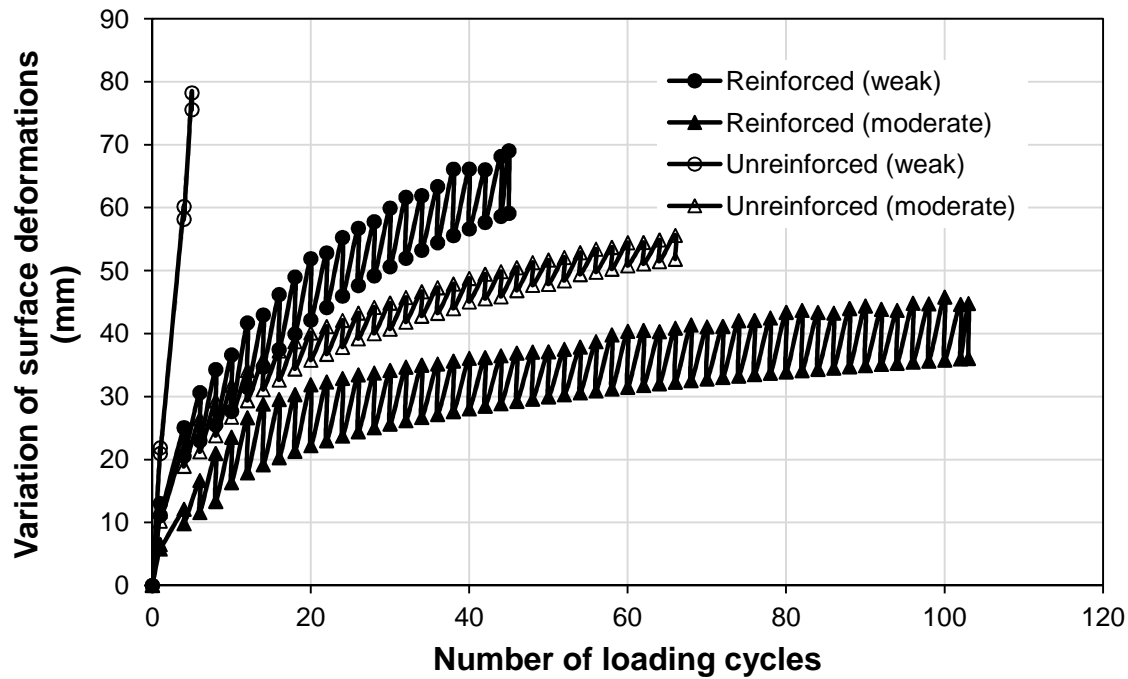
(c) 300 mm thick base

Fig. 4.4.2   Variation of surface deformations versus the number of loading cycles

(continued)

4.4.3 Surface permanent deformation

Thompson and Smith (1990) reported permanent deformation or rutting as the most common criteria to determine the performance of roads. The total surface deformations at each loading cycle were measured by the displacement transducers installed on top of the prepared sections. The total deformation consisted of permanent and resilient deformations. The permanent and resilient deformations for each loading cycle were separated from the total deformation and are presented separately in this chapter. The surface permanent deformations at the center of the loading plate were calculated by averaging the permanent deformations recorded by two displacement transducers

95

installed on top of the loading plate, while the surface permanent deformations at the locations away from the center of the loading plate were kept same as those recorded by the displacement transducers installed at each particular location. The surface permanent deformations at the center of the loading plate versus the number of loading cycles for 150, 230, and 300 mm thick bases over weak and moderate subgrades are shown in **Figs. 4.4.3a**, **b**, and **c**, respectively. The permanent deformations increased with the number of loading cycles. The rate of increase in permanent deformations decreased with the increasing number of loading cycles. All geocell-reinforced sections had lower permanent deformations and rate of increase in permanent deformations than the corresponding thick unreinforced sections under a similar condition of construction. The thicker base sections had lower permanent deformations than the thinner bases under a similar condition of construction. The 230 mm R_W section had higher permanent deformations than the 150 mm R_W section. This result was due to a lower CBR of the base resulting from less compaction of the base in the 230 mm R_W section. The sections constructed over moderate subgrade had lower permanent deformations than those over soft subgrade. The unreinforced bases over moderate subgrade had lower permanent deformations than the corresponding thick reinforced bases over weak subgrade. This result indicates that geocell confinement and subgrade strength play a vital role in improving the performance of test sections. The subgrade strength had more significant effect than geocell confinement in reducing surface permanent deformations.
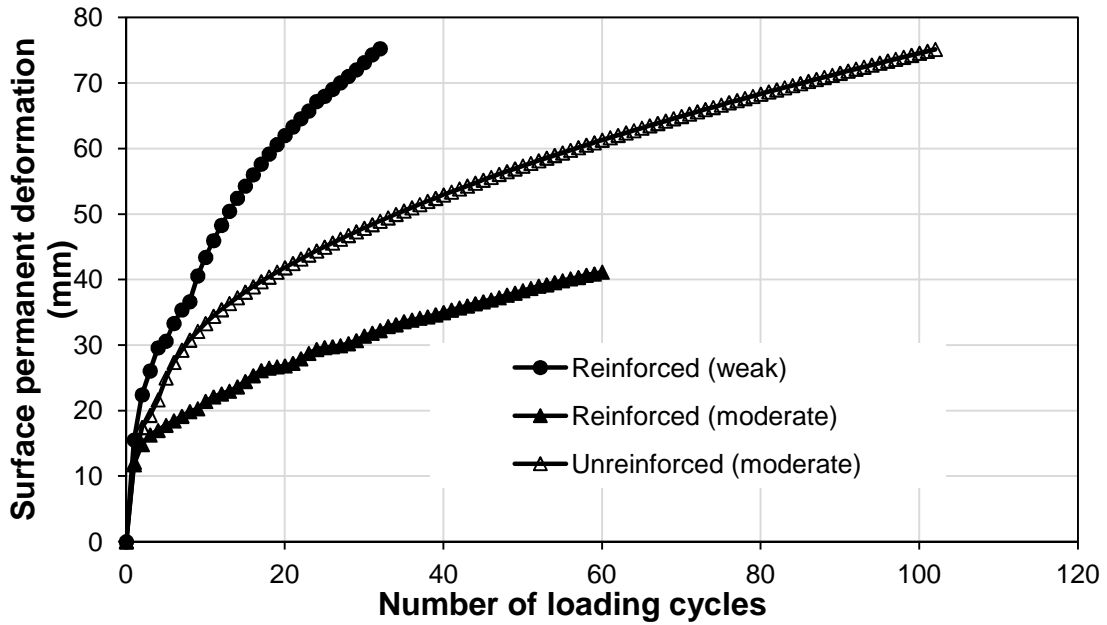
(a) 150 mm thick base
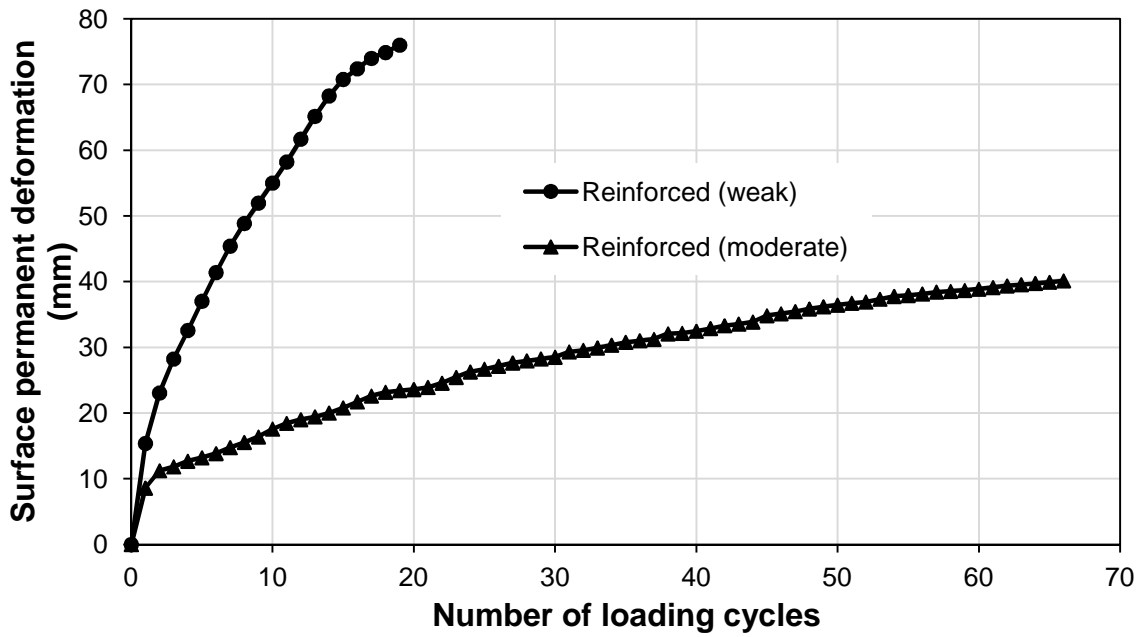
(b) 230 mm thick base

Fig. 4.4.3 Surface permanent deformation at the center of the loading plate versus the number of loading cycles
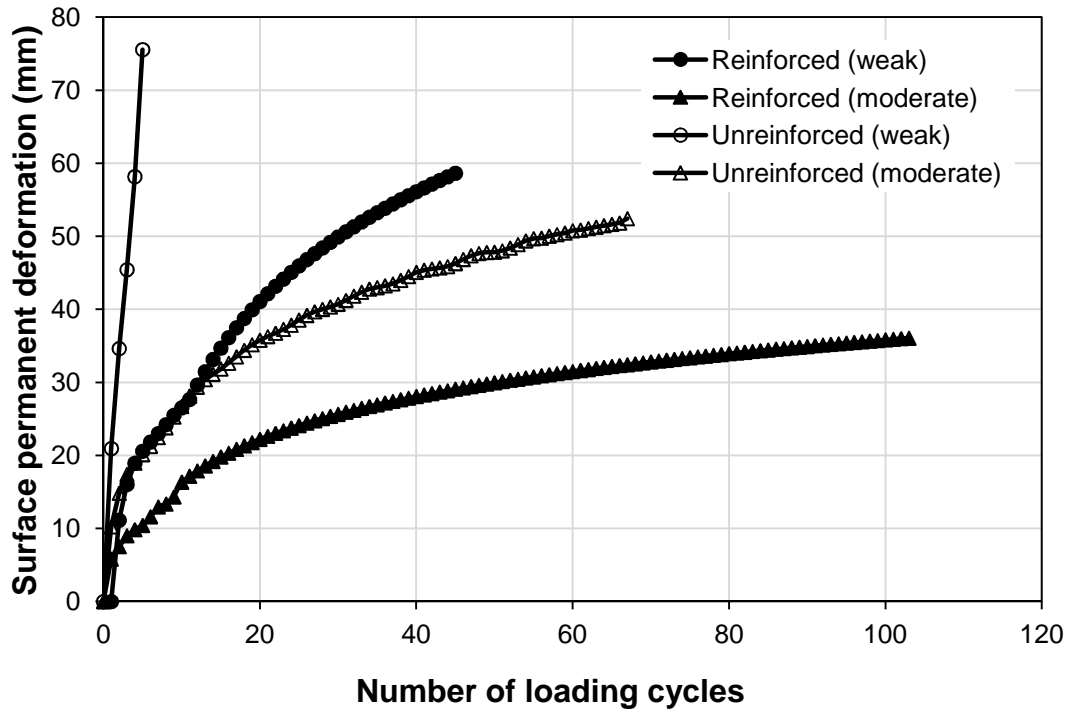
(c) 300 mm thick base

Fig. 4.4.3 Surface permanent deformation at the center of the loading plate versus the number of loading cycles (continued)

4.4.4 Traffic improvement factor (TIF)

The numbers of loading cycles at different permanent deformations were used to calculate Traffic Improvement Factor (TIF). The TIF is the ratio of the number of loading cycles for the strong section to that for the weak section at the same permanent deformation. The TIF versus surface permanent deformation curves were plotted to demonstrate the influence of four factors (i.e. base thickness, geocell reinforcement, and base and subgrade strengths) in improving the performance of unpaved roads with RAP bases. To demonstrate the effect of one factor on the TIF, the other three factors were considered the same.

The effect of base thickness is quantified by the traffic improvement factor, TIF_{BT}, which is defined as the ratio of the number of loading cycles for the thick base section to that of a similar thin base section at the same permanent deformation. The TIF_{BT} versus surface permanent deformation curves for the 300 mm thick reinforced base sections are presented in **Fig 4.4.4**. The TIF_{BT} for 300 mm thick base sections were calculated with respect to 150 mm thick corresponding base sections to demonstrate the benefits of additional 150 mm thick RAP material. The TIF_{BT} for 300 mm R_W, 300 mm R_M, and 300 mm UR_M sections were calculated with respect to 150 mm R_W, 150 mm R_M, and 150 mm UR_M sections. The test results show that an addition of 150 mm RAP material improved the performance of the test sections by a factor of 1.1 to 2.7. All test sections had the largest TIF_{BT} values at highest permanent deformations.
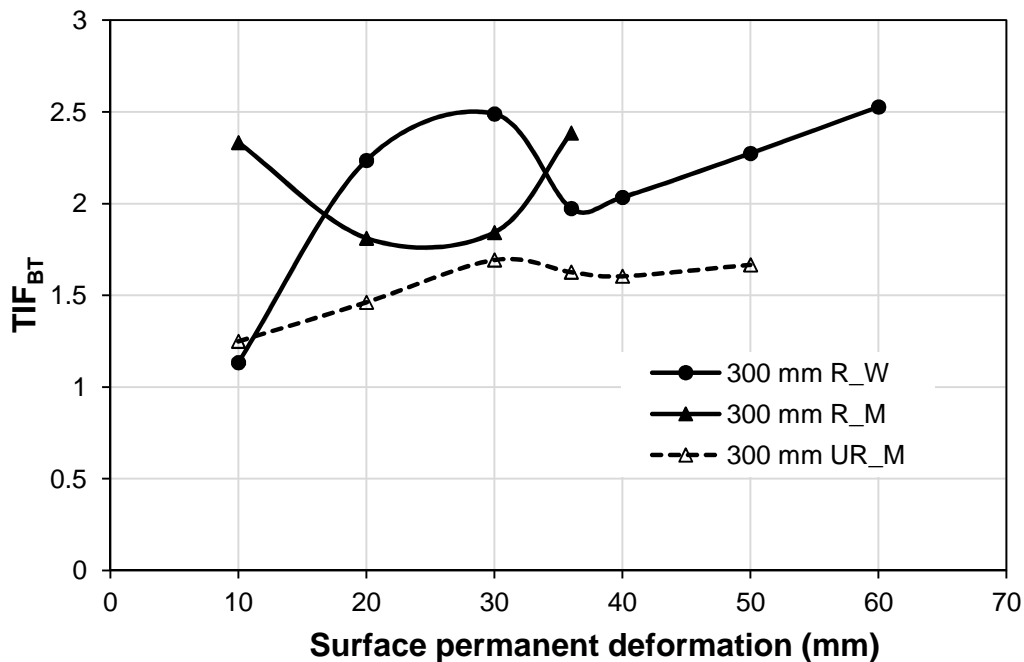
Fig. 4.4.4 Effect of base course thickness on Traffic improvement factor (TIF_{BT})

Effect of geocell reinforcement

The effect of geocell reinforcement is quantified by the traffic improvement factor, TIF_{GR}, which is defined as the ratio of the number of loading cycles for the geocell-reinforced section to that of the unreinforced section at the same permanent deformation. The TIF_{GR} versus surface permanent deformation curves for the 150 and 300 mm thick reinforced base sections are presented in **Fig. 4.4.5**. The 150 and 300 mm thick reinforced base sections consisted of two layers and single layer of 100 mm high geocells, respectively. The TIF_{GR} for reinforced base sections were calculated with respect to the corresponding unreinforced base sections to demonstrate the benefits geocell reinforcement. The TIF_{GR} for 300 mm R_W, 300 mm R_M, and 150 mm R_M sections were calculated with respect to 300 mm UR_W, 300 mm UR_M, and 150 mm UR_M sections, respectively. The test results show that the geocell-reinforced bases improved the performance of test sections by a factor of 1.1 to 11.4 as compared with the corresponding unreinforced base sections. The reinforced sections with two layers of geocell had higher TIF_{GR} than that with single layer of geocell. The TIF_{GR} increased with increasing permanent deformation. This result was because the geocell was mobilized at larger permanent deformations and improved the performance by the mechanism of the induced beam effect and tensioned membrane effect of geocell-reinforced bases as reported by Thakur et al. (2012).
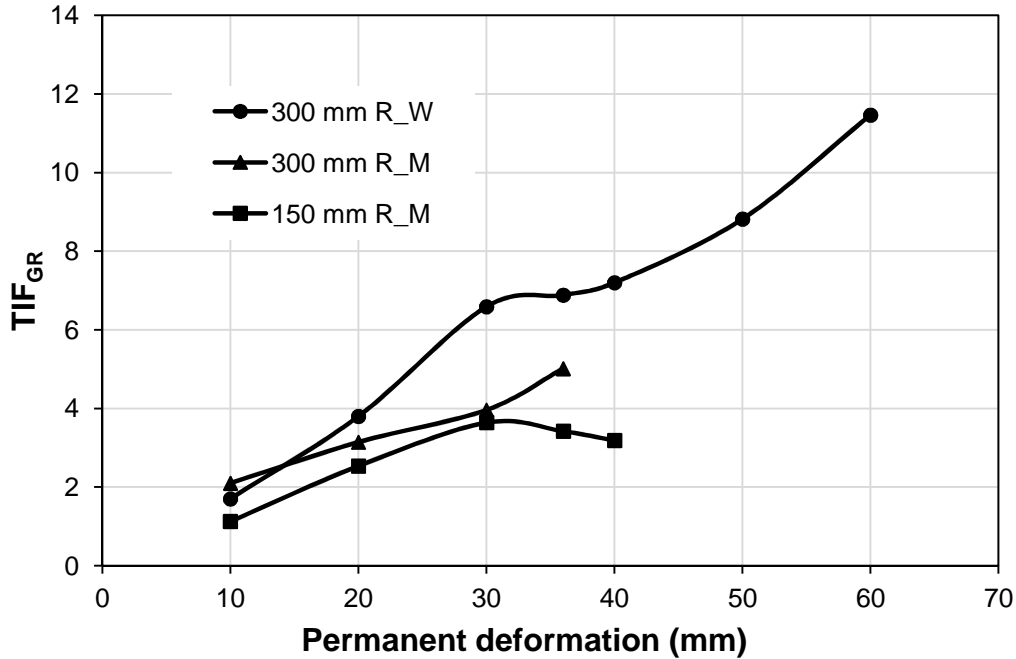
Fig. 4.4.5 Effect of geocell-reinforcement on Traffic Improvement Factor (TIF$_{GR}$)

Effect of base course strength

The effect of base course strength is quantified by the traffic improvement factor, TIF$_{BC}$, which is defined as the ratio of the number of loading cycles for the strong base section to that of the weak base section at the same permanent deformation. The TIF$_{BC}$ versus surface permanent deformation curve for the 230 mm R_W section is presented in **Fig. 4.4.6**. The TIF$_{BC}$ for the 230 mm R_W section was calculated with respect to the 150 mm R_W section to demonstrate the effect of base course strength on the performance of the test section. The CBR values of base courses for 150 mm R_W and 230 mm R_W sections were 6.3 and 11.4%, respectively. The TIF$_{BC}$ of 230 mm R_W ranged from 0.5 to 1.0 with respect to 150 mm R_W. This comparison indicated that the 230 mm R_W performed poorer than the 150 mm R_W. It could be concluded that the strength of the base course played more crucial role than the thickness of the base

course in the performance of unpaved roads.
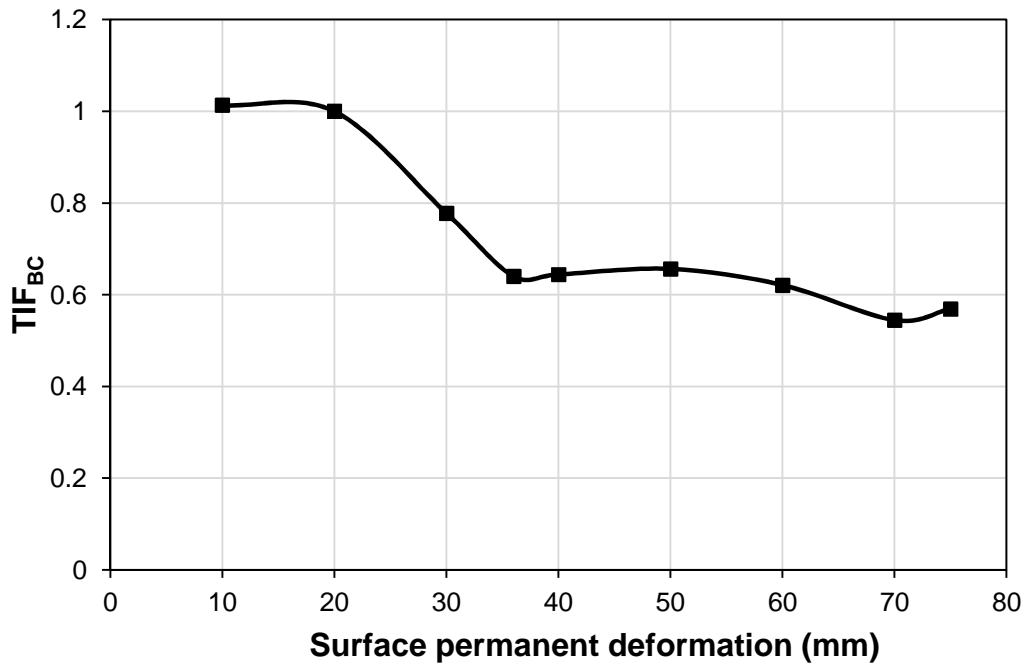
Fig. 4.4.6 Effect of base course strength on Traffic Improvement Factor (TIF$_{BC}$)

Effect of subgrade strength

The effect of subgrade strength is quantified by the traffic improvement factor, TIF$_{SG}$, which is defined as the ratio of the number of loading cycles for the section with strong subgrade to that for the section with weak subgrade at the same permanent deformation. The TIF$_{SG}$ versus surface permanent deformation curves for the base sections over moderate subgrade are presented in **Fig. 4.4.7**. The TIF$_{SG}$ values of 150 mm R_M, 230 mm R_M, 300 mm R_M, and 300 mm UR_M sections were calculated with respect to 150 mm R_W, 230 mm R_W, 300 mm R_W, and 300 mm UR_W sections, respectively to demonstrate the effect of subgrade strength on the performance of RAP bases. The TIF$_{SG}$ increased with the permanent deformation. The

test results show that RAP bases over moderate subgrade had 1.2 to 17.2 times better performance than the corresponding bases over weak subgrade.
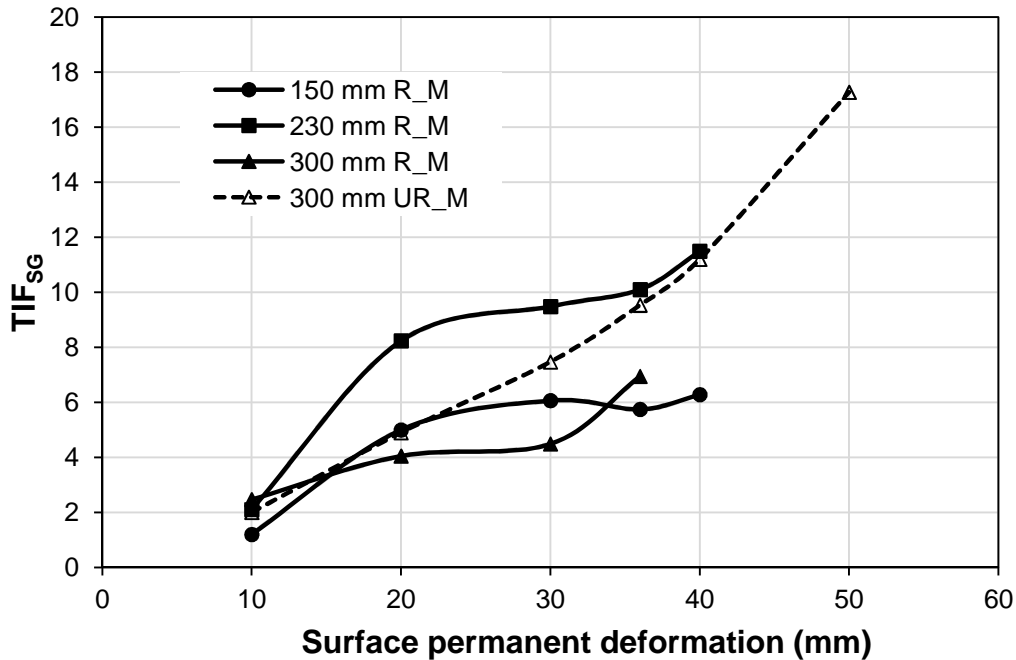
Fig. 4.4.7 Effect of subgrade strength on Traffic Improvement Factor (TIF$_{SG}$)

Overall performance

The overall performance is quantified by the traffic improvement factor, TIF$_{OP}$, which is defined as the ratio of the number of loading cycles for other section with respect to the weakest section at the same permanent deformation. The 300 mm UR_W section had the highest permanent deformation at particular loading cycles and is considered the weakest section among all nine sections. The TIF value of each test section was calculated with respect to the 300 mm UR_W section to determine the overall relative performance. The TIF$_{OP}$ versus permanent deformation curve is shown in **Fig. 4.4.8** to demonstrate the relative performance of each test section with respect to the weakest

103

test section (i.e., 300 mm UR_W). The test result show that the 300 mm R_W section performed best, followed by 230 mm R_M , 150 mm R_M, 300 mm UR_M, 150 mm UR_M, 300 mm R_W, 150 mm R_W, 230 mm R_W, and 300 mm UR_W sections. The degree of improvement as shown in **Fig. 4.4.8** was due to the combined effects of base course thickness, geocell reinforcement, and base and sugrade strengths. The overall improvement factors ranged from 1.1 to 47.8.
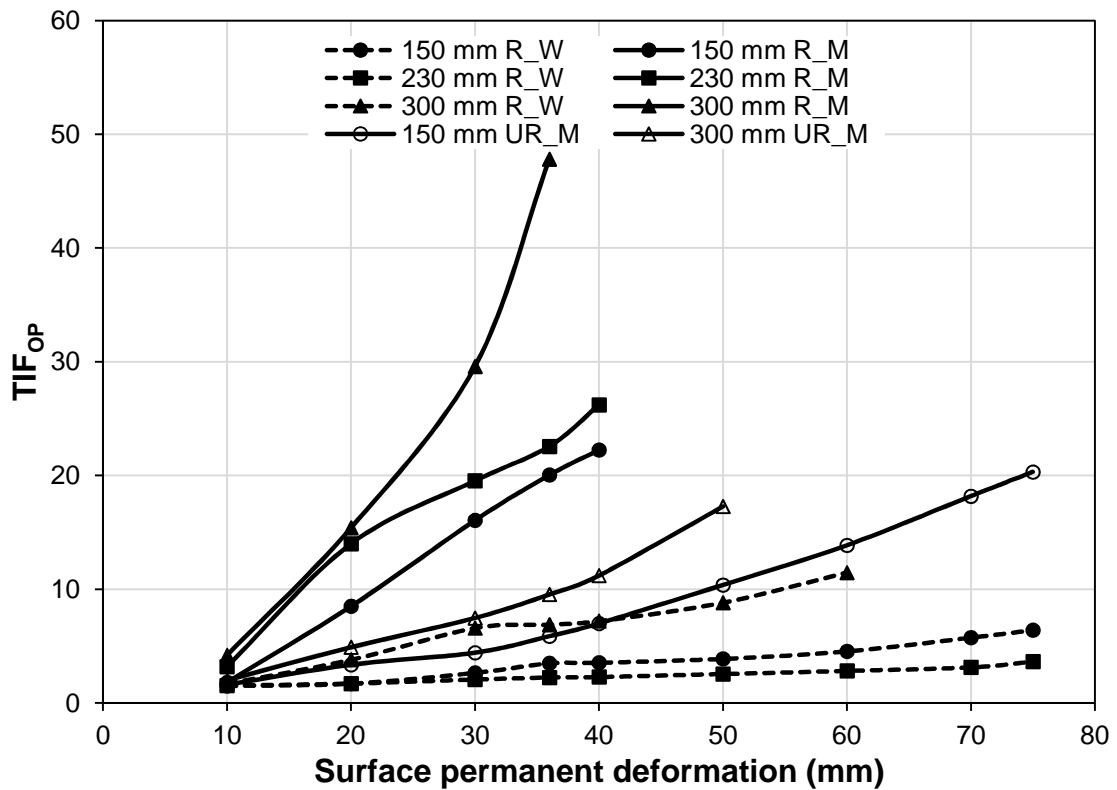
Fig. 4.4.8   Traffic Improvement Factor (TIF$_{OP}$) with respect to the 300 mm UR_W

section

4.4.5 Surface permanent deformation profile

The surface permanent deformation profiles at the 5th loading cycle as shown in **Fig. 4.4.9** were drawn using the deformation data recorded by five displacement transducers installed at the center of the loading plate, 250, 500, and 750 mm away from the center of the loading plate. The surface deformation profiles were assumed symmetric along the vertical axis. The 5th loading cycle was chosen for demonstration purposes because the weakest test section (i.e. 300 mm UR_W) failed after five loading cycles. Only a small amount of compression was observed at 250 mm away from the center for all test sections except the 230 mm R_W and 150 mm thick UR_M sections. These two sections showed a small amount of heave at 250 mm away from the center. All test sections constructed over weak subgrade showed more compression at the center of the loading plate and more heave at 500 and 750 mm away from the center of the loading plate than the corresponding sections over moderate subgrade. The unreinforced section showed more compression at the center and more heave at 500 and 750 mm away from the center than the corresponding reinforced sections. All test sections showed more heave at 500 mm away from the center of the loading plate than at 750 mm away from the center of the loading plate. The thick sections had less heave and compression than the corresponding thin sections. The 300 mm thick unreinforced base over weak subgrade showed the largest amount of compression (i.e., 75.5 mm) and heave (i.e., 7.0 mm). The increase in the subgrade strength, the geocell reinforcement, and the base course thickness reduced the amount of surface heave and compression.

(a) 150 mm thick base
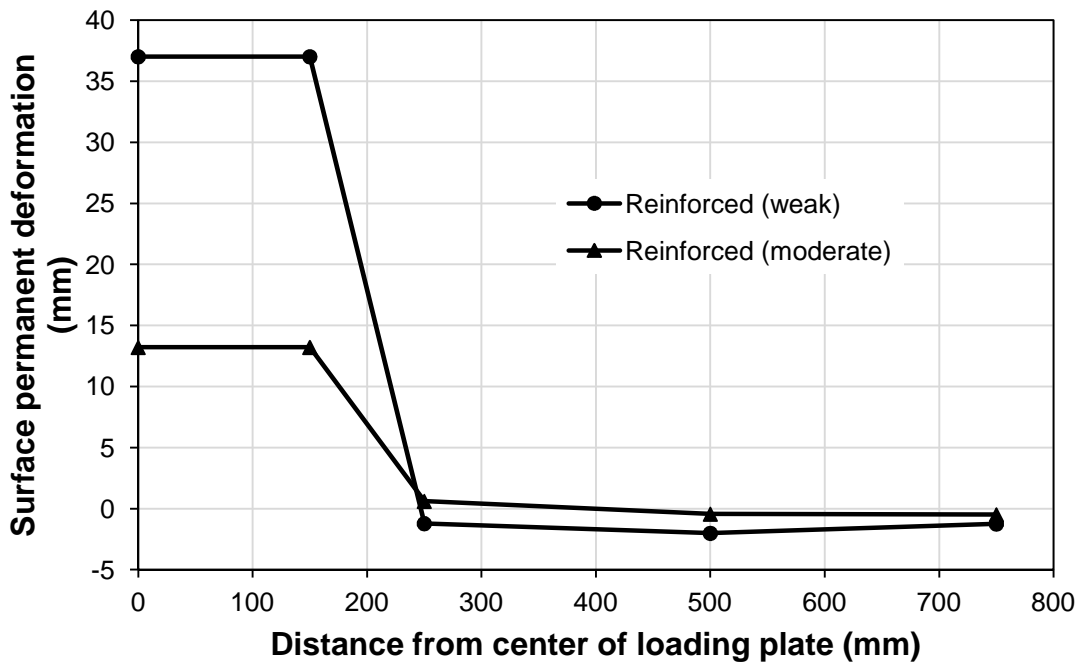
(b) 230 mm thick base

Fig. 4.4.9   Surface permanent deformation profiles at the 5th loading cycle

106
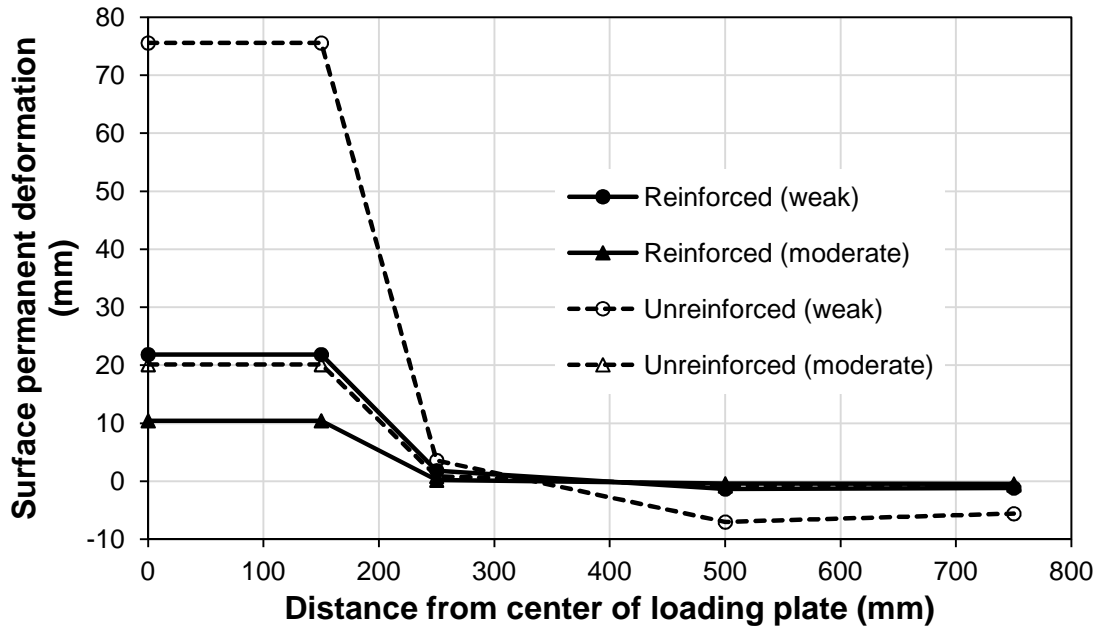
(c) 300 mm thick base

Fig. 4.4.9 Surface permanent deformation profiles at the 5th loading cycle

(continued)

4.4.6 Resilient deformation

The resilient deformation is defined as the rebound deformation of a test section under

cyclic loading and can be obtained when unloaded from the maximum load (40 kN) to

the minimum load (0.5 kN).   The resilient deformation at each loading cycle was

calculated by deducting the permanent deformation from the total deformation at that

cycle.   The amount of resilient deformation at each cycle was then divided by the total

deformation at that cycle to obtain the percentage of resilient deformation.   The resilient

deformation and percentage of resilient deformation at the center of the loading plate

versus the number of loading cycles are shown in **Figs. 4.4.10** and **4.4.11**, respectively.

The amount of resilient deformation and percentage of resilient deformation increased sharply for the first few loading cycles and stabilized to a nearly constant value for each test section except the 300 mm UR_W section. All reinforced sections had more resilient deformation and percentage of resilient deformation than the corresponding unreinforced sections. The reinforced sections constructed over weak subgrade had more resilient deformation and less percentage of resilient deformation as compared with those over moderate subgrade. All reinforced sections constructed over weak subgrade and the 300 mm R_M section had about same maximum resilient deformation (i.e., 10 mm). The 150 mm UR_M and the 300 mm UR_W sections had about the same maximum resilient deformation (i.e., 2.7 mm) and the 150 mm R_M, 230 mm R_M, and 300 mm R_M had about the same maximum resilient deformation (i.e., 6 mm). All test sections except the 300 mm UR_W section shook down to a steady state, showing largely resilient behavior. The 300 mm UR_W section did not shake down to a steady state and underwent continuous permanent deformation without showing much resilience. Overall, the resilient deformations and percentages of resilient deformations among some unreinforced and reinforced sections were close. The exact reasons for their similar resilient deformations and percentages of resilient deformation are unknown. The resilient and total deformations on the surface under each loading cycle depended on the deformations of the RAP base and the subgrade, and that induced by the slab or tensioned membrane effect of the geocell-reinforced base. Numerical analysis is needed to separate the contribution by each component, which will be recommended for a future study. The slab effect (also referred as a beam effect) is used to describe a structural element with bending resistance while the tensioned

membrane effect is used to describe a structural element with tensile resistance but no bending resistance. These results demonstrate that the geocell improved the resilient behavior and reduced the plasticity of the test section after an initial period of plastic strain accumulation which might be associated with locking up of the geocell framework. In general, these results demonstrate that the geocell improved the resilient behavior of RAP bases and the degree of improvement was higher for the sections over weak subgrade than those over moderate subgrade.
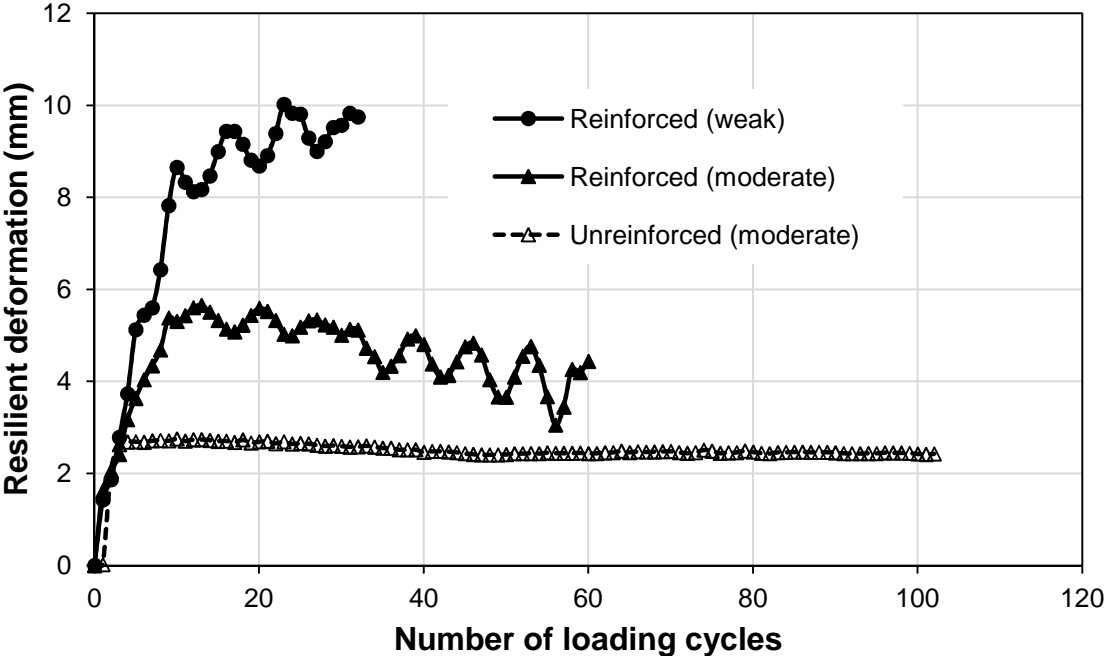
(a) 150 mm thick base

Fig. 4.4.10   Resilient deformation at the center of the loading plate versus the number of loading cycles
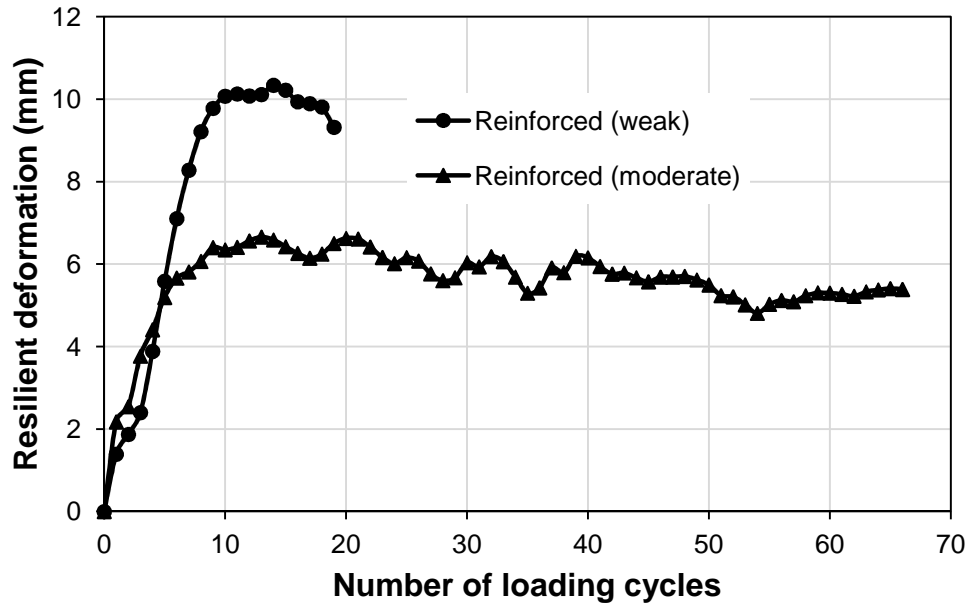
(b) 230 mm thick base
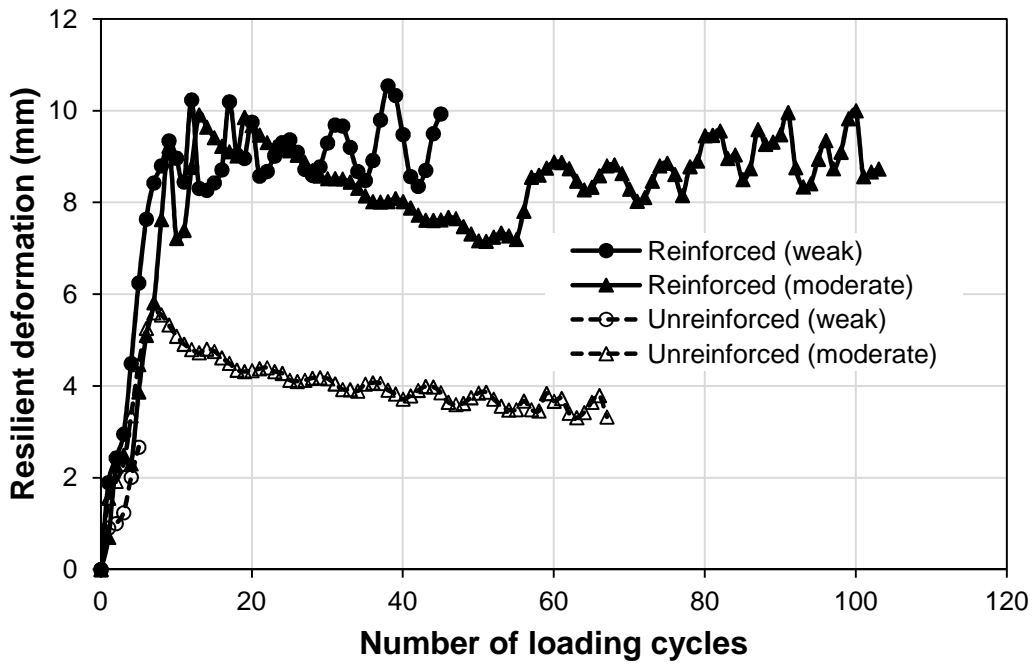
(c) 300 mm thick base

Fig. 4.4.10   Resilient deformation at the center of the loading plate versus the number
of loading cycles (continued)

(a) 150 mm thick base
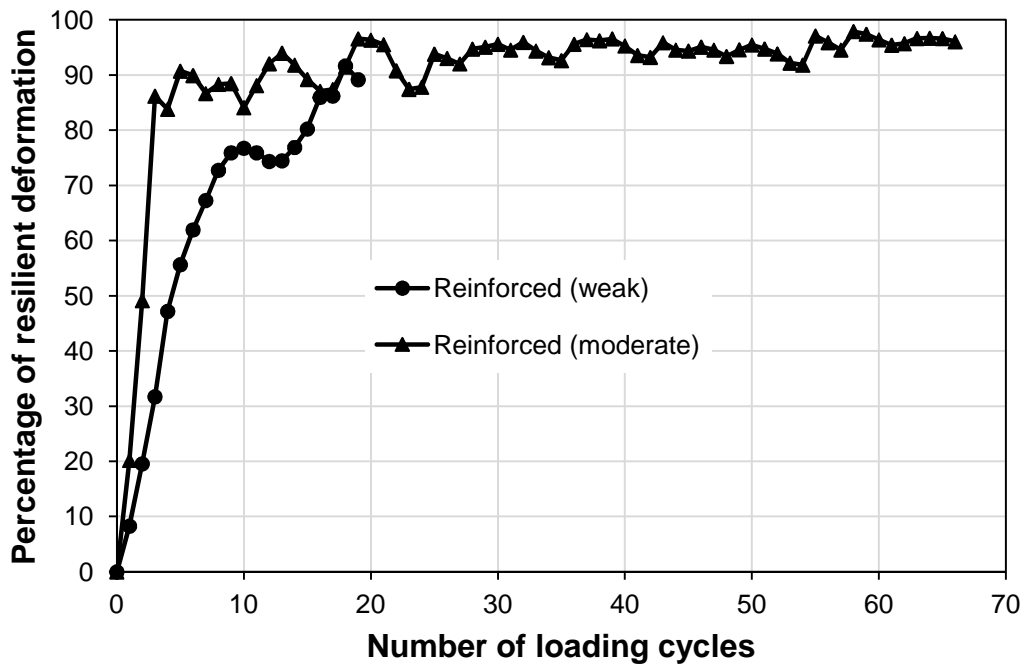
(b) 230 mm thick base

Fig. 4.4.11   Percentage of resilient deformation at the center of the loading

plate versus the number of loading cycles

111
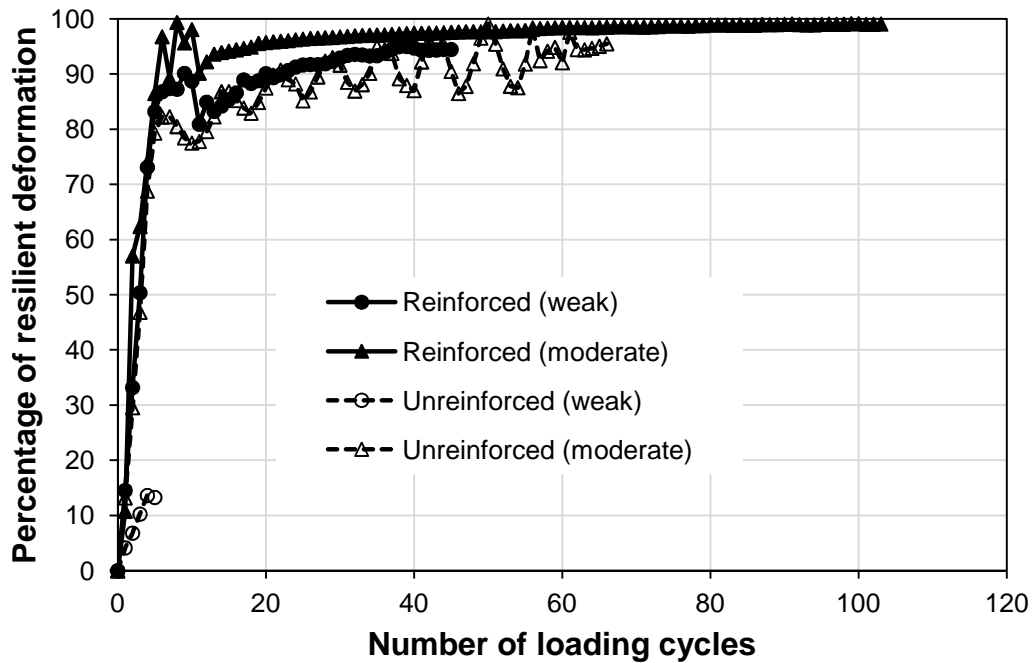
(c) 300 mm thick base

Fig. 4.4.11   Percentage of resilient deformation at the center of the loading plate

versus the number of loading cycles (continued)

4.4.7 Maximum vertical stress at the interface of subgrade and base

The vertical stresses at the interface of subgrade and base course were measured by the earth pressure cells located at 0, 125, 250, 500, and 750 mm from the center of the loading plate. **Fig. 4.4.12** shows the measured vertical stresses at the interface of subgrade and base course versus the number of loading cycles at the center. It is shown that the vertical stresses increased rapidly during the initial cycles and later they decreased slowly by a small magnitude or stabilized to a constant value

for the reinforced cases. For the unreinforced case, the vertical stresses kept increasing until failure. The maximum vertical stresses measured at the center and 125 mm away from the center for all test sections are shown in **Table 4.4.3**. At these two locations, the maximum vertical stresses occurred. The reduction of the vertical stresses in the reinforced sections resulted from the slab or tensioned membrane effect. The slab effect was observed for the thicker section whereas the tensioned membrane effect was observed for the thinner sections in the measurement of the strains on the geocell walls, which are presented and discussed later. The maximum vertical stress at the center was highest in the 150 mm UR_M section and lowest in the 300 mm R_W section where as vertical stress at 125 mm away from the center was highest in the 150 mm UR_M and lowest in the 300 mm R_M. In addition, the maximum vertical stresses were higher in the 150 mm R_W section than those in the 300 mm R_W section. It is no surprise for the 150 mm R_W section to have higher vertical stresses at the interface than those in the 300 mm R_W section because of their large thickness difference. In addition, at the same base thickness, the reinforced sections had much lower vertical stresses than the unreinforced sections. These comparisons demonstrate that the vertical stresses at the interface decreased with an increase of base thickness and geocell reinforcement.
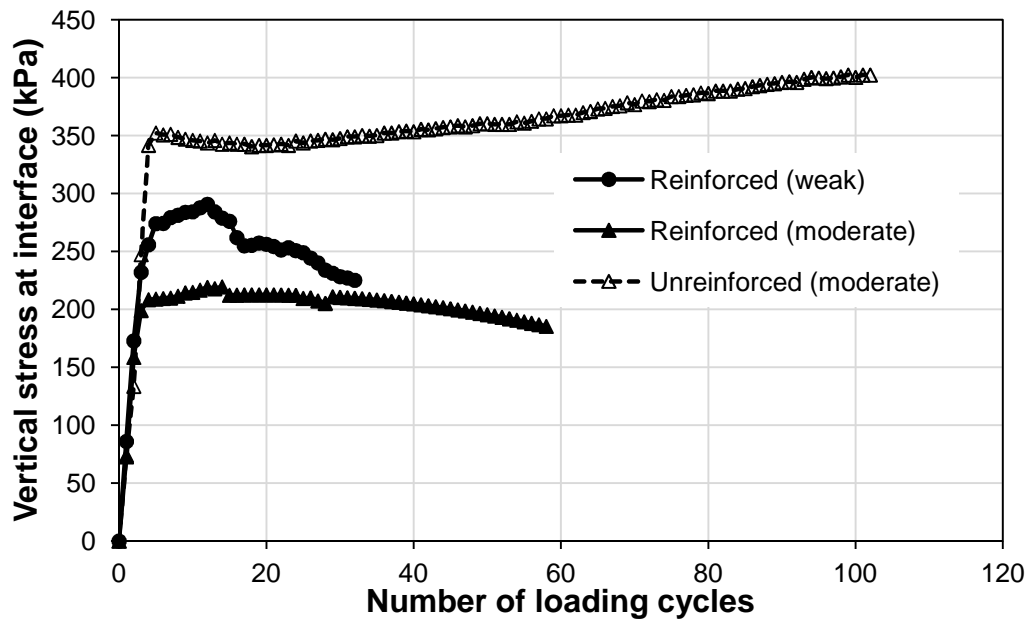
(a) 150 mm thick base
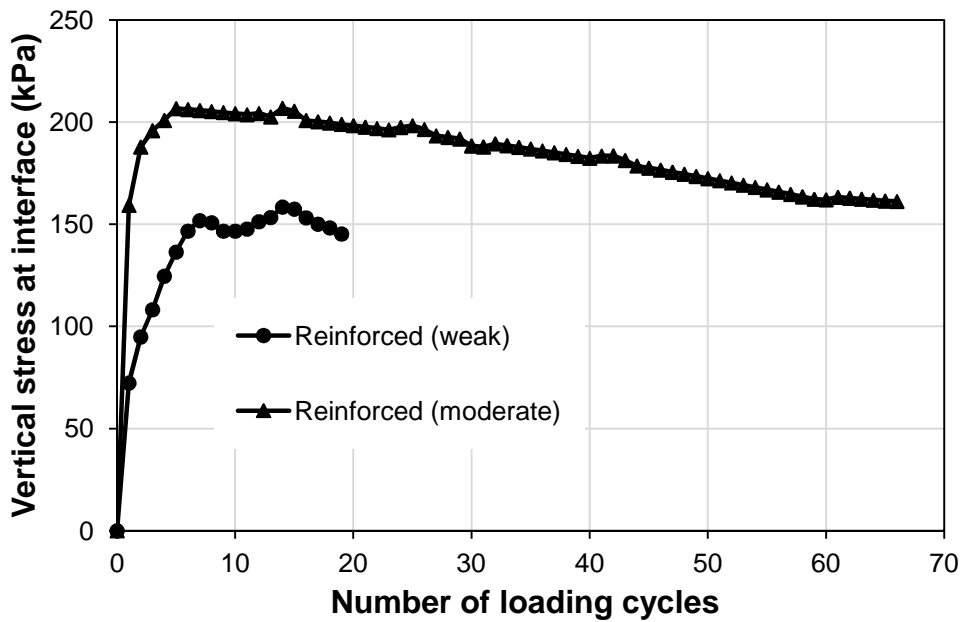
(b) 230 mm thick base

Fig. 4.4.12   Vertical stresses at the interface of subgrade and base at center of
the loading plate
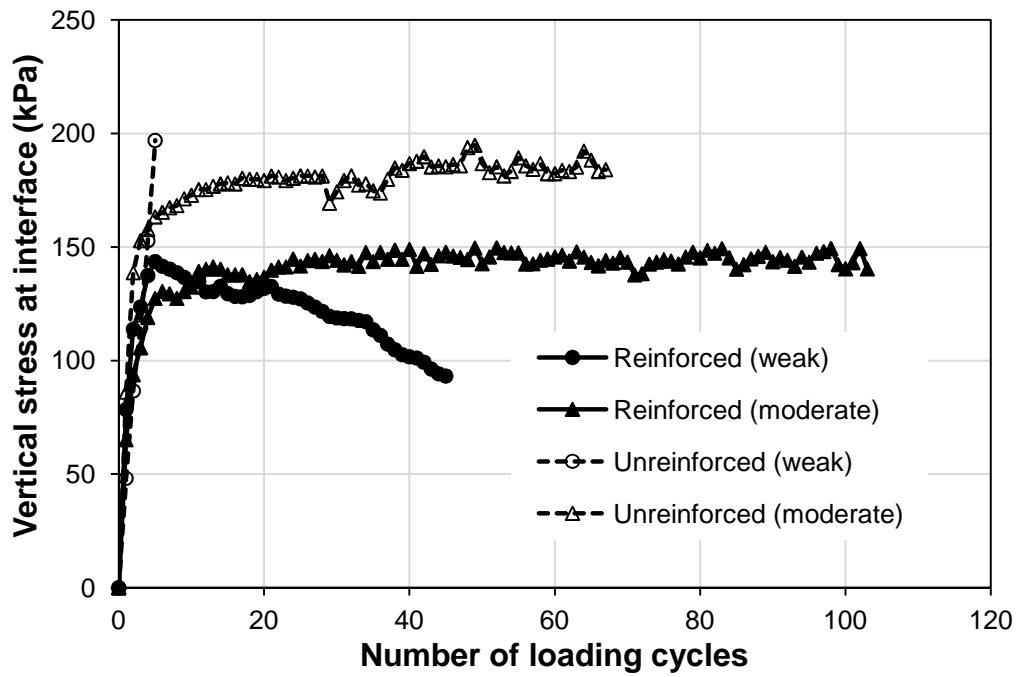
(c) 300 mm thick base

Fig. 4.4.12 Vertical stresses at the interface of subgrade and base at center of the loading plate (continued)

Table 4.4.3 Maximum vertical stress and minimum stress distribution angle for different test sections

Test sections	Maximum vertical stress at the interface (kPa)		Minimum stress distribution angle (degree)
	At center	At 125 mm away from center	
150 mm R_W	291	329	21
230 mm R_W	159	210	29
300 mm R_W	144	148	26
300 mm UR_W	197	182	19
150 mm R_M	219	201	30
230 mm R_M	207	NA	22
300 mm R_M	150	88	25
150 mm UR_M	402	409	10
300 mm UR_M	195	171	19

The vertical stress at the center of the interface can be approximately expressed in terms of a stress distribution angle. The stress distribution angle was calculated using **Eq. 4.4.4**.

$$p_i = \frac{P}{\pi(r + h \tan \alpha)^2}$$ **(4.4.4)**

where

p_i = the distributed vertical stress at the center of the interface of base course and subgrade (kPa)

P = the applied load (i.e., 40 kN in this study)

r = the radius of the tire contact area (i.e., 0.15 m)

h = the thickness of the base course (m, varied)

α = the stress distribution angle in degree with respect to the vertical.

The calculated stress distribution angles for all nine test sections at each loading cycle are shown in **Fig. 4.4.13**. The initial distribution angle depended on the initial conditions of the base and subgrade. It is shown that the stress distribution angle decreased rapidly within the first few loading cycles. The reduction in the stress distribution angle was attributed to the deterioration of the base quality (Han et al., 2004a, b; Qian et al., 2011). The stress distribution angle approached a constant value or increased slowly for the reinforced sections, which demonstrated the stable response behavior. The increase of the stress distribution angle resulted from the slab effect and/or tensioned membrane effect by the geocell-reinforced layer, which is similar to a tensioned membrane effect by a planar reinforcement at large deformation. For the unreinforced section, however, the stress distribution angle continued to decrease until failure, which demonstrated the unstable response behavior. The minimum stress distribution angles for all test sections are presented in **Table 4.4.3**. The stress distribution angle for the 300 mm UR_W section could continue decreasing if the test had continued. Similar observations for the stress distribution angles were made by Han et al. (2011) for 250 mm thick fractionated RAP bases (i.e. 33 to 36° for the reinforced bases and 26° for the unreinforced base) during full-scale moving wheel load tests. It can be concluded that the geocell reinforcement reduced the vertical stress by distributing the load to a wider

117

area.
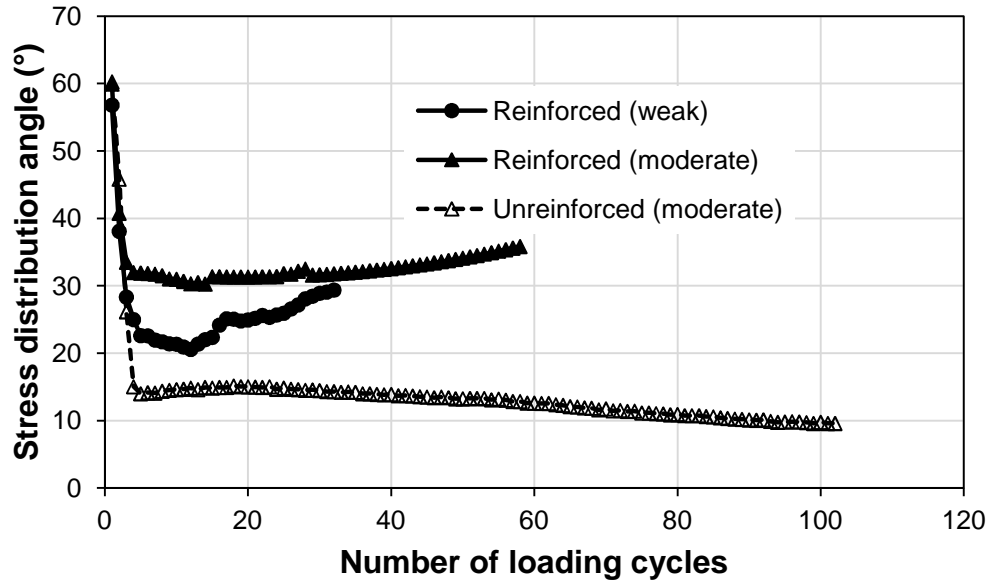
(a) 150 mm thick base
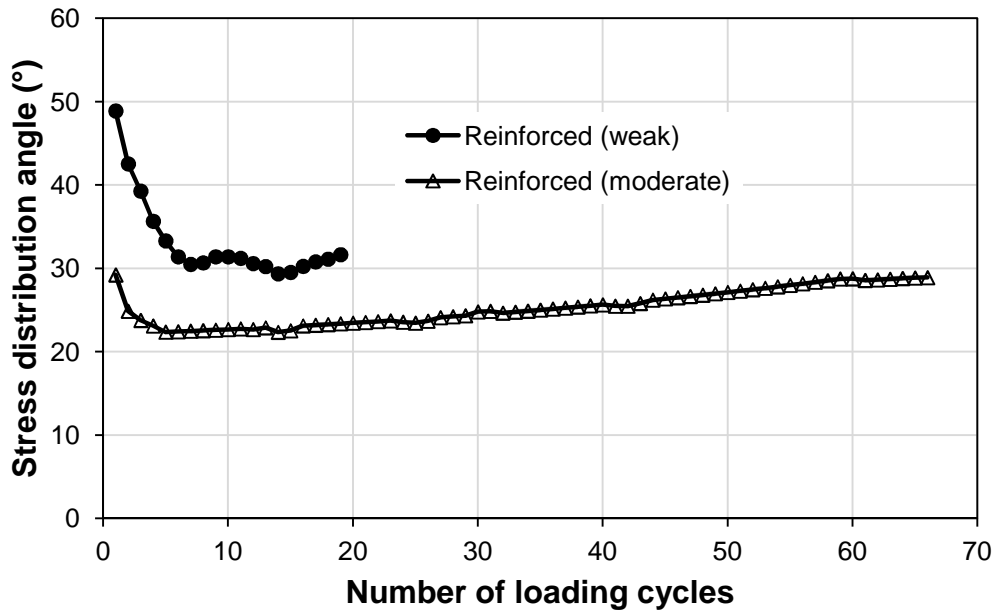
(b) 230 mm thick base

Fig. 4.4.13   Stress distribution angle versus the number of loading cycles
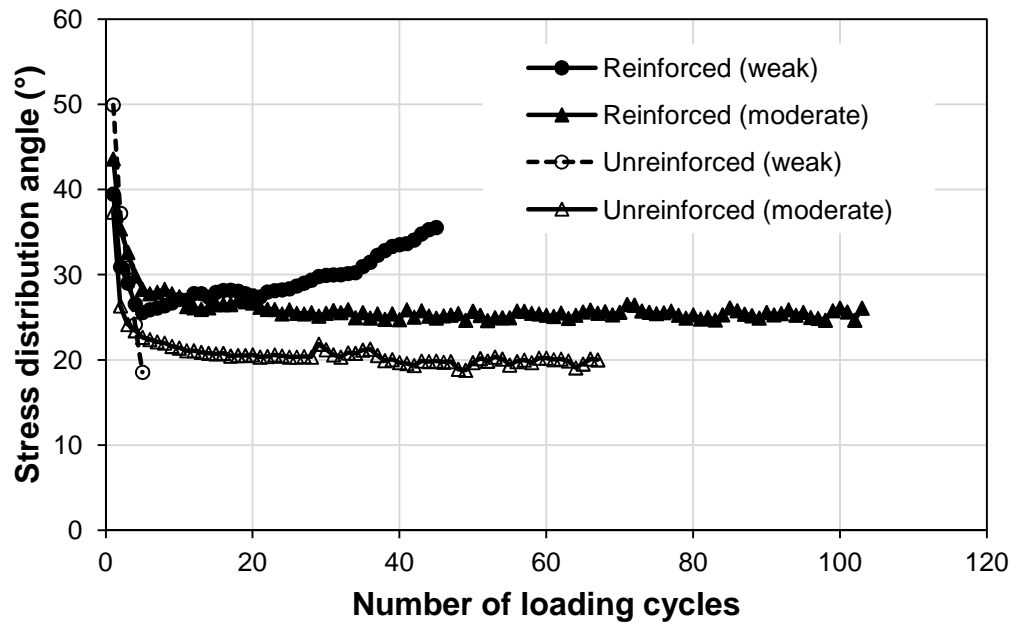
(c) 300 mm thick base

Fig. 4.4.13   Stress distribution angle versus the number of loading cycles (continued)

4.4.8 Vertical stress distribution at the interface

Fig. 4.4.14 presents the vertical stress distributions along the interface of subgrade and base at the 36 mm of permanent deformation at the center. The permanent deformation of 36 mm was chosen for demonstration purpose because the test for 300 mm R_M section was stopped after that amount of deformation. The vertical stresses at 125 mm from the center were slightly higher than those at the center in some test sections. The vertical stresses for the reinforced bases decreased rapidly at the distances of more than 125 mm away from the center and the lowest vertical stresses were observed at the farthest distance from the the center. The section having higher vertical stresses at

the center and 125 mm away from the center showed lower vertical stresses at the remaining loctions compared to other sections. This result follows the force equilibrium, i.e., the applied force is equal to the reaction force, which is equal to the total area under the stress distribution curve. The higher stresses at a distance of 125 mm away from the center in the thinner (150 and 230 mm thick) sections might be caused by the vertical stress distribution underneath the rigid loading plate (i.e., the vertical stress near the edge is much higher than that in the center as shown by Muki (1961) in his theoretical solution). The pressure cells at 125 mm away from the center of loading plate in 230 mm R_M section stopped working during the test, so the stress at 125 mm away from center of the loading plate were assumed same as that at center for obtaining stress distribution profile. The influence of this stress distribution became less significant when the base thickness and subgrade strength increased. This is why such a distribution did not appear in the 300 mm thick sections and section over moderate subgrade.
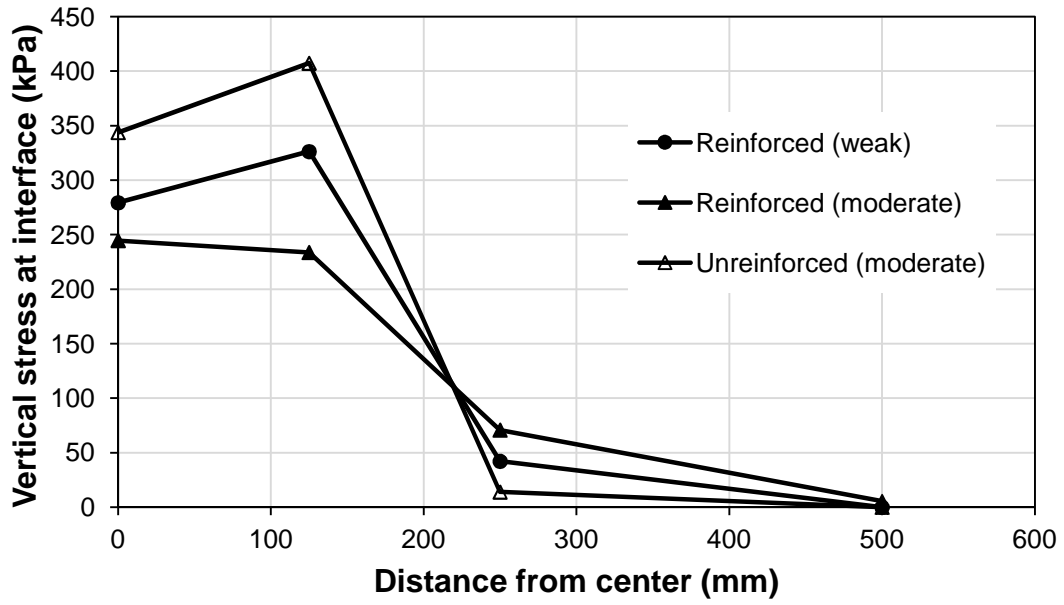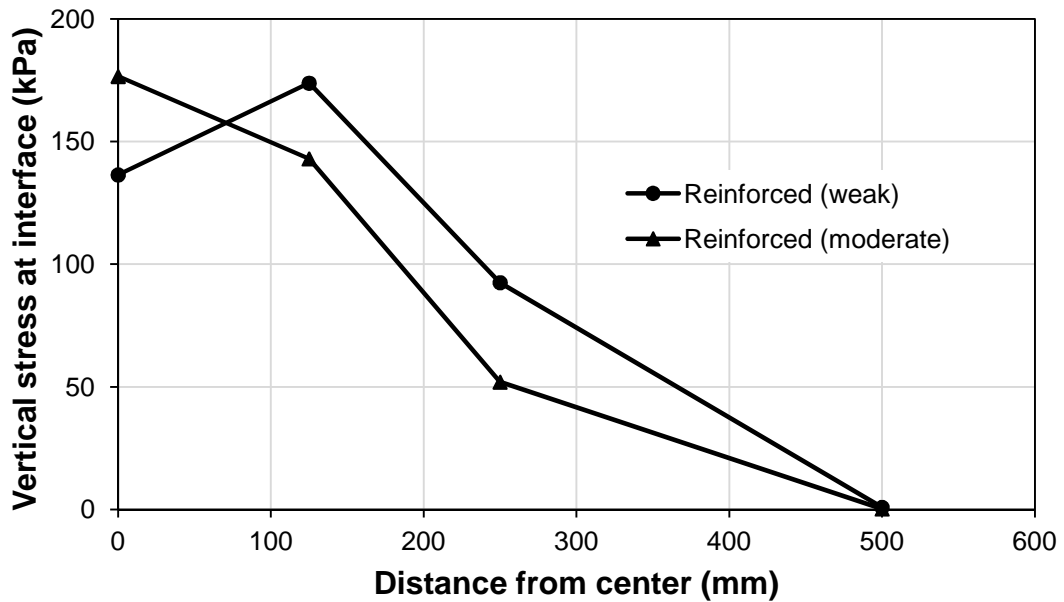
(a) 150 mm thick base

(b) 230 mm thick base

Fig. 4.4.14 Vertical stress distribution at the interface of subgrade and base at

36 mm of permanent deformation at center
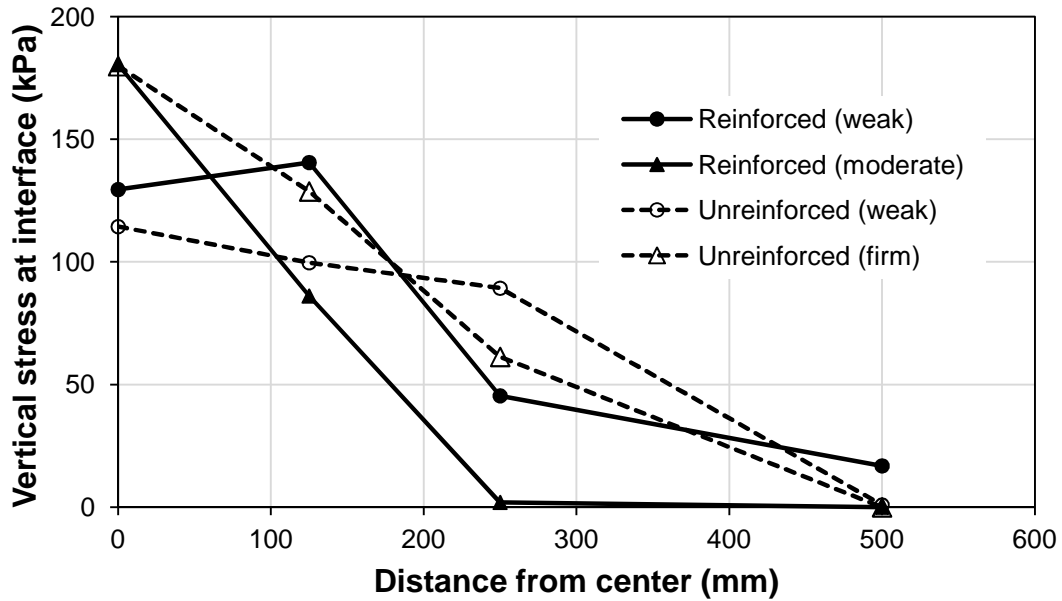
(c) 300 mm thick base

Fig. 4.4.14 Vertical stress distribution at the interface of subgrade and base at 36 mm

of permanent deformation at center (continued)

4.4.9 Vertical stress versus permanent deformation

Fig. 4.4.15 shows the measured vertical stresses at the interface of subgrade and base

course versus the permanent deformation at the center. Qian et al. (2012) found that

the tensioned membrane effect became significant when the vertical permanent

deformation reached 33% the base thickness. In this study, the reduction of the vertical

stress happened at the permanent deformations of 48, 52, 22, 23, 20, and 30 mm for

the 150 mm R_W, 230 mm R_W, 300 mm R_W, 150 mm R_M, 230 mm R_M, 300 mm

R_M sections, respectively, which correspond to 32, 22, 7, 15, 9, and 10% of their base

thicknesses.   These results imply that the 150 mm R_W section behaved as a

tensioned membrane while the 300 mm R_W and all test sections over moderate

122

subgrade behaved as a slab and the 230 mm R_W section behaved as a slab first and then a tensioned membrane. Therefore, the slab effect had a recognized benefit at a smaller permanent deformation than the tensioned membrane effect.
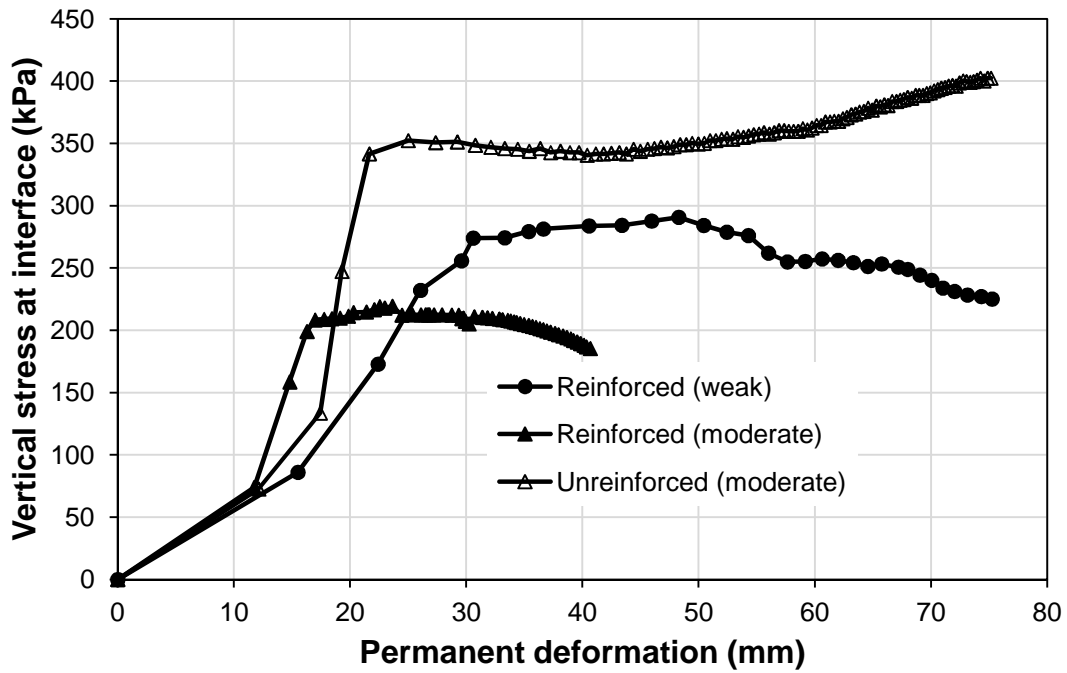
(a) 150 mm thick base

Fig. 4.4.15   Vertical stress at interface of subgrade and base versus the surface

permanent deformation at center
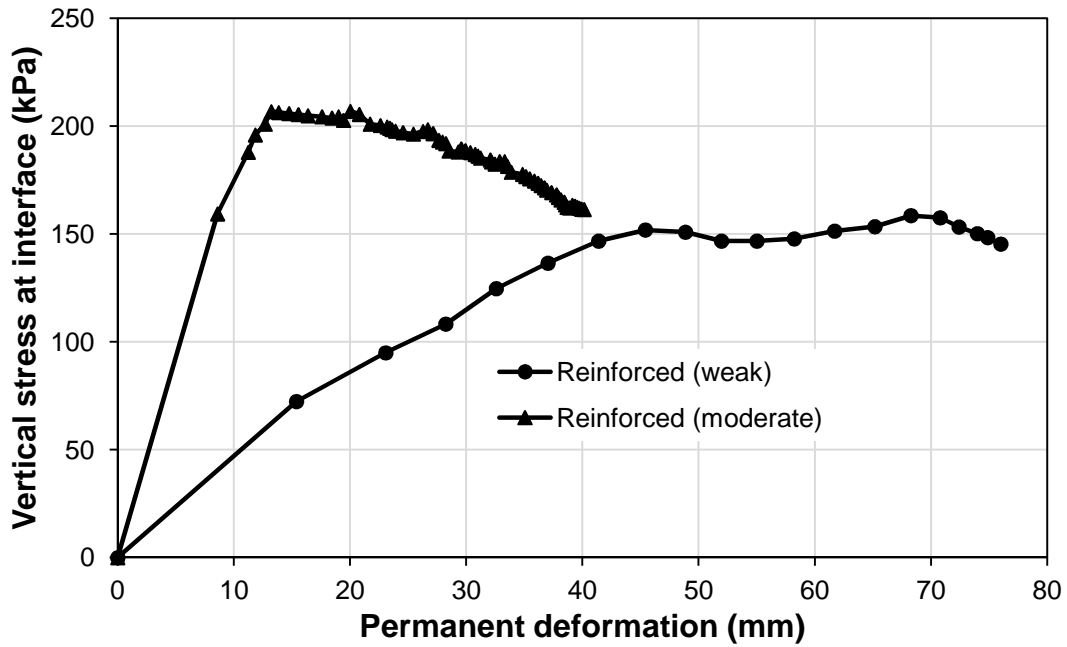
(b) 230 mm thick base
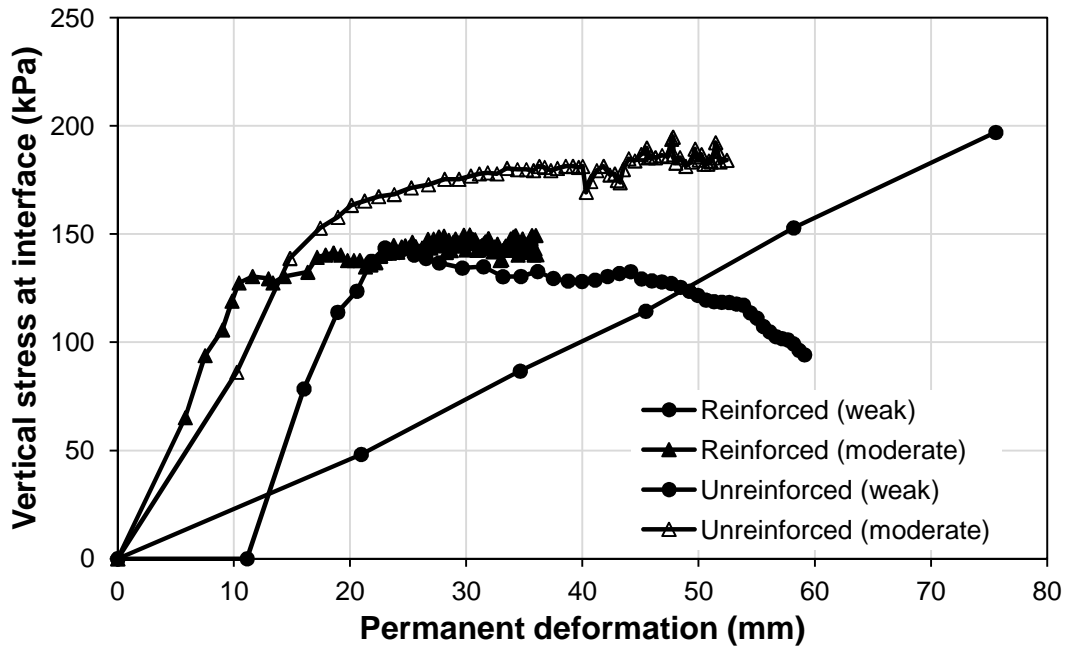
(c) 300 mm thick base

Fig. 4.4.15   Vertical stress at interface of subgrade and base versus the surface

permanent deformation at center (continued)

4.4.10 Strain at the geocell wall

Three strain gages were installed on the central cell just under the loading plate (one each at top, middle and bottom of the wall), two gages were istalled at the top and middle of the geocell wall on the adjacent cell (250 mm away from the loading plate), and one gage was installed at the top of the geocell wall on the next neighbouring cell (500 mm away from the loading plate) as shown earlier in **Fig. 4.3.6** in which the symbol, location, and orientation of each strain gage are provided. Strain gages affixed on the top and bottom of the geocell walls (G1, G3, G4, G6, G7, G9, G10, and G12) measured the horizontal strains while the strain gages affixed on the middle of the walls (G2, G5, G8, and G11) measured the vertical strains. The maximum strains induced at central geocell walls versus the number of loading cycles for the 150, 230, and 300 mm thick reinforced sections are shown in **Fig. 4.4.16**. The maximum strains measured by different gages installed at geocell walls of all reinforced test sections are shown in **Table 4.4.4**. Positive and negative strains refer to tensile and compressive strains, respectively. During the preparation of base courses, G6 in the 150 mm R_M; G2 in the 230 mm R_W; G3 and G4 in the 230 mm R_M; G1 and G7 in the 300 mm R_W; and G1, G4, G7, and G12 in the 300 mm R_M sections were damaged; therefore, no strain was measured at these locations.

All the strain gages affixed to the bottom of the geocell wall showed horizontal tensile strains, among which G3 and G9 measured the highest values. The top gages affixed on the central geocell (G1) in the 150 mm R_W and 230 mm R_W sections first measured small horizontal compressive strains (i.e., slab behavior at a smaller deformation) and then horizontal tensile strains (i.e., tensioned membrane behavior at a

125

larger deformation) as shown in **Fig. 4.4.16**. The top gage affixed on the central geocell (G1) in the 230 mm R_M section first measured small horizontal tensile strains and then horizontal compressive strains **Fig. 4.4.16**. G4 and G6 measured horizontal tensile strains with the least value on G6. All the middle gages (G2, G5, G8, and G11) showed vertical compressive strains irrespective of the locations of cells with the higher value on the central geocell. It should be pointed out that the data recorder could only record strains of up to 2.1%. Therefore, the two strain gauges (G3 and G9) in the 300 mm R_W section as shown in **Fig. 4.4.16** and **Table 4.4.4** reached this limit. From these measured strains, it can be concluded that the 300 mm R_W section and all sections over moderate subgrade behaved as a slab with bending resistance whereas the other two reinforced bases (150 mm R_W and 230 mm R_W) showed such behavior for initial few loading cycles and then turned to tensioned membrane behavior when the deformation became larger.
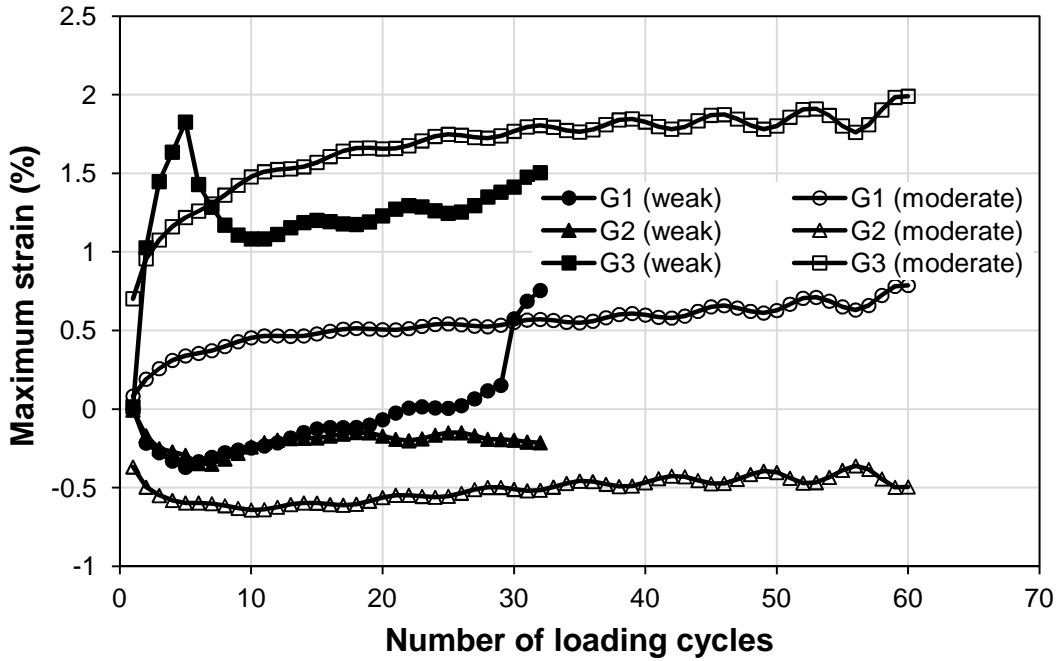
(a) 150 mm thick base
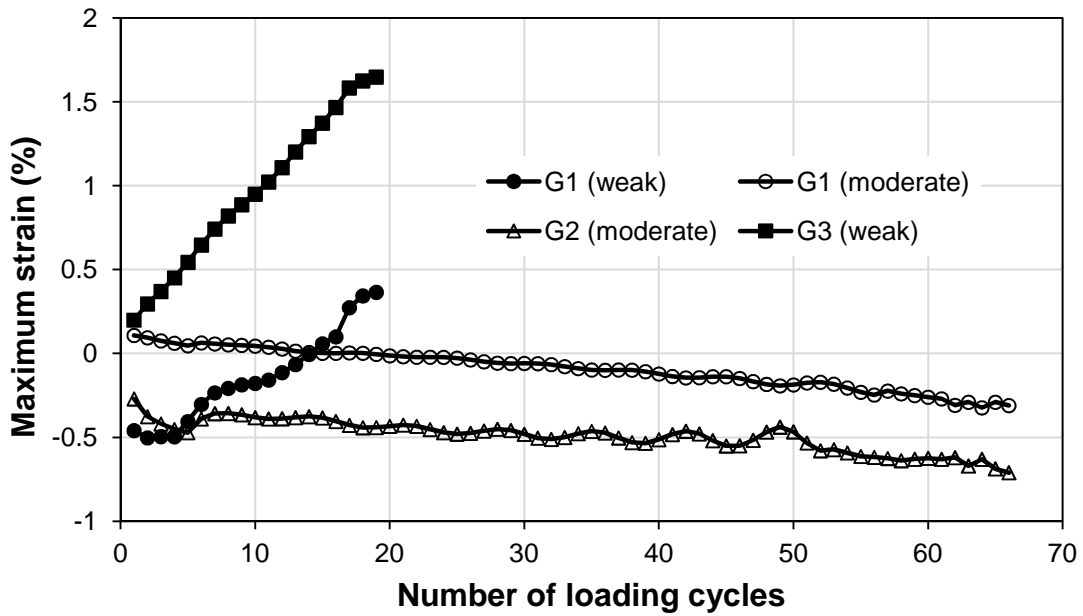
(b) 230 mm thick base

Fig. 4.4.16   Strains at the central geocell wall versus the number of loading cycles
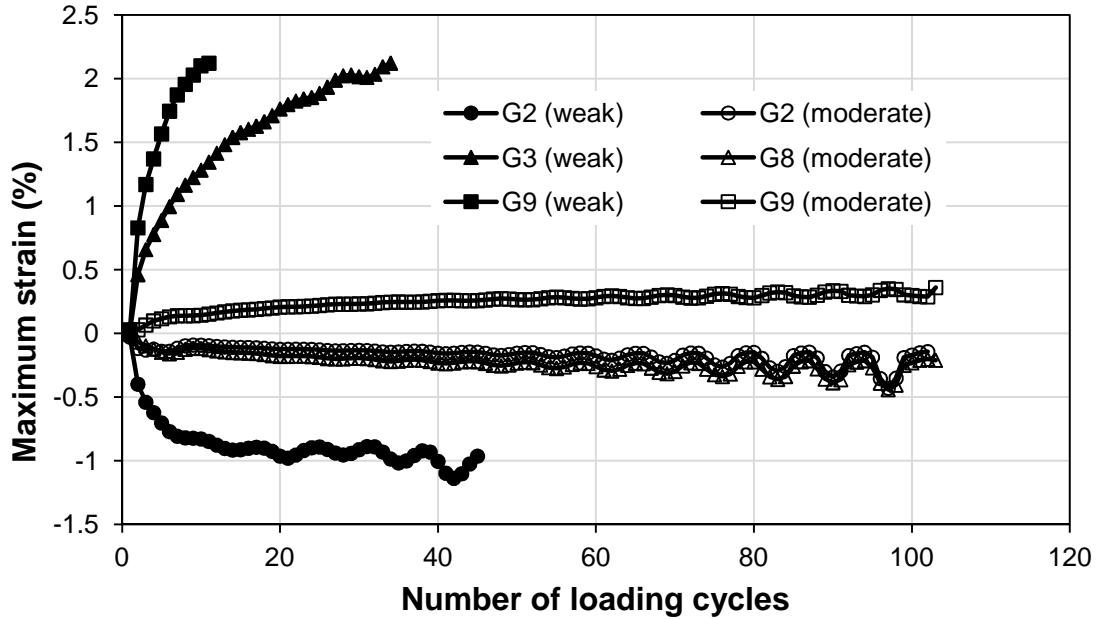
(c) 300 mm thick base

Fig. 4.4.16   Strains at the central geocell wall versus the number of loading cycles

(continued)

Table 4.4.4   Maximum strains at the geocell wall of the reinforced sections

Strain gages	Maximum strains (%) on the geocell walls					
	150 mm R_W	150 mm R_M	230 mm R_W	230 mm R_M	300 mm R_W	300 mm R_M
G1	0.75	0.79	0.37	0.11	Broken	Broken
G2	-0.35	-0.64	Broken	-0.71	-1.13	-0.43
G3	1.83	1.99	1.65	Broken	2.10	0.40
G4	0.67	0.40	0.78	Broken	0.30	Broken
G5	-0.06	-0.04	-0.11	-0.10	-0.40	-0.09
G6	0.21	Broken	0.16	0.12	0.06	0.12
G7	NA	NA	NA	NA	Broken	Broken
G8	NA	NA	NA	NA	-1.30	-0.44
G9	NA	NA	NA	NA	2.10	0.35
G10	NA	NA	NA	NA	0.64	0.10
G11	NA	NA	NA	NA	-1.20	-0.01
G12	NA	NA	NA	NA	0.10	Broken

4.4.11 Strain distribution at the geocell wall

The variations of strains measured along the centerline of the geocells at the end of tests are presented in **Figs. 4.4.17**. The strain distribution profile is only shown for 150 and 230 mm thick reinforced sections as only limited data were available for 300 mm thick reinforced sections. All top gages (G1, G4, and G6), middle gages (G2 and G5), and top gage G6 were represented by S1, S2, and S3, respectively to make presentation easy. The highest tensile or compressive strains were measured directly beneath the center of the loading plate by all gages except the top gages installed at the geocell wall of 230 mm R_M section. In general, the strains measured at the geocell wall decreased as it moved away from the center of the loading plate. The highest strains measured directly beneath the center of the loading plate indicated that the maximum lateral movement of the base course materials occurred at the center of the loading plate.
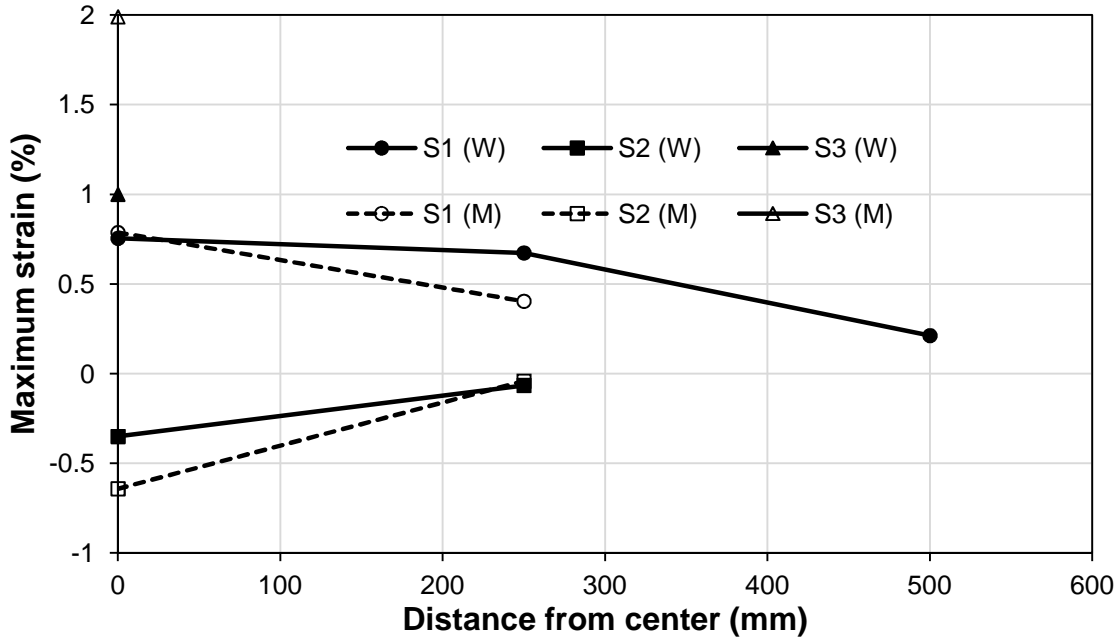
(a) 150 mm thick base
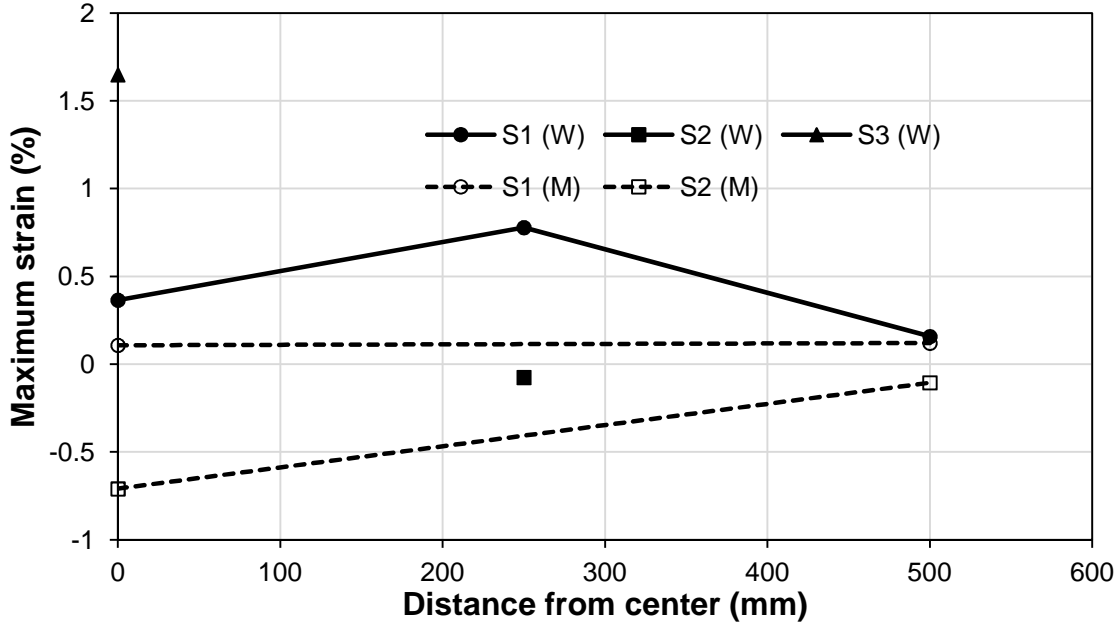
(b) 230 mm thick base

Fig. 4.4.17   Strain distribution profile

4.5 Summary

This chapter presents an experimental study to evaluate the performance of unpaved roads with unreinforced or geocell-reinforced recycled asphalt pavement (RAP) bases over weak or moderate subgrades under cyclic loading. This study was conducted based on typical conditions in field for the construction of geocell-reinforced unpaved roads over weak to moderate subgrade. A nonwoven geotextile was placed between the subgrade and the geocell-reinforced RAP base. The thickness of the RAP cover over the geocell was 50 to 80 mm and the thickness of the RAP between two layers of geocell was 30 mm. Three large-scale cyclic plate loading tests were conducted on geocell-reinforced RAP bases with thicknesses of 150, 230, and 300 mm over a weak (CBR ≈ 2%) and moderate (CBR ≈ 5%) subgrade, each. For a comparison purpose, three large-scale cyclic plate loading tests were also conducted on an unreinforced RAP base. The influence of geocell reinforcement, base course thickness, base course strength, and subgrade strength on deformation behavior of RAP bases was also investigated. The following conclusions can be made from this study:

(i) 100% recycled asphalt pavement (RAP) can be used as a base course material with geocell confinement as a sustainable roadway construction technology.

(ii) The amount and rate of permanent deformation increased with number of loading cycles.

(iii) The geocell reinforcement improved the permanent deformation performance of geocell-reinforced RAP bases by a factor of 1.1 to 11.4 as compared with unreinforced bases.

(iv)   The increase of RAP base thickness by 150 mm improved the permanent deformation performance of RAP base section by a factor of 1.1 to 2.7.

(v)   The strengths of base course and subgrade layer influenced the performance of RAP base section. The infill density influenced the performance of geocell-reinforced RAP base section.

(vi)   The increase of Subgrade CBR from 2% to 5% improved the permanent deformation performance of RAP base section by a factor of 1.2 to 17.2.

(vii)   The 300 mm R_W section performed best followed by 230 mm R_M , 150 mm R_M, 300 mm UR_M, 150 mm UR_M, 300 mm R_W, 150 mm R_W, 230 mm R_W, and 300 mm UR_W sections. The overall improvement factors ranged from 1.6 to 47.8 with respect to 300 mm UR_W section.

(viii)   The increase in the subgrade strength, the geocell-reinforcement, and the base course thickness reduced the amount of permanent surface compression and heave.

(ix)   The geocell improved the resilient behavior of RAP bases and the degree of improvement is higher for the sections over weak subgrade than those over moderate subgrade.

(x)   The geocell-reinforced base sections and the base sections over moderate subgrade showed a stable response whereas the unreinforced base over weak subgrade showed unstable response.

(xi)   The geocell reinforcement reduced the vertical stresses transferred to the subgrade by distributing the load over a wider area.

(xii)   The vertical stresses at the interface decreased with an increase of base

thickness and geocell reinforcement.

(xiii)   The vertical stresses in the unreinforced section increased with the number of load cycles until failure, whereas those in the reinforced sections increased in the first few cycles and then decreased or became constant due to the slab or tensioned membrane effect of the geocell-reinforced layer.

(xiv)   The strain measurements showed that the thicker geocell-reinforced RAP base showed a slab with bending resistance and the thinner base behaved as a slab initially at a smaller deformation and then as a tensioned membrane at a larger deformation.

CHAPTER 5

LARGE-SCALE CYCLIC PLATE LOADING TESTS ON PAVED ROADS

Six large-scale laboratory cyclic plate loading tests were conducted on paved road (flexible pavement) test sections in a large geotechnical test box available at the University of Kansas. The paved road test sections consisted of unreinforced RAP bases (150 and 300 mm thick) or geocell-reinforced RAP bases (150, 230, and 300 mm thick) over moderate (target CBR = 5%) subgrade overlaid by 50 mm thick Hot Mix Asphalt (HMA) surface.

5.1 Test materials

5.1.1 Geosynthetics

Geocells (100 and 150 mm high) were used to reinforce RAP bases and a non-woven geotextile was placed at the interface of subgrade and RAP base course as a separator in all the test sections. The properties of geocells and geotextile are presented in **Chapter 3**.

5.1.2 Subgrade

A mixture of 25% Kaolin and 75% Kansas River (KR) sand was used as a subgrade layer for all test sections. The properties of subgrade materials are presented in **Chapter 3**. The subgrade was compacted at 10.4% moisture content to achieve a

target CBR value of 5%.

5.1.3 Base material

The same RAP, the properties of which are presented in **Chapter 3**, was used as the base material. The RAP base was compacted at 5.5% moisture content to achieve 95% of the maximum dry density.

5.1.4 Tack coat

Slow setting asphalt emulsion, commonly known as tack coat, was applied between the HMA surface and the RAP base to provide adequate bonding between the base course (RAP) and the surface course (HMA).

5.1.5 Surface course

Hot Mix Asphalt (HMA) concrete, the properties of which are presented in **Chapter 3**, was used as the surface course layer for all test sections.

5.2   Test box and loading system

The tests box, the loading system, and the type of loading curve were same as those used for unpaved road test sections as described in **Section 4.2**.

5.3   Test section preparation and instrumentation

Six cyclic plate loading tests were conducted on paved road test sections prepared in a large geotechnical test box system including two unreinforced RAP bases (150 and 300

mm thick) and four reinforced bases (two 150, one 230, and one 300 mm thick) over moderate (target CBR = 5%) subgrade overlaid with a 50 mm thick HMA surface. One 150 mm thick reinforced base was constructed initially to get the subgrade target CBR of 5%. Due to delay in the delivery of HMA material by the plant because of bad weather condition, however, the test section became strong due to moisture loss from the subgrade and the base. Hence five sections were constructed and tested with moderate (CBR ≈5%) subgrade whereas one test section was tested with stronger (CBR ≈ 9%) subgrade. **Fig. 5.3.1** shows the schematic diagram for the setup of the cyclic plate loading tests for paved road test sections. The detailed cross-sections of test sections with different base course thicknesses and types are shown in **Fig. 5.3.2**. The test sections are represented by the short names as shown in **Table 5.3.1** to make discussion and presentation of test results easier.
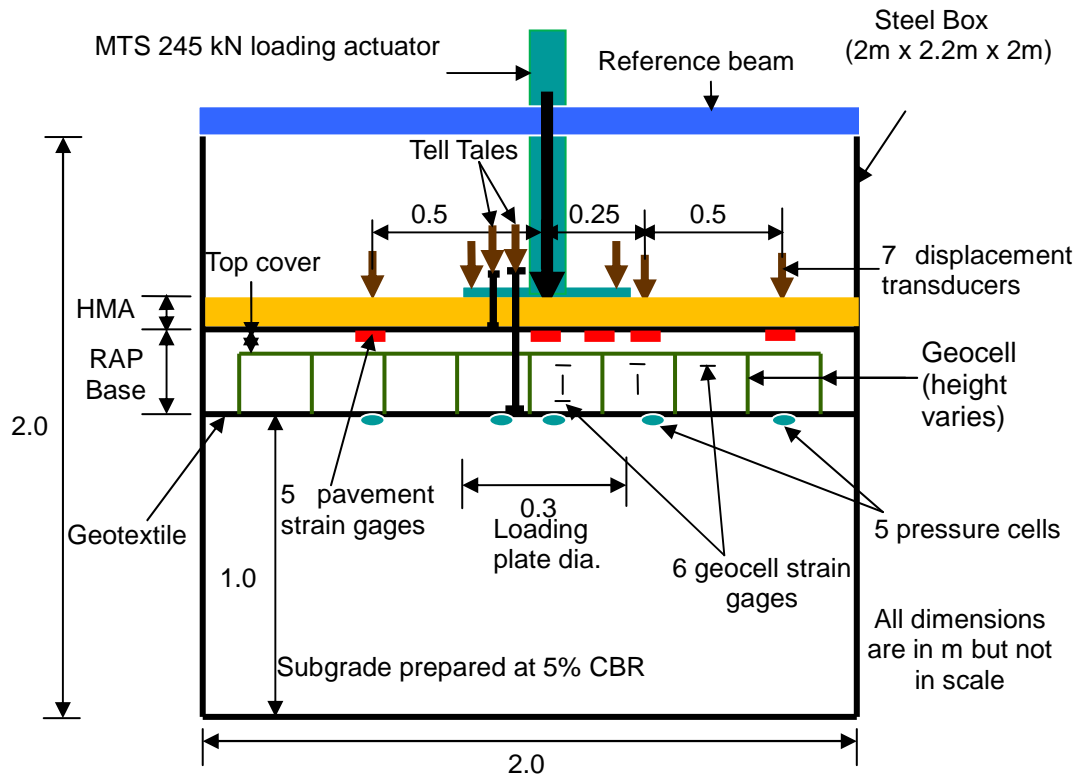
Fig. 5.3.1 Schematic diagram for the setup of the cyclic plate loading tests on paved

road test sections
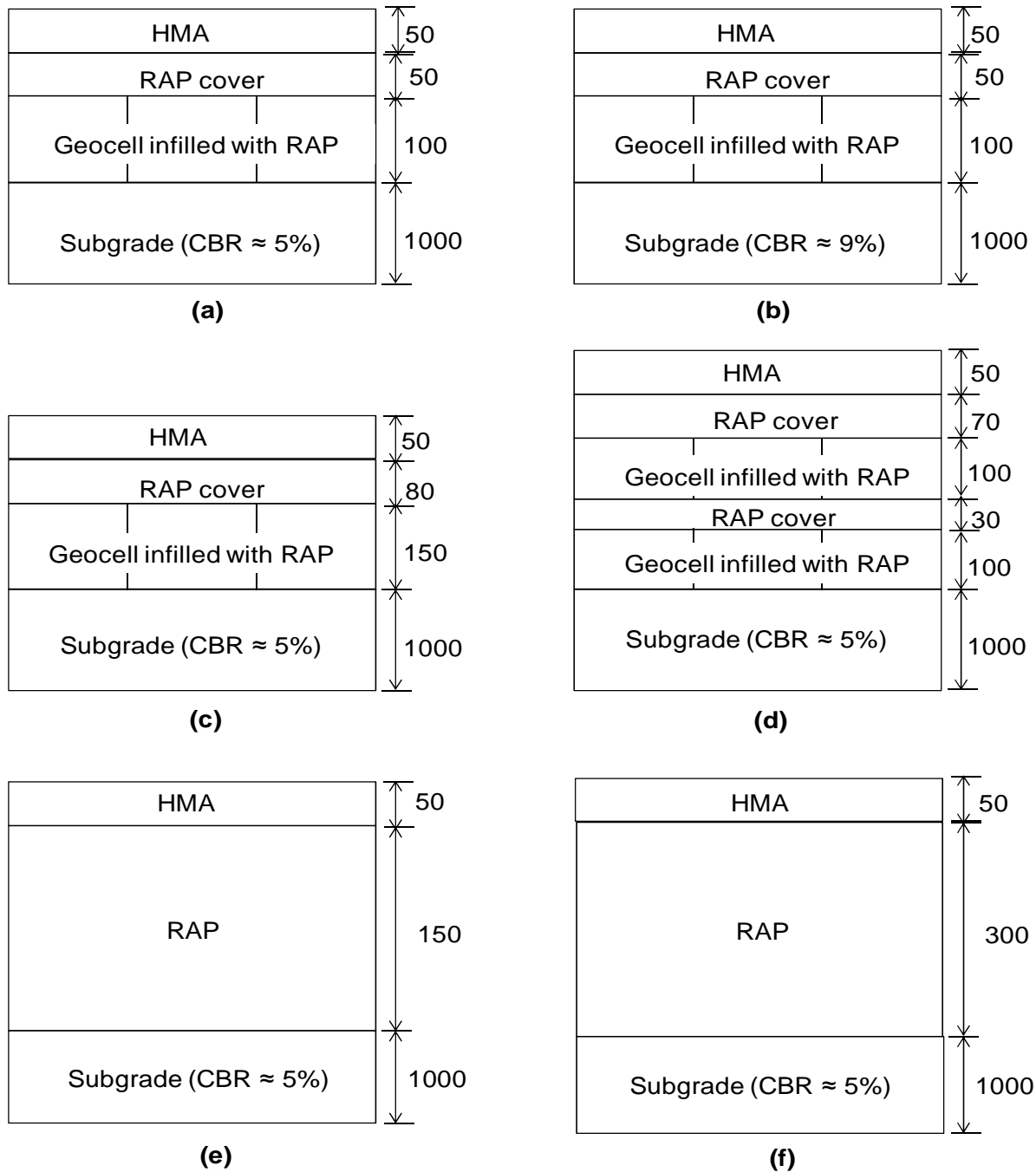
Fig. 5.3.2 Paved road test sections: (a) 150 mm thick geocell-reinforced RAP base, (b)150 mm thick geocell-reinforced RAP base (c) 230 mm thick geocell-reinforced RAP base, (c) 300 mm thick geocell-reinforced RAP base, and (d) 150 mm thick unreinforced RAP base, (e) 300 mm thick unreinforced RAP base

Table 5.3.1 Representations of the paved road test sections

Test section	Representation
HMA over 150 mm thick geocell-reinforced base over moderate subgrade	150 mm R1
HMA over 150 mm thick geocell-reinforced base over strong subgrade	150 mm R2
HMA over 230 mm thick geocell-reinforced base over moderate subgrade	230 mm R
HMA over 300 mm thick geocell-reinforced base over moderate subgrade	300 mm R
HMA over 150 mm thick geocell-reinforced base over moderate subgrade	150 mm UR
HMA over 300 mm thick geocell-reinforced base over moderate subgrade	300 mm UR

The subgrade and the base course were prepared in the same manner as those in the unpaved road test sections described in **Section 4.3**. Vane shear tests and Light Weight Deflectometer (LWD) tests were conducted just after the preparation of subgrade to check the required subgrade strength. DCP tests and LWD tests were conducted one day after the preparation of a base course to verify the strength and stiffness of subgrade and base course. The vane shear and DCP tests were conducted in the same manner as those in unpaved roads. The LWD tests were conducted at five different locations on subgrade and base courses as shown in **Fig. 5.3.3**.

Fig. 5.3.3   Light Weight Deflectometer (LWD) test on subgrade

During the preparation of subgrade and base course, five earth pressure cells were placed at the interface between subgrade and base course and their locations were the same as those in the unpaved road test sections. Two tell-tales were installed below the loading plate and at the interfaces of subgrade/base and base/HMA surface as shown in **Fig. 5.3.4**. Each tell-tale contained a steel rod (3.15 mm in diameter) inside a hollow aluminum pipe (6.3 mm in diameter and 0.40 mm in thickness) with a small metal plate (15 mm in diameter) at bottom. The 15 mm wide aluminum plate was installed on top of each steel rod using nuts which served as a base for placing displacement transducers to measure interface deformations. Tell-tales were not installed in the 150 mm R2 and 300 mm R sections because of their unavailability at that time. The tell-tales were used to measure the vertical deflections at base-subgrade interface and HMA-base interface. Two small holes of 8 mm diameter were made on

the loading plate to make tell-tales run through these holes.

Figure 5.3.4 Tell-tale measurements

Strain gages were installed on geocell in the same way and at the same locations as those in the unpaved road tests. Tack coat was heated in the oven and applied on the top of the RAP base to ensure an adequate bond between the RAP base and the HMA surface. The pavement strain gages (PVST) were installed on top of the base course after applying tack coat to measure the strains developed at the bottom of the HMA layer. Literature shows that mostly an H-type strain gages have been used to measure HMA strains. The author believe that the size of H-type PVST is large for this kind of indoor test and may affect the test results by providing additional reinforcement to the test sections. So, a new type of PVST was prepared using a thin aluminum sheet and the same strain gages which were used to measure geocell strains. A rectangular shape aluminum sheet (Length = 80 mm, Width = 7 mm, and Thickness = 1 mm) was

smoothened using a sand paper and cleaned by isopropyl alcohol before installing the strain gages. The strain gages were then installed at both sides of the smoothened aluminum sheet using Cyanoacrylate adhesive and then covered with M-Coat C coating material. The coating was left for 24 hours to get cured and then 3145 RTV silicon rubber coating was applied and allowed to cure for another 24 hours before the aluminum sheet with coated strain gages was installed. The aluminum sheet with coated strain gages were referred here as PVST as shown in **Fig. 5.3.5.** The strain gages used here could generally withstand temperature of about 82°**C**. The purpose of applying M-Coat C and 3145 RTV silicon rubber coating was to protect the strain gages and its wire from high temperature (i.e. 135°**C**) of HMA.

Fig. 5.3.5   Pavement strain gages (PVST)

After the tack coat was applied and the HMA was placed, the PVST were installed on top of the tack coat applied RAP base and were covered by a thin layer of cold mix asphalt to provide extra safety against high temperature of the HMA. The wires of strain gages were taken to the side of the box through a small and shallow

trench on the surface of RAP base, and were covered with RAP base. Strain gages were installed at the bottom of the HMA surface at the center and 12.5, 25. 50, and 75 mm away from the center of the loading plate to measure the strains induced in the HMA surface. One day after application of tack coat, the HMA surface was placed on top of the RAP base and compacted in one lift with a vibratory plate compactor. The compacted thickness of the HMA surface was 50 mm in each test. The quantities (weights) of the HMA concrete were calculated by multiplying the assumed density of the HMA by the volume of the material (corresponding to 5 mm thick) to fill in the box. The LWD tests were conducted three days after the preparation of the HMA surface at five different locations to verify its stiffness and then the displacement transducers were installed. The test setup is shown in **Fig. 5.3.6**. All the displacement transducers, earth pressure cells, and strain gauges were connected to the data recorders before a cyclic plate loading test was started. Connecting the sensors to the data recorders was done in the same manner as that in the unpaved road tests. In addition, a manual data recorder was used in these tests in which the number of sensors was more than the number of data connection ports available to four smart dynamic strain recorders. In this case, one port of the smart dynamic strain recorder was connected to the manual data recorder. The strain values at certain intervals of loading cycles (i.e. interval of 200 cycles) were measured manually for those strain gages which were connected to the manual data recorder. The pictures of the manual and smart dynamic strain recorders are shown in **Fig. 5.3.7**. Each cyclic test was terminated only after the permanent deformation reached more than 25 mm.

Fig. 5.3.6   Test setup for paved road test sections

Fig. 5.3.7   Manual and smart dynamic strain recorders

At least five HMA samples were cored at the end of each test using a core cutter of 75 or 100 mm diameter to determine the air void content of the HMA surface. The locations to core samples were randomly selected to achieve a better representation of the quality of the HMA surface. The actual asphalt content in HMA was also determined

from the cored HMA sample using the ignition method. The pictures of the core cutter and cored samples are shown in **Fig. 5.3.8**.

(a) Core cutter machine   **(b)** cored HMA sample

Fig. 5.3.8   Core cutter machine and cored HMA sample

5.4   *Test results and discussions*

The test results for strains at the bottom of HMA surface are presented in Han et al. (2011) and not presented here. The other test results were analyzed and are discussed in the following sections:

5.4.1 Quality control test results

The vane shear, DCP, and LWD tests were conducted to check the strength of each layer of paved road test sections. In addition, the HMA samples were cored using the

core cutter machine and the samples were tested for air void content and asphalt content in the HMA for quality assurance.

<u>Vane shear and DCP test results</u>

The required strengths of the subgrade layer were checked by conducting five vane shear tests at five different locations at depths of 100, 175, and 250 mm just after preparation of a subgrade and four DCP tests were conducted at four different locations one day after the preparation of a base course. The CBR values of subgrade and base layers were calculated from vane shear and DCP test data using the correlations provided earlier in **Eqs. 4.4.1** and **4.4.2**, respectively.

The CBR profiles obtained from DCP tests for all test sections are shown in **Fig. 5.4.1**. The CBR profile of 150 mm R2 section as shown in **Fig. 5.4.1** was based on DCP tests conducted after cyclic plate loading tests. The average, standard deviation (σ), and coefficient of variance for the CBRs of base and subgrade were determined from the vane shear and DCP tests and are presented in **Table 5.4.1**. The average CBR values of the subgrades obtained from the DCP tests were slightly higher than those from vane shear tests. This may be because the DCP tests were conducted one day after the preparation of test sections. Average CBR values of each subgrade and base course ranged from 4.9 to 6.1% and 8.9 to 10.9% except 150 mm R2 section. The average CBR values of subgrade and base course obtained from DCP tests conducted after cyclic plate loading tests for 150 mm R2 section were 9 and 13.8%, respectively. The standard deviation (σ) and coefficient of variation (COV) for the CBR of subgrade ranged from 0.5 to 1.8% and 8.9 to 28.8%, whereas those for the CBR of base ranged

from 1.0 to 2.3% and 9.0 to 18.7%, respectively as shown in **Table 5.4.1**.
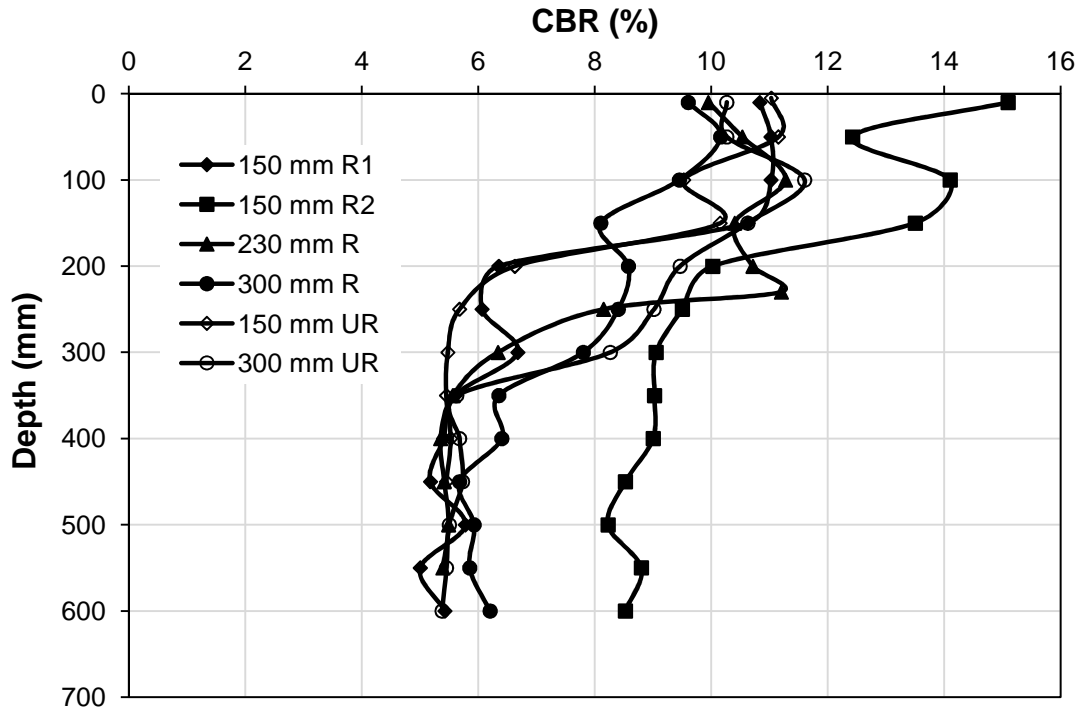
Fig. 5.4.1   CBR profiles obtained from DCP tests

Table 5.4.1 CBR of subgrade and base course obtained from vane shear and DCP tests on different paved road test sections

Test sections	Subgrade CBR (%) (Vane shear/DCP)			Base CBR (%) (DCP)		
	Average	σ	COV	Average	σ	COV
150 mm R1	5.1/5.7	1.1/1.1	21.9/19.0	10.9	1.0	9.0
*150 mm R2	5.2/5.9(9.0*)	0.8/1.8*	15.4/20.1*	10.2(13.8*)	1.6(2.3*)	15.7/16.7
230 mm R	5.1/5.6	0.9/1.6	17.4/28.8	9.9	1.5	15.0
300 mm R	5.3/6.1	0.6/1.0	11.7/16.3	8.9	1.4	16.7
150 mm UR	4.9/5.7	0.7/1.1	13.8/20.1	10.5	1.9	18.7
300 mm UR	5.1/5.6	0.9/0.5	17.4/8.9	9.9	1.6	15.4

Note: * represents section with strong subgrade and base

LWD test results

LWD tests were conducted on the prepared surface of each layer (subgrade, RAP base, and HMA surface) of all paved road test sections following the manufacturer recommendations as shown in **Fig. 5.3.3** and the dynamic deformation modulus (E_{vd}) on each layer was determined. The ZFG 3000 LWD manufactured by Zorn instruments, Germany was used in this study. During the LWD tests, the loading plates with diameters of 150, 200, and 300 mm were used for each layer at six locations in each test sections. During the tests, a falling weight of 10 kg was dropped from a distance of 730 mm on the loading plate equipped with an acceleration sensor set up on the flat surface of each layer. The acceleration signal generated because of the impact load was captured by the sensor and the data (deformation, dynamic modulus, and degree of compactness) were calculated. **Table 5.4.2** presents the average, standard deviation

(σ), and coefficient of variation (COV) of E_{vd} obtained from LWD tests using a different size of loading plate. The average, standard deviation (σ), and COV of E_{vd} for each layer of each test section were calculated using six numbers of LWD test data. It can be seen from the table that there are large variation and noise in the values of E_{vd}. Literature shows that LWD tests are generally suitable for fine to coarse grained soils but used in limited extend for an HMA surface. It was concluded that the LWD test results obtained here were not appropriate for the HMA layer because the test results conducted with different diameters of loading plate on HMA surface layer did not show similar trend as those on base and subgrade, and hence further analysis of LWD test results for the HMA surface was not conducted. The LWD tests conducted on the surfaces of subgrade, base, and HMA gave the subgrade E_{vd}, combined (subgrade + base) E_{vd}, and combined (subgrade + base + HMA) E_{vd}, respectively. It can also be seen that the combined modulus of base and subgrade was greater than the modulus of subgrade and can be concluded that the base was stiffer than the subgrade. The reinforced base was stiffer than the unreinforced base.

The influence of the LWD loading plate diameter on E_{vd} of subgrade and base is presented in **Fig. 5.4.2**. The E_{vd} values increased with increasing diameter of loading plates. The linear relationship of E_{vd} obtained using the 300 mm diameter plate (E_{vd-300}) with E_{vd} obtained using 150 and 200 mm diameter plates (E_{vd-150} and E_{vd-200}) were developed and are shown in **Fig. 5.4.2**. The regression relations are strong with R^2 values ranged from 0.91 to 0.99 and are similar to those developed by Vennapusa and White (2009) with different constant values which depended on types of tested materials.

Table 5.4.2 Dynamic deformation moduli (E_{vd}) of pavement layers obtained from LWD tests using different sizes of loading plates

LWD Loading Plate Diameter (mm)	Test sections	Subgrade			Base			HMA		
		Average	σ	COV (%)	Average	σ	COV (%)	Average	σ	COV (%)
300	150 mm R1	29.1	6.6	22.7	26.1	4.7	18.1	82.7	11.5	13.9
	150 mm R2	17.1	5.0	29.5	35.2	4.7	13.4	104.1	13.4	12.9
	230 mm R	11.3	1.8	0.2	28.9	4.0	0.1	75.3	30.5	0.4
	300 mm R	16.9	7.7	45.7	48.3	3.4	7.0	95.2	8.3	8.7
	150 mm UR	6.8	1.9	28.0	17.2	4.6	26.4	51.5	30.6	5.9
	300 mm UR	11.3	1.8	16.2	30.6	6.0	19.7	109.6	5.6	5.1
200	150 mm R1	20.0	4.7	23.7	19.9	5.3	26.5	98.1	11.9	12.0
	150 mm R2	12.2	3.2	26.3	28.8	3.9	13.7	105.8	28.6	27.0
	230 mm R	7.4	1.3	0.2	19.9	2.0	0.1	92.7	7.1	0.1
	300 mm R	10.5	3.5	33.1	38.8	4.3	11.1	98.1	13.5	13.7
	150 mm UR	4.9	1.1	22.4	15.7	4.0	25.3	66.3	12.8	19.3
	300 mm UR	7.4	1.3	17.9	22.3	3.7	16.5	117.7	15.1	12.8
150	150 mm R1	14.1	3.6	25.6	16.4	3.5	21.1	81.1	9.7	11.9
	150 mm R2	11.0	3.7	33.6	21.5	2.3	10.9	96.4	10.6	11.0
	230 mm R	7.0	2.2	0.3	15.0	2.7	0.2	81.7	7.7	0.1
	300 mm R	9.2	3.1	33.4	31.9	1.7	5.4	98.6	24.3	24.7
	150 mm UR	4.7	1.2	24.7	10.6	4.4	42.1	56.0	7.8	13.9
	300 mm UR	7.0	2.2	30.8	18.1	4.3	23.7	86.0	4.3	5.0
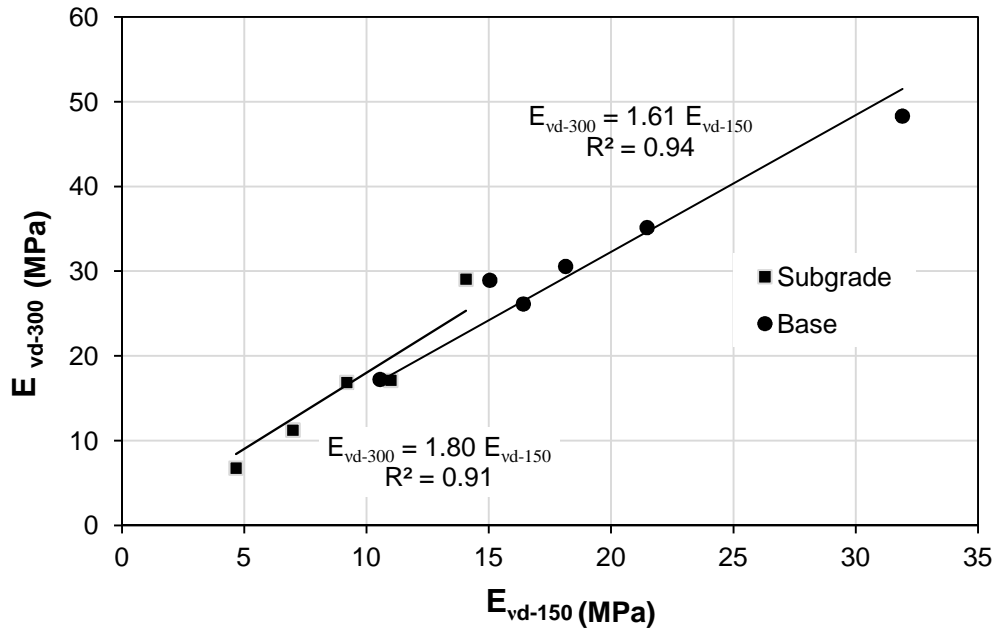
(a) Relationship between E_{vd-150} and E_{vd-300}
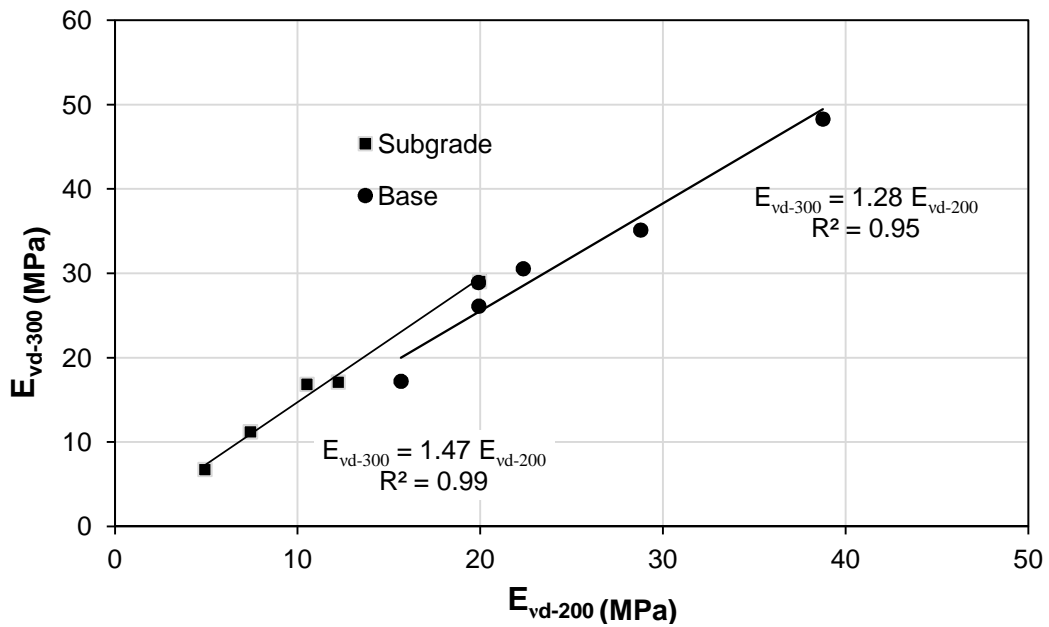
(b) Relationship between E_{vd-200} and E_{vd-300}

Fig. 5.4.2 Influence of LWD loading plate diameter on E_{vd} of subgrade and base

(continued)

151

<u>Properties of cored HMA samples</u>

Percentage of air voids (V_a) in HMA indicates the degree of compactness of HMA surface. It is known hat HMA performs best at optimum V_a. However, permeability increases with increase in V_a and water can pass through more permeable HMA layer and may cause raveling of HMA surface. The bulk specific gravity (G_{mb}) and the theoretical maximum specific gravity (G_{mm}) of cored HMA samples were determined following ASTM D-3203 and the percentage of air voids (V_a) was calculated using **Eq. 5.4.1.** Asphalt contents of HMA samples were determined by the ignition method. The test results are presented in **Table 5.4.3**. The V_a of the cored HMA samples ranged from 6.08 to 7.64%. The 300 mm R section had the lowest V_a whereas the 150 mm UR had the highest V_a among all six sections. The test sections with strong base and subgrade had lower V_a than those with relatively weak base and subgrade. The test sections with the reinforced base had a lower V_a than those with the unreinforced base. It can be concluded that the strong base and subgrade and the geocell-reinforced bases provided a strong platform for the HMA and helped in compaction of the HMA.

$$\text{Va} = \left(1 - \frac{G_{mb}}{G_{mm}}\right) \text{x } 100 \qquad \textbf{(5.4.1)}$$

Table 5.4.3 Properties of cored HMA samples from different test sections

Test sections	HMA properties			
	Asphalt content (%)	Bulk specific gravity (G_{mb})	Theoretical maximum specific gravity (G_{mm})	Air voids (%)
150 mm R1	5.4	2.08	2.23	6.81
150 mm R2	5.3	2.18	2.33	6.59
230 mm R	5.5	2.14	2.31	7.01
300 mm R	5.9	2.16	2.3	6.08
150 mm UR	5.8	2.09	2.26	7.64
300 mm UR	5.4	2.15	2.31	7.18

5.4.2 Recorded surface deformation

Fig.5.4.3 presents the recorded displacements of the loading plate (averaged from two displacement transducers installed on the loading plate) developing with the number of loading cycles during all the tests, which included the accumulated permanent (plastic) deformation and the resilient deformation (elastic rebound). The total surface deformations at each loading cycle were measured by the displacement transducers installed on top of the prepared sections. There is less variation in the surface deformations of paved road sections as compared with that of unpaved road sections. The permanent deformations and resilient deformations were separated from the total deformation and are discussed later in this chapter.
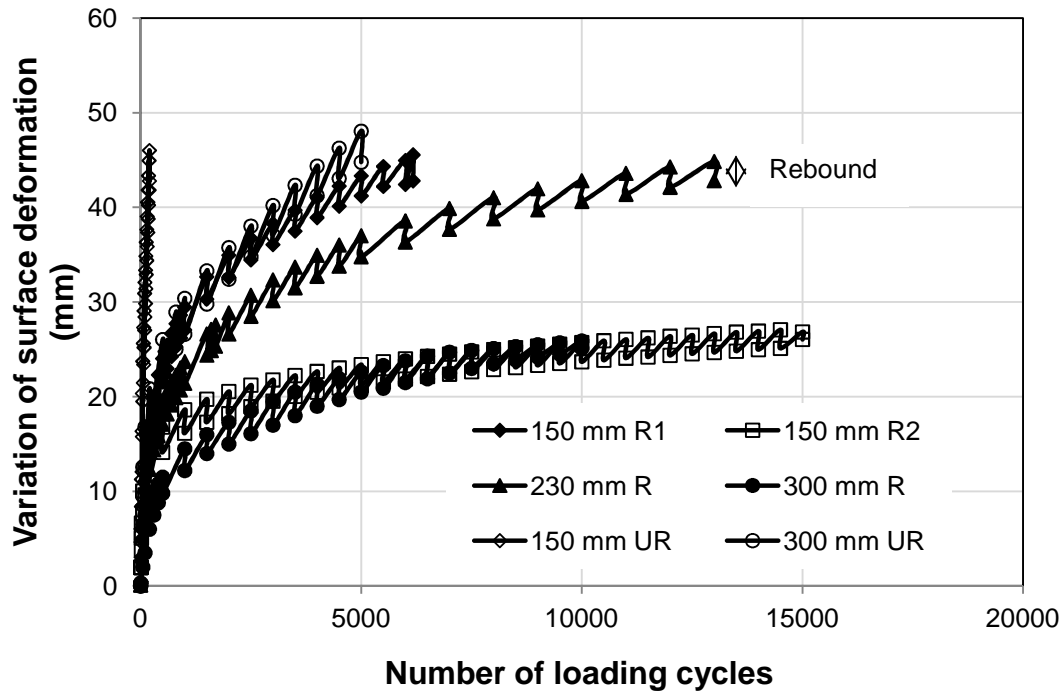
Fig. 5.4.3   Variation of surface deformations versus the number of loading cycles

5.4.3 Surface permanent deformation

The total surface deformations at each loading cycle were measured by the displacement transducers installed on top of the prepared sections.   The total deformation consisted of permanent and resilient deformations.   The permanent and resilient deformations for each loading cycle were separated from the total deformations and are presented separately in this chapter.   The surface permanent deformations at the center of the loading plate were calculated by averaging the permanent deformations recorded by two displacement transducers installed on top of the loading plate, while the surface permanent deformations at the locations away from the center of the loading plate were kept same as those recorded by the displacement transducers installed at each particular location.   The permanent surface deformations at the center

154

of the loading plate versus the number of loading cycles for all paved road test sections are shown in **Fig. 5.4.4**. The permanent deformations increased with the number of loading cycles. The rate of increase in permanent deformations decreased with increasing number of loading cycles. All geocell-reinforced sections had lower permanent deformations and rate of increase in permanent deformations than the corresponding thick unreinforced sections and the thicker base sections had lower permanent deformations than the thinner bases under a similar condition of construction. The 150 mm R1 section had an equivalent performance than the 300 mm UR section which indicated that the thickness of base course could be reduced by using geocell reinforcement in paved road construction. Similarly, the 150 mm R2 section had an equivalent or even better performance initially than the 300 mm R which further indicated that the thickness of base course could be reduced by increasing the strength of base and subgrade. It can be concluded that geocell confinement, base and subgrade strengths play a vital role in improving the performance of test sections.
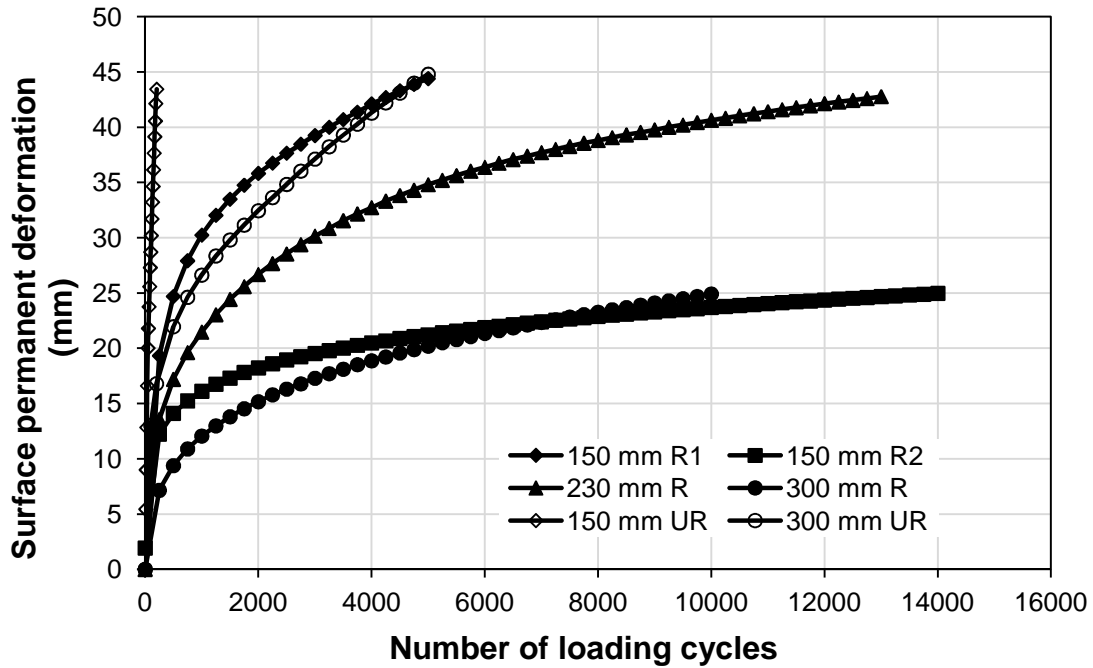
Fig. 5.4.4   Surface permanent deformation at the center of the loading plate versus the number of loading cycles

5.4.4 Interface permanent deformation

The permanent deformations at the interface of HMA surface and base and the interface of base and subgrade were recorded by two displacement transducers installed on top of the tell-tales placed on top of base course and subgrade, respectively. The tell-tales were not used for 150 mm R2 and 300 mm R sections. The interface permanent deformations at the center of the loading plate versus the number of loading cycles for paved road test sections are shown in **Fig. 5.4.5**. The interface permanent deformation increased with the number of loading cycles. The rate of increase in the interface deformation decreased with increasing number of loading cycles. The 230 mm R

section had the least permanent deformation at the interface of HMA surface and base, followed by 300 mm UR, 150 mm R1, and 150 mm UR sections as shown in **Fig. 5.4.5a**. The 300 mm UR section had the least permanent deformation at the interface of base and subgrade, followed by 230 mm R, 150 mm R1, and 150 mm UR sections as shown in **Fig. 5.4.5b**. The geocell-reinforced sections had lower interface permanent deformations and rate of increase in permanent deformations at the interfaces than the corresponding thick unreinforced sections, and the thicker base sections had lower permanent deformations at the interfaces than the thinner base sections under a similar condition of construction.
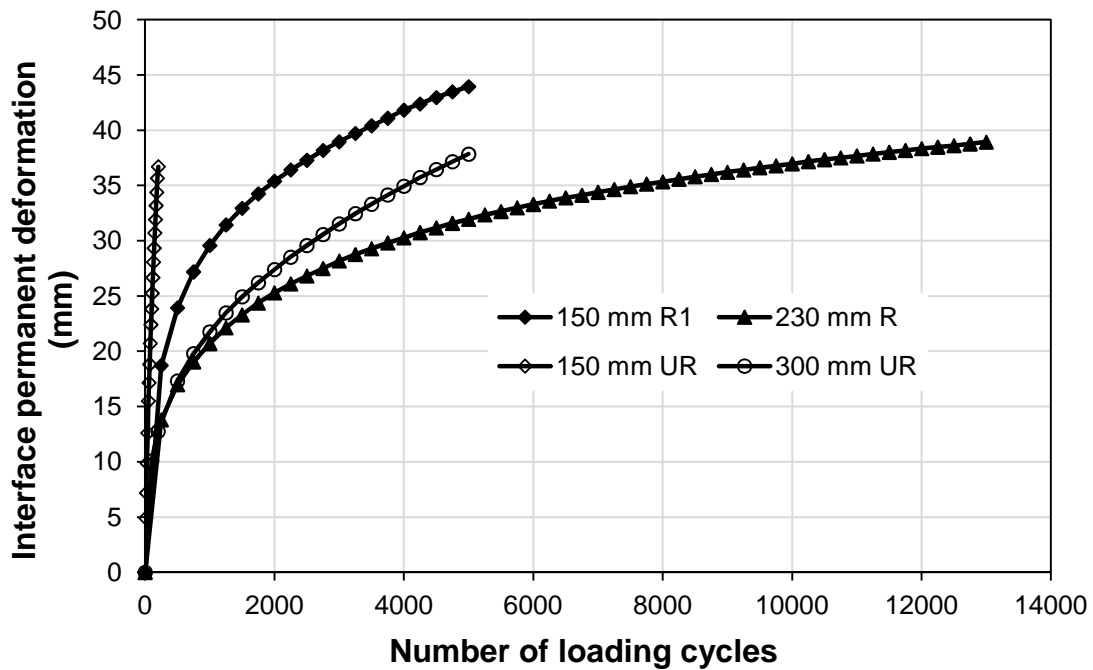
(a) HMA surface-base interface

Fig. 5.4.5   Interface permanent deformation at the center of the loading plate versus the number of loading cycles
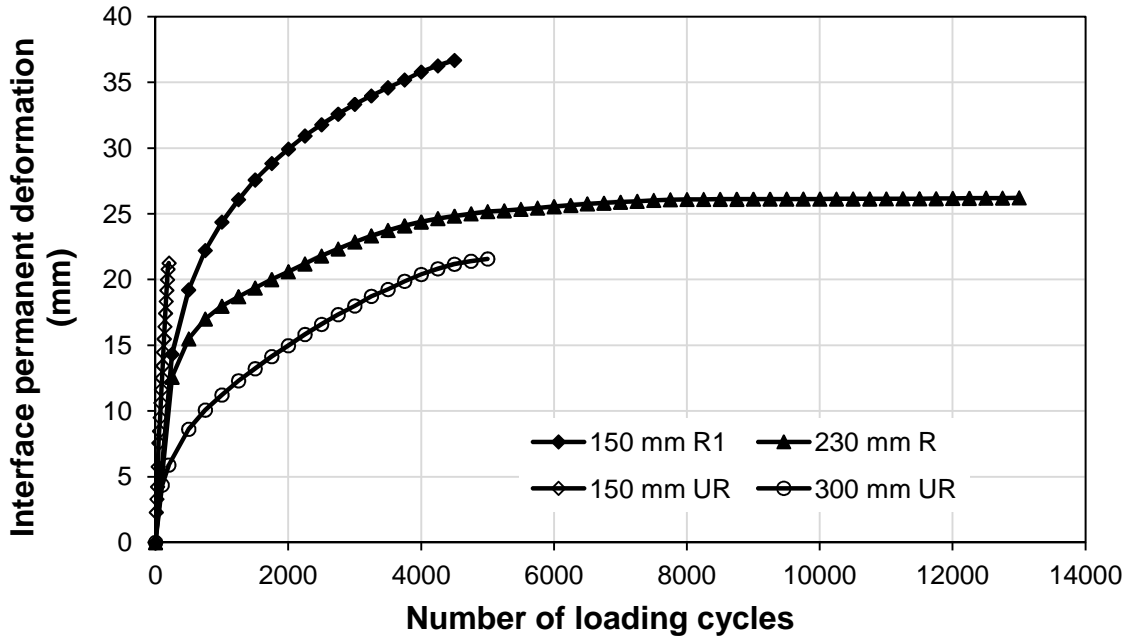
(b) Base-subgrade interface

Fig. 5.4.5 Interface permanent deformation at the center of the loading plate versus the number of loading cycles (continued)

5.4.5 Traffic Improvement Factor (TIF)

The performance of a pavement is determined based on the total surface permanent deformation rather than the interface deformation. The surface permanent deformation of 25 mm is often considered an intolerable deformation in paved roads. Hence the TIF values were calculated up to the surface permanent deformation of 25 mm. The TIF versus surface permanent deformation curves were plotted to demonstrate the influence of four factors (i.e., base thickness, geocell reinforcement, and base and subgrade strengths) in improving the performance of paved roads with RAP bases. To demonstrate the effect of one factor on the TIF, the other three factors were considered the same.

<u>Effect of base thickness</u>

The effect of base thickness is quantified by the traffic improvement factor, TIF_{BT}, which is defined as the ratio of number of loading cycles for the thick section to that of similar thin section at the same permanent deformation. The TIF_{BT} versus surface permanent deformation curves for the 230 mm R, 300 mm R, and 300 mm UR sections are presented in **Fig 5.4.6**. The TIF_{BTs} for 230 mm R and 300 mm R sections were calculated with respect to 150 mm R1 section to demonstrate the benefits of additional 80 and 150 mm thick RAP material. The test results showed that an addition of 80 and 150 mm RAP materials improved the performance of reinforced test sections (230 mm R and 300 mm R) by a factor of 1.2 to 3.1 and 6.0 to 19.2, respectively as compared with 150 mm R1 section. Similarly, an addition of 150 mm RAP material improved the performance of the unreinforced section (300 mm UR) by a factor of 1.3 to 10.2 as compared with 150 mm UR section. The TIF_{BT} increased with increasing surface permanent deformation. All test sections had the largest TIF values at highest permanent deformations and vice versa.

159
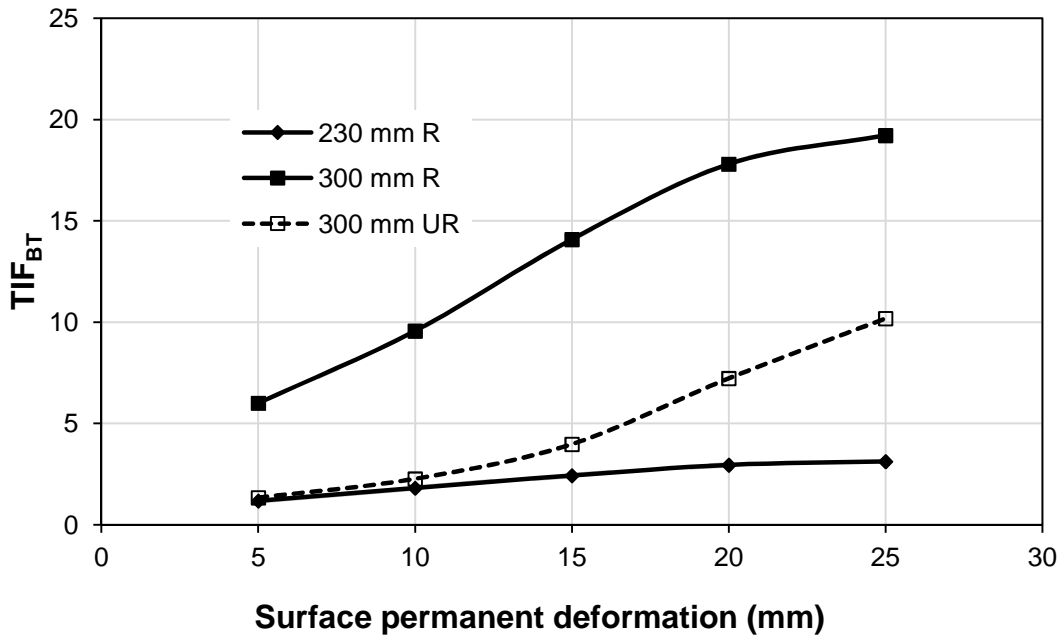
Fig. 5.4.6 Effect of base course thickness on traffic improvement factor (TIF$_{BT}$)

<u>Effect of geocell reinforcement</u>

The effect of geocell reinforcement is quantified by the traffic improvement factor, TIF$_{GR}$, which is defined as the ratio of number of loading cycles for the geocell-reinforced section to that of unreinforced section at the same permanent deformation. The TIF$_{GR}$ versus surface permanent deformation curves for the 150 mm R1 and 300 mm R sections are presented in **Fig. 5.4.7**. The 150 mm R1 and 300 mm R sections consisted of single layer and double layers of 100 mm high geocells, respectively. The TIF$_{GR}$ for reinforced (150 mm R1 and 300 mm R) sections were calculated with respect to the corresponding unreinforced (150 mm UR and 300 mm UR) sections to demonstrate the benefits geocell reinforcement. The test results showed that the geocell-reinforced bases improved the performance of paved road test sections (150 mm R1 and 300 mm R) by a factor of 1.9 to 6.7 and 8.5 to 12.6, respectively, as

compared with the corresponding unreinforced test sections (150 mm UR and 300 mm UR). The reinforced section with double layers of geocell had a higher TIF_{GR} than that with single layer of geocell. The TIF_{GR} increased or remained almost the same with increasing permanent deformation. This was because the geocell was mobilized at larger permanent deformation and improved the performance by the mechanism of the induced beam effect and tensioned membrane effect of geocell-reinforced bases as reported by Thakur et al. (2012).
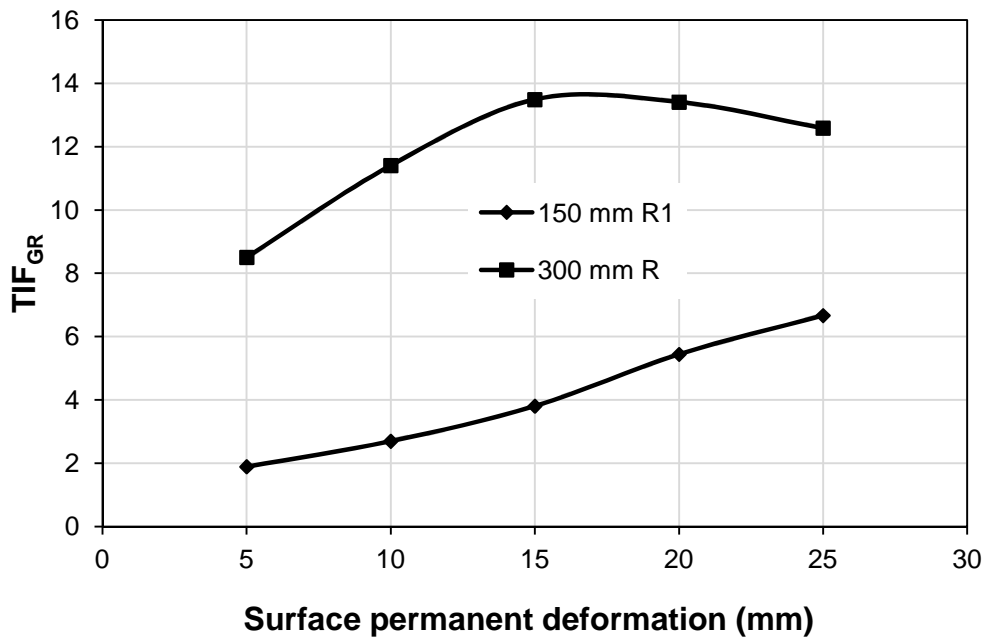
Fig. 5.4.7   Effect of geocell reinforcement on traffic improvement factor (TIF_{GR})

Effect of base course and subgrade strengths

The effect of base course and subgrade strengths is quantified by the traffic improvement factor, TIF_{BC-SG}, which is defined as the ratio of number of loading cycles

for section with strong base and subgrade to that of section with weak base and subgrade at the same permanent deformation. The TIF$_{BC-SG}$ versus surface permanent deformation curve for the 150 mm R2 section is presented in **Fig. 5.4.8**. The TIF$_{BC-SG}$ was calculated with respect to 150 mm R1 section to demonstrate the effect of base course and subgrade strength on the performance of test section. The CBR values of base and subgrade for 150 mm R1 and 150 mm R2 sections were 5.7 and 10.9%, and 9.0 and 13.8%, respectively. The subgrade and base course had higher CBR at lower moisture content. These CBR values were obtained from DCP tests. The TIF$_{BC-SG}$ of 150 mm R2 section ranged from 1.2 to 27.2 with respect to 150 mm R1 section. It can be concluded that the strength of base course and subgrade played a crucial role in the performance of paved roads.
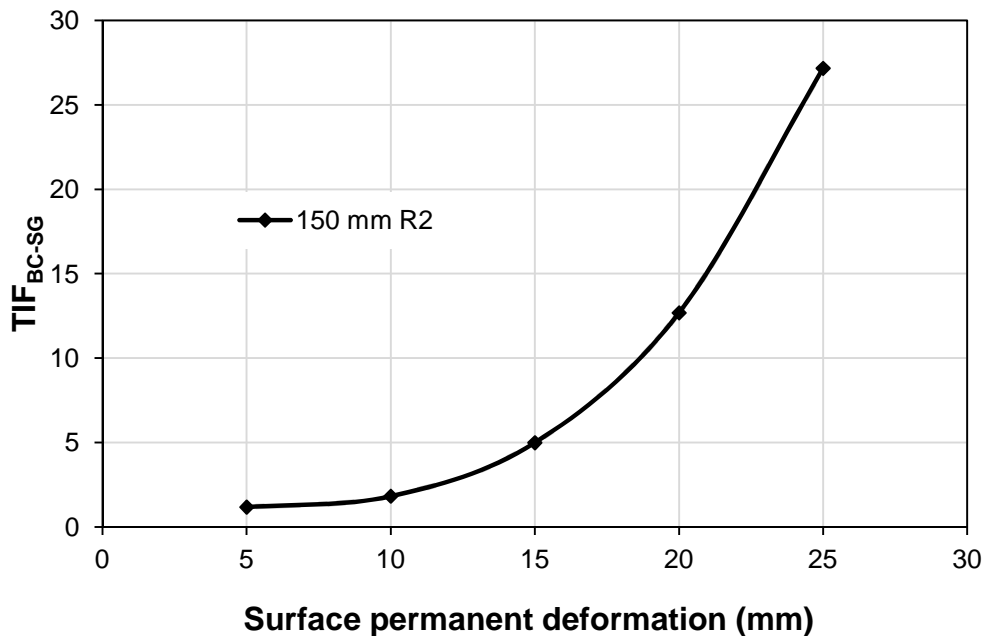
Fig. 5.4.8   Effect of base course and subgrade strength on traffic improvement factor (TIF$_{BC-SG}$)

Overall performance

The effect of geocell reinforcement is quantified by the traffic improvement factor, TIP_{OP}, which is defined as the ratio of number of loading cycles for other sections to that of weakest section (150 mm UR) at the same permanent deformation. The 150 mm UR section had largest surface permanent deformation at particular loading cycles and concluded the weakest section among all six sections. The TIF_{OP} value of each test section was calculated with respect to 150 mm UR section to determine the overall relative performance. The TIF_{OP} versus surface permanent deformation curve is shown in **Fig. 5.4.9** to demonstrate the relative performance of each test section with respect to weakest test section (i.e. 150 mm UR). The overall test result showed that the 300 mm R section performed best followed by 150 mm R2, 230 mm R, 300 mm UR, 150 mm R1, and 150 mm UR upto surface permanent deformation of 25 mm as shown in **Fig. 5.4.9**. At surface permanent deformation of 25 mm, the 150 mm R2 section performed better than 300 mm R section. The degree of improvement as shown in **Fig. 5.4.9** was due to the combined effects of base course thickness, geocell-reinforcement, and base and subgrade strengths. The improvement factors ranged from 1.3 to 181.1.
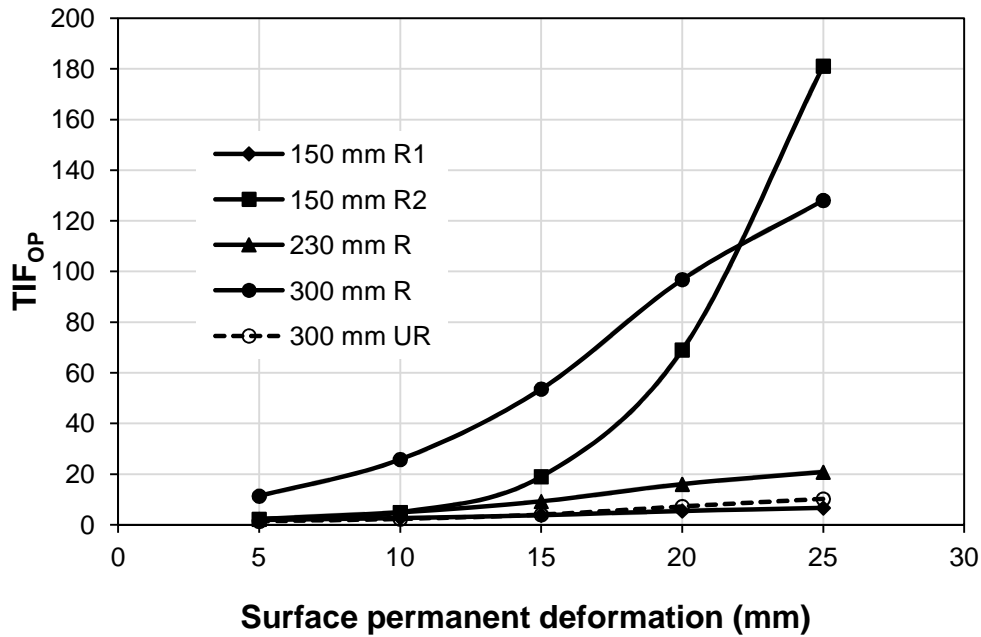
Fig. 5.4.9   Traffic improvement factor (TIF$_{OP}$) with respect to 150 mm UR

section

5.4.6 Surface permanent deformation profile

The surface permanent deformation profiles at the 200th loading cycles as shown in **Fig. 5.4.10** were drawn using the deformation data recorded by five displacement transducers installed at the center of the loading plate, 250, and 500 mm away from center of the loading plate. The surface deformation profiles were assumed symmetric along vertical axis. The 200th loading cycles were chosen for demonstration purpose because the cyclic plate loading test on weakest test section (i.e. 150 mm UR) were stopped after loading cycles of 200. Only a small amount of compression was observed at 250 and 500 mm away from the center for all test sections except 150 mm UR section. The 150 mm UR section had largest compression (i.e., 6.0 mm) at 250 mm away from the center and had a small amount of heave (i.e. 1.2 mm) at 500 mm away

from the center. All unreinforced test sections showed more compression at the center of loading plate than corresponding reinforced sections. The thick sections had less heave and compression than corresponding thin sections. The 150 mm UR section showed largest amount of compression (i.e. 43.4 mm) and heave (i.e. 1.2 mm). The increase in the base and subgrade strength, the geocell-reinforcement, and the base course thickness reduced the amount of surface heave and compression.
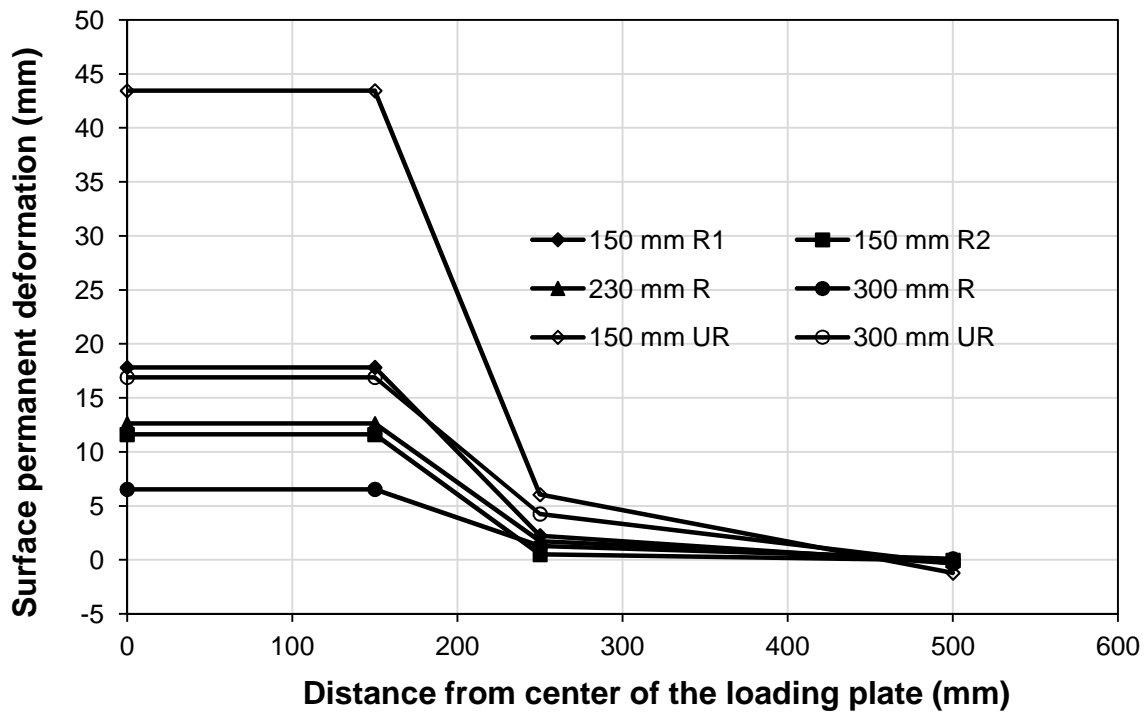
Fig. 5.4.10   Surface permanent deformation profiles at 200th loading cycle

5.4.7 Permanent deformations of pavement layers

Total surface permanent deformation is the sum of permanent deformations of individual layers (HMA surface, base, and subgrade) of pavement. The permanent deformations of individual layers can be calculated from the measured surface permanent

deformations and interface permanent deformations. The permanent deformations of HMA surface layer were calculated by subtracting the permanent deformations measured at the interface of HMA surface and RAP base from the measured surface permanent deformations. Similarly, the permanent deformations of RAP base were calculated by subtracting the permanent deformations measured at the interface of RAP base and subgrade from the permanent deformations measured at the interface of HMA surface and RAP base. The permanent deformations of pavement layers (i.e. HMA surface, RAP base, and subgrade) versus number of loading cycles are shown in **Figs. 5.4.11a**, **b**, and **c**, respectively. As tell-tales were not installed at 150 mm R2 and 300 mm R sections, the permanent deformations of individual layers of these two test sections could not be calculated and are not presented in the **Fig. 5.4.11**.

The HMA layers of unreinforced sections had larger permanent deformations than those of reinforced sections as shown in **Fig. 5.4.11a**. This may be due to more air void contents in HMA layers of unreinforced sections than in reinforced sections. In addition, the HMA layers of unreinforced sections carried larger concentrated stresses than those of reinforced sections because of lower strength of base and subgrade layers of unreinforced sections than those of reinforced sections. The permanent deformation of HMA increased with increasing number of loading cycles for all sections except 150 mm R1 section. The permanent deformation of HMA layer in 150 mm R1 section increased with increasing number of loading cycles up to loading cycles of 500 and then started decreasing which may not be true fundamentally. Therefore, the measured permanent deformation at the interface of base and subgrade might be erroneous after loading cycles of 500.

The permanent deformation of RAP base increased with increasing number of loading cycles and the unreinforced RAP bases had larger permanent deformations than the reinforced bases as shown in **Fig. 5.4.11b**. The larger permanent deformation in the unreinforced base layer was due to the fact that the unreinforced bases had lower stiffness than the geocell-reinforced bases (Thakur et al., 2012b) and the CBR of unreinforced base was slightly lower than that of reinforced bases which might be due to less compaction of unreinforced base than that of reinforced bases.

The permanent deformation of subgrade increased with increasing number of loading cycles and the 150 mm UR section had largest permanent deformation of subgrade followed by 150 mm R1, 230 mm R, and 300 mm UR sections as shown in **Fig. 5.4.11c**. The rate of increase of subgrade deformation was higher for unreinforced sections than that for reinforced section.
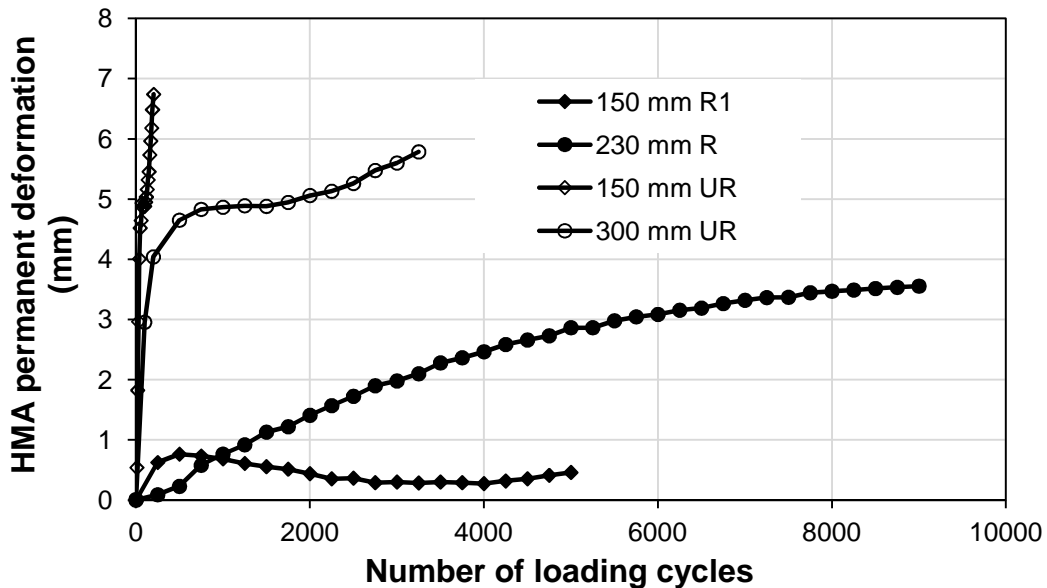
(a) HMA layer

Fig. 5.4.11   Permanent deformations of pavement layers versus the number of loading cycles

167
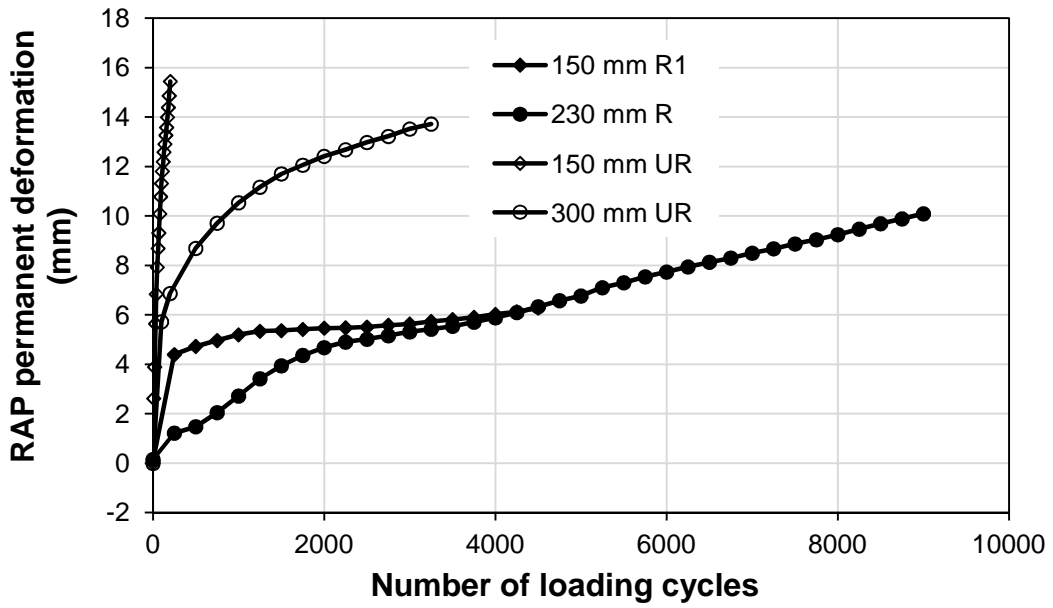
(b) RAP base
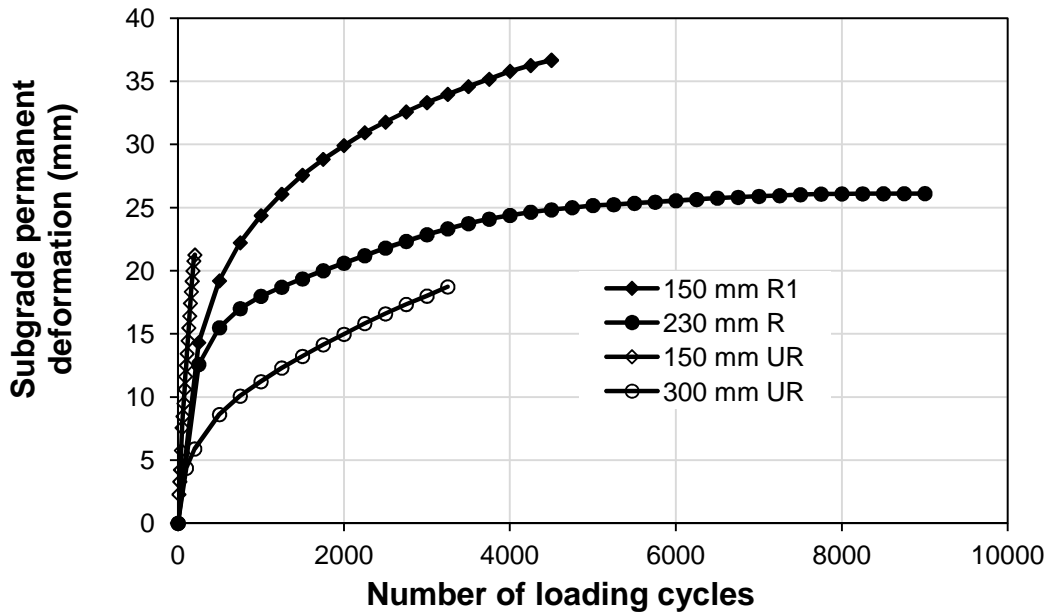
(c) Subgrade

Fig. 5.4.11 Permanent deformations of pavement layers versus the number of loading

cycles (continued)

168

The contributions of permanent deformations of each pavement layer in total surface permanent deformations are demonstrated in **Fig. 5.4.12** and the surface permanent deformation of 25 mm was chosen to demonstrate the contributions. For all test sections, the subgrade deformed most followed by RAP base and HMA layer. The subgrade of reinforced sections deformed more than that of unreinforced sections. In contrast, the RAP base and HMA layer of reinforced sections deformed less than those of unreinforced sections. The percentage contributions of permanent deformations of individual layers in total surface permanent deformations are presented in **Table 5.4.4**. The contributions of subgrade, RAP base and HMA layer in total surface permanent deformations of reinforced sections were about 40, 40, and 20%, respectively. On the other hand, the contributions of subgrade, RAP base and HMA layer in total surface permanent deformations of reinforced sections were about 78, 17 to 19, and 3 to 5%, respectively.
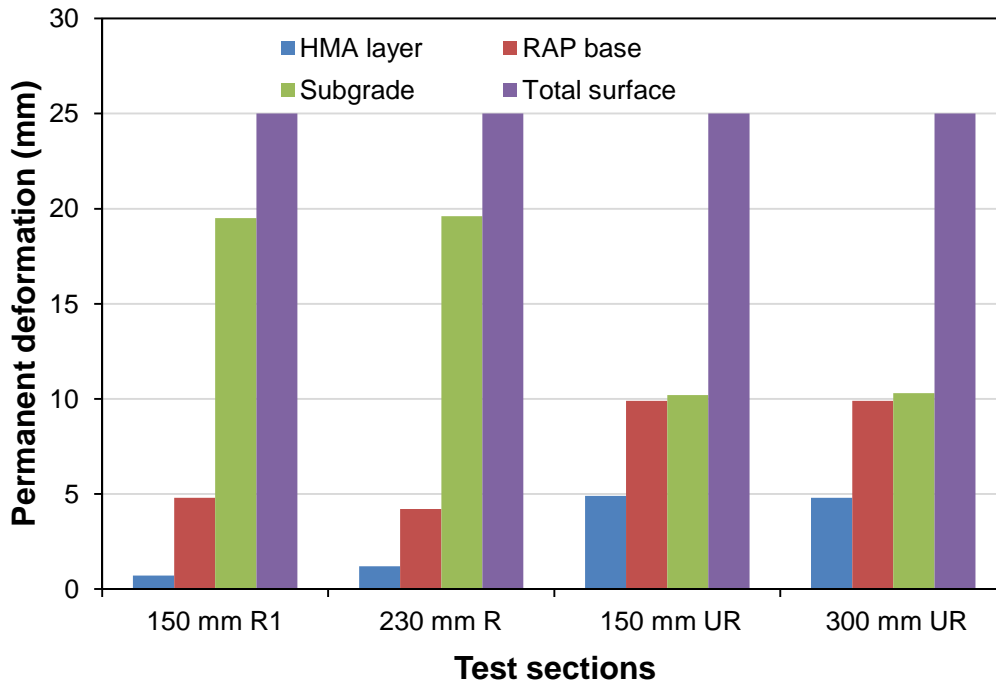
Fig. 5.4.12   Permanent deformation of pavement layers of different test sections at toal

permanent deformation of 25 mm

Table 5.4.4   Contributions of pavement layers in total surface permanent deformation

of test sections

Pavement layers	Contributions in permanent deformation of test sections (%)			
	150 mm R1	230 mm R	150 mm UR	300 mm UR
HMA layer	2.8	4.8	19.6	19.2
RAP base	19.2	16.8	39.6	39.6
Subgrade	78	78.4	40.8	41.2
Total	100	100	100	100

5.4.8 Maximum vertical stress at the interface of base and subgrade

Fig. 5.4.13 shows the measured vertical stresses at the interface of subgrade and base course versus the number of loading cycles at the center. It is shown that the vertical stresses increased rapidly during the initial cycles and slowly at later cycles. The maximum vertical stresses measured at the center and 125 mm away from the center for all test sections at loading cycles of 200 are shown in **Table 5.4.5**. The 200th loading cycles were chosen for demonstration purpose because the cyclic plate loading test on weakest test section (i.e. 150 mm UR) was stopped after loading cycles of 200. The maximum vertical stresses and the rate of increase of vertical stresses at the interface of base and subgrade in unreinforced sections were higher than that of reinforced sections as shown in **Fig. 5.4.13**. The reduction of the vertical stresses in the reinforced sections resulted from the slab effect. The slab effect was observed for the reinforced sections in the measurement of the strains on the geocell walls, which are presented and discussed later. The maximum vertical stress at the center was highest in the 150 mm UR section and lowest in the 300 mm R section at 200th loading cycles as shown in **Table 5.4.5**. Overall, the maximum vertical stress was highest in the 150 mm UR section followed by 300 mm UR, 230 mm R, 150 mm R1, 150 mm R2, and 300 mm R sections. It is no surprise for the 230 mm R section to have higher vertical stresses at the interface than those in the 150 mm R1 and 150 mm R2 sections because the CBR values of subgrade and base of 230 mm R section were lower than those of 150 mm R1 and 150 mm R2 sections. In addition, at the same base thickness, the reinforced sections had much lower vertical stresses than the unreinforced sections. These comparisons demonstrate that the vertical stresses at the interface decreased with an

171

increase of base thickness and geocell reinforcement.
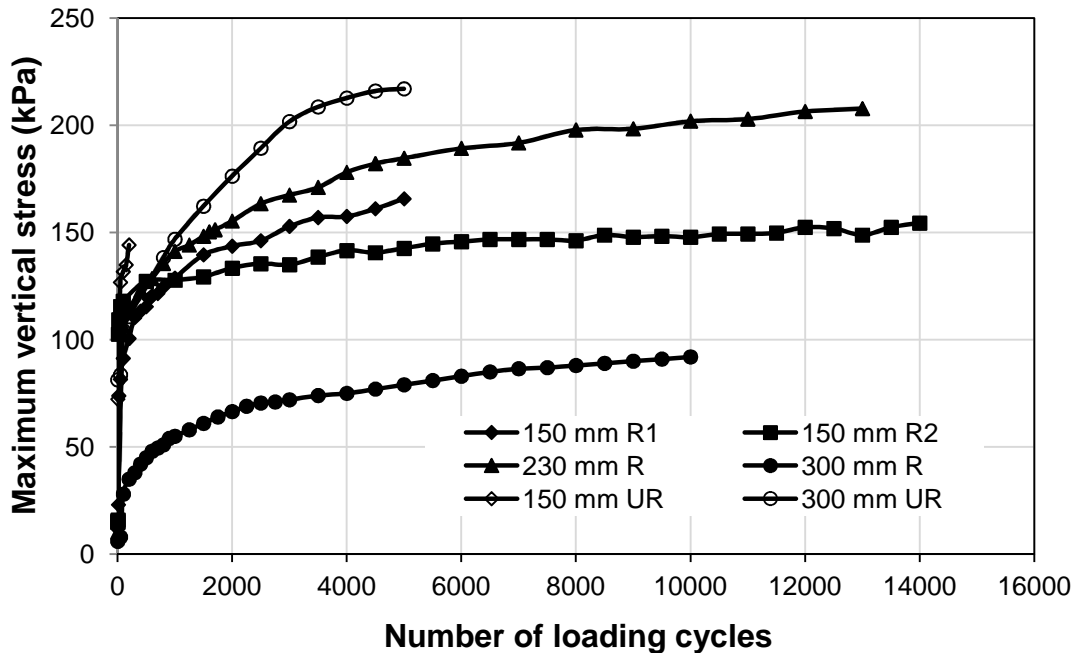
Fig. 5.4.13 Vertical stresses at the interface of subgrade and base at center of the loading plate

The stress distribution angle was calculated using **Eq. 4.4.4**. All symbols used in **Eq. 4.4.4** carry the same meaning as presented in **Chapter 4** except "h", which represents the thickness of HMA layer and base course (i.e. 0.05 m + base thickness in m) in the paved road test sections. The calculated stress distribution angles for all six test sections at each loading cycle are shown in **Fig. 5.4.14**. It is shown that the stress distribution angle decreased rapidly within the first few loading cycles. The reduction in the stress distribution angle was attributed to the deterioration of the base quality (Han et al., 2004a, b; Qian et al., 2011). The stress distribution angle approached a constant

172

value or decreased slowly for the reinforced sections and thick unreinforced section (i.e. 300 mm UR), which demonstrated the stable response behavior. However, for the 150 mm UR section, the stress distribution angle continued to decrease until failure, which demonstrated the unstable response behavior. The minimum stress distribution angles for all test sections are presented in **Table 5.4.5**. It can be concluded that the geocell reinforced and thicker base sections reduced the vertical stress by distributing the load to a wider area.
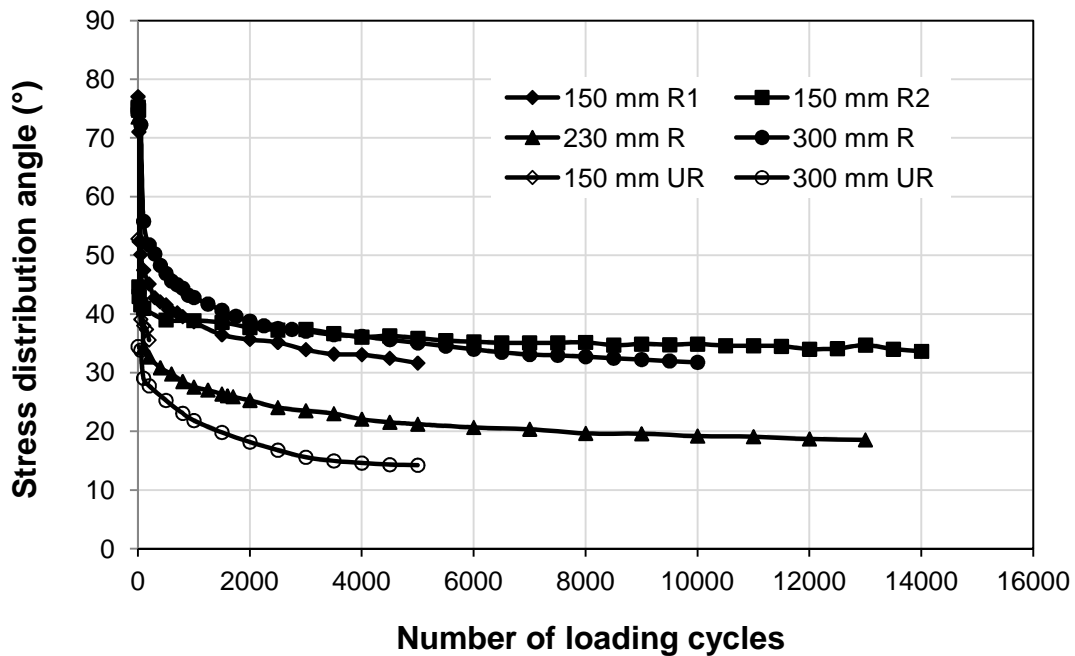
Fig. 5.4.14   Stress distribution angle versus the number of loading cycles

Table 5.4.5 Maximum vertical stress and minimum stress distribution angle for different test sections at 200th loading cycles

Test sections	Maximum vertical stress at the interface (kPa)		Stress distribution angle (degree)
	At center	At 125 mm away from center	
150 mm R1	101	87	45.1
150 mm R2	123	156	39.9
230 mm R	114	53	32.7
300 mm R	35	18	51.8
150 mm UR	144	132	35.5
300 mm UR	111	93	27.7

5.4.9 Vertical stress distribution at the interface

Fig. 5.4.15 presents the vertical stress distributions along the interface of subgrade and base at 200th loading cycles at the center. The loading cycles of 200 was chosen for demonstration purpose because the test for 150 mm UR section was stopped after that number of loading cycles. The vertical stresses for all test sections were highest at the center than those at other locations except for 150 mm R2 section in which vertical stress was higher at 125 mm away from center than that at center. The lowest vertical stresses were observed at the farthest distance from the the center for all test sections. Overall, the vertical stresses at the interface of base and subgrade decreased with increasing distances from center of the loading plate.

174
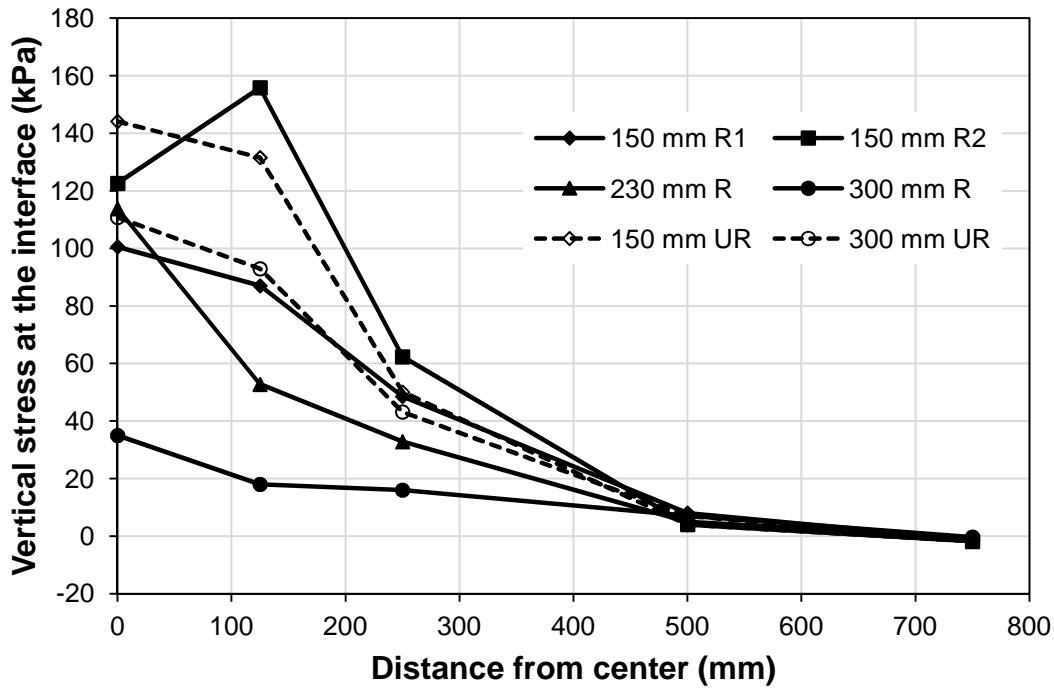
Fig. 5.4.15   Vertical stress distribution at the interface of subgrade and base at

200th loading cycles

5.4.10 Vertical stress versus permanent deformation

Figs. 5.4.16 and **5.4.17** show the measured vertical stresses at the interface of

subgrade and base course versus the total surface permanent deformation and the

measured vertical stresses at the interface of subgrade and base course versus the

subgrade permanent deformation, respectively. The permanent deformation of surface

and subgrade increased with increasing vertical stresses at the interface.
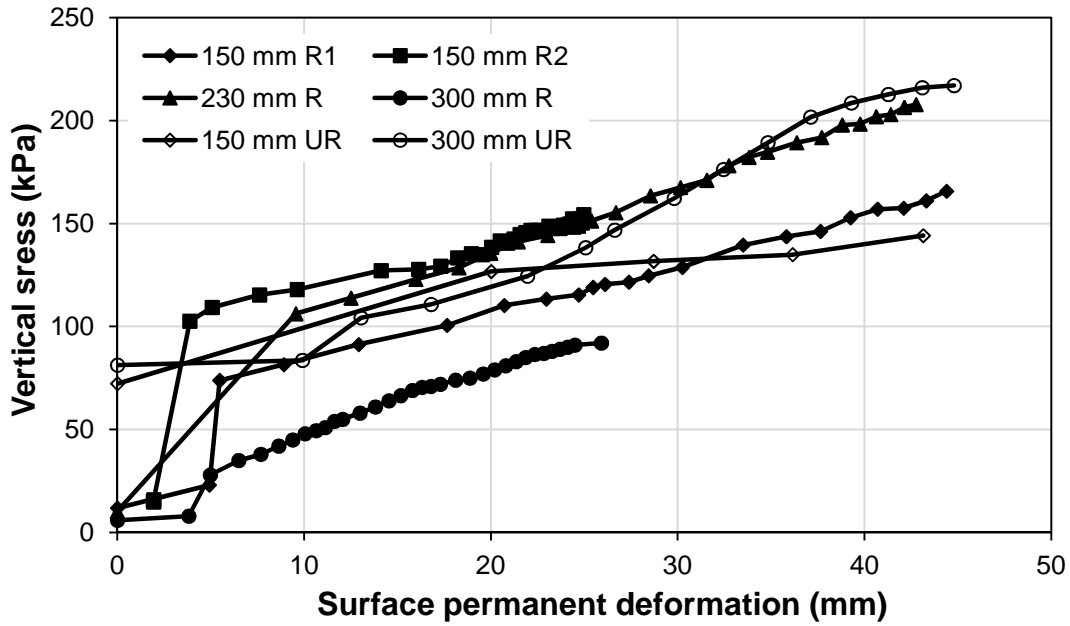
Fig. 5.4.16   Vertical stress at the interface of subgrade and base versus the surface permanent deformation at center
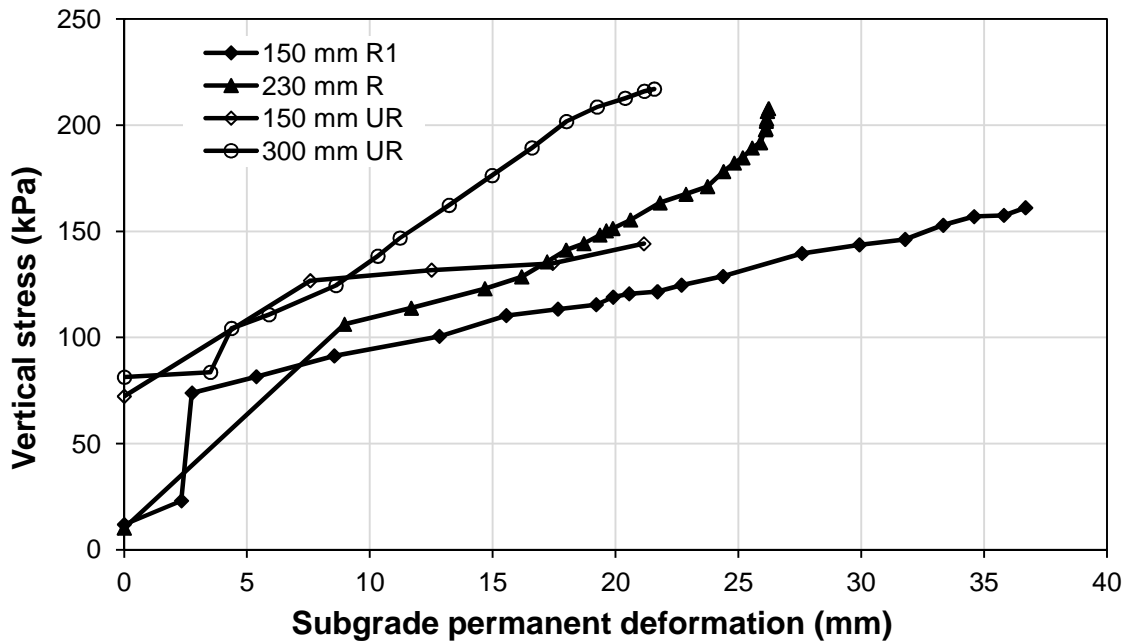
Fig. 5.4.17   Vertical stress at the interface of subgrade and base versus the surface permanent deformation at center

5.4.11 Strain at the geocell wall

The maximum strains induced at central geocell walls versus the number of loading cycles for the 150 mm R1, 150 mm R2, 230 mm R, and 300 mm R sections are shown in **Fig. 5.4.18**. The maximum strains measured by different gages installed at geocell walls of these sections are shown in **Table 5.4.6**. Positive and negative strains refer to tensile and compressive strains, respectively. During the preparation of base courses, G3 and G6 in 150 mm R1; G3 in 150 mm R2; G3 and G9 in 300 mm R sections were damaged; therefore, no strain was measured at these locations.

Overall, the strain gages affixed to the top, middle, and bottom of the geocell wall showed horizontal tensile, vertical compressive, and horizontal tensile strains, repspectively. From these measured strains, it can be concluded that the reinforced sections behaved as a slab with bending resistance and geocell prevented the lateral spreading of base course materials. The middle gage affixed on the geocell pocket at 250 mm away from the center (G5) in the 230 mm section measured small horizontal tensile strain as shown in **Table 5.4.6**. The top gage (G7) at the central geocell of bottom layer and middle gage (G2) at the central geocell of top layer in 300 mm R section showed maximum tensile (0.66%) and compressive (-0.8%) strains, respectively among all gages installed at reinforced sections. The bottom gage showed larger tensile strains as compared with top gages.
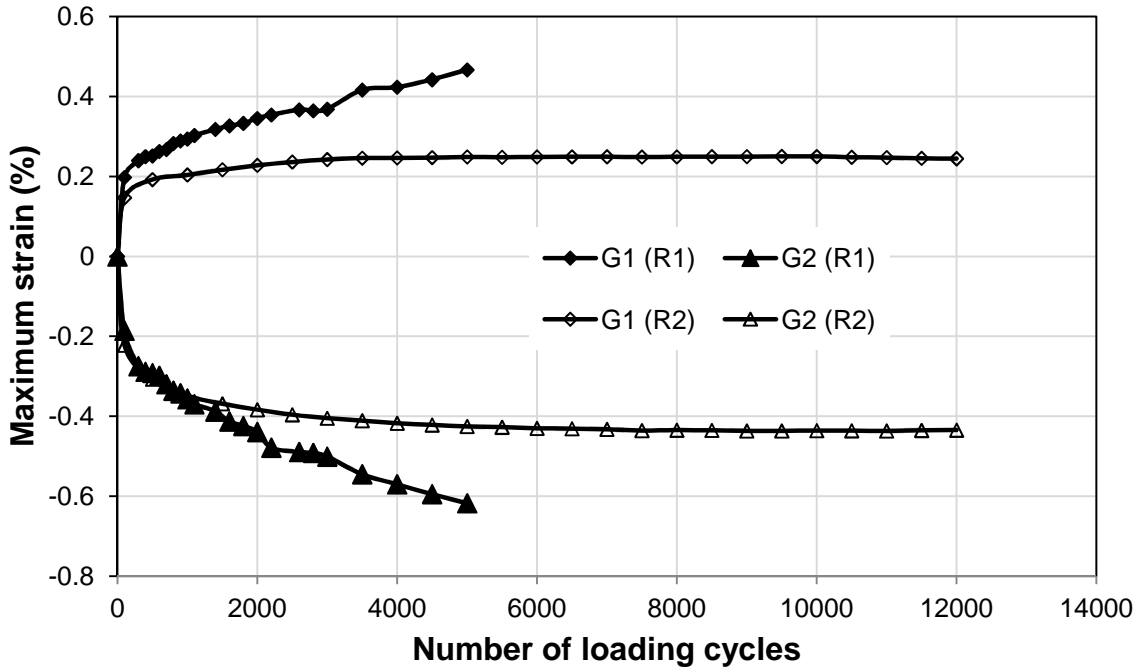
(a) 150 mm thick base
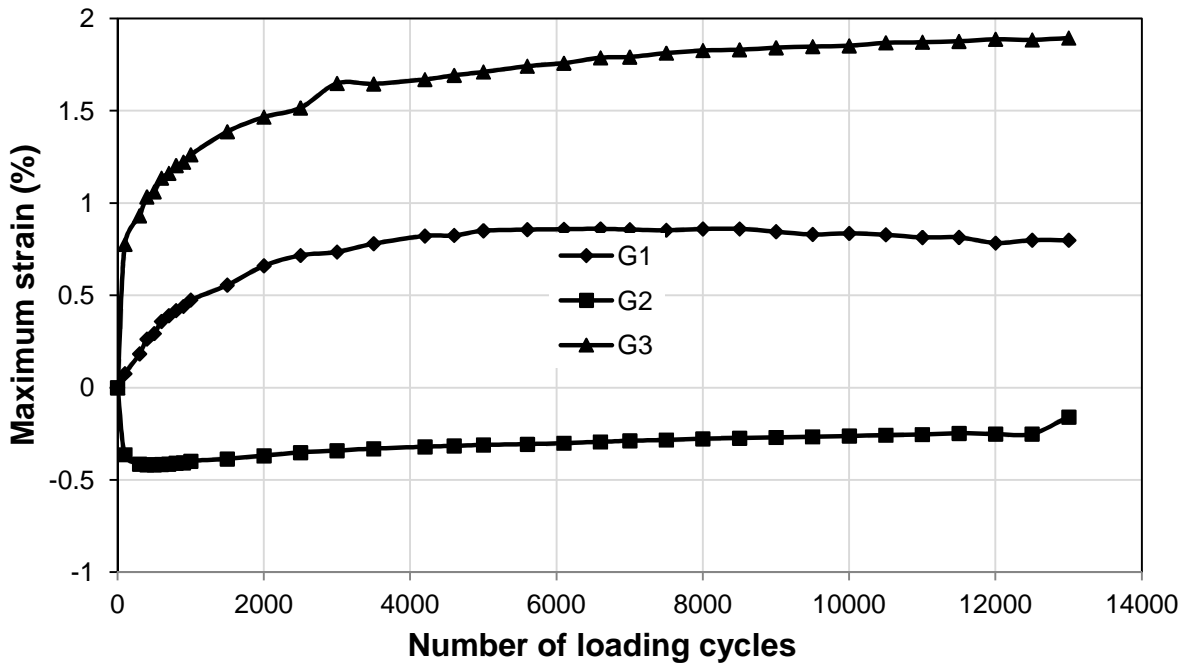
(b) 230 mm thick base

Fig. 5.4.18   Strains at the central geocell wall versus the number of loading

cycles

178
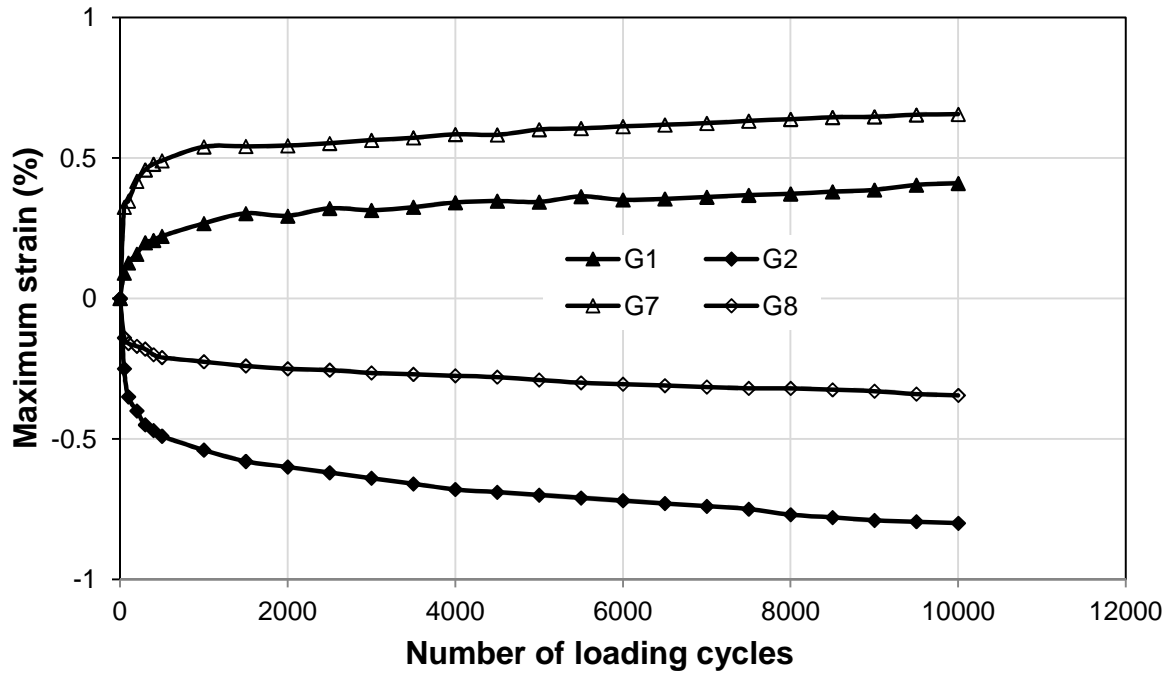
(c) 300 mm thick base

Fig. 5.4.18   Strains at the central geocell wall versus the number of loading cycles

(continued)

Table 5.4.6   Maximum strains at the geocell wall of the reinforced sections

Strain gages	Maximum strains (%) on the geocell walls			
	150 mm R1	150 mm R2	230 mm R	300 mm R
G1	0.47	0.25	0.86	0.41
G2	-0.62	-0.44	-0.42	-0.8
G3	Broken	Broken	1.89	Broken
G4	0.21	0.07	0.27	0.17
G5	-0.17	-0.06	0.13	-0.19
G6	Broken	0.03	0.49	0.07
G7	NA	NA	NA	0.66
G8	NA	NA	NA	0.35
G9	NA	NA	NA	Broken
G10	NA	NA	NA	0.45
G11	NA	NA	NA	-0.26
G12	NA	NA	NA	0.023

5.4.12 Strain distribution at the geocell wall

The variations of strains measured along the centerline of the geocells (i.e. top and middle of geocell walls) at 5000th loading cycles for all reinforced sections are presented in **Figs. 5.4.19 a** and **b**, respectively. Since, the bottom gages were only installed at central geocell of each section, the strain distribution at bottom of geocell walls is not presented. Overall, the highest tensile or compressive strains at the geocell walls were measured directly beneath the center of the loading plate by all gages except few exceptions. In general, the strains measured at the geocell wall decreased as it moved away from the center of the loading plate. The highest strains measured directly

beneath the center of the loading plate indicated that the maximum lateral movement of the base course materials occurred at the center of the loading plate. For 230 mm R section, the tensile strain was highest at central geocell followed by geocell pocket at 500 mm and 250 mm away from the center of the loading plate. The strain gage (G5) installed at the middle of geocell pocket located 250 mm away from center showed very small tensile strain rather than usual compressive strains.
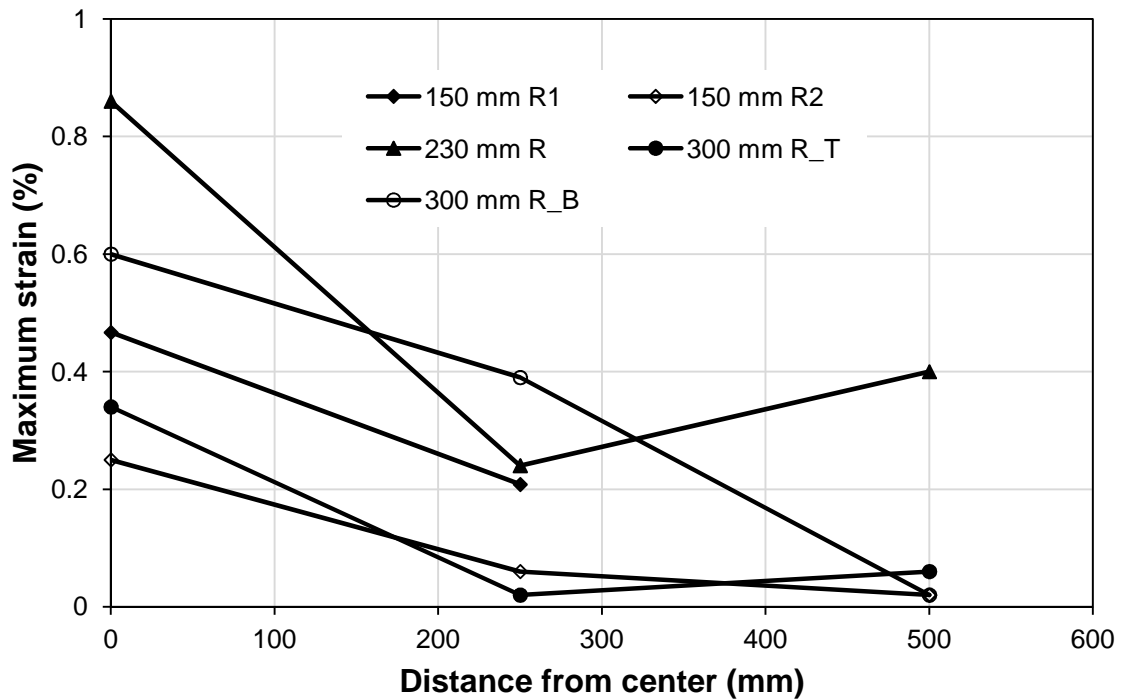
(a) Top gages

Fig. 5.4.19 Geocell strain distribution profile
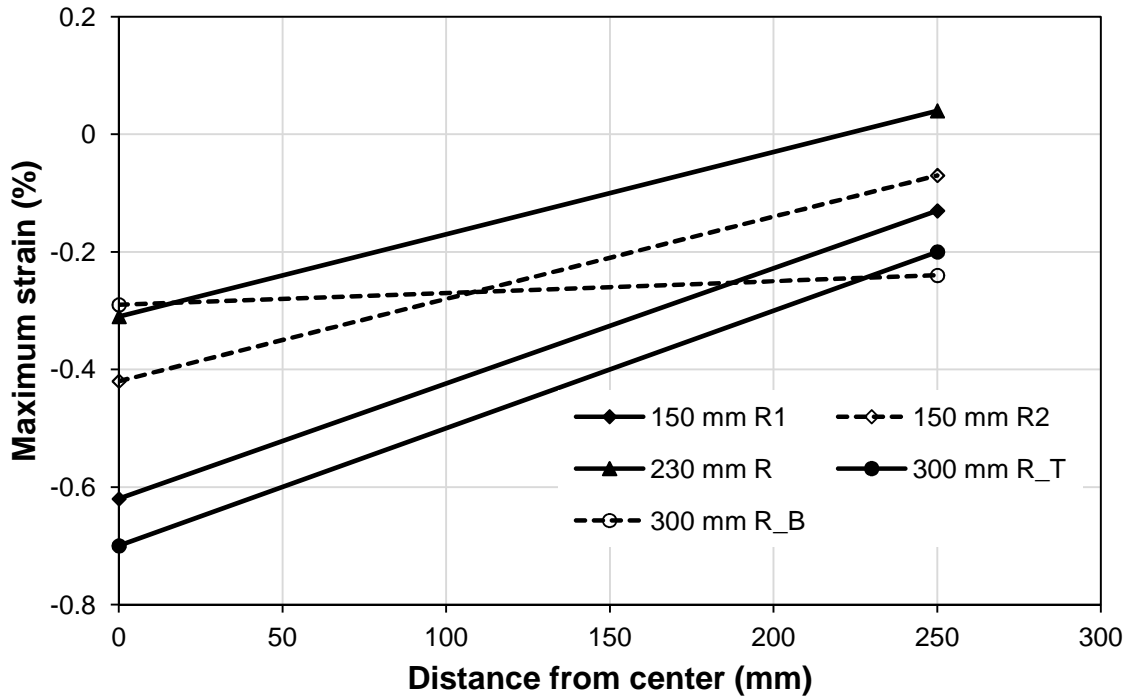
(b) Middle gages

Fig. 5.4.19   Geocell strain distribution profile (continued)

5.5   Summary

This chapter presents an experimental study to evaluate the performance of paved roads with unreinforced or geocell-reinforced recycled asphalt pavement (RAP) bases over weak or moderate subgrades overlaid by thin hot mix asphalt (HMA) surface under cyclic loading. The influence of geocell reinforcement, base course thickness, base course and subgrade strength on performance of flexible pavements was investigated. The following conclusions can be made from this study:

(i) About 30% RAP can be mixed with virgin aggregates and binder to prepare hot mix asphalt concrete and can be used as surface course of flexible pavements.

(ii) 100% RAP with geocell confinement can be used as a base course material in flexible pavements.

(iii) An addition of 80 and 150 mm RAP materials improved the permanent deformation performance of geocell-reinforced flexible pavement test sections by a factor of 1.2 to 19.2 at permanent deformations of 5 to 25 mm. The improvement is larger at higher permanent deformations,

(iv) The geocell-reinforced bases improved the permanent deformation performance of flexible pavement test sections by a factor of 1.9 to 12.6 as compared with corresponding unreinforced test sections at permanent deformations of 5 mm to 25 mm. The improvement is larger at higher permanent deformations.

(v) The increase of subgrade CBR from 5 to 9% and base CBR from 11 to 14% improved the permanent deformation performance of flexible pavement by a factor of 1.2 to 27.2 at permanent deformations of 5 mm to 25 mm. The improvement is larger at higher permanent deformations.

(vi) The geocell-reinforced flexible pavements had lower surface and interface permanent deformations and rate of increase in permanent deformations than the corresponding thick unreinforced sections.

(vii) The increase in the base and subgrade strength, the geocell-reinforcement, and the base course thickness reduced the amount of surface heave and compression.

(viii) The contributions of subgrade, RAP base and HMA layer in total surface permanent deformations of reinforced sections were about 40, 40, and 20%, respectively. On the other hand, the contributions of subgrade, RAP base and

HMA layer in total surface permanent deformations of reinforced sections were about 78, 17 to 19, and 3 to 5%, respectively. The subgrade contributed to most of the total permanent deformation, followed by the RAP base and the HMA surface.

(ix) The resilient deformations at the surface of HMA layer were observed mainly due to the elastic rebound in the HMA layer of sections and there were very little elastic rebound observed in the RAP base and subgrade layers.

(x) All reinforced sections shook down to a steady state showing largely resilient behavior whereas both unreinforced sections did not shake down to a steady state and underwent continuous permanent deformation without showing much resilience. The percentage of resilient deformation increased sharply for the first few loading cycles.

(xi) The vertical stresses increased rapidly during the initial cycles and slowly at later cycles.

(xii) The maximum vertical stresses and the rate of increase of vertical stresses at the interface of base and subgrade in unreinforced sections were higher than that of reinforced sections.

(xiii) The vertical stresses at the interface decreased with an increase of base and subgrade strength, base thickness and geocell reinforcement.

(xiv) The geocell reinforced and thicker base sections reduced the vertical stress at the interface of base and subgrade by distributing the load to a wider area.

(xv) The vertical stresses at the interface of base and subgrade decreased with increasing distances from center of the loading plate.

(xvi) The strain gages affixed to the top, middle, and bottom of the geocell wall showed horizontal tensile, vertical compressive, and horizontal tensile strains, repspectively. The strains measured at the geocell wall decreased as it moved away from the center of the loading plate.

(xvii) The reinforced sections behaved as a slab with bending resistance and geocell prevented the lateral spreading of base course materials.

Chapter 6

Development of Damage Model for permanent deformation

A damage model for rutting is the empirical correlation between the permanent strain with the number of loading cycles and/or resilient strain. Rutting is the sum of the permanent deformations of individual layers of pavement sections:

$Rutting = PD_{surface} + PD_{base} + PD_{subgrade}$

where

$PD_{surface} = \varepsilon_{surface} * h_{surface}$

$PD_{base} = \varepsilon_{base} * h_{base}$

$PD_{subgrade} = p_i\ \pi.\ a.\ (1-v^2)/ (2*E)$

$PD_{surface}$ = permanent deformation of surface layer

$\varepsilon_{surface}$ = vertical compressive strain of surface layer

$h_{surface}$ = thickness of surface layer

PD_{base} = permanent deformation of base course

ε_{base} = vertical compressive strain of base course

h_{base} = thickness of base course

$PD_{subgrade}$ = permanent deformation of subgrade

p_i = vertical stress at the top of subgrade

a = radius of loading area

ν = Poisson's ratio

E = Modulus of elasticity of subgrade.

This chapter presents different empirical permanent deformation models developed for unpaved and paved roads with unreinforced and geocell-reinforced RAP bases. This chapter also presents the calibration of mechanistic-empirical permanent deformation models for unreinforced and geocell-reinforced RAP bases.

6.1   Empirical permanent deformation model

Empirical permanent deformation models which correlate the permanent deformation with the number of loading cycles were developed for unpaved and paved roads and are discussed in the following sections:

6.1.1   Unpaved and paved roads

Power model

Sweere (1990) proposed a power model as expressed in **Eq. 6.1.1** to determine the permanent deformation of a granular material based on repeated load triaxial tests. Based on the experimental results, model parameters of **Eq. 6.1.1** were obtained by correlation to calculate the permanent deformations of unpaved and paved roads with unreinforced and geocell-reinforced RAP bases.

$$PD = A \cdot N^B \qquad\qquad \textbf{(6.1.1)}$$

where

PD = surface permanent deformation in mm

N = number of loading cycles

A, B = model parameters.

The measured and calculated permanent deformations versus the number of loading cycles for unpaved and paved roads are shown in **Figs. 6.1.1** and **6.1.2**, respectively. The power equation presented above fitted well with the test results. The coefficient of correlation varied from 0.98 to 1.0. The solid lines in **Figs. 6.1.1** and **6.1.2** show the calculated permanent deformations of different test sections. The values of model parameters A and B depend on base thickness, base and subgrade strengths, and degree of confinement and are presented in **Tables 6.1.1** and **6.1.2** for unpaved and paved roads, respectively. The values of model parameter A for unpaved roads varied from 6.50 to 20.43. The values of model parameter A for unpaved roads were higher for the unreinforced sections and the sections over weak subgrade as compared with the corresponding reinforced sections and the sections over moderate subgrade, respectively. The values of model parameter A for unreinforced unpaved roads were 1.3 to 2.0 times those of the corresponding reinforced unpaved roads. The values of model parameter B for unpaved roads varied from 0.45 to 0.55 with an average value of 0.49 for the reinforced sections over weak subgrade, from 0.32 to 0.41 with an average value of 0.37 for the reinforced sections over moderate subgrade as shown in **Table 6.1.1.** The model parameter A for paved roads was higher for the unreinforced sections as compared with the corresponding reinforced sections. The values of model parameter B for paved roads with the reinforced bases varied from 0.26 to 0.33 with an average value of 0.29 in **Tables 6.1.2.** The variations of parameter A with base thickness for

different sections of unpaved and paved roads are presented in **Fig. 6.1.3**.
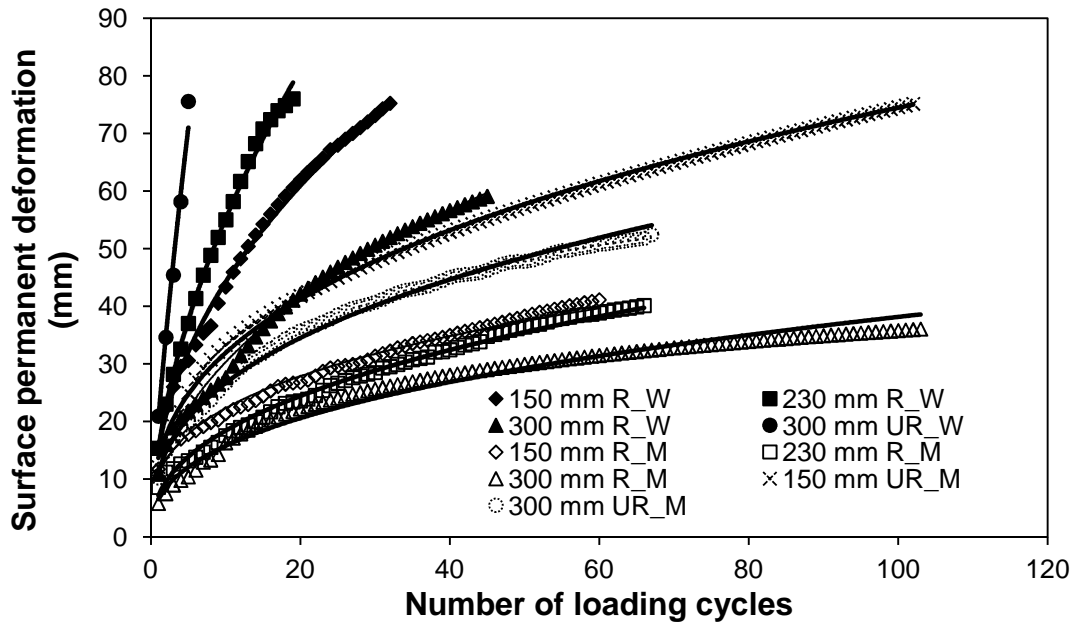
Fig. 6.1.1   Measured and calculated permanent deformations for unpaved road test

sections (Power model)
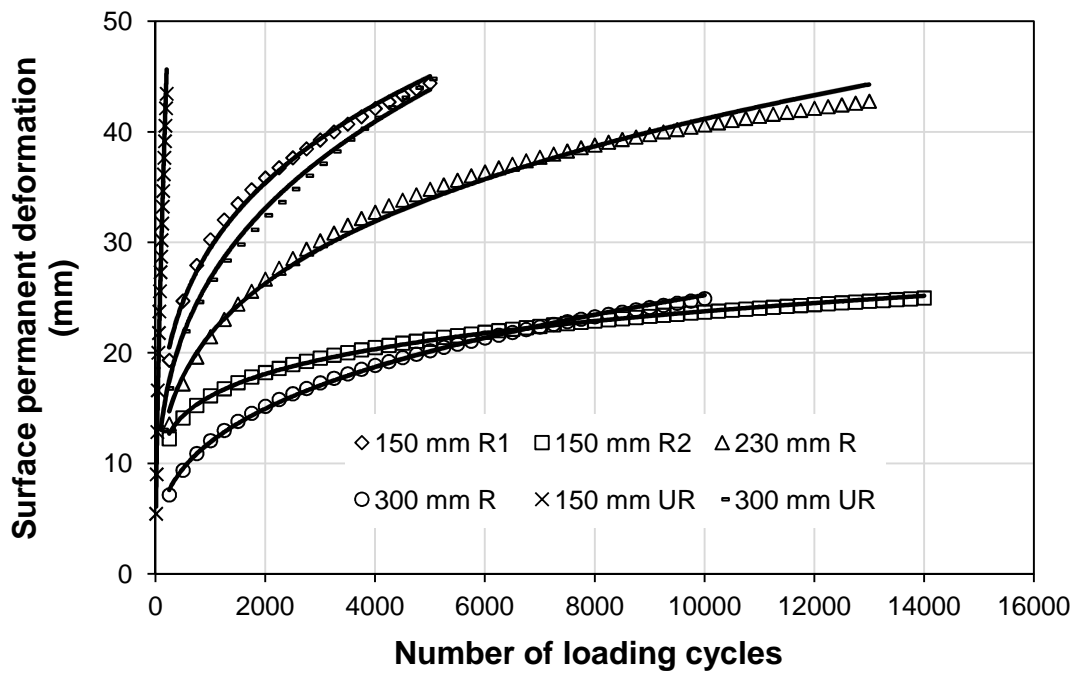
Fig. 6.1.2   Measured and predicted permanent deformations for paved road test

189

sections (Power model)

Table 6.1.1   Values of power model parameters for permanent deformations of
unpaved roads calculated from experimental data

Test sections	Parameters		Coefficient of correlation (R^2)
	A	B	
150 mm R_W	15.25	0.46	0.99
230 mm R_W	15.40	0.55	0.99
300 mm R_W	10.73	0.45	0.99
300 mm UR_W	20.43	0.77	0.99
150 mm R_M	10.64	0.32	0.99
230 mm R_M	7.20	0.41	0.99
300 mm R_M	6.50	0.38	0.98
150 mm UR_M	13.70	0.37	1.00
300 mm UR_M	11.36	0.32	0.99

Table 6.1.2   Values of power model parameters for permanent deformations of paved
roads calculated from experimental data

Test sections	Parameters		R^2
	A	B	
150 mm R1	4.81	0.26	0.99
150 mm R2	4.98	0.17	0.99
230 mm R	3.16	0.28	0.99
300 mm R	1.26	0.33	0.99
150 mm UR	1.31	0.67	0.99
300 mm UR	3.2	0.31	0.99
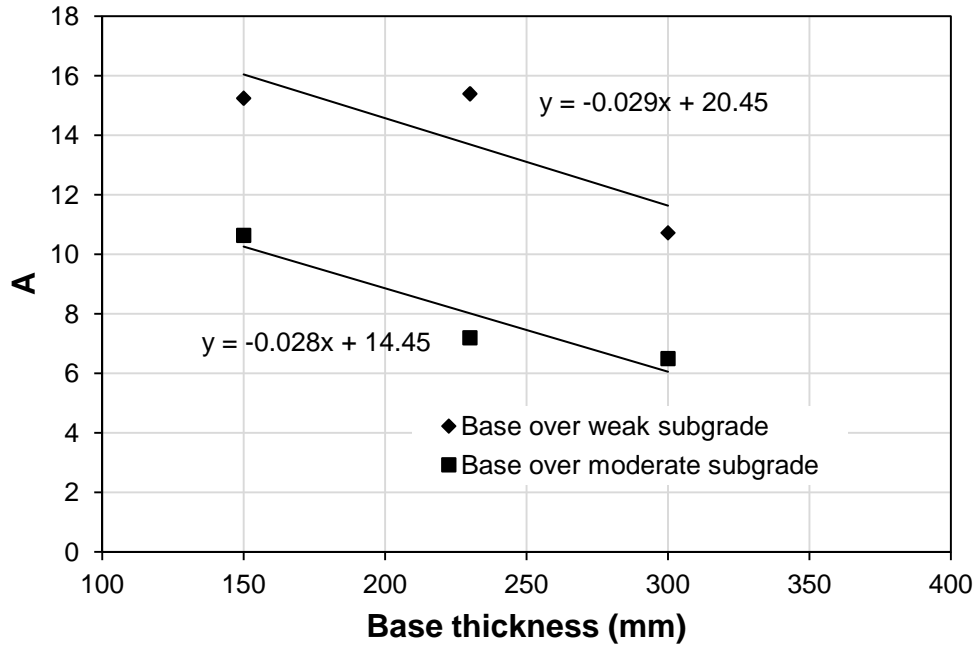
(a) Unpaved roads (reinforced case)
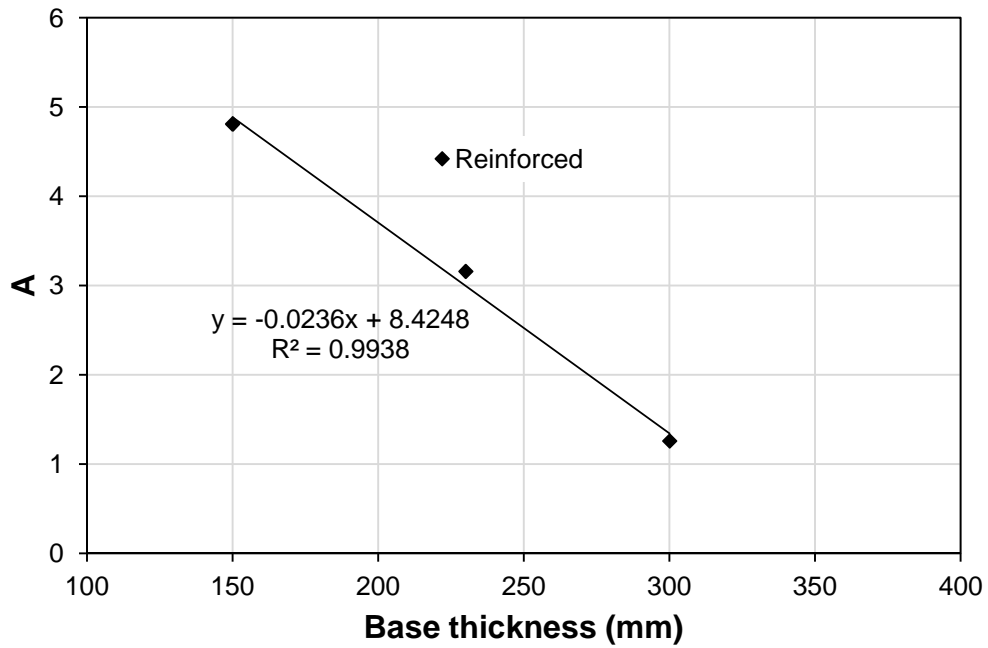
(b) Paved roads (reinforced case)

Fig. 6.1.3 Variation of model parameter A with base thickness

191

Log normal model

Barksdale (1972) proposed a log normal model as expressed in **Eq. 6.1.2** to determine the permanent deformation of a granular material based on repeated load triaxial tests. Based on the experimental results, model parameters of **Eq. 6.1.2** were obtained by correlation to calculate the permanent deformations of unpaved and paved roads with unreinforced and geocell-reinforced RAP bases.

$$PD = A + B \cdot \log N \qquad\qquad \textbf{(6.1.2)}$$

where

PD = surface permanent deformation in mm

N = number of loading cycles

A, B = model parameters.

The measured and calculated permanent deformations versus the number of loading cycles for unpaved and paved roads are shown in **Figs. 6.1.4** and **6.1.5**, respectively. The log normal equation presented above fitted well with the test results. The coefficient of correlation varied from 0.92 to 0.99. The values of model parameters A and B depend on base thickness, base and subgrade strengths, and degree of confinement and are presented in **Tables 6.1.3** and **6.1.4** for unpaved and paved roads, respectively. The values of model parameters A and B for unpaved roads varied from -0.60 to 16.49 and 7.86 to 31.82, respectively, whereas those values for paved roads varied from -33.55 to -6.55 and 7.5 to 30.6, respectively. The solid lines in **Figs. 6.1.4** and **6.1.5** show the calculated permanent deformations of different sections.
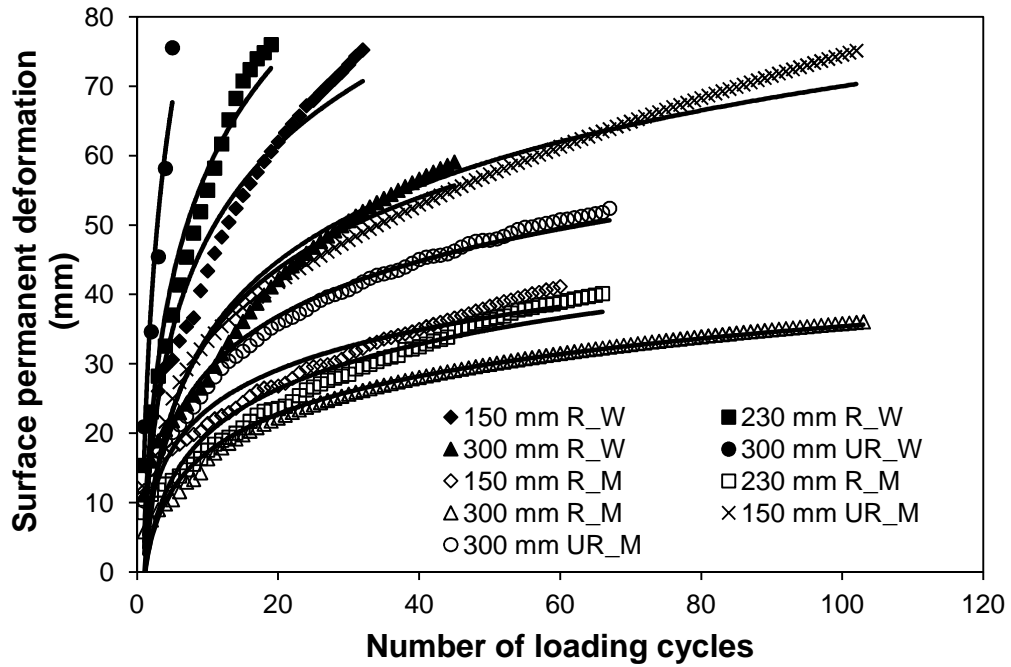
Fig. 6.1.4   Measured and calculated permanent deformations for unpaved road test

sections (Log normal model)

Fig. 6.1.5   Measured and calculated permanent deformations for paved road test

sections (Log normal model)

193
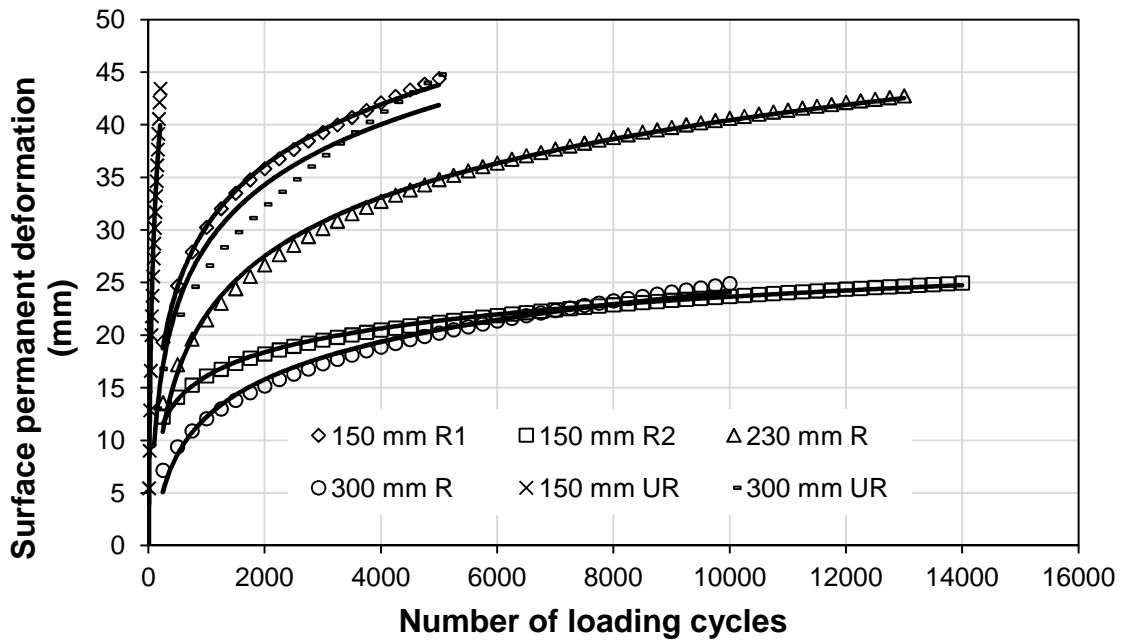
Table 6.1.3 Values of log normal model parameters for permanent deformations of unpaved roads calculated from experimental data

Test sections	Parameters		Coefficient of correlation (R^2)
	A	B	
150 mm R_W	3.51	19.39	0.94
230 mm R_W	5.36	22.84	0.95
300 mm R_W	-0.60	14.79	0.93
300 mm UR_W	16.49	31.82	0.92
150 mm R_M	4.38	8.26	0.93
230 mm R_M	-1.56	9.32	0.92
300 mm R_M	-0.81	7.86	0.98
150 mm UR_M	-2.15	15.67	0.96
300 mm UR_M	2.56	11.45	0.98

Table 6.1.4 Values of log normal model parameters for permanent deformations of paved roads calculated from experimental data

Test sections	Parameters		Coefficient of correlation (R^2)
	A	B	
150 mm R1	-27.38	19.23	0.99
150 mm R2	-6.55	7.54	0.99
230 mm R	-33.55	18.47	0.99
300 mm R	-23.38	11.85	0.98
150 mm UR	-30.90	30.65	0.96
300 mm UR	-28.36	19.04	0.95

6.1.2 Different layers of paved roads

The permanent deformations of individual layers as presented in **Chapter 5** (i.e. HMA surface, RAP base, and subgrade) were obtained from measured surface and interface deformations. As the interface deformations were not measured for the 150 mm R2 and 300 mm R sections, the permanent deformations of individual layers of these two test sections could not be obtained. The interface deformation measured for the 150 mm R1 section is not correct as discussed in Chapter 5. The permanent deformations of individual layers for the 150 mm R2, 230 mm R, and 150 mm UR sections were used to obtain the parameters for the power and log normal models to calculate permanent deformations.

Power model

The measured and calculated permanent deformations versus the number of loading cycles for the HMA surface, the RAP base, and the subgrade are shown in **Figs. 6.1.6, 6.1.7,** and **6.1.8**, respectively. The power equation presented earlier in **Eq. 6.1.1** fitted better for the base and the subgrade than for the HMA surface. The coefficient of correlation varied from 0.80 to 0.94, 0.98 to 0.99, and 0.97 to 0.99 for the HMA surface, the RAP base, and the subgrade, respectively. The values of the model parameters A and B depend on the compactness of pavement layers, the base thickness, the base and subgrade strengths, and the degree of confinement and are presented in **Tables 6.1.5, 6.1.6,** and **6.1.7** for the HMA surface, the RAP base, and the subgrade, respectively.
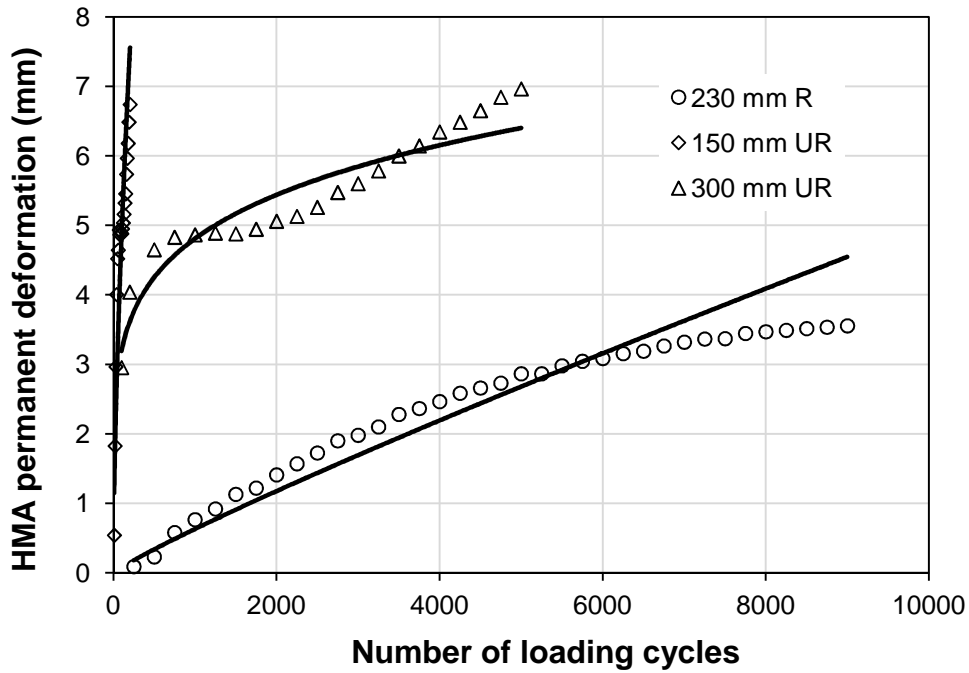
Fig. 6.1.5   Measured and calculated permanent deformations for the HMA layer of

paved roads (Power model)
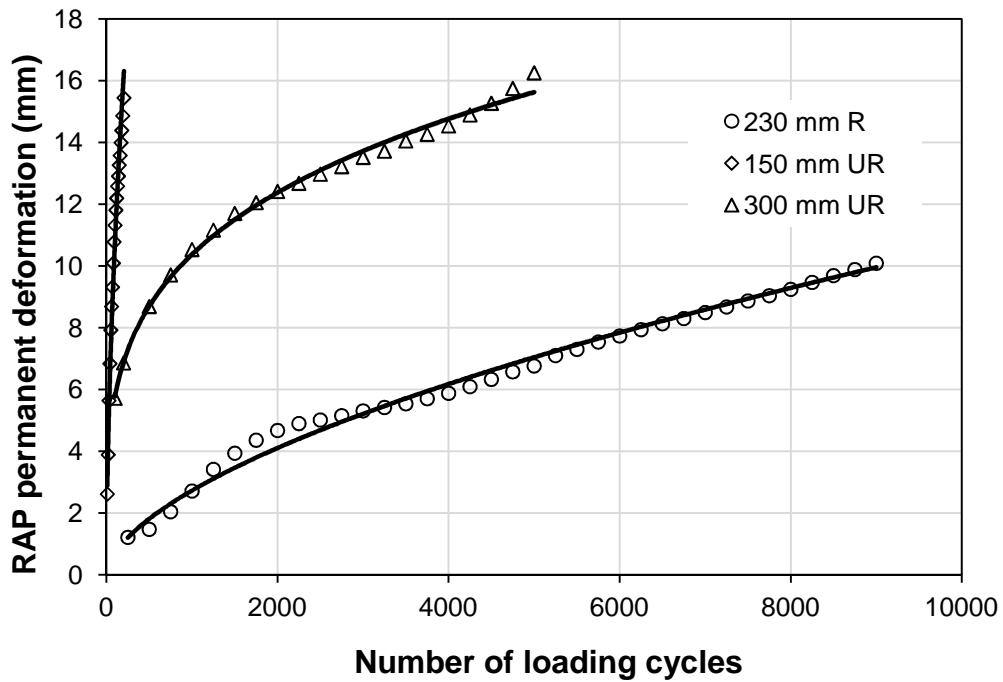
Fig. 6.1.6   Measured and calculated permanent deformations for the RAP base layer

of paved roads (Power model)

196
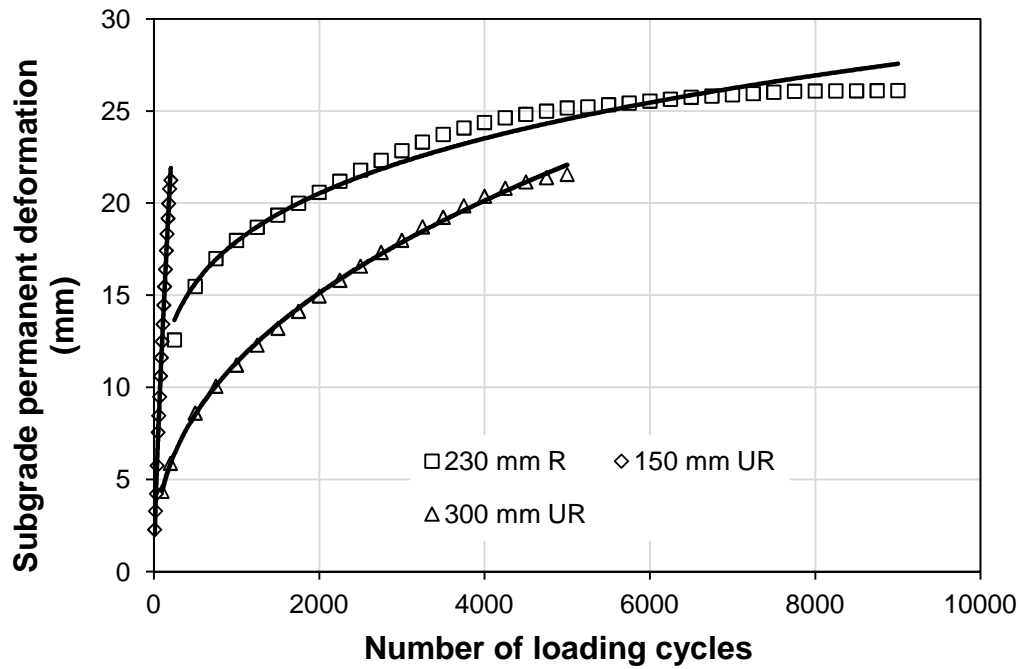
Fig. 6.1.7　　　Measured and calculated permanent deformations for the subgrade layer

of paved roads (Power model)

Table 6.1.5　Values of power model parameters for permanent deformations of the

HMA layer of paved roads

Test sections	Parameters		Coefficient of correlation (R^2)
	A	B	
230 mm R	0.0013	0.90	0.94
150 mm UR	0.27	0.63	0.80
300 mm UR	1.41	0.18	0.90

Table 6.1.6   Values of power model parameters for permanent deformations of the RAP base layer of paved roads

Test sections	Parameters		Coefficient of correlation (R^2)
	A	B	
230 mm R	0.046	0.59	0.98
150 mm UR	0.77	0.57	0.98
300 mm UR	1.78	0.25	0.99

Table 6.1.7   Values of power model parameters for permanent deformations of the subgrade layer of paved roads

Test sections	Parameters		Coefficient of correlation (R^2)
	A	B	
150 mm R1	2.76	0.31	0.99
230 mm R	4.63	0.20	0.97
150 mm UR	0.33	0.79	0.99
300 mm UR	0.65	0.41	0.99

Log normal model

The measured and calculated permanent deformations versus the number of loading cycles for the HMA surface, the RAP base, and the subgrade are shown in **Figs. 6.1.9, 6.1.10,** and **6.1.11**, respectively. The log normal equation presented earlier in **Eq. 6.1.2** was used to calculate the permanent deformation of each layer. The coefficient of correlation varied from 0.86 to 0.94, 0.64 to 0.98, and 0.91 to 0.95 for the HMA surface, the RAP base, and the subgrade, respectively. The values of model parameters A and B depend on the compactness of pavement layers, the base thickness, the base and

subgrade strengths, and the degree of confinement and are presented in **Tables 6.1.8,**

6.1.9, and **6.1.10** for the HMA surface, the RAP base, and the subgrade, respectively.
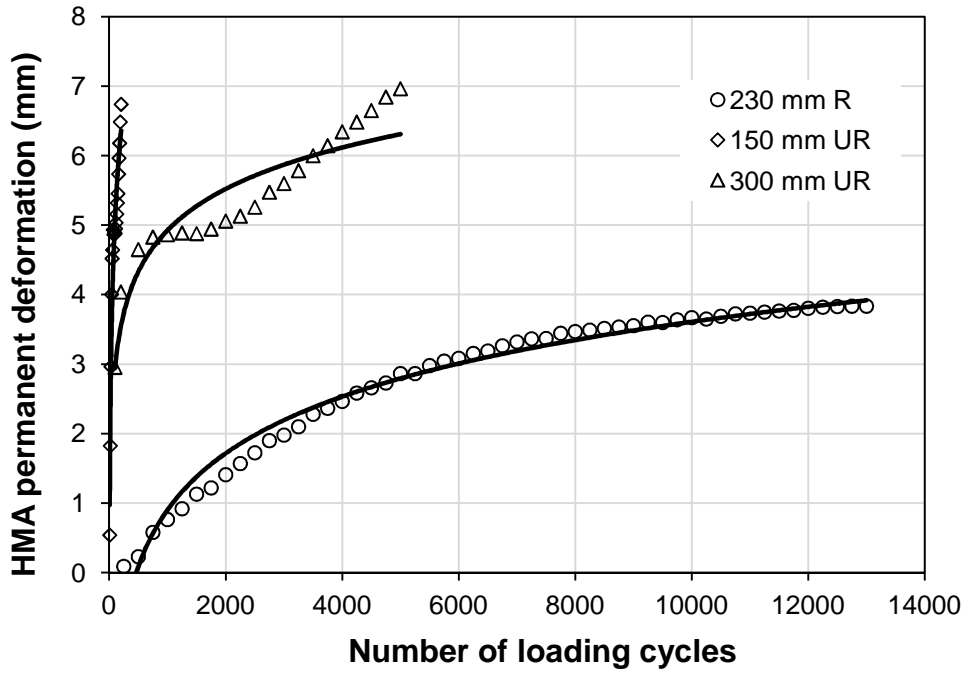
Fig. 6.1.9   Measured and calculated permanent deformations for the HMA layer of

paved roads (Log normal model)
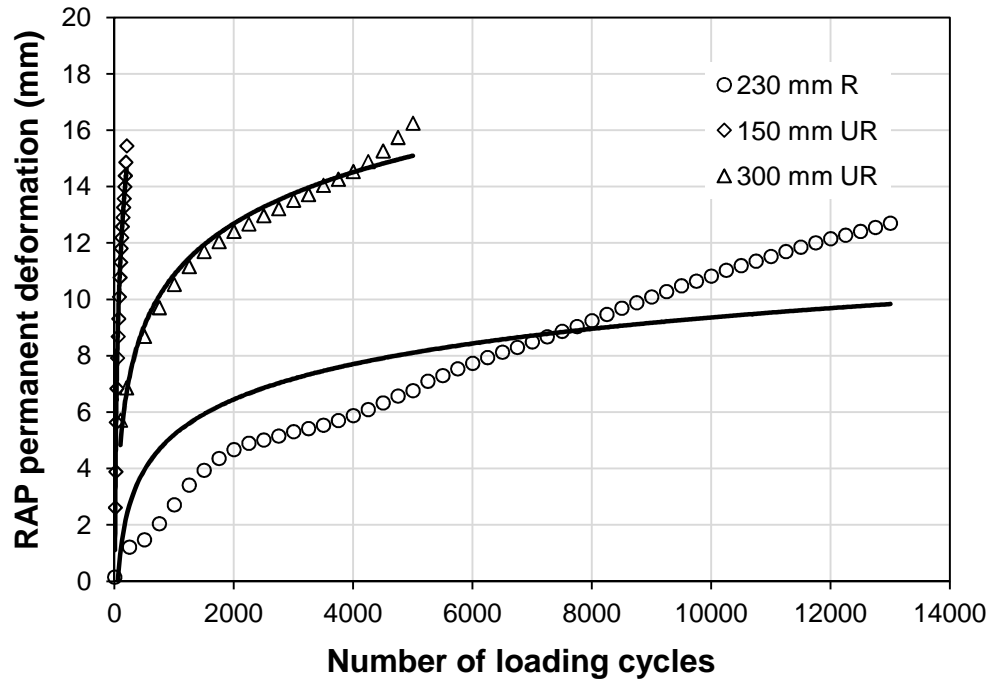
Fig. 6.1.10   Measured and calculated permanent deformations for the RAP base layer

of paved roads (Log normal model)
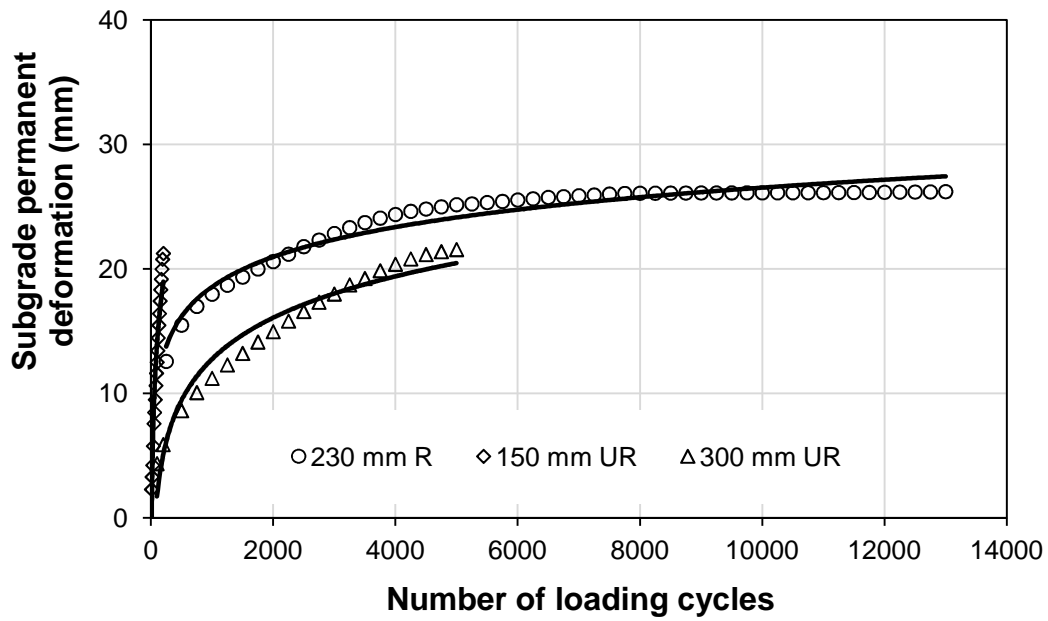
Fig. 6.1.11   Measured and calculated permanent deformations for the subgrade layer

of paved roads (Log normal model)

200

Table 6.1.8 Values of log normal model parameters for permanent deformations of the HMA layer of paved roads

Type of sections	Parameters		R^2
	A	B	
230 mm R	-7.22	2.691	0.97
150 mm UR	-3.15	4.111	0.94
300 mm UR	-1.02	1.978	0.86

Table 6.1.9 Values of log normal model parameters for permanent deformations of the RAP base layer of paved roads

Test sections	Parameters		R^2
	A	B	
230 mm R	-7.29	4.156	0.64
150 mm UR	-9.21	10.309	0.98
300 mm UR	-7.25	6.026	0.97

Table 6.1.10 Values of log normal model parameters for permanent deformations of the subgrade layer of paved roads

Test sections	Parameters		
	A	B	R^2
230 mm R	-5.35	7.963	0.95
150 mm UR	-18.55	16.215	0.91
300 mm UR	-20.36	11.017	0.95

6.2 Mechanistic empirical permanent deformation model
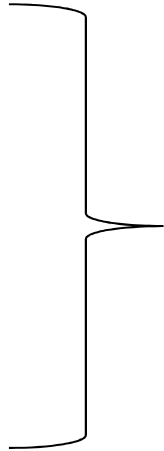
6.2.1 Existing mechanistic empirical permanent deformation model

The permanent deformation model for granular base materials used in the current mechanical-empirical pavement design guide (MEPDG) was modified from the mechanistic-empirical model developed by Tseng and Lytton (1989). Tseng and Lytton (1989) developed the mechanistic-empirical permanent deformation model as shown in **Eq. 6.2.1** for different materials of flexible pavement layers, which correlates permanent strain with resilient strain and number of loading cycles. The model was developed based on repeated load triaxial tests for a large number of loading cycles at which the material response became stable.

$$\frac{\varepsilon_p}{\varepsilon_v} = \left(\frac{\varepsilon_0}{\varepsilon_r}\right) \cdot e^{-\left(\frac{\rho}{N}\right)^\beta}$$

$$\varepsilon_p = \varepsilon_v \cdot \left(\frac{\varepsilon_0}{\varepsilon_r}\right) \cdot e^{-\left(\frac{\rho}{N}\right)^\beta} \qquad (6.2.1)$$

$$PD = h_{soil} \cdot \varepsilon_v \cdot \left(\frac{\varepsilon_0}{\varepsilon_r}\right) \cdot e^{-\left(\frac{\rho}{N}\right)^\beta}$$

where

ε_p = accumulated permanent strain in a layer

ε_v = average vertical resilient strain in a layer

$\left(\dfrac{\varepsilon_0}{\varepsilon_r}\right)$, ρ, β = material constants obtained from permanent deformation test

PD = accumulated permanent deformation in a layer

h_{soil} = thickness of a layer.

The Tseng and Lytton (1989) reported that the parameters $\left(\dfrac{\varepsilon_0}{\varepsilon_r}\right)$, ρ, β were affected by the stress state, density, moisture content, temperature, and environmental characteristics. They developed the following relations to calculate these model parameters for granular materials:

$$\text{Log}\left(\dfrac{\varepsilon_0}{\varepsilon_r}\right) = 0.80978 - 0.06626W_c + 0.003077\sigma_\theta + 0.000003E_r$$

$$\text{Log } \beta = -0.9190 + 0.03105W_c + 0.001806\sigma_\theta - 0.0000015E_r$$

$$\text{Log } \rho = -1.78667 + 1.45062W_c - 0.0003784\sigma_\theta^2 - 0.002074Wc2\sigma_\theta - 0.0000105E_r$$

where

W_c = water content of material

σ_θ = applied bulk stress

E_r = resilient modulus of material.

The Tseng and Lytton model was calibrated using permanent deformation data collected from the Long Term Pavement Performance (LTPP) program in the National Cooperative Highway Research Program (NCHRP) project 1-37a and the calibrated

model for granular base materials as shown in **Eq. 6.2.2** was used in the current MEPDG. It should be seen from **Eq. 6.2.2** that the water content is the only parameter needed in the MEPDG model.

$$PD = K_{S1} \cdot \beta_{S1} \cdot h_{Soil} \cdot \varepsilon_v \cdot \left(\frac{\varepsilon_0}{\varepsilon_r}\right) \cdot e^{-\left(\frac{\rho}{N}\right)^{\beta}}$$

$$Log\beta = -0.61119 - 0.017638 W_c$$

$$\rho = 10^9 \left(\frac{-4.89285}{1-(10^9)^{\beta}}\right)^{\frac{1}{\beta}}$$

$$\left(\frac{\varepsilon_0}{\varepsilon_r}\right) = \frac{0.15 \cdot e^{(\rho)^{\beta}} + 20 \cdot e^{\left(\frac{\rho}{10^9}\right)^{\beta}}}{2}$$

(6.2.2)

where

PD = accumulated permanent deformation in a layer

K_{s1} = global calibration coefficient which is 1.673 for a granular material or 1.35 for a fine-grained material

β_{s1} = local calibration coefficient which is assigned 1.0 as a default value

h_{soil} = thickness of a layer

ε_v = average vertical resilient strain in a layer

$\left(\frac{\varepsilon_0}{\varepsilon_r}\right)$, ρ, β = material constants which depend on the water content of a layer

N = number of axle load applications

W_c = water content in a layer.

204

6.2.2 Calibration of mechanistic empirical permanent deformation model

In this study, the Tseng and Lytton model and the model used in MEPDG were calibrated using the permanent deformation data obtained from cyclic plate loading tests for unreinforced and geocell-reinforced RAP bases. The 150 mm UR section failed without showing a stable response and the interface deformation measured for the 150 mm R1 section was erroneous due to the error in tell-tale measurement. Thus, the permanent deformation data collected for the 230 mm R and 300 mm UR sections were used to calibrate these models for the unreinforced and geocell-reinforced RAP bases and were not validated because of limited test data.

The vertical stresses at the mid depth of unreinforced and geocell-reinforced RAP base courses were obtained from the response model. The response model was created using the KENLAYER software (Huang, 1993), which works on the principle of the layered theory. The average vertical resilient strain (ε_v) was calculated by dividing the vertical stress at the mid depth of the base layer by the resilient modulus of the base material. The applied load, the material properties, and the thicknesses of the pavement layers were the inputs for the KENLAYER analysis which were keyed in the KENLAYER using menu "LAYERINP". The applied load was assigned as a single axle with a single tire of contact radius of 150 mm and contact pressure of 550 kPa. The types of materials used in the pavement layers were considered linearly elastic to make the analysis easier. The resilient modulus of the asphalt concrete was assumed 2,000,000 kPa (a typical value). The resilient modulus of the unreinforced RAP was determined to be 138,000 kPa using static plate loading tests. The resilient modulus of the geocell-reinforced RAP was 1.6 times that of the resilient modulus of the

205

unreinforced RAP (Thakur et al., 2012b). Hence the resilient modulus of the geocell-reinforced RAP was assigned to be 1.6* 138,000 kPa = 220,800 kPa. The resilient modulus (M_R) of the subgrade was determined from its CBR using the correlation M_R (psi) = 1500 *CBR. The CBR of the subgrade obtained from DCP tests was 5.6 % and hence the M_R of the subgrade was calculated to 57,960 kPa. The thickness of each layer of the pavement was inputted into the software. After inputting all these parameters, the KENLAYER software was run for paved roads with unreinforced and reinforced bases to evaluate the stress at the mid depth of each base layer. The resilient strains at the mid depth of the 300 mm thick unreinforced and 230 mm thick reinforced RAP bases were found to be 0.00139 and 0.00098, respectively using the KENLAYER software.

The permanent deformations accumulated in unreinforced and geocell-reinforced RAP bases can be calculated from the average vertical resilient strains obtained from the KENLAYER analysis. In this study, the permanent deformation model proposed by Tseng and Lyton (1989) was modified by introducing a calibration factor K as shown in **Eq. 6.2.3**:

$$PD = K \cdot h_{soil} \cdot \varepsilon_v \cdot \left(\frac{\varepsilon_0}{\varepsilon_r} \right) \cdot e^{-\left(\frac{\rho}{N} \right)^{\beta}} \qquad \textbf{(6.2.3)}$$

The calibration factor K was introduced to account for the differences in the conditions between the soil samples under repeated load triaxial tests and the soil layers under large-scale cyclic plate loading tests. Since no triaxial tests were conducted on unreinforced and geocell-reinforced RAP bases, the model parameters

$\left(\dfrac{\varepsilon_0}{\varepsilon_r}\right)$, ρ, and β also need to be calibrated. Thus, the model parameters, $K\left(\dfrac{\varepsilon_0}{\varepsilon_r}\right)$, ρ, and

β, were calibrated based on the permanent deformation data obtained from the cyclic

plate loading tests. The calibration was carried out by a trial and error method until the

model calculated permanent deformation matched the measured permanent

deformation. For comparison purposes, the permanent deformation model used in the

MEPDG (**Eq. 6.2.2**) was also calibrated by replacing the global and local calibration

factors by a single factor K as shown in **Eq. 6.2.3**. In this model, the model parameters

$\left(\dfrac{\varepsilon_0}{\varepsilon_r}\right)$, ρ, and β for RAP bases were obtained according to the water content of 5.6%

using **Eq. 6.2.2**. The calibration factor K was determined by the hit and trial method

until the model calculated permanent deformation matched the measured permanent

deformation.

The calibrated parameters for both models are presented in Table **6.2.1**. The

model calculated and measured permanent deformations versus the number of loading

cycles for unreinforced RAP bases are shown in **Fig 6.2.1**. The calculated permanent

deformations for the unreinforced RAP bases matched well with the measured

permanent deformations. The model-calculated and measured permanent

deformations versus the number of loading cycles for geocell-reinforce RAP bases are

shown in **Fig 6.2.2**. For the geocell-reinforced RAP base, the calculated data using the

Tseng and Lytton model matched well with the measured data up to the loading cycles

of 5,000 and did not match well after that cycle as shown in **Fig. 6.2.2**. The deviation of

the model-predicted permanent deformation from the measured permanent deformation

after the loading cycles of 5000 may be because of the damage of geocell after that

number of loading cycles. For the geocell-reinforced RAP base, the calculated data using the MEPDG model did not match well with the measured permanent deformations as shown in **Fig 6.2.2**. This comparison may be due to the fact that the MEPDG model only considers the effect of the water content of the base layer but does not consider the effect of geosynthetics on the permanent deformation behavior. Hence it is concluded that Tseng and Lytton's model predicted the permanent deformation of the geocell-reinfoced RAP well up to the number of loading cycles corresponding to a stable base. However, the MEPDG model did not predict the permanent deformation of the geocell-reinforced RAP base well at different number of loading cycles.

Table 6.2.1   Model calibration parameters for permanent deformations of RAP bases

Types of RAP base	Model parameters	
	Tseng and Lytton (1989)	**MEPDG**
Unreinforced RAP	$K\left(\dfrac{\varepsilon_0}{\varepsilon_r}\right) = 92$ $\rho = 3764$ $\beta = 0.2$	$K = 4.2$ $\left(\dfrac{\varepsilon_0}{\varepsilon_r}\right) = 21.8$ $\rho = 3764$ $\beta = 0.2$
Geocell-reinforced RAP	$K\left(\dfrac{\varepsilon_0}{\varepsilon_r}\right) = 70$ $\rho = 3764$ $\beta = 0.4$	$K = 2.7$ $\left(\dfrac{\varepsilon_0}{\varepsilon_r}\right) = 21.8$ $\rho = 3764$ $\beta = 0.2$
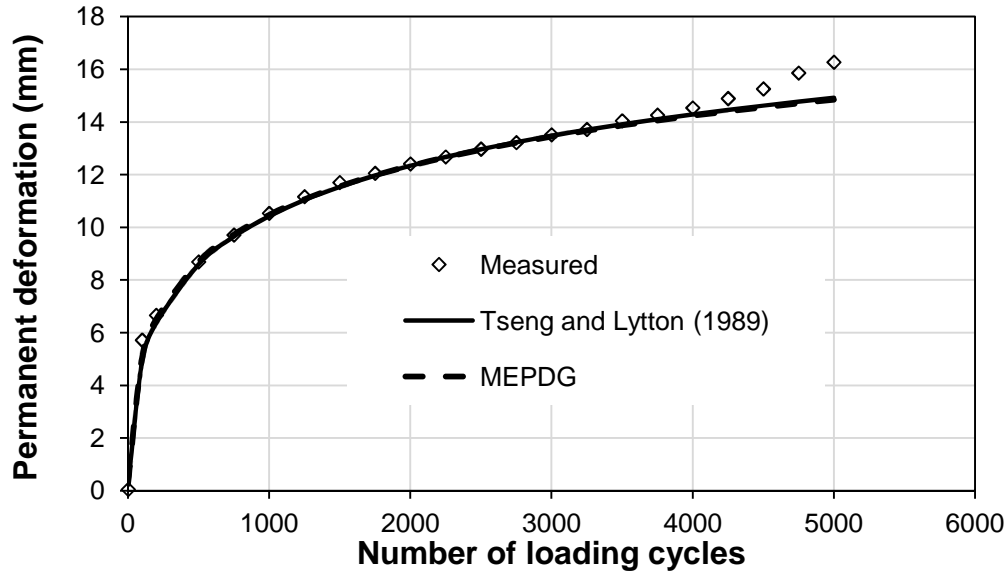
Fig. 6.2.1   Measured and calculated permanent deformations of unreinforced RAP bases
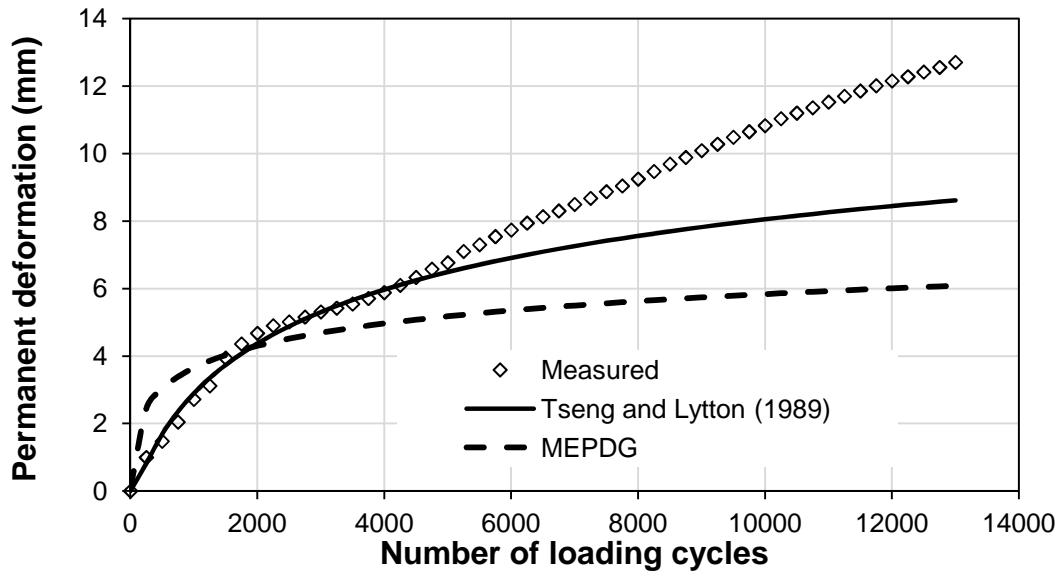
Fig. 6.2.2   Measured and calculated permanent deformations of geocell-reinforced RAP bases

209

Further analysis was carried out by varying Tseng and Lytton's model parameters to evaluate the effect of these parameters on the predicted permanent deformations of geocell-reinforced RAP bases. The parameter ρ was kept constant and equal to 3,764 as it does not have much effect on the shape of permanent deformation curves whereas the values of parameters $K\left(\dfrac{\varepsilon_0}{\varepsilon_r}\right)$ and β were varied. The calculated permanent deformations for different values of parameters are plotted and compared with each other and with the measured permanent deformations as shown in Fig. 6.2.3. The legend (70, 0.2) In **Fig. 6.2.3** represents the calculated permanent deformations at K $\left(\dfrac{\varepsilon_0}{\varepsilon_r}\right)$ = 70 and β = 0.2 and similar representation holds good for other values. It is shown that the model with $K\left(\dfrac{\varepsilon_0}{\varepsilon_r}\right)$ = 80 and β = 0.45 had the best estimate of the permanent deformations in average as compared with the measured data.
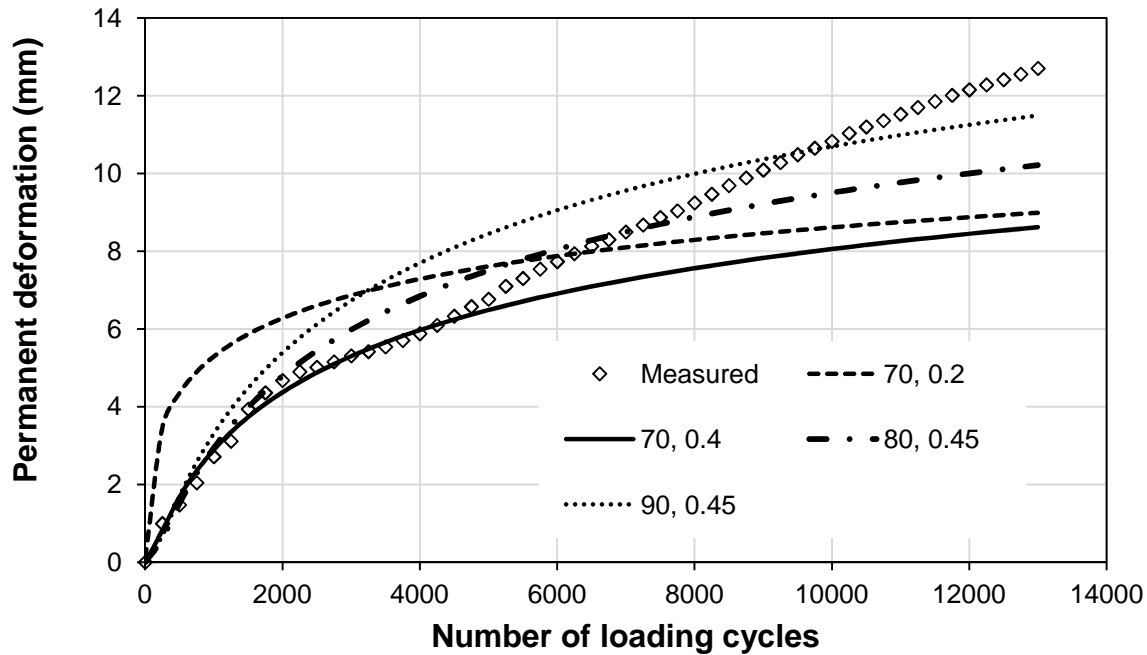
Fig. 6.2.3 Measured and calculated permanent deformations of geocell-reinforced RAP

bases for different values of Tseng and Lytton's model parameters

6.3   Summary

The development and calibration of empirical and mechanistic-empirical permanent

deformation models were described in this chapter.   The empirical model was

developed using correlation techniques whereas the mechanistic-empirical model was

developed using the hit and trial method.   The developed permanent deformation

models can be used to calculate the permanent deformations of unreinforced and

geocell-reinforced RAP bases at different number of loading cycles.   Following

conclusions can be made from this chapter:

(i) Two empirical permanent deformation models (the power model and the log

   normal model) were adopted to calculate the overall permanent deformations of

   unpaved and paved roads with unreinforced and geocell-reinforced RAP bases.

211

These models can also calculate the permanent deformations of individual layers of paved roads. Overall, the power model calculated the permanent deformation better than the log normal model.

(ii) The key assumption of the mechanistic-empirical model is that the permanent deformation of each pavement layer becomes stable after a large number of loading cycles. The mechanical-empirical model developed in this study was also based on this assumption and well calculated the permanent deformations of pavement layers. The Tseng and Lytton model and the model used in the MEPDG were calibrated based on the test results from cyclic plate loading tests on paved roads.

(iii) Overall, the calculated permanent deformations for unreinforced and geocell-reinforced RAP bases using the Tseng and Lytton model matched well with the measured permanent deformations. For the geocell-reinforced RAP bases, the calculated data using the MEPDG model did not match well with the measured data. This result may be due to the fact that the MEPDG model has only considered the effect of the water content of the layer and does not consider the effect of geosynthetics on the permanent deformation behavior.

(iv) The Tseng and Lytton model was recommended in this study to predict the permanent deformations of unreinforced and geocell-reinforced RAP bases.

(v) The calibrated models for RAP bases need to be validated with more test data with different base thickness and degree of geocell-confinement. The validated models should only be used to predict the permanent deformations of RAP bases.

Chapter 7

Conclusions and Recommendations

7.1   Conclusions

A series of large-scale laboratory cyclic plate loading tests were conducted on unpaved and paved roads with geocell-reinforced Recycled Asphalt Pavement (RAP) bases to demonstrate the benefit of geocell reinforcement in terms of reduced permanent deformation, and increased resilient deformation and vertical stress distribution angle. The empirical permanent deformation models were proposed for unpaved and paved roads with RAP bases and different layers of paved roads based on the experimental data from cyclic plate loading tests on unpaved and paved roads.   In addition, mechanistic empirical models were calibrated for unreinforced and geocell-reinforced RAP bases based on experimental data from cyclic plate loading tests on paved roads. The following conclusions can be drawn from the experimental study and damage model development:

7.1.1 Experimental study

Large-scale cyclic plate loading tests on unpaved roads

The conclusions drawn from the cyclic plate loading tests on unpaved roads are:

(i)   100% Recycled Asphalt Pavement (RAP) can be used as a base course material with geocell confinement to construct sustainable unpaved roads.

(ii)   The geocell reduced the permanent deformation and increased the

percentage of resilient deformation of geocell-reinforced RAP bases as compared with unreinforced bases. The amount and rate of permanent deformation increased with the number of loading cycles.

(iii) The Traffic Improvement Factor (TIF) can be used to determine relative performance of unpaved roads and also can be used to select an economic unpaved road section during design step.

(iv) The increase in the subgrade strength, the degree of geocell confinement, and the base course thickness reduced the amount of surface permanent compression and heave.

(v) The geocell-reinforced base sections and the base sections over moderate subgrade showed a stable response whereas the unreinforced base over weak subgrade showed an unstable response.

(vi) The geocell reinforcement reduced the vertical stresses transferred to the subgrade by distributing the load over a wider area. The vertical stresses at the interface of subgrade and base decreased with an increase of base thickness and degree of geocell confinement.

(vii) The vertical stresses in the unreinforced section increased with the number of load cycles until failure whereas those in the reinforced sections increased in the first few cycles and then decreased or became constant due to the slab or tensioned membrane effect of the geocell-reinforced layer.

(viii) The strain measurements showed that the thicker geocell-reinforced RAP base behaved as a slab with bending resistance while the thinner base behaved as a slab initially at a smaller deformation and then as a tensioned

membrane at a larger deformation.

<u>Large-scale cyclic plate loading tests on paved roads</u>

(i)   100% RAP with geocell confinement can be used as a base to construct sustainable unpaved and paved roads.

(ii)   The geocell-reinforced flexible pavements had lower surface and interface permanent deformations and a lower rate of increase in permanent deformations than the corresponding thick unreinforced sections.

(iii)   The Traffic Improvement Factor (TIF) can be used to determine relative performance of paved roads and also can be used to select an economic paved road section during design step.

(iv)   The increase in the base and subgrade strengths, the degree of geocell confinement, and the base course thickness reduced the amount of surface heave and compression.

(v)   The subgrade contributed to most of the total permanent deformation of the flexible pavement followed by the RAP base and the HMA surface.

(vi)   All reinforced sections shook down to a steady state showing largely resilient behavior whereas unreinforced sections did not shake down to a steady state and underwent continuous permanent deformation without showing much resilience. The percentage of resilient deformation increased sharply for the first few loading cycles.

(vii)   The maximum vertical stresses and the rate of increase of vertical stresses at the interface of base and subgrade in unreinforced sections were higher than

those in reinforced sections. The vertical stresses at the interface decreased with an increase of base and subgrade strengths, base thickness, and geocell reinforcement. The geocell-reinforced and thicker base sections reduced the vertical stress at the interface of base and subgrade by distributing the load to a wider area. The vertical stresses increased rapidly during the initial cycles and slowly at later cycles.

(viii) The strain gages affixed to the top, middle, and bottom of the geocell wall showed horizontal tensile, vertical compressive, and horizontal tensile strains, repspectively. The strains measured at the geocell wall decreased as it moved away from the center of the loading plate. The reinforced sections behaved as a slab with bending resistance and the geocell prevented the lateral spreading of base course materials.

7.1.2 Development of Damage Model

Two empirical permanent deformation models (the power model and the log normal model) were adopted to calculate the overall permanent deformations of unpaved and paved roads with unreinforced and geocell-reinforced RAP bases. These models can also calculate the permanent deformations of individual layers of paved roads. Overall, the power model calculated the permanent deformation better than the log normal model. The mechanistic-empirical models adopted in this study can be used to predict the permanent deformations of unpaved as well as paved roads with unreinforced and geocell-reinforced RAP bases. The key assumption of the mechanistic-empirical model was that the permanent deformations of pavement layers became stable after a large

number of loading cycles. The mechanical empirical model calibrated in this study well predicted the permanent deformations of unreinforced and geocell-reinforced RAP bases.

7.2 Recommendations for future studies

Following issues were identified in this study and are recommended to address in future studies:

(i) This study has considered only one type of geocell and RAP. A study with other types of geocell and RAP is needed to verify performance of geocell-reinforced RAP bases. A future study also needs to focus on resilient modulus of RAP and field performance of geocell-reinforced unpaved and paved roads.

(ii) Some important parameters, such as the effect of RAP cover thickness, the effect of RAP thickness between two layers of geocell, the effect of geocell layers (more than two layers), and the effect of amplitude of cyclic load, should be investigated to provide more comprehensive understanding of the behavior of geocell-reinforced unpaved and paved roads.

(iii) All the cyclic plate loading tests were carried out under a wheel load of 40 kN. The behavior of geocell-reinforced unpaved and paved roads under different wheel loads should be investigated.

(iv) The mechanistic empirical model was developed assuming a stable shakedown response of soil. The threshold stress level beyond which the soil

will fail under a repeated load can be determined by conducting repeated load triaxial tests under different cyclic deviatoric stresses.

(v)   The damage models developed in this study need to be validated with more cyclic plate loading tests and full-scale moving wheel tests of different base thickness and degree of geocell confinement.

(vi)   The experimental test results in this study can be used as a base for development of design methods for unpaved and paved roads with geocell-reinforced RAP bases and numerical modeling in the future.

REFERENCES

Abdelrahman, M., Alam, T.B., and Zollars, J. (2010). "Performance of high recycled asphalt pavement (RAP) content as base layer in flexible pavement." *Journal of Solid Waste Technology and Management,* 36 (3), 131-142.

Arsad, A.K.B. (2007). Flexible pavement design: Transitioning from empirical to mechanistic-based design methods. Retrieved February 20, 2013 from http://www.scribd.com/doc/98972857/14-15-18-19flexible-paveme

Attia, MIE-S. (2010). *Characterization of the structural behavior of reclaimed asphalt pavement as pavement base layer.* Ph.D. dissertation*,* Civil Engineering Department, the North Dakota State University.

Barksdale, R. D. (1972). "Laboratory evaluation of rutting in base course materials." *Third International Conference on Structure Design of Asphalt Pavements*, 161-174.

Bennert, T. and Maher, A. (2005). *The development of a performance specification for granular base and subbase material.* Report, New Jersey Department of Transportation, CN 600 Trenton, NJ 08625; 2005 Feb, Report No. FHWA-NJ-2005-003.

Bennert, T., Papp Jr, W.J., Maher A, and Gucunski N. (2000). "Utilization of construction and demolition debris under traffic-type loading in base and subbase applications." Transportation Research Record; 1714, 33-39.

Bortz, B.S., Hossain, M., Halami, I, and Gisi, A. (2012). "Low-volume paved road improvement with geocell reinforcement." Online publication, *Transportation Research Board,* Annual Meeting.

Clary, J.A., DeGroot, D.J., Highter, W.H. (1997). Structural numbers for reclaimed asphalt pavement base and subbase course mixes. *Final Report*. Department of Civil and Environmental Engineering, University of Massachusetts, Amherst, MA.

Copeland, A. (2011). *Reclaimed asphalt pavement in asphalt mixtures: State of the Practice.* Report No. FHWA-HRT-11-021, retrieved April 10, 2013 from: http://www.fhwa.dot.gov/publications/research/infrastructure/pavements/11021/1102 1.pdf.

Copeland, A., Jones, C., and Bukowski, J. (2010). *Reclaiming Roads*. Publication Number FHWA-HRT-10-001, 73 (5), retrieved March 2, 2013 from: http://www.fhwa.dot.gov/publications/publicroads/10mar/06.cfm.

Cosentino, P.J., Kalajian, E.H., Bleakley, A.M., Diouf, B.S., Misilo, T.J., Petersen, A.J., Krajcik, R.E., and Sajjadi, A.M. (2012). *Improving the properties of reclaimed asphalt pavement for roadway base applications.* Final Report, Florida Institute of Technology, Civil Engineering Department. Report No. FL/DOT/BDK81-97702.

Cosentino, P.J., Kalajian, E.H., Shieh, C.S, Mathurin, W.J.K., Gomez, F.A., Cleary, E.D., and Treeratrakoon, A. (2003). *Developing specifications for using recycled asphalt pavement as base, subbase or general fill materials*, Phase II. Final Report, Report No. FL/DOT/RMC/06650-7754, Florida Institute of Technology, Civil Engineering Department, 272p.

Das, B.M. and Shin, E.C. (1998). "Strip foundation on geogrid-reinforced clay: behavior under cyclic loading." *Geotextiles and Geomembranes,* 13(10), 657-666.

Donovan, H. (2011). "Recycled aggregate and geosynthetic study- City of Edmonton." *Annual Conference of the Transportation Association of Canada*, Edmonton, Alberta, 19p.

Edil, T.B., Benson, C.H., Bin-Shafique, S.M., Tanyu, B.F., Kim, W., and Senol, A. (2002). "Field evaluation of construction alternatives for roadways over soft subgrade." *Transportation Research Record,* 1786, 36-48.

Foye, K.C. (2011). "Use of reclaimed asphalt pavement in conjunction with ground improvement: A case history." *Advances in Civil Engineering*, Hindawi Publishing Corporation, 7p.

Garg, N. and Thompson, M.R. (1996). "Lincoln Avenue reclaimed asphalt pavement base project." Transportation Research Record; No. 1547, 89-95.

Giroud, J.P. and Han, J. (2004a). "Design method for geogrid-reinforced unpaved roads: I Development of design method." *Journal of Geotechnical and Geoenvironmental Engineering*, 130 (8), 775-786.

Giroud, J.P. and Han, J. (2004b). "Design method for geogrid-reinforced unpaved roads: II Calibration of applications." *Journal of Geotechnical and Geoenvironmental Engineering*, 130 (8), 787-797.

Gnanendran, C.T. and Woodburn, L.J. (2003). "Recycled aggregate for pavement construction and the influence of stabilization." *Proceedings on Australian Road Research Board,* Cairns, QLD, Australia, 1755-1768.

Guthrie, W.S., Cooley, D., and Eggett, D.L. (2007). "Effects of reclaimed asphalt pavement on mechanical properties of base materials." *Transportation Research Record,* 2005, 44-52.

Han, J., Acharya, B., Thankur, J.K., and Parsons, R.L. (2012). *Onsite use of recycled asphalt pavement materials with geocells to reconstruct pavements damaged by heavy trucks.* Report No. 25-1121-0001-462, Mid-America Transportation Center, 121p.

Han, J., Pokharel, S.K., Yang, X., Manandhar, C., Leshchinsky, D., Halahmi, I., and Parsons, R.L., (2011). "Performance of geocell-reinforced RAP bases over weak subgrade under full-scale moving wheel loads." *ASCE Journal of Materials in Civil Engineering,* 23(11), 1525–1534.

Han, J., Yang, X., Parsons, R.L., and Leshchinsky, D. (2007). *Design of geocell-reinforced bases.* Internal Report to PRS, the University of Kansas.

Han, J., Yang, X.M., Leshchinsky, D., and Parsons, R.L. (2008a). "Behavior of geocell-reinforced sand under a vertical load." *Journal of Transportation Research Board*, 2045, 95-101.

Han, J., Yang, X.M., Leshchinsky, D., Parsons, R.L., and Rosen, A. (2008b). "Numerical analysis for mechanism of a geocell-reinforced base under a vertical load." *Proceeding of 4th Asian Regional Conference on Geosynthetics*, June 17-20, 2008 Shanghai, China, 741-746.

Huang, Y.H. (1993). Pavement Analysis and Design. Englewood cliffs: Prentice-Hall, 805p.

Kim, W. and Labuz, J.F. (2007). *Resilient modulus and strength of base course with recycled bituminous material.* Final Report, Minnesota Department of Transportation. Report No.: MN/RC-2007-05, retrieved on March 10 from: http://www.lrrb.org/pdf/200705.pdf.

Khedr, S. (1985). Deformation characteristic of granular base course in flexible pavement. *Transportation Research Record* 1043, Transportation Research Board, Washington, D.C., 131-138.

Lekarp, F., Isacsson, U., and Dawson, A. (2000). State of the art II: Permanent strain response of unbound aggregates. *Journal of Transportation Engineering,* 126 (1), 76-83.

Li, K., Henson, C.H., Edil, T.B., and Hatipoglu, B. (2007). "Evaluation of recycled asphalt pavement material stabilized with fly ash." *Proceedings of Sessions of Geo-Denver,* Soil and Material inputs for Mechanistic-Empirical Pavement Design, 169, 77-86.

McGarrah, E.J. (2007). *Evaluation of current practices of reclaimed asphalt pavement/virgin aggregate as base course material.* WSDOT Research Report, Report No. WA-RD 713.1, 41p.

Mengelt, M. J., Edil, T. B., and Benson, C. H. (2000). *Reinforcement of flexible pavements using geocells. Geo Engineering Report No. 00-04*, University of Wisconsin-Madison, Madison, WN.

Mhaiskar, S.Y. and Mandal, J.N. (1992). "Soft clay subgrade stabilization using geocells." *Proceedings on Grouting, Soil Improvement and Geosynthetics,* ASCE Geotechnical Special Publication, 30 (2), 1092-1103.

Missouri Asphalt Pavement Association (2010). *Recycling of asphalt pavement.* Retrieved December 10, 2012 from: http://www.moasphalt.org/facts/environmental/recycling.htm.

Papp, W.J. Jr., Maher, M.H., Bennert, T.A., and Gucunski, N. (1998). "Behavior of construction and demolition debris in base and subbase applications." *Proceedings of Sessions of Geo-Congress*: Recycled materials in geotechnical applications, ASCE Annual Convention, Boston, 1998 October, 79, 122-36.

Paute, J. L. (1988). "Modèle de calcul pour le dimensionnement des chaussees souples." *Bull. de Liaison des Laboratoires des Ponts et Chaussées*, 156, 21-36, (in French).

Paute, J. L. (1994). "Comportement mécanique des graves non traitées." *Bull. de Liaison des Laboratoires des Ponts et Chaussees*, 190, 27-38, (in French).

Pokharel, S.K. (2010). *Experimental study on geocell-reinforced bases under static and dynamic loadings.* Ph.D. Dissertation*,* CEAE Department, the University of Kansas, 316p.

Pokharel, S.K., Han, J., Leshchinsky, D., Parsons, R.L, and Halahmi, I. (2010). "Investigation of factors influencing behavior of single geocell-reinforced bases under static loading." *Geotextiles and Geomembranes*, 28 (6), 570-578.

Potturi, A.K. (2006). *Evaluation of resilient modulus of cement and cement-fiber treated reclaimed asphalt pavement (RAP) aggregates using repeated load triaxial test.* MS Thesis, The University of Texas at Arlington.

Presto Geosystems (2007). *Geoweb load support system: Technical overview*, 19p.

Rajagopal, K., Krishnaswamy, N.R., and Madhavi Latha, G. (1999). "Behaviour of sand confined with single and multiple geocells." *Geotextiles and Geomembranes,* 17 (3), 171-184.

Recycled Material Research Center (RMRC, 2008). *User guideline for byproducts and secondary use materials in pavement construction.* Retrieved May 24, 2012 from: http://www.recycledmaterials. org/tools/uguidelines/rcc4.asp.

Samad, E. (2011). Sensitivity analysis in flexible pavement performance using mechanistic empirical method (Case study: Cirebon-Losari road segment, West Java). *Civil Engineering Forum,* Vol. 20, 12p.

Sweere, G. T. H. (1990). Unbound granular bases for roads*. Ph.D. Dissertation*, University of Delft, Delft, Netherlands.

Taha, R., Ali, G., Basma, A., and Al-Turk, O. (1999). "Evaluation of reclaimed asphalt pavement aggregate in road base and subbase." *Transportation Research Record*. 1652, 264-69.

Thakur, J.K., Han, J., Leshchinky, D., Halahmi, I., and Parsons, R.L. (2011). "Creep deformation of unreinforced and geocell-reinforced recycled asphalt pavements." Advances in Geotechnical Engineering, Geotechnical Special Publication No. 211, *Proceedings of GeoFrontiers 2011,* Han, J. and Alzamora, D.E. (editors), Dallas, TX; 2011 March 13-16, 4723-4732.

Thompson, M.R. (1992). ILLI-Pave base conventional flexible pavement design procedure, *Proceedings of the 7th International Conference on Asphalt Pavements*, 318-333, London, ISAP.

Tseng, K. and Lytton, R. (1989). "Prediction of permanent deformation in flexible pavement materials." *Implication of Aggregates in the Design, Construction, and Performance of Flexible Pavements*, ASTM STP 1016, 154-172.

Vennapusa, P.K.R. and White, D.J. (2009). "Comparison of light weight deflectometer measurements for pavement foundation materials." *Geotechnical Testing Journal*, 32(3), 239-251.

Veverka, V. (1979). Raming van de spoordiepte bij wegen met een bitumineuze veharding. *De Wegentechniek*, 24(3), 25-45 (in Dutch).

Viyanant, C., Rathje, E.M., and Rauch, A.F. (2007). "Creep of compacted recycled asphalt pavement." *Canadian Geotechnical Journal,* National Research Council of Canada, 44(6), 687-697.

Wen, H. and Wu, M. (2011). *Evaluation of high percentage recycled asphalt pavement as base materials.* Final Technical Report, United States Department of Transportation, Report No. TNW2011-15.

Wen, H., Warner, J., Edil T, and Wang, G. (2010). "Laboratory comparison of crushed aggregate and recycled pavement material with and without high carbon fly ash." *Geotechnical and Geological Engineering*; 28, 405-11.

Wen, H., Warner, J., Edil, T., and Wang, G. (2010). "Laboratory comparison of crushed aggregate and recycled pavement material with and without high carbon fly ash." *Geotechnical and Geological Engineering*, 28, 405-411.

West, R.C. (2011). *Reclaimed asphalt pavement management: Best practices.* National Center for Asphalt Technology (NCAT) Report, sponsored by Federal highway administration (FHWA), 34p.

Wu, Z. (1999). "Structural performance of cold recycled asphalt pavements." *Transportation Scholars Conference Compendium of Student Papers.* Midwest Transportation Consortium, Iowa State University, Ames, IA.

Yang, X.M. (2010). *Numerical Analyses of Geocell-Reinforced Granular Soils under Static and Repeated Loads.* Ph.D. Dissertation, CEAE Department, the University of Kansas, 192p.